Studies on Structural and Dynamical Aspects of Non-adiabatic Effects in Small Polyatomic Molecules

A thesis
submitted by

Satyam Ravi

in partial fulfillment of
the requirements for the degree of

Doctor of Philosophy

Indian Institute of Science Education and Research (IISER), Mohali

July 2019

Certificate of Examination

I hereby certify that the thesis titled *"Studies on Structural and Dynamical Aspects of Non-adiabatic Effects in Small Polyatomic Molecules"* submitted for the degree of Doctor of Philosophy by **Mr. Satyam Ravi** (Reg. No. PH11080) is the record of research work carried out by him during the period Aug 2011 to April 2019 under my guidance and supervision and further state that this work has not formed the basis for the award of any degree, diploma or a fellowship to any other University or Institute. I further state that this work in this thesis was carried out independently by Mr. Satyam Ravi. In my capacity as the supervisor of the candidate's PhD thesis work, I certify that the above statements are true to the best of my knowledge.

Place: Mohali
Date: 29th July, 2019

Dr. K. R. Shamasundar
(Research Supervisor)

Declaration

The work presented in this thesis has been carried out by me under the guidance of Dr. K. R. Shamasundar at the Indian Institute of Science Education and Research Mohali. This work has not been submitted in part or in full for a degree, diploma or a fellowship to any other University or Institute. Whenever contributions of others are involved, every effort has been made to indicate this clearly, with due acknowledgement of collaborative research and discussions. This thesis is a bonafide record of original work done by me and all sources listed within have been detailed in the bibliography.

Place: Mohali **Satyam Ravi**

Date: 29th July, 2019 **(Candidate)**

Acknowledgements

My venture of pursuing theoretical chemistry as my profession over the last seven years at IISER Mohali, has finally reached to its fruition with the completion of my thesis. Though only my name appears on the cover of this dissertation, I can not neglect the contributions of a great many people from whom I have benefited a lot directly or indirectly. I take this opportunity to show my deepest gratitude to all the people who have made this dissertation possible and because of whom this incredible journey of mine has become the one which I will cherish forever.

First of all, I would like to express my sincere gratitude towards my thesis supervisor Dr. K. R. Shamasundar for his constant and unwavering guidance during my thesis work and for sharing his valuable insights into chemistry with me. I have been amazingly fortunate to have an supervisor like him, who gave me the freedom to explore on my own and at the same time the guidance to recover when my steps faltered. He has always been like a friend guiding me through the beauty of Quantum chemistry and myriad experiences of life as well. I have learned a lot of things from him both professionally and personally as he is a great philosopher and a chemist as well. I shall remain forever indebted to him for his patience, support and encouragement which has helped me to overcome many crisis situations and finish my dissertation in time. I am also thankful to Mrs. Nagashree for her support during my stay in IISER Mohali.

In particular, I would like to thank Prof. Michael Baer from Israel as he has always been supportive of me and has helped me a lot by his vast knowledge and experience in the subject of my thesis. He taught me various aspect of non-adiabatic effect and has also helped me a lot as a collaborator in finishing one of my thesis work (Chapter3).

I am thankful to Professor N. Sathyamurthy, former Director of IISER Mohali for teaching me fundamentals of reaction dynamics and providing me the excellent research facilities. I am also thankful to Professor Arvind, Director of IISER Mohali for providing me the excellent research facilities.

I would like to thank Prof. K. S. Viswanathan and Dr. Ramesh Ramchandran for being the members of my peer review committee. They all have been very generous in offering constant academic support, valuable insights and suggestions during the peer review evaluation of my thesis work.

I am also grateful to Dr. Sanjay Singh and his group members Prasanth, Kuldeep, Deepender for their immense support and hard work which has helped me a lot to finish a number of interesting problems during my time as a Ph.D student at IISER Mohali.

I also thank my teachers at IISER Mohali, Dr. P. Balanarayan, Dr. A. K. Dey, Prof. J.S. Bagla, Prof. R. S. Johal, Dr. Samrat Mukhopadhyay, Prof. Sanjay Mandal who taught me various subjects during my course work. I always feel to be blessed enough for having teachers like them who made my foundations strong in the subject.

I gratefully acknowledge the help and support from all the faculty members of Chemical sciences, staff, library, and HPC facility at IISER.

I thank the Ministry of Human Research and Development (MHRD), India for providing me financial assistance during my research. I am grateful to the Department of Chemical Sciences, the institute and CICS for providing financial support for national and international conferences as well as an excellent environment for pursuing my research smoothly.

During my stay here at IISER Mohali I grew fond of my seniors, Dr. Devmalya Das, Dr. C. Jebarathinam, Dr. Saurabh Srivastava and Dr. Pradeep. I have learnt a lot of things professionally and personally from them which really expedited my research work and made my stay at the campus pleasurable. My special thanks to my two lab mates Dr. Jitender Gupta and pratip for sharing the work place and discussed many interesting things during the course of thesis work. I am also indebted to the most important people Chinmoy, Shruti, Shilpa, Sumyra, Swagatam, Rajnessh, Anshul Arnob, Sudhanshu, Avinash, Ankit, Priyanka, Pooja, Ayushi, Abhinay, Mayank, Abhishek and Gaurav in my life here at IISER Mohali who have always given me strength, support and encouragement to achieve my goals whenever I was at my lowest. I am lucky to have these wonderful friends in my life who are fast becoming a part of my extended family. My friends Meghna, Avdhoot and Rajwant deserve an additional thank from me as they have always been there for me and have helped me a lot in my research in many ways.

I am grateful to my M.sc. friends Shashank, Indrani, Shivani, Madhulika, Avinash, Ajay, Sushobhan and Sonshree for their valuable friendship, affection and support towards me.

I would also like to thank my friends from graduation days Shashank, Aviral, Rahul, Deepak and Pankaj and many more who have always been an integral part of my life.

Last but not the least, all of my success in life and achievements would not have been made possible without the constant love and support from my family members and close relatives. It is not be possible for me to express in words the debt and gratitude I owe to my parents. I shall forever remain grateful to them for their love, care, blessings and sacrifices they made for me. I would also like to thank my two elder brothers Rohan and Shashawat, sister-in-laws Shalini and Tulika for their love,

support and constant encouragement through all ups and downs in my life. Without them I could not have fulfilled my dreams and achieved what I have achieved today.

Satyam Ravi

Dedicated

to

My parents

List of Abbreviation

BO	Born-Oppenheimer
BOA	Born-Oppenheimer approximation
AA	Adiabatic approximation
TISE	Time-independent Schrödinger Equation
TDSE	Time-dependent Schrödinger Equation
PES	Potential energy surface
CI	Conical intersection
ADT	Adiabatic to diabatic transformation
NACT	Non-adiabatic coupling term
NAC	Non-adiabatic coupling
MECI	Minimum energy conical intersection
MEP	Minimum energy path
TS	Transition state
IRC	Intrinsic reaction coordinate
IRD	Inrinsic relaxation direction
AIMD	*Ab-initio* molecular dynamics
MCTDH	Multi-configuration time dependent hartree
GWP	Gaussian wave-packet
FGA	Frozen gaussian approach
AIMS	*Ab-initio* multiple spawning
FMS	Full multiple spawning
TSH	Trajectory surface hopping
FSA	Fewest switches algorithm
TBF	Trajectory basis function
v-MCG	Variational multiconfigurational gaussian
DD-v-MCG	Direct-dynamics variational multiconfigurational gaussian
CCS	Coupled-coherent state
SR	Single reference
MR	Multi reference
MO	Moleular orbital
HF	Hartree-Fock
MP2	Møller-Plesset second order perturbation theory

CCSD	Coupled-Cluster singles and doubles
EOM-CCSD	Equation-of-motion Coupled-Cluster singles and doubles
MRCI	Multireference configuration interaction
MCSCF	Multiconfiguration self-consistent-field method
SA-MCSCF	State-averaged multiconfiguration self-consistent-field method
CASSCF	Complete-active-space self-consistent-field method
CASPT2	Complete-active space second order perturbation theory
MS-CASPT2	Multistate complete-active space second order perturbation theory
TRPES	Time-resolved photoelectron spectroscopy
FC	Frank-Condon
IC	Internal conversion
ISC	Intersystem crossing
SCO	Spin-orbit coupling
AC	Acrolein
CR	Crotonaldehyde
CPO	2-Cyclopentaenone
MVK	Methyl vinyl ketone
MA	Methacrolein
FN	Formaldonitrone
Oxz	Oxaziridine
NM	Nitrosomethane
FO	Formaldoxime
FA	Formamide

Synopsis

The thesis is based on our recent research efforts aimed to further understanding on certain aspects of non-adiabatic paradigm as well as to explore a few applications of computational methods of electronic structure and dynamics to describe electronic relaxation and reaction paths in photochemistry of small organic molecules.

The Born-Oppenheimer approximation (BOA) has been one of the most important milestone towards conceptual understanding and computational description of chemical phenomena. Its result - the potential energy surface (PES) - has been an important element of chemist's visualization of bonding in different isomeric structures of molecules explaining their rovibronic spectra, energetic and kinetics of chemical reactions. In combination with Franck-Condon (FC) principle, it makes it possible to interpret absorption and fluorescence spectra using both ground and excited state PES.

Over past few decades, a number of phenomena collectively referred to as non-adiabatic effects [1–4] have been observed in chemical physics that require one to go beyond BOA. They are manifested in a wide-variety of situations such as the appearance of irregular band structure in electronic absorption spectroscopy, the non-radiative electronic quenching transitions and chemi-luminescent reactions in photochemistry, the geometric phase effects in low-energy reactive scattering of small molecules [5]. They have been now understood to be linked to the invalidity of adiabatic separation of nuclear and electronic degrees of freedom that underlies BOA. Making use of the Born-Huang expansion, a strong coupling of these degrees of freedom can be seen to occur around the intersection region of PESs. Though the existence of such region had been known for a long-time, being the subject of the non-crossing rule [6] and the crossing conditions [7, 8], their importance was brought out in efforts to understand internal conversion in photochemical reactions. A type of intersection point around which two intersecting PESs exhibit a double-cone structure, known as conical intersection (CI), has been identified as an important conceptual element of the non-adiabatic paradigm. Their prevalence in polyatomic molecules is now a well-established fact.

A variety of modern ultrafast spectroscopic techniques designed to explore sub-picosecond to sub-femtosecond molecular processes have demonstrated the ubiquitous presence of non-adiabatic effects at such time-scales. Although such techniques have been used to probe a number of interesting situations such as the primary photo-isomerization event in vision and the photo-stability of DNA and RNA bases, it relies upon models of CI crossings and nuclear dynamics in the probed systems. The interpretation of such results from such methods is benefited by a development of

computational approaches to account for non-adiabatic effects.

Several works have been carried out in the last three decades to develop theoretical and computational methods for the description non-adiabatic effects in polyatomic molecules. This requires correct description of quantum effects arising from propagation, spreading, branching and recrossing of the nuclear wave-packet around low-energy accessible CI regions. Many methods developed in the last two decades have mainly focused on achieving an approximate description of nuclear dynamics on multiple coupled PES [9–11]. Such methods vary from very accurate fully quantum wave-packet based descriptions to more approximate ones based on semi-classical and classical trajectories.

Electronic structure methods to locate intersection geometries on excited states have also allowed to reach a better mechanistic understanding of the photochemical reactions. This has made it possible, for example, to rationalize formation of different photo-products and their relative branching ratios [12, 13].

The first part of the thesis covers two case-studies intended to explore the structural features of intersection seams in small polyatomic molecules. The second part discusses two applications utilizing currently available electronic structure and trajectory based nuclear dynamics methods to study the non-adiabatic population transfer and photochemical reaction pathways in two prototype cases of photochemical reactions. The thesis is planned to include a total of seven chapters, with four chapters describing these case studies. The remaining chapters are a chapter on introduction, a chapter on review of computational photochemistry and a chapter on summary at the end.

In the introduction chapter of the thesis, we briefly discuss the prevalence and importance of non-adiabatic effects in chemical physics, drawing a few examples from the literature to give a picture of current state of this vast area. We present different frameworks used for theoretical description of non-adiabatic effects highlighting the important elements necessary for its conceptual understanding. A general outline of currently available *ab initio* electronic structure and nuclear dynamics methodologies applicable for non-adiabatic studies is presented.

The next two chapters explore the theme of the first part of thesis - exploring the structure of intersections seams in the nuclear configuration space. It is well-known that the CIs are not isolated features but a part of a continuous, highly-irregular, multidimensional structure known as intersection seams. Earlier studies have shown that a seam can have different branches which meet at points known as confluences. Some examples have been known where seams of different pair of states merge at three-state intersections. Although a detailed structure of the seam

is not necessary for many successful applications, examples are known where seam information improves the quality of computational descriptions. Since understanding and characterizing the structure of the seam of polyatomic molecules is a formidable task, we have performed two case studies to gain some understanding on this aspect.

The second chapter explores the seam structure of a simple triatomic molecule H_3^{++}. In triatomic molecules, the seam is usually a one-dimensional line which makes it easy to visualize. Simple electronic structure of this molecules allows us to use simple degeneracy tracking procedures to construct and visualize the seam over a larger region of nuclear configuration space. When visualized in hyperspherical coordinate system, the seam shows several interesting structures involving several confluences of its different symmetry branches.

In the third chapter, a case-study to explore the utility of another approach based on behaviour of non-adiabatic couplings (NAC) in the vicinity of a seam point to reveal the local structure of a general seam is presented. Considering Ethylene as a prototype system, we explore the geometry of intersecting seam within certain geometrical planes around two minimum energy conical intersections (MECIs) reported to be relevant for its S_1-S_0 photochemistry [14, 15]. According to the quantization rules [16], integrating the component of NAC vector along a closed contour containing one or more CI points yields a multiple of π. Following the approach of Bäer and coworkers [1, 2], we setup a set of simple closed contours described by angular and radial coordinates in the nuclear configuration space at the chosen MECI geometries. We attempt to relate the behaviour NACs along a series of contours corresponding to different radial coordinates to the seam geometry within the plane of containing these contours.

The ensuing three chapters focus on the theme of the second part - computational investigation of photochemical reaction paths in simple organic molecules. The fourth chapter serves as a brief introduction to some of the current concepts and methods of computational photo-chemistry - an active area of modern chemical physics. After a brief overview of basic photochemical processes, with the help of an example we discuss how the modern view of photochemical processes involving CIs differs from the classical view. We discuss how computations of minimum energy conical intersection (MECI), minimum energy path (MEP), intrinsic relaxation direction (IRD) are used build a picture of static picture of photochemical reaction. The role of dynamical aspects not included in such a picture is also emphasized. The chapter ends with a description of direct dynamics methods for photochemical investigation, with a special emphasis on the *ab initio* multiple spawning (AIMS) method which has been used in our studies.

Fifth chapter is a comparative study of electronic relaxation in Acrolein and its methylated derivative Crotonaldehyde. In the recent years, substituent effects have been used to as a way to infer general relaxation mechanisms in related molecules, as illustrated in the case of conjugated hydrocarbons [17–19]. Significantly different relaxation behaviours observed in experiments on methyl substituted Acrolein have not been understood fully [18,20]. In this work, we describe our attempts to validate the existing static picture of first three singlet and two triplet electronic states of Acrolein and Crotonaldehyde molecules based on calculations performed at high-level multireference methods. Our results confirm that static models are not able to fully account the observed differences. We have attempted to understand whether approximate dynamics calculations using AIMS simulations can provide additional clarity on this. While our results clearly establish that ultrafast relaxation in S_2 state is very similar for both molecules, they are not enough to attribute the experimentally observed differences to the corresponding differences in S_1 state dynamics.

Chapter six is an account of our attempts to understand electronic relaxation in photochemical electrocyclic reactions involving heteroatom using a simple model system. We have carried out a computational study on a prototype nitrone-oxaziridine system [21–24]. The ground state and the excited state PES have been explored to locate several minima, transition states and minimum energy conical intersection (MECI). Intrinsic reaction coordinate (IRC) and intrinsic reaction direction (IRD) calculations have also been performed to identify photo-products. A $200fs$ two-state AIMS simulation has been carried out to augment these studies and to describe the dynamical effects. We have attempted to develop a general mechanistic framework which can be useful to rationalize photochemical reactions of other nitrone systems

Contents

List of Tables

List of Figures

Chapter 1

Introduction

1.1 The Non-adiabatic Effects

Description and understanding of non-adiabatic effects is now one of the important research endeavours of chemical physics [1–5, 9–11, 30–33]. These effects originating from a strong coupling between electronic and nuclear degrees of freedom, and manifest themselves in a wide-variety phenomena such as the ultrafast quenching of electronic excitations [34] or the presence of irregular bands in electronic spectroscopy [35]. To obtain a qualitative understanding of the phenomena and to provide its reliable quantitative descriptions, a number of theoretical, computational and experimental approaches need to be synergistically used [10, 11]. Electronically non-adiabatic processes involve multiple electronic states strongly coupled via the nuclear motions. Such strong couplings, which become singular at some localized regions of nuclear configuration space, invalidate one of the most widely used approximation in chemical physics - the Born-Oppenheimer Approximation (BOA) [30, 31].

The BOA underlies one of the fundamental concepts of chemistry - the concept of molecular geometry and intuitive understanding of chemical reactions in terms of changes in molecular geometry. The large difference in masses of electrons and nuclei justifies an apriori separation of the faster electronic degrees of freedom from the slower degrees of nuclei. Although this itself is not BOA, it indicates that, in principle, it is possible to treat quantum mechanical motion of a molecular system by first solving the time-independent Schrödinger equation (TISE) for its electronic degrees followed by a time-dependent Schrödinger equation (TDSE) for the remaining nuclear degrees. The electronic TISE treatment results in potential energy surface (PES) which, along with the inter- and intra-surface non-adiabatic coupling (NAC),

allow for a complete description of the nuclear motion as implied by the TDSE. The large energetic separation between ground and excited electronic states observed for most molecules indicates that corresponding NACs appearing in treatment of nuclear motion can be neglected, eventually leading to the BOA. The nuclear motion can be thought of as happening on ground PES, without any interference from excited states. The BOA gives legitimacy to the use of ground state PES obtained from quantum chemical calculations, for understanding ground state chemical structures, their stabilities and reactivities, without performing further computations involving nuclear TDSE [36–38].

Although the situations involving breakdown of BOA were also identified and discussed much before, in the last three decades, with considerable advances in theoretical and experimental techniques, several such cases have been explored in depth [3, 9, 32, 33]. Extensive efforts made by several research groups have brought out a paradigmatic shift in the conventional BOA, and many conceptual elements of a new paradigm - the non-BO paradigm - have been developed.

One important element of non-BO paradigm is the conical intersection (CI) of two electronic states, defined as a molecular geometry where the states are exactly degenerate. Despite being structural features of the electronic Hamiltonian, they produce strong non-adiabatic effects in their vicinity due to the singular nature of NACs at their location. The pioneering works of Teller [7] and Longuet-Higgins [8] clarified the conditions and the consequences of existence of CIs arising from accidental degeneracies in general polyatomic molecules. Despite this, such fully accidental CIs were considered to be much rarer in occurrance as compared to the well-known symmetry-induced CIs arising in Jahn-Teller systems [39, 40]. Subsequent developments of theoretical and computational non-adiabatic frameworks [1, 3, 34, 41–44], important advances in time-resolved experimental methods to probe sub-picosecond dynamics, and introduction of analytic gradient techniques in quantum chemistry completely changed this perception. Initial applications by Baer, Robb, Yarkony, Ruedenberg and several others groups have demonstrated that presence of accidental CIs is a norm rather than an exception for most molecules.The non-BO paradigm with its CI concept has significantly altered the thinking in many areas. Qualitative mechanistic understanding of photochemical reactions is now much benefited by a knowledge about the presence of low-lying CIs in the vicinity of pathways originating from the Franck-Condon region [9, 12, 13, 45, 46]. The concept of geometric phase, another non-BO concept, has been found to be important in non-adiabatic reactive scattering calculations [47–52].

In the first part of this thesis covering first three chapters, we have set out to

explore certain aspects of conical intersection seams through some examples. In the second part, covered by remaining chapters, we have applied a variety of methods of computational photochemistry to study non-adiabatic photochemical pathways and ultrafast electronic quenching dynamics in small organic molecules. In this chapter, we provide a brief and general overview of some of the important theoretical concepts, methods and literature on non-adiabatic dynamics. A limited overview of computational photochemistry mainly relevant for the second part of the thesis is given in Chapter 4.

1.2 Framework for Non-adiabatic Effects

In this section, we discuss one of the most widely used theoretical framework for treatment of non-adiabatic effects - the Born-Huang (BH) framework. This originates from the work of Born and Huang [36], and fully accounts for geometry dependence of electronic wave-functions. Later, the framework has been extended to include diabatic transformations and geometric phase effects through several important contributions of Baer, Mead, Yarkony, Cederbaum and others [43, 44, 53–55]. An alternative framework is Jahn-Teller expansion [56] where electronic wave-functions at a special geometry are used.

1.2.1 The Born-Huang (BH) Treatment

The quantum mechanical dynamics of molecules - a collection of electrons and nuclei bound through electromagnetic forces - is governed by the fundamental time-dependent Schrödinger equation (TDSE).

$$\hat{H}|\Psi\rangle = i\hbar \frac{d}{dt}|\Psi\rangle. \tag{1.1}$$

where $\hat{H}$ is the molecular Hamiltonian, and $|\Psi\rangle$ is a wave-function representing the state of a molecule at a point of time t. According to the principles of quantum mechanics [57,58], the Hamiltonian is an operator (denoted by a hat) which represents the sum of total kinetic energy of particles and potential energies of interactions between them. It operates in the space of all possible wave-functions of a molecule. The TDSE describes the time evolution of a quantum system starting with a certain initial wave-function. For example, when a molecule is prepared in a specific photo-excited state, this initial state then evolves according to the TDSE into a combination of different molecular states representing outcomes of different photo-processes. As

per the linear superposition principle, the resulting molecular wave-function can be decomposed into a linear combination of wave-functions representing different outcomes.

To construct the molecular Hamiltonian, we consider an isolated molecule consisting of n electrons and N nuclei, and their positions denoted by labels $\mathbf{q}$ and $\mathbf{Q}$ respectively. The charge and mass of the electron are denoted by $-e$ and m_e. Similarly, the charge and mass of a nucleus with label α are denoted by $Z_\alpha \cdot e$ and M_α. The standard non-relativistic Hamiltonian can be defined as,

$$\hat{H}(\mathbf{q}, \mathbf{Q}) = \hat{T}_n(\mathbf{Q}) + \hat{T}_e(\mathbf{q}) + \hat{V}_n(\mathbf{Q}) + \hat{V}_e(\mathbf{q}) + \hat{V}_{ne}(\mathbf{Q}, \mathbf{q}) \tag{1.2}$$

where $\hat{T}_n$ and $\hat{T}_e$ are operators for total kinetic energy of the electron and the nuclei, respectively. The quantity $\hat{V}_n$ is the sum of Coulomb repulsion between nuclei, $\hat{V}_e$ is the sum of Coulomb repulsion between electrons, and $\hat{V}_{ne}$ is the sum of Coulomb attraction between nuclei and electrons. The operators for nuclear and electronic kinetic energy can be defined as,

$$\hat{T}_n(\mathbf{Q}) = -\frac{\hbar^2}{2} \sum_{\alpha}^{N} \frac{1}{M_\alpha} \nabla_\alpha^2 \tag{1.3a}$$

$$\hat{T}_e(\mathbf{q}) = -\frac{\hbar^2}{2m_e} \sum_{k=1}^{n} \nabla_k^2 \tag{1.3b}$$

The scalar operators total potential energy is defined as,

$$\hat{V_n}(\mathbf{Q}) = e^2 \sum_{\alpha<\beta}^{N} \frac{Z_\alpha Z_\beta}{|Q_\alpha - Q_\beta|} \tag{1.4a}$$

$$\hat{V_{ne}}(\mathbf{Q}, \mathbf{q}) = -e^2 \sum_{\alpha=1}^{N} \sum_{k=1}^{n} \frac{Z_\alpha}{|Q_\alpha - q_k|} \tag{1.4b}$$

$$\hat{V_e}(\mathbf{q}) = e^2 \sum_{k<l}^{n} \frac{1}{|q_k - q_l|} \tag{1.4c}$$

By choosing units such that $\hbar$ can be set to unity, nuclear masses can be expressed in units of an average nuclear mass M. Adapting a set of scaled cartesian coordinates, the nuclear kinetic energy operator $\hat{T}_n$ in equation (1.3a) can written in a simple form as follows.

$$\hat{T}_n(\mathbf{Q}) = -\frac{1}{2M} \sum_{\alpha}^{N} \nabla_\alpha^2 = -\frac{1}{2M} \nabla \cdot \nabla \tag{1.5}$$

For a fixed configuration of nuclei represented by $\mathbf{Q}$, an electronic Hamiltonian $\hat{H}_e$ can defined as follows.

$$\hat{H}_e(\mathbf{q};\mathbf{Q}) = \hat{T}_e(\mathbf{q}) + \hat{V}_e(\mathbf{q}) + \hat{V}_{ne}(\mathbf{q};\mathbf{Q}) + \hat{V}_n(\mathbf{Q}) \tag{1.6}$$

The electronic Hamiltonian can be viewed as an operator acts only on electronic wave-functions and depends parametrically on nuclear configuration $\mathbf{Q}$. Its eigenfunctions $\Phi_i(\mathbf{q};\mathbf{Q})$ and corresponding eigenvalues $V_i(\mathbf{Q})$ (here i labels electronic states) can be obtained by solving the electronic TISE,

$$\hat{H}_e(\mathbf{q};\mathbf{Q})\Phi_i(\mathbf{q};\mathbf{Q}) = V_i(\mathbf{Q})\Phi_i(\mathbf{q};\mathbf{Q}) \tag{1.7}$$

which is an eigenvalue equation. The subject of quantum chemistry deals with methods for its solution, taking into account of the fully quantum nature of electrons, their intrinsic spins, and their indistinguishability according to the anti-symmetry principle. This will be discussed later in section 1.4.1.

It is important to note that due to the parametric dependence of electronic Hamiltonian (a separate Hamiltonian operator for each nuclear configuration $\mathbf{Q}$), electronic eigenfunction $\Phi_i(\mathbf{q};\mathbf{Q})$ will also have the same type of parametric dependence. Electronic eigenvalue $V_i(\mathbf{Q})$ is usually referred to as potential energy surface (PES) for i-th electronic state. Since quantity $\hat{V}_n$ is a constant (nuclear repulsion energy) for a fixed $\mathbf{Q}$, it can be subtracted from each $V_i(\mathbf{Q})$ to obtain corresponding purely electronic energies. The electronic wave-functions and eigenvalues constructed using the above procedure are also referered to as *adiabatic*.

The set of electronic eigenfunctions $\Phi_i(\mathbf{q};\mathbf{Q})$ are orthogonal and form a complete basis for every $\mathbf{Q}$.

$$\int \Phi_i^*(\mathbf{q}';\mathbf{Q})\Phi_j(\mathbf{q};\mathbf{Q})\mathbf{dq} = \langle j(\mathbf{Q})|i(\mathbf{Q})\rangle = \delta_{ij} \tag{1.8a}$$

$$\sum_i \Phi_i^*(\mathbf{q}';\mathbf{Q})\Phi_i(\mathbf{q};\mathbf{Q}) = \delta(\mathbf{q}-\mathbf{q}') \tag{1.8b}$$

For isolated molecules, the orthonormal electronic eigenfunctions Φ_i can be chosen to be real and can used as a basis to represent a total molecular wave function $\Psi(\mathbf{q},\mathbf{Q},t)$ as,

$$\Psi(\mathbf{q},\mathbf{Q},t) = \sum_i \chi_i(\mathbf{Q},t)\Phi_i(\mathbf{q};\mathbf{Q}) \tag{1.9}$$

The expansion for the state of a molecular system as in equation (1.9) is known as Born-Huang expansion or as *adiabatic representation* [2, 36, 59]. After projecting

to the left of equation (1.9) with electronic eigenfunction Φ_i, we obtain a set $\chi_i(\mathbf{Q})$ of nuclear wave-functions, one associated with each electronic state. Since electonic wave-functions are assumed to be time-independent, the nuclear wave function for each electronic state explicitly depends upon both the nuclei coordinate $\mathbf{Q}$ and time t.

$$\chi_i(\mathbf{Q},t) = \langle \Phi_i(\mathbf{q};\mathbf{Q}) | \Psi(\mathbf{q},\mathbf{Q},t) \rangle_q \tag{1.10}$$

After inserting the *ansatz*[1] equation (1.9) into TDSE equation (1.1), one can derive a set of coupled equations for the evolution of unknown nuclear wave-functions $\chi_j(\mathbf{Q},t)$. Upon multiplication by $\Phi^*(\mathbf{q};\mathbf{Q})$ from the left and integrating over the electronic coordinates $\mathbf{q}$ leads to,

$$[\hat{T}_n(\mathbf{Q}) + \hat{V}_j(\mathbf{Q})]\,\chi_j(\mathbf{Q},t) - \sum_i \hat{\Lambda}_{ji}(\mathbf{Q})\,\chi_i(\mathbf{Q}) = i\hbar\,\frac{\partial \chi_j(\mathbf{Q},t)}{\partial t} \tag{1.11}$$

This equation describes the non-adiabatic dynamics of nuclei within the BH framework. The quantities $\hat{\Lambda}_{ji}$ $(\mathbf{Q})$ are the matrix elements of the non-adiabatic coupling operator whose explicit form can be obtained by using definition of $\hat{T}_n$ as given in equation (1.5).

$$\hat{\Lambda}_{ji}(\mathbf{Q}) = \frac{1}{2M}[2\tau_{ji}(\mathbf{Q})\cdot\nabla + \tau^2_{ji}(\mathbf{Q})] \tag{1.12}$$

where τ_{ji} are the first-order non-adiabatic coupling terms (NACT) defined as,

$$\tau_{ji} = \langle \Phi_j(\mathbf{q};\mathbf{Q}) | \nabla \Phi_i(\mathbf{q};\mathbf{Q}) \rangle_q \tag{1.13}$$

For every pair (j,i) of electronic states, τ_{ji} can be thought as a vector defined at every point in the nuclear coordinate space. The collection of τ_{ji} for all geometries is a vector field configuration. Similarly, the quantities τ^2_{ji} are the second-order non-adiabatic scalar couplings.

$$\tau^2_{ji} = \langle \Phi_j(\mathbf{Q}) | \nabla^2 \Phi_i(\mathbf{Q}) \rangle_q \tag{1.14}$$

As discussed in references [2,53], the BH equation (1.11) can be compactly written by making use of matrix notations. A matrix form of the gradient operator can be defined as $\boldsymbol{\nabla} = \nabla\,\mathbb{I}$, where $\mathbb{I}$ denotes the identity matrix of dimension as the number of states in the BH expansion. The matrix $\mathbf{V}(\mathbf{Q})$ is a diagonal matrix with electronic

[1] In mathematics, an assumption about the form of an unknown function which is made in order to facilitate solution of an equation or other problem. *Ansatz* is German word that corresponds to English word *attempt* or *approach*.

energies $V_i(\mathbf{Q})$ as diagonal entries. Similarly, the matrix $\boldsymbol{\tau}$ represents a matrix with entries as vectors τ_{ji}, $\boldsymbol{\tau^2}$ is a matrix of scalars τ_{ji}^2, and $\boldsymbol{\chi}(\mathbf{Q},t)$ is column vector with entries $\chi_j(\mathbf{Q},t)$. With this, the matrix form of equation (1.11) is given by,

$$\Big[-\frac{1}{2M}\boldsymbol{\nabla}\cdot\boldsymbol{\nabla}+\mathbf{V}-\frac{1}{2M}\left(2\,\boldsymbol{\tau}\cdot\boldsymbol{\nabla}+\boldsymbol{\tau^2}\right)\Big]\boldsymbol{\chi}(\mathbf{Q},t)=i\,\frac{\partial\boldsymbol{\chi}(\mathbf{Q},t)}{\partial t} \tag{1.15}$$

The term in the square brackets is the nuclear Hamiltonian operator represented in terms of adiabatic electronic eigenfunctions. It is a matrix which, in principle, can be constructed if PES matrix $\mathbf{V}(\mathbf{Q})$ and NACT matrices $\boldsymbol{\tau}$ and $\boldsymbol{\tau^2}$ are available. Once constructed, such a Hamiltonian can be used within any convenient time-propagation methods as discussed in section 1.4.2.

It must be emphasized that the terms containing NACTs are the ones responsible for the non-adiabatic transitions. By setting them to zero in equation (1.11), one obtains a set of decoupled equations for the nuclear wave-functions associated with each electronic states. The population of each electronic wave-function in the total wave-function remains unchanged. Without the inclusion of NACTs, each component of nuclear wave-function moves on its own PES without interacting with others. Therefore, the NACTs are the fundamental quantities which need to be included for a non-adiabatic treatment based on BH expansion.

Both NACTs essentially contain structural information about the adiabatic eigenfunctions. From their definitions, it can be seen that their magnitude is a measure of extent of variation of electronic eigenfunctions with respect to nuclear coordinates. Such a variation indicates an exchange of energy between electronic and nuclear degrees of freedom. Such an exchange of energy will be signficant around nuclear regions where the NACTs have significant magnitude. To characterize such regions, one can make use of the Hellman-Feynman theorem [2]. By applying the gradient to equation (1.7) and using the definition of the τ, the following expression for first-order NACTs can be obtained.

$$\tau_{ji}(\mathbf{Q})=\frac{\langle\Phi_j(\mathbf{q};\mathbf{Q})|\nabla\hat{H}_e(\mathbf{q};\mathbf{Q})|\Phi_i(\mathbf{q};\mathbf{Q})\rangle}{V_i(\mathbf{Q})-V_j(\mathbf{Q})} \tag{1.16}$$

From equation (1.16), it can seen that magnitude of τ steeply increases as the adiabatic PES comes closer *i.e.* $\tau \propto (\mathrm{V_1}\text{ - }\mathrm{V_2})^{-1}$. In other words, assuming that numerator in equation (1.16) remains finite and non-zero, the first-order NACT becomes large around electronic degeneracies. At the point of electronic degeneracies, irrespective of how it arises, the NACTs diverge. Therefore, within BH framework, non-adiabatic effects can be conceptualized to originate in the vicinity of nuclear

geomerties where electronic degeneracies are present.

As shown in references [2, 53], it is possible to show that first- and second-order NACTs are related. Assuming that adiabatic electronic eigenfunctions are real and making use of their completeness, one can derive the following exact relation, by taking the gradient of $\tau_{ji}(\mathbf{Q})$.

$$\tau_{ji}^2 = \nabla \cdot \tau_{ji} + \sum_k \tau_{jk} \cdot \tau_{ki} \tag{1.17}$$

where use of the anti-Hermitian property $\tau_{jk} = -\tau_{kj}$ of first-order NACTs has been made. It must be emphasized that the above relation only holds for complete real electronic basis and holds only approximately when a truncated basis is used. The above equation can be converted into the following matrix form.

$$\boldsymbol{\tau}^2 = \boldsymbol{\nabla} \cdot \boldsymbol{\tau} + \boldsymbol{\tau} \cdot \boldsymbol{\tau} \tag{1.18}$$

This shows that first-order NACTs can be thought of as fundamental quantities and second-order NACTs are derived ones. Inserting equation (1.18) into equation (1.15) and further manipulations give,

$$\Big[-\frac{1}{2M} (\boldsymbol{\nabla} + \boldsymbol{\tau})^2 + \mathbf{V} \Big] \boldsymbol{\chi}(\mathbf{Q}, t) = i \frac{\partial \boldsymbol{\chi}(\mathbf{Q}, t)}{\partial t} \tag{1.19}$$

The above form resembles TDSE of particle in a potential $\mathbf{V}$ with the bare kinetic energy operator replaced by a *dressed kinetic energy operator* [2]. The dressed operator contains the influence of NACTs serving as vector fields which give raise to additional momentum. The relation of the above equation to classical gauge-field theories has been discussed in detail by Baer [2] and Pacher and coworkers [43].

1.2.2 Born-Oppenheimer and Adiabatic Approximations

The BH treatment presented in the previous subsection is formal and so far we have not discussed any approximations. The usefulness of this formalism depends on further approximations and viability of computational treatments for solution of the resulting nuclear TDSE equation (1.19), as well as on the feasibility of constructing the required PESs and NACTs from the electronic eigen problem.

The main assumption behind BH treatment is the unequal treatment of electronic and nuclear degrees of freedom. The early treatment of electronic degrees through the time-independent electronic eigenfunctions implies that these degrees are fast and respond instantaneously to the motion of nuclei. The physical justification for

this lies in the experimentally observed large differences in masses of electrons and nuclei ($m_e \ll M$). In the BH formalism, this fact is incorporated into the conceptual picture of electron-nuclear dynamics that the formalism provides and does not in itself constitute an approximation. Although it makes the contribution of NACTs to the dynamics through Λ quantity in equation (1.12) to be scaled by M^{-1}, it does not imply that these contributions will be small and hence can be neglected. The $\boldsymbol{\tau}$ in equation (1.19) can be neglected only if it is much smaller as compared to gradient of nuclear wave-functions $\boldsymbol{\chi}(\mathbf{Q}, t)$.

The BH formalism becomes computationally viable only if the expansion in equation (1.11) can be limited to a small number of N electronic states. We assume that a group of N electronic states to be energetically well-separated from the remaining ones, and that the NACTs between these two groups are smaller as compared to the NACTs within the first group. The interest is to describe the dynamics of a molecular wave-function constructed from these N states and further assume that the dynamics remains largely confined within this group. This does not imply that intergroup interactions are set to zero. In such a case, the matrix equation equation (1.19) can be truncted to dimension N.

$$\Big[-\frac{1}{2M} \{(\boldsymbol{\nabla} + \boldsymbol{\tau})^2\}^N + \mathbf{V}^N \Big] \boldsymbol{\chi}(\mathbf{Q}, t)^N = i \frac{\partial \boldsymbol{\chi}(\mathbf{Q}, t)^N}{\partial t} \tag{1.20}$$

where superscript N on matrices and vector quantities indicates their truncation to N components. The restriction of dressed kinetic energy operator can be expressed as [2, 53],

$$\{(\boldsymbol{\nabla} + \boldsymbol{\tau})^2\}^N = (\boldsymbol{\nabla}^N + \boldsymbol{\tau}^N)^2 - \boldsymbol{\tau}_c \cdot \boldsymbol{\tau}_c^\dagger \tag{1.21}$$

where $\boldsymbol{\tau}_c$ is the matrix of first-order NACTs which couple N selected states with states in their orthogonal complement. To derive the above relation, one needs to use the fact that both $\boldsymbol{\nabla}$ and $\boldsymbol{\tau}$ matrices are anti-Hermitian. This leads to the following matrix equation.

$$\Big[-\frac{1}{2M} (\boldsymbol{\nabla}^N + \boldsymbol{\tau}^N)^2 + \mathbf{V}^N + \frac{1}{2M} \boldsymbol{\tau}_c \cdot \boldsymbol{\tau}_c^\dagger \Big] \boldsymbol{\chi}(\mathbf{Q}, t)^N = i \frac{\partial \boldsymbol{\chi}(\mathbf{Q}, t)^N}{\partial t} \tag{1.22}$$

Unlike equation (1.19), the above equation describes the dynamics of nuclei confined to a group of N electronic states weakly interacting with states in the complementary group. On the left hand side, the first two terms contain all scalar and vectorial interactions within these N states, while the last term containing $\boldsymbol{\tau}_c$ provides a scalar potential matrix capturing the weak interactions. In the spirit of adiabatic approximation [60], this can be referred to as *group adiabatic approximation*. The

term adiabatic means that dynamics is restricted to the chosen group of N states.

Since each element of $\boldsymbol{\tau}_c$ is small in magnitude due to large electronic energy difference between the group and its complement, the contribution of last term of equation (1.22) is usually small and can be neglected. The resulting approximation is known as *group Born-Oppenheimer approximation*.

Since ground state is usually well-separated from all excited states, it is possible to limit the group of states to one state - the ground state. The BH ansatz then reduces to,

$$\Psi(\mathbf{q},\mathbf{Q},t) = \chi_0(\mathbf{Q},t)\Phi_0(\mathbf{q};\mathbf{Q}) \tag{1.23}$$

which is the well-known BO ansatz [36,61]. Although this ansatz is usually applicable for the ground state, it is also possible to employ this for an electronic state which is energetically separated the remaing ones. For the BO ansatz, the TDSE equation (1.11) reduces to,

$$[\hat{T}_n(\mathbf{Q}) + \hat{V}_0(\mathbf{Q}) + \hat{\Lambda}_{00}(\mathbf{Q})]\chi_0(\mathbf{Q},t) = i\hbar\frac{\partial\chi_0(\mathbf{Q},t)}{\partial t} \tag{1.24}$$

which is known as adiabatic approximation (AA) [37,38]. The term $\hat{\Lambda}_{00}(\mathbf{Q})$ is known as Diagonal-Born-Oppenheimer Correction (DBOC). It can be shown that the DBOC is given by the following equivalent expressions.

$$\hat{\Lambda}_{00}(\mathbf{Q}) = \langle\Phi_0(\mathbf{q};\mathbf{Q})|\hat{T}_n|\Phi_0(\mathbf{q};\mathbf{Q})\rangle_q = -\frac{1}{2M}\sum_{k\neq 0}\tau_{0k}\cdot\tau_{k0} \tag{1.25}$$

This shows that DBOC provides a mass-dependent correction potential-like term to the mass-independent BO-PES $\hat{V}_0(\mathbf{Q})$. It has been extensively used in high-accuracy computations of ground state ro-vibronic spectra [62]. In the adiabatic approximation, even though the nuclear motion is restricted to a single-state, the DBOC term contains indirect and smaller influence of excited states. Dropping this term leads to the standard BO approximation in which the motion is truly confined to a single PES without any influence of the excited states.

Therefore, truncation of the Born-Huang expansion leads to single-state BO and adiabatic approximations which do not include non-adiabatic effects, as well as to the corresponding group-level approximations where the non-adiabatic effects and vibronic interactions within the group are fully taken into account.

1.2.3 Diabatic Representation

Despite the approximations discussed in the previous subsection, the BH treatment based on adiabatic electronic states turns out to be not suitable for computational studies. This was already recognized in early studies on diatomic molecules involving collision of ions and atoms [63, 64]. In diatomic molecules, the character of adiabatic electronic wave-functions changes very rapidly across the avoided crossings of interacting states, particularly for weakly avoided crossings such as ionic-covalent avoided crossing in alkali halides. As a result, the NACTs become larger in magnitude and become spiky around the crossing region. This introduces severe numerical difficulties to account for rapid changes of nuclear wave-functions resulting from such a variation of NACTs. The situation worsens in polyatomic molecules where, unlike diatomics, the NACTs diverge at the intersection points.

Another reason for unsuitability of adiabatic electronic states comes from the effect of CIs on their continuity properties. To be useful for dynamics, it must be possible to choose the phases of adiabatic electronic eigenfunctions appearing in BH expansion such that they are single-valued and continuous functions of nuclear coordinates. This is to ensure that associated nuclear wave-functions have the same property, thus allowing them to be determined in terms of simple basis set functions of nuclear coordinates. Starting with the important work of Longuet-Higgins [65], it has been established that such a choice of phases for adiabatic wave-functions is not possible within regions containing electronic degeneracies. This demonstrated that adiabatic wave-functions are multi-valued and can not be considered as simple functions. As a consequence, the nuclear wave-functions are required to behave in the same way. These effects are known as geometric phase effects [66, 67]. These further complicate computational treatment of non-adiabatic effects based on adiabatic representation.

Alternate representation known as *diabatic representation* has been introduced based on the works of London [63], Lichten [64, 68] and Smith [69]. Here, the adiabatic states are replaced by a set of states which retain their electronic nature across the crossing point. Such states, by choice, are smooth and single-valued functions of nuclear coordinates. Since the space of electronic wave-functions around a crossing point is expected to be smooth, it can be imagined that diabatic states can be constructed as suitable linear combinations of adiabatic wave-functions. They form a new electronic basis in which the magnitudes of the derivative couplings are small or become zero. The basic idea of constructing diabatic states is to have a weaker dependence on the nuclear coordinate so that their NACTs can be neglected.

1.2.3.1 Nuclear Equations in Diabatic Representation

Even though individual adiabatic electronic wave-functions appearing in the group BH expansion undergo rapid changes in the CI region, the total space spanned by these electronic wave-functions is expected to vary smoothly as long as interaction of the group states with the complementary states remains small. Therefore, it must be possible to construct a set of diabatic states which reflects this smoothness by taking them to be suitable linear combinations of adiabatic wave-functions at every nuclear geometry.

Assuming that such diabatic states $\tilde{\Phi}_i(\mathbf{q};\mathbf{Q})$ have been constructed (the tilde over Φ indicates diabatic), the total wave-function $\Psi(\mathbf{q},\mathbf{Q},t)$ can be re-expressed as,

$$\Psi(\mathbf{q},\mathbf{Q},t) = \sum_i \tilde{\Phi}_i(\mathbf{q};\mathbf{Q})\,\tilde{\chi}_i(\mathbf{Q},t) \tag{1.26}$$

where $\tilde{\chi}_i(\mathbf{Q},t)$ are the corresponding diabatic nuclear wave functions. For simplicity, $\tilde{\Phi}_i(\mathbf{q};\mathbf{Q})$ can be assumed to be orthonormal. In this case, the diabatic states can be related to the adiabatic ones through a unitary transformation $\mathbf{U}(\mathbf{Q})$ as follows.

$$\tilde{\Phi}_i(\mathbf{q};\mathbf{Q}) = \sum_k \mathbf{U}_{ki}(\mathbf{Q})\Phi_k(\mathbf{q};\mathbf{Q}) \tag{1.27a}$$

or in a matrix form as,

$$\tilde{\mathbf{\Phi}}(\mathbf{q};\mathbf{Q}) = \mathbf{U}^{\mathsf{T}}(\mathbf{Q})\mathbf{\Phi}(\mathbf{q};\mathbf{Q}) \tag{1.27b}$$

Since the underlying molecular wave-function remains the same, in matrix form the following relation holds.

$$\Psi(\mathbf{q},\mathbf{Q},t) = \mathbf{\Phi}^{\mathsf{T}}\boldsymbol{\chi} = \tilde{\mathbf{\Phi}}^{\mathsf{T}}\tilde{\boldsymbol{\chi}} \tag{1.28}$$

which gives the following relation between nuclear wave-functions.

$$\boldsymbol{\chi}(\mathbf{Q},t) = \mathbf{U}(\mathbf{Q})\tilde{\boldsymbol{\chi}}(\mathbf{Q},t) \tag{1.29a}$$

$$\tilde{\boldsymbol{\chi}}(\mathbf{Q},t) = \mathbf{U}^{\dagger}(\mathbf{Q})\boldsymbol{\chi}(\mathbf{Q},t) \tag{1.29b}$$

The matrix $\mathbf{U}(\mathbf{Q})$ is referred as adiabatic to diabatic transformation (ADT) matrix. Using the above relations, the nuclear Schrödinger equation can be converted to diabatic representation.

$$\Big[-\frac{1}{2M}\boldsymbol{\nabla}\cdot\boldsymbol{\nabla} + \tilde{\mathbf{V}} - \frac{1}{2M}\left(2\,\tilde{\boldsymbol{\tau}}\cdot\boldsymbol{\nabla} + \tilde{\boldsymbol{\tau}}^2\right)\Big]\,\tilde{\boldsymbol{\chi}}(\mathbf{Q},t) = i\,\frac{\partial\tilde{\boldsymbol{\chi}}(\mathbf{Q},t)}{\partial t} \tag{1.30}$$

where, $\tilde{\mathbf{V}}$ is the diabatic electronic energy which is non-diagonal whose matrix element is defined as,

$$\tilde{V}_{ij}(\mathbf{Q}) = \langle \tilde{\Phi}_i(\mathbf{q};\mathbf{Q}) | \hat{H}_{el} | \tilde{\Phi}_j(\mathbf{q};\mathbf{Q}) \rangle_q \tag{1.31}$$

and the NACTs of diabatic wave-functions are

$$\tilde{\tau}_{ji}(\mathbf{Q}) = \langle \tilde{\Phi}_j(\mathbf{Q}) | \nabla \tilde{\Phi}_i(\mathbf{Q}) \rangle_q \tag{1.32a}$$

$$\tilde{\tau}^2_{ji}(\mathbf{Q}) = \langle \tilde{\Phi}_j(\mathbf{Q}) | \nabla^2 \tilde{\Phi}_i(\mathbf{Q}) \rangle_q \tag{1.32b}$$

The nuclear equations in diabatic representations as given by equation (1.30) have exactly the same form as the adiabatic equation (1.15) with adiabatic quantities replaced by corresponding diabatic equivalents. This is known as gauge transformation in non-adiabatic dynamics, and extensively discussed in [43].

The potential energy matrix in diabatic representation is given by,

$$\tilde{\mathbf{V}}(\mathbf{Q}) = \mathbf{U}^\dagger(\mathbf{Q}) \mathbf{V}(\mathbf{Q}) \mathbf{U}(\mathbf{Q}) \tag{1.33}$$

Unlike adiabatic one, this is not diagonal which reflects the nature of diabatic states not being eigenfunctions of electronic Hamiltonian and so they are coupled through it. The diabatic NACTs are related to the adiabatic ones as follows.

$$\tilde{\boldsymbol{\tau}}(\mathbf{Q}) = \mathbf{U}^\dagger(\mathbf{Q}) \left[\nabla \mathbf{U}(\mathbf{Q}) + \boldsymbol{\tau}(\mathbf{Q}) \mathbf{U}(\mathbf{Q}) \right] \tag{1.34a}$$

$$\tilde{\boldsymbol{\tau}}^2(\mathbf{Q}) = \mathbf{U}^\dagger(\mathbf{Q}) \left[(\nabla + \boldsymbol{\tau}(\mathbf{Q})) \cdot (\nabla \mathbf{U}(\mathbf{Q}) + \boldsymbol{\tau}(\mathbf{Q}) \mathbf{U}(\mathbf{Q})) \right] \tag{1.34b}$$

The relations in equation (1.18) can be shown to hold also in the diabatic representation. Using this, the matrix form works out to be,

$$\left[-\frac{1}{2M} (\boldsymbol{\nabla} + \tilde{\boldsymbol{\tau}})^2 + \tilde{\mathbf{V}} \right] \tilde{\boldsymbol{\chi}}(\mathbf{Q}, t) = i \frac{\partial \tilde{\boldsymbol{\chi}}(\mathbf{Q}, t)}{\partial t} \tag{1.35}$$

which when compared to equation (1.19) contains non-diagonal potential matrix as well as transformed NACTs. With the use of diabatic states, these NACTs are expected to be smoother than the adiabatic ones, reducing the numerical difficulties encountered. The truncation approximations discussed before may now be applied to obtain diabatic equivalents of equation (1.22). In this case, the ADT transformation are assumed to be performed only within the group states.

1.2.3.2 Strictly Diabatic States

Unlike adiabatic states, the diabatic states are not uniquely defined because the physical criteria of smoothness can be defined in many different ways. However, both representations are unitarily equivalent and lead to the same results. The advantage of diabatic representation is that it leads to numerically well-behaved nuclear TDSE and offers an easier physical interpretation of the results.

A unique set of diabatic states can be defined as those states for which the first-order NACTs vanish everywhere. For this, the following condition must hold.

$$\tilde{\boldsymbol{\tau}}(\mathbf{Q}) = \mathbf{U}^{\dagger}(\mathbf{Q})\left[\nabla\mathbf{U}(\mathbf{Q}) + \boldsymbol{\tau}(\mathbf{Q})\mathbf{U}(\mathbf{Q})\right] = 0 \tag{1.36}$$

This implies that they are related to adiabatic states via the following equation [53].

$$\nabla\mathbf{U}(\mathbf{Q}) + \boldsymbol{\tau}(\mathbf{Q})\mathbf{U}(\mathbf{Q}) = 0 \tag{1.37}$$

The above equation, known as ADT condition, has been a subject of numerous works since their first derivation by Smith for diatomic molecules [69], and their generalization to polyatomic cases by Baer [2, 53]. The existence of the solutions as well computational methods to obtain them has been discussed by Baer [1], and others [42, 59, 70]. The diabatic states satisfying the above conditions are referred to be *strictly diabatic*. In a diabatic representation involving such states, the nuclear TDSE simplifies considerably.

$$\Big[-\frac{1}{2M}\boldsymbol{\nabla}\cdot\boldsymbol{\nabla} + \tilde{\mathbf{V}}\Big]\tilde{\boldsymbol{\chi}}(\mathbf{Q},t) = i\,\frac{\partial\tilde{\boldsymbol{\chi}}(\mathbf{Q},t)}{\partial t} \tag{1.38}$$

As a consequence of equation (1.37), the kinetic energy matrix becomes diagonal and all non-adiabatic interactions are fully contained within the non-diagonal potential matrix. This represents the best possible case for smoothness.

It has been shown that strictly diabatic states exist only in some simple situations. Using an exponential representation for $\mathbf{U}(\mathbf{Q})$ as [71],

$$\mathbf{U}(\mathbf{Q}) = e^{\mathbf{A}(\mathbf{Q})} \tag{1.39}$$

the equation (1.37) can be converted to

$$\nabla\mathbf{A}(\mathbf{Q}) + \boldsymbol{\tau}(\mathbf{Q}) = 0 \tag{1.40}$$

This resembles the equation which determines a potential from a given force-field. A

unique path-independent potential up to a constant can be obtained only if and only if the force-field has zero curl everywhere. In this case, the $\tau(\mathbf{Q})$ field is not a simple vector field, but its components can be thought of as $N \times N$ matrices. Such a field is known as *non-Abelian* field. The definition of curl in this case is given by [2, 53],

$$F_{pq} = \frac{\partial \tau_p}{\partial q} - \frac{\partial \tau_q}{\partial p} - [\tau_p, \tau_q] \tag{1.41}$$

where τ_p matrices are components of $\boldsymbol{\tau}$ along nuclear coordinate $\mathbf{Q}_p$. It can be shown that, for complete set of electronic states, the non-Abelian Curl F_{pq} vanishes everywhere. Therefore, strict diabatic states exist for this case. They have been also shown to exist for the case of diatomic molecules, where ADT equation (1.37) can be integrated and the curl in this is zero due to anti-symmetry condition $F_{pq} = -F_{qp}$.

For all other cases, strict diabatic states do not exist. For the case of group of N states weakly interacting with complementary states, the curl can be shown to have only contributions from NACTs between these two groups [2, 72]. Since these do not vanish, only approximate solution of ADT equations are possible under the condition that such contributions are neglected.

Several choices of this transformation will offer a variety of the methods for construction of the diabatic states which has been subject of intense research in last decades [43, 73].

1.2.3.3 Quasi-Diabatic Representations

Non-existence of strict diabatic states in polyatomic molecules has motivated the construction of *quasi-diabatic* or approximately diabatic states. There is no standard definition of quasi-diabatic states. It is expected that their NACTs are small enough to be ignored in dynamical treatments, although this fact is not been established to happen for quasi-diabatic states constructed from different prescriptions. A nice discussion of different approaches for construction of quasi-diabatic states can be found in [73].

Earliest attempts to construct quasi-diabatic states involved approximate numerical solutions of multi-dimensional ADT equations. This approach has been explored in detail by Baer and coworkers [1, 2, 74], and requires the knowledge of first-order NACTs from *ab initio* calculations. The method starts from a nuclear configuration where diabatic states are easily identified and then integrates the ADT equations along different contours within the nuclear configuration space. Baer and coworkers have shown [2, 75] that such an approach yields a set of quasi-diabatic states and single-valued diabatic potential matrix when a set of quantization conditions on

NACTs are satisfied. For a number of cases, they have demonstrated that these conditions are satisfied to a good degree of approximation in practice. Cederbaum and coworkers have analyzed the relation of quasi-diabatic states obtained in this procedure with an alternative definition based on minimization of integral of the norm of NACTs over the entire nuclear configuration space [43, 59].

A number of methods to produce quasi-diabatic states without the explicit knowledge of NACTs have been proposed and investigated. Such methods adapt easily implementable alternate ways which produce electronic states varying smoothly with nuclear coordinates. The states obtained by diagonalization of a property operator such as dipole and quadruple moment have been shown to produce smooth diabatic states [76, 77]. Cederbaum and coworkers have proposed simple condition to determine a transformation which block-diagonalizes the Hamiltonian leading to quasi-diabatic states [59, 78].

The regularized diabatization procedure extracts linear vibronic parameters from accurate PES computations, and uses them to define an approximate ADT to produce quasi-diabatic states [79–81]. It has been shown that such a transformation eliminates the singular part of NACTs [73]. It is shown that such a procedure can be easily setup when an element of symmetry is present and provides accurate diabatic potential matrix.

1.3 Conical Intersections

In the previous section, the importance of intersection points - the molecular geometries at which two or more electronic states are exactly degenerate - on non-adiabatic dynamics was briefly mentioned. Even though such points are much rarer in nuclear configuration space (resembling needle in a haystack situation), an extended volume of region surrounding them becomes important. Since the first-order NACTs at intersection points diverge, they remain large at within such regions. Therefore, intersection regions can be viewed as focal points from where non-adiabatic effects originate. Therefore, it is of importance to understand structural aspects of intersection points.

The conical intersections (CIs) is the most commonly occurring intersection point in polyatomic molecules. The PESs around a CI point exhibit a special type of conical shape of topography when one moves away in directions which lift the degeneracy in the first-order of displacement.

1.3.1 Discovery and Importance

In the context of non-adiabaticity, theoretical framework of CIs was laid down by Teller in 1937 in his investigations on crossing of two PES [7]. The condition for existence of crossings of two electronic states had been already formulated by Von-Nueman and Wigner, in terms of a rule known as *non-crossing* rule. This rule is strictly valid only for diatomic molecule and usually fails for polyatomic molecule [6]. At that time, CIs were considered just as a mathematical construction, rather than an unified concept for explaining non-adiabatic effects.

Decades later, several features arising from CIs were explored starting from the pioneering work of Longuet-Higgins and Herzberg [8]. Very early on, Longuet-Higgins revealed an interesting topological feature of CIs. They found that the sign of standard adiabatic electronic wave-functions changes when a molecular system is transported around a closed loop which encircled a CI geometry. Consequently, they become double-valued type of functions of nuclear coordinates. To obtain a single-valued adiabatic wave function, it needs to be multiplied by an additional phase factor. This is known as Longuet-Higgins or geometric phase [65]. To ensure single-valuedness of adiabatic wave function, Mead introduced a vector potential in BH expansion. With this single-valued nuclear wave function, one can perform exact wave-packet dynamics [54]. Later, several groups have employed this approach and emphasized the importance of Longuet-Higgins phase in quantum reactive scattering and bound-state calculations [1, 48–52, 82]. An overview of mathematical background of geometric phase and its importance can be found in Ref [67]. Presence of CIs introduces a geometry dependent phase factor that influences nuclear dynamics and its inclusion has been shown to be necessary to obtain accurate results [5, 83, 84].

Another major area where importance of CIs has been recognized is photochemistry. Here, important contributions have come from the works of Teller, Zimmerman, Michl, Robb, Ruedenberg, Yarkony and many others [3, 12, 45, 85–87]. Since CIs couple two electronic states, they facilitate radiationless transitions. They provide an efficient deactivation channel for radiationless relaxation, acting as some sort of *funnels* for non-adiabatic transitions. In many molecules, presence of CIs enables rapid conversion of the excess electronic energy into nuclear motions. Therefore, they play a decisive role in mechanistic descriptions of photochemical reactions. Several computational efficient techniques have enabled locating CIs [88] in molecules, and assess their involvement and importance in dynamics. Structural aspects of CIs are crucial for developing qualitative descriptions of ultrafast deactivation of photo-induced excitations [89, 90].

1.3.2 Two-State Intersection Model

Intersections of two electronic states are one of the most frequently occurring intersections. The structural aspects of intersection points can be understood by considering a 2×2 model to describe two-state intersections. The model is also useful for understanding the behaviour of PESs around an intersection geometry, to explain the concepts of branching and intersection spaces, and to illustrate the appearance of geometrical phase. The model can also be applied to extract the structural parameters of intersections from *ab initio* calculations [55, 91]. Detail discussions of this model can be found in the works of Yarkony [92] and Rudenberg [87]. The two-state model and its conceptual outcomes have also been extended for intersections of three and more states [93, 94].

To understand the general conditions for occurrence of electronic degeneracies of two states, the electronic Hamiltonian $\hat{H}_e(\mathbf{q};\mathbf{Q})$ is represented in a basis of two electronic wave-functions $\tilde{\Phi}_1(\mathbf{q};\mathbf{Q})$ and $\tilde{\Phi}_2(\mathbf{q};\mathbf{Q})$ as follows.

$$\mathbf{H}_e(\mathbf{Q}) = \begin{bmatrix} H_{11}(\mathbf{Q}) & H_{12}(\mathbf{Q}) \\ H_{21}(\mathbf{Q}) & H_{22}(\mathbf{Q}) \end{bmatrix} \tag{1.42}$$

Here, the matrix elements are defined as,

$$H_{ij}(\mathbf{Q}) = \langle \tilde{\Phi}_i(\mathbf{q};\mathbf{Q}) | \hat{H}_e(\mathbf{q};\mathbf{Q}) | \tilde{\Phi}_j(\mathbf{q};\mathbf{Q}) \rangle_{\mathbf{q}} \,. \tag{1.43}$$

It is assumed that the matrix completely describes the two electronic states within the intersection region. This can be ensured if the exact electronic eigenfunctions at each geometry within the entire region are contained in the space spanned by $\tilde{\Phi}_1$ and $\tilde{\Phi}_2$. It is further assumed that these functions are smoothly varying, continuous and single-valued within the region including at the points of degeneracy. These assumptions essentially imply that these states are diabatic.

The two eigenvalues of electronic Hamiltonian equation (1.42), $V_+(\mathbf{Q})$ and $V_-(\mathbf{Q})$, can be obtained by solving the corresponding secular equation.

$$V_\pm(\mathbf{Q}) = \frac{H_{11}(\mathbf{Q}) + H_{22}(\mathbf{Q})}{2} \pm \frac{1}{2}\sqrt{(H_{11}(\mathbf{Q}) - H_{22}(\mathbf{Q}))^2 + 4H_{12}(\mathbf{Q})^2} \tag{1.44}$$

To obtain degeneracy at a geometry $\mathbf{Q}^*$, the term under the square root must vanish. This yields the following two conditions must be simultaneously fulfilled.

$$H_{11}(\mathbf{Q}^*) = H_{22}(\mathbf{Q}^*) \tag{1.45a}$$

$$H_{12}(\mathbf{Q}^*) = 0 \tag{1.45b}$$

In other words, *the diagonal elements must be equal* and *off-diagonal elements must vanish*. These are two independent conditions for the existence of crossing of two PES at a special geometry $\mathbf{Q}^*$. This implies that in the neighborhood of such a geometry, there must exist at least one $(N-2)$-dimensional surface passing through the geometry upon which the degeneracy is exactly preserved (N is the number of vibrational degrees of freedom). Such a surface represents a locus of all neighboring geometries satisfying the conditions equation (1.45) and is referred to as *the intersection seam* of two electronic states considered.

The point-group symmetry can influence the presence of intersections by ensuring that one or both the degeneracy conditions to hold exactly at a geometries where the symmetry is present. When both the conditions are satisfied solely by symmetry, this results in symmetry-required (or symmetry-enforced) intersections. This usually happens when non-Abelian point groups such as D_{3h} which have degenerate irreps. In such a case, the symmetry-required seam usually covers an extended portion of the symmetry subspace. Symmetry allowed different symmetry intersections result when off-diagonal elements vanish due to states belonging to different irreps of a symmetry group. When symmetry does not play any role, the degeneracy is then completely accidental and this case is referred to as same-symmetry accidental intersections. Further discussions on this will be given in Chapter 2.

To delineate the behaviour of eigenvalues and eigenvectors of equation (1.42), it is convenient to express it in the following form [92],

$$\mathbf{H}_e(\mathbf{Q}) = S(\mathbf{Q})\mathbb{I} + \begin{bmatrix} -G(\mathbf{Q}) & W(\mathbf{Q}) \\ W(\mathbf{Q}) & G(\mathbf{Q}) \end{bmatrix} \tag{1.46}$$

where,

$$S(\mathbf{Q}) = \frac{(H_{11}(\mathbf{Q}) + H_{22}(\mathbf{Q}))}{2} \tag{1.47a}$$

$$G(\mathbf{Q}) = \frac{(-H_{11}(\mathbf{Q}) + H_{22}(\mathbf{Q}))}{2} \tag{1.47b}$$

$$W(\mathbf{Q}) = H_{12}(\mathbf{Q}). \tag{1.47c}$$

The eigenvalues (1.44) and degeneracy conditions (1.45) can be expressed as,

$$V_{\pm}(\mathbf{Q}) = S(\mathbf{Q}) \pm \frac{1}{2}\sqrt{G(\mathbf{Q})^2 + W(\mathbf{Q})^2} \tag{1.48a}$$

$$G(\mathbf{Q}^*) = 0 \tag{1.48b}$$

$$W(\mathbf{Q}^*) = 0, \tag{1.48c}$$

and the corresponding eigenfunctions are given by,

$$\Phi_+(\mathbf{Q}) = \cos(\frac{\Lambda}{2})\tilde{\Phi}_1(\mathbf{Q}) + \sin(\frac{\Lambda}{2})\tilde{\Phi}_2(\mathbf{Q}) \tag{1.49a}$$

$$\Phi_-(\mathbf{Q}) = -\sin(\frac{\Lambda}{2})\tilde{\Phi}_1(\mathbf{Q}) + \cos(\frac{\Lambda}{2})\tilde{\Phi}_2(\mathbf{Q}) \tag{1.49b}$$

$$\tan\Lambda(\mathbf{Q}) = \frac{W(\mathbf{Q})}{G(\mathbf{Q})}. \tag{1.49c}$$

Taylor expansion of quantities S, G, W around intersection geometry $\mathbf{Q}^*$ gives,

$$S(\mathbf{Q}) = S(\mathbf{Q}^*) + \nabla S(\mathbf{Q}^*) \cdot \delta Q + \cdots \tag{1.50a}$$

$$G(\mathbf{Q}) = \nabla G(\mathbf{Q}^*) \cdot \delta\mathbf{Q} + \cdots \tag{1.50b}$$

$$W(\mathbf{Q}) = \nabla W(\mathbf{Q}^*) \cdot \delta\mathbf{Q} + \cdots \tag{1.50c}$$

where $\delta\mathbf{Q} = (\mathbf{Q} - \mathbf{Q}^*)$. In the last two equations, the degeneracy conditions (1.48b) have been applied. The gradient quantities $\mathbf{g} = \nabla G(\mathbf{Q}^*)$, $\mathbf{h} = \nabla W(\mathbf{Q}^*)$ and $\nabla S(\mathbf{Q}^*)$ characterize the intersection. The first two are referred in the literature as the gradient difference and the non-adiabatic coupling vectors [92,95] respectively. An intersection is said to *conical intersection* when both these quantities are non-zero and not parallel to each other, .i.e. $\mathbf{g} \neq \mathbf{0}$, $\mathbf{h} \neq \mathbf{0}$.

Conical intersection (CI) is most commonly occurring type of intersection in molecules. For a CI, in the plane spanned by $\mathbf{g}$ and $\mathbf{h}$ vectors, the degeneracy is lifted linearly in the displacements $\delta\mathbf{Q}$ in the vicinity of the CI geometry. This plane is known as *branching space* or *branching plane* or also as $g-h$ plane. The $(N-2)$-dimensional hyperspace which is orthogonal to the branching space is known as the *intersection space*. The lifting of the degeneracy in the intersection space near to the CI geometry is at least quadratic in displacements. It must be noted that the branching and intersection spaces are specific to a given geometry on the CI seam. Both the spaces change their orientations as along the seam and this is a manifestation of the curvature of the CI seam.

To illustrate the conical nature of a CI, it is necessary to introduce a set of orthogonal coordinates for the branching and intersection spaces. The most convenient choice is the *intersection adapted coordinates* considered by Yarkony [92].

Two unit vectors $\hat{\mathbf{x}}$ and $\hat{\mathbf{y}}$ for the branching space are defined as,

$$\hat{\mathbf{x}} = \frac{\mathbf{g}(\mathbf{Q}^*)}{\| \mathbf{g}(\mathbf{Q}^*)\|} \tag{1.51a}$$

$$\hat{\mathbf{y}} = \frac{\mathbf{h}(\mathbf{Q}^*)}{\| \mathbf{h}(\mathbf{Q}^*)\|} \tag{1.51b}$$

It is assumed that $\mathbf{g}$ and $\mathbf{h}$ vectors are orthogonal which can be ensured by a special procedure discussed by Yarkony [96–98]. The vectors $\hat{\mathbf{x}}$ and $\hat{\mathbf{y}}$, along with a choice of orthonormal vectors $\hat{\mathbf{w}}_i, i = 1, (N-2)$ for the intersection space, define a set of coordinates (x, y, w_i). The components of $\nabla S(\mathbf{Q}^*)$ along these vectors can be obtained as,

$$\begin{aligned} s_x &= \nabla S(\mathbf{Q}^*) \cdot \hat{\mathbf{x}} \\ s_y &= \nabla S(\mathbf{Q}^*) \cdot \hat{\mathbf{y}} \\ s_{w_i} &= \nabla S(\mathbf{Q}^*) \cdot \hat{\mathbf{w}}_i \end{aligned}$$

With these definitions, the Hamiltonian matrix in equation (1.46) can be written in these coordinates as follows.

$$\mathbf{H}_e(x, y, w_i) = (s_x x + s_y y + \sum_{i=1}^{N-2} s_{w_i} w_i)\mathbb{I} + \begin{bmatrix} -gx & hy \\ hy & gx \end{bmatrix} \tag{1.52}$$

The PESs in the vicinity of $\mathbf{Q}^*$ are given by,

$$V_{\pm}(x, y, w_i) = (s_x x + s_y y + \sum_{i=1}^{N-2} s_{w_i} w_i) \pm \sqrt{g^2 x^2 + h^2 y^2} \tag{1.53}$$

Within the branching space which corresponds to $(x, y, w_i = 0)$, the energy gap between two PESs is given by,

$$\Delta V_{\pm}(x, y, w_i = 0) = 2\sqrt{g^2 x^2 + h^2 y^2} \tag{1.54}$$

From the above equation (1.54), the energy gap within the branching plane can be seen to be described by a general conical form [87]. Close to the CI point, each of PESs in the branching space is represented by a cone. The two cones are connected at the CI point forming a *double-cone*.

To obtain the parameters characterizing the double-cone of a CI, the equation (1.53) can be simplified by introducing polar coordinates (ρ, θ) within the

branching space through $\mathbf{x} = \rho\cos(\theta)$ and $\mathbf{y} = \rho\sin(\theta)$. Defining two new quantities $q(\theta)$ and $\lambda(\theta)$ as,

$$\begin{aligned} g\cos\theta &= q(\theta)\cos(\lambda(\theta)) \\ h\sin\theta &= q(\theta)\sin(\lambda(\theta)) \\ q^2(\theta) &= g^2\cos^2\theta + h^2\sin^2\theta \end{aligned}$$

the eigenvalues can be expressed as,

$$V_{\pm}(\rho,\theta,w_i) = (\rho s_x\cos\theta + \rho s_y\sin\theta + \sum_{i=1}^{N-2} s_{w_i}w_i) \pm \rho\delta_{gh}\sqrt{1+\Delta_{gh}\cos(2\theta)} \tag{1.55}$$

where d_{gh} and Δ_{gh} and are coordinate-independent quantities characterizing the shape of the double cone. The quantity δ_{gh} is the *pitch* of the double cone measuring its steepness.

$$d_{gh} = \sqrt{\frac{|g|^2+|h|^2}{2}} \tag{1.56}$$

The *asymmetry* in the pitch is measured by the Δ parameter.

$$\Delta_{gh} = \frac{|g|^2-|h|^2}{|g|^2+|h|^2} \tag{1.57}$$

The quantities s_x and s_y represent *tilts* of double cone along unit vectors $\hat{\mathbf{x}}$ and $\hat{\mathbf{y}}$ directions.

These four quantities, s_x, s_y, d_{gh} and Δ_{gh}, are known as *topographical parameters* of a CI double cone. They can be easily obtained from *ab initio* methods by computing $\mathbf{g}$ and $\mathbf{h}$ vectors, and the projection of $\nabla S(\mathbf{Q})$ on the branching space [96]. These parameters have been used to classify the CIs into namely two categories - peaked and sloped intersections [87]. The efficiency of a CI point for inducing non-adiabatic transitions has been related their topographical parameters and the category they belong to [99].

The appearance of geometric phase can be explicitly illustrated by looking at the behaviour of eigenfunctions given in equations (1.49). From the above treatment, it can be seen that the quantity $\Lambda\mathbf{Q}$ can be identified with $\lambda(\theta)$. When the polar angle θ is changed by 2π, it represents one complete traversal around the CI point along a circular path. The quantity $\lambda(\theta)$ can also be shown to change by 2π in such a traversal. However, since both eigenfunctions contain $\frac{\Lambda}{2}$, the cos and sin change sign causing the eigenfunctions to change their sign. As discussed in Ruedenberg [100], this sign change is a result of the closed path crossing the surfaces $G(\mathbf{Q}) = 0$ and

$W(\mathbf{Q}) = 0$ four times which in turn forces Λ to change by 2π.

The two-state CI model demonstrates that the eigenfunctions of electronic Hamiltonian change sign when traversing a loop enclosing a CI point. The sign-change behaviour of eigenfunctions was first discovered by Longuet-Higgins in 1963. Subsequently, this has been found to be a special of the more general concept of geometric phase introduced by Berry. This has also been referred by Mead and Truhlar as molecular Aharnov-Bohm effect [67].

The sign change of the eigenfunctions means that, in the vicinity of intersections, the electronic eigenfunctions can not be assumed to be real, continuous and single-valued functions of nuclear coordinates. However, it is possible to choose their optional phases to be complex functions of angular coordinate θ so as to restore their continuity and single-valuedness. In two-state CI model, this can be easily done by multiplying each of them by a geometry-dependent phase factor of $e^{-i\frac{\theta}{2}}$.

1.4 Computational Methods

To apply the theoretical concepts and formalism presented in the previous sections, it is necessary to have some compact representations of electronic and nuclear wave-functions and accurate and efficient methods to compute such wave-functions and their properties. Such methodologies have been developed over past several decades and continue to be developed to address newer physical situations. While quantum chemistry addresses computations of electronic structure of molecules, the area of molecular quantum dynamics deals with a numerical methods for time-propagation of nuclear wave-functions.

In this section, we provide a brief overview some of the important concepts and methodological developments. Both the areas, either in themselves or in combination, provide many opportunities for numerous applications of the developed methods to understand aspects of chemical physics phenomena.

1.4.1 Electronic Structure Methods

The subject of quantum chemistry is mainly concerned with concepts, wave-function ansatzs and methodologies for their computation to describe electronic structure of molecules. It is assumed that the electronic wave-functions and energies obtained by solving the eigenvalue problem of electronic Hamiltonian $\hat{H}_e$ can be meaningfully used. As discussed before, this is correct when BOA holds. Given the importance of the ground state and the validity of BOA for it, particularly at energies relevant for

normal temperature chemical phenomena, the primary focus of quantum chemistry is the ground electronic state. Although we are concerned with excited electronic states in this thesis, it is important to discuss the ground state methods. Many of the well-established ground-state methods can be extended to be applicable for excited states. Investigation of possibilities for such extensions is a currently an active area of research in quantum chemistry.

1.4.1.1 Many-Electron Wave-Functions

Understanding the binding of electrons to a stationary nuclear framework requires that the electrons be treated fully quantum mechanically. Further, as the electrons are indistinguishable, any computational approach also needs to ensure that calculated underlying wave-function treats all electrons on the same-level.

In quantum chemistry, many-electron wave-functions are constructed from a set of one-electron wave functions known as *molecular orbitals* (MO) [101]. The MOs are usually constructed as special linear combinations of *atomic orbitals* (AO) which are specially designed one-electron functions positioned at nuclei of a given molecular geometry. Alternate and more general prescriptions for MO constructions can also be envisaged and have been used. The MOs which are mainly delocalized over the bonding region are known as valence MO. Similarly, core and virtual types MOs can be defined. The set of MOs are assumed to be complete which happens when the set of AOs are complete.

To account for electron spin, the MOs are multiplied with spin-functions $\sigma(\omega)$ to obtain *spin-orbitals* (SO) as,

$$\varphi_{p,\sigma}(\mathbf{x}) = \varphi_p(\vec{r})\sigma(\omega), \tag{1.58}$$

where $\mathbf{x} = (\vec{r}, \omega)$ is a combined coordinate representing electronic spatial $\vec{r}$ and spin ω coordinates. The spin-function σ can take two possible choices $\{\alpha, \beta\}$ indicating up-spin and down-spin cases. The electronic Hamiltonian $\hat{H}_e$ is expressed in terms of one-electron $\hat{h}$ and two-electron $\hat{g}$ integrals over SOs as follows.

$$\sum_{p,q,\sigma} \langle \varphi_{p,\sigma_1} | \hat{h} | \varphi_{q,\sigma_2} \rangle \, a^\dagger_{p,\sigma_1} a_{q,\sigma_2} + \frac{1}{2} \sum_{p,q,r,s,\sigma} \langle \varphi_{p,\sigma_1} \varphi_{q,\sigma_2} | \hat{g} | \varphi_{r,\sigma_3} \varphi_{s,\sigma_4} \rangle \, a^\dagger_{p,\sigma_1} a^\dagger_{q,\sigma_2} a_{s,\sigma_4} a_{r,\sigma_3} \tag{1.59}$$

This is known as the second-quantization representation which makes use of electron creation $a^\dagger_{p,\sigma}$ and annihilation $a^\dagger_{q,\sigma}$ operators [101].

Starting with a collection of M SOs, $\{\varphi_{1,\sigma_1}, \varphi_{2,\sigma_2}, \ldots, \varphi_{M,\sigma_M}\}$, one constructs

a large set of special many-electron wave-functions known as Slater determinants (SD). This is done by selecting a set N SOs (N is the number of electrons) with repetitions not being allowed to account for the Pauli exclusion principle. The selected SOs are ordered according to a pre-defined order and the selection is denoted as $I = \{\varphi_{i,\sigma_1}, \varphi_{j,\sigma_2}, \ldots, \varphi_{k,\sigma_N}\}$ by a collective label I. The corresponding SD, denoted by Φ_I, is written as follows.

$$\Phi_I(\mathbf{x}_1, \mathbf{x}_2, \ldots, \mathbf{x}_N) = \frac{1}{N!} \begin{vmatrix} \varphi_{i,\sigma_1}(\mathbf{x}_1) & \varphi_{j,\sigma_2}(\mathbf{x}_1) & \ldots & \varphi_{k,\sigma_N}(\mathbf{x}_1) \\ \varphi_{i,\sigma_1}(\mathbf{x}_2) & \varphi_{j,\sigma_2}(\mathbf{x}_2) & \ldots & \varphi_{k,\sigma_N}(\mathbf{x}_2) \\ & \ldots\ldots\ldots\ldots\ldots & & \\ \varphi_{i,\sigma_1}(\mathbf{x}_N) & \varphi_{j,\sigma_2}(\mathbf{x}_N) & \ldots & \varphi_{k,\sigma_N}(\mathbf{x}_N) \end{vmatrix} \tag{1.60}$$

A SD is completely anti-symmetric with respect to permutations of electronic labels. One can also provide the following short notation for SD in which only the SOs and corresponding spins are indicated.

$$\Phi_I = |\varphi_{i,\sigma_1}\varphi_{j,\sigma_2}\ldots\varphi_{k,\sigma_N}\rangle \tag{1.61}$$

A general many-electron is then expressed as a linear combination of all possible N-electron SDs that can be constructed from the given set of M spin-orbitals.

$$\Psi(\mathbf{x}_1, \mathbf{x}_2, \ldots, \mathbf{x}_N) = \sum_I C_I \, \Phi_I \tag{1.62}$$

One of the fundamental difficulty of an electronic structure method is to capture correlated motions of electrons arising due to inter-electron Coulomb repulsion terms in the electronic Hamiltonian - an effect commonly referred to as *electron correlation*. In absence of such terms, all electronic states of molecules can be represented in terms of single SDs (or some fixed linear combination of SDs if spin needs to be properly accounted) constructed by solving a much easier one-electron eigen-problem.

The electron-electron repulsion prevents this from happening, leading to the necessity of having to represent the electronic states in terms of more complicated ansatz (1.62). Apart from this Coulomb correlation, the anti-symmetry requirement results in additional Fermi correlations between same-spin electrons. Two electrons of same spin can not come spatially closer as much as the ones with opposite spin can. This correlated electron motions results in a complicated structure in the wave-function, which is difficult to capture in a wide-variety of situations occurring in nature.

1.4.1.2 Hartree-Fock Method

One of the most important approximation used in quantum chemistry is the Hartree-Fock (HF) approximation where the many-electron wave-function is described as a *single* Slater determinant constructed from a set of MOs known as occupied orbitals. Since a single SD description does not describe the effects of electron repulsion, this is indirectly included by assuming that each electron moves in a spherically-averaged potential influenced by the remaining $(N-1)$ electrons.

In HF method, the occupied MOs are required to be found so as to minimize the energy of the corresponding HF determinant. This is carried out by the application of variation principle by treating the MOs as parameters. The energy of a SD $\Phi = |\varphi_{1,\sigma_1}\varphi_{2,\sigma_2}\cdots\varphi_{N,\sigma_N}\rangle$,

$$E = \langle\Phi|\hat{H}_{el}|\Phi\rangle \tag{1.63}$$

can be simplified by the application of Slater-Condon rules [101] and expressed in in terms of one- and two-electron integrals over occupied orbitals. Minimization of the expression with respect to orbital variations leads to an intego-differential eigenvalue equation known as the Hartree-Fock equation. The HF orbitals are shown to be eigenvectors of an effective one-electron operator $\hat{f}$, known as the *Fock* operator.

$$\hat{f}_\sigma(\mathbf{x})\varphi_{p,\sigma}(\mathbf{x}) = \epsilon_{i,\sigma}\varphi_{i,\sigma}(\mathbf{x}), \tag{1.64}$$

The Fock operator itself depends on the final set of occupied orbitals through the terms which describe Coulomb and Fermi-exchange electron-repulsion effects. The HF equations need to be solved in a self-consistent field (SCF) iterative procedure known as the HF-SCF method. The restricted HF (RHF) method of Roothan is one the most commonly used procedure where the HF state represents a closed-shell electronic configuration (each spatial occupied orbital is spin-paired).

For a majority of closed-shell molecules in their ground-state, the restricted HF-SCF method provides qualitatively correct electronic wave-functions and properties [101]. This is due to the fact that the SCF procedure manages to incorporate important part of electron repulsion effects into the resulting optimized HF orbitals.

1.4.1.3 Post-HF Methods

Even though the HF method treats electron repulsion effects in an averaged manner, it manages to recover almost 99% of the total electronic energy in most cases. The remaining 1% can be attributed to the instantaneous electron-electron repulsions

which can not be described within the SD picture. Although this 1% difference is small relative to the total energy, it is of the same magnitude as the energy differences relevant for most many chemical phenomenon. Further, weak dispersion interactions such as van der Waal interactions can not be described at the HF level.

As discussed later, the SD description becomes intrinsically inaccurate in many important cases. However, even when it is qualitatively adequate and the HF wave-function remains the dominant part of full wave-function, the HF results fail to provide sufficient quantitative accuracy for many properties. For thermo-chemical energies such as bond-dissociation and reaction energies, it is necessary to have results accurate within 1 kcal/mol. Calculations based on HF method have been shown to be unable to reach this level of accuracy.

The reason for this inaccuracy comes from the difference between the exact and HF energies, which is referred to as *electron-correlation energy*. This can only be recovered by going beyond the SD approximation employed in the HF theory. It includes contributions from determinants generated by moving electrons from HF occupied orbitals to unoccupied orbitals. While each such contribution itself is small in magnitude, all of them tend add up to result in a significant contribution to the correlation energy. This type of electron-correlation which results from a vast number of small contributions is usually referred to as *dynamical correlation*. Methods which seek to compute accurate dynamical correlation contributions are collectively known as *Post-HF methods*. The HF provides a good starting point for such methods.

Post-HF methods attempt to compute corrections to the total wave function by including a limited number of important SDs by the application of variational and perturbation approaches. The configuration interaction (CI) method is the simplest of post-HF methods. A CI wave function is given as follows.

$$\Psi = C_0\Phi_{HF} + \sum_{i,a} C_i^a \Phi_a^i + \sum_{\substack{i<j \\ a<b}} C_{ij}^{ab}\Phi_{ij}^{ab} + \cdots \tag{1.65}$$

where Φ_i^a and Φ_{ij}^{ab} are singly and doubly excited SDs. They are generated from the HF determinant Φ_{HF} by moving one and two electrons in occupied spin-orbitals $i, j, \ldots$ into the unoccupied spin-orbitals $a, b, \ldots$. When all possible SDs are included in the above expansion, the resulting method is known as *full CI*. The full CI methods yields exact results for a given MO basis.

Since the number of SDs grow exponentially with number of MOs, full CI calculations are not feasible even for small and medium-sized molecules. A truncation of equation (1.65) based on importance of determinants to be included gives raise to

a variety of truncated CI methods. Since the difference between exact Hamiltonian and Fock-operator contains terms up to two-electron excitations, most important determinants after the HF determinant are the single and doubly excited ones as indicated in equation (1.65). The resulting truncated CI is known as the CISD method. Due to the Brillouin condition obeyed by the HF wave-function, the contribution of singly excited terms remain much smaller when HF orbitals are used for CI treatment [101].

When perturbation approach is used with the Fock-opertor as zeroth-order Hamiltonian, the resulting methods are referred to as Møller-Plesset (MP) methods. The second-order MP2 method is one of the most widely used method as it is computationally cheaper than CISD without a significant loss of accuracy.

Benchmarks of CI methods have shown that CISD recovers up to 90% of electron-correlation correlation energy for small to medium-sized molecules. This performance becomes poorer with increase in molecular size [102]. This has been attributed to failure of truncated CI methods to satisfy size-consistency and size-extensivity properties [102]. Although the MP methods satisfy them, the slow convergence of perturbation series necessitates alternative electron correlation methods. The coupled-cluster (CC) method is another widely used post-HF electron-correlation method. It is a size-consistent and size-extensive method, and employs an exponential wave-function ansatz which allows contributions from higher excitations to be indirectly included even with singles and doubles level of truncation. The CC methods CCSD, CCSD(T) and CCSDT have now been established to be a sequence of increasingly accurate methods for ground state electronic structure and properties [103].

1.4.1.4 Multi-Reference Methods

Post-HF methods can only be used when HF determinant turns out to be qualitatively correct. There are many cases when the HF fails to be so. A well-understood case is the inability of the RHF method to describe the PES along a bond coordinate leading to homolytic bond-dissociation of a molecule in its ground state into two radical fragments. This failure is attributed to the intrinsic two-determinant nature of the wave-functions at the dissociation asymptote, which is qualitatively described by a valence-bond wave-function expressed in terms the separated atomic orbitals [101]. Another situation arises in excited states where electron are promoted to high-lying orbitals resulting in unpaired electrons. Transition metals systems containing multiple unpaired d-electrons are also cases when HF fails. It must be

stressed that most of the post-HF methods also fail when the HF fails.

Methods based on the assumption that a SD (such as HF state) dominates the wave-function are usually referred to as *single reference* (SR) methods. The failure of SR methods in many physical situations can be remedied by introducing *multi-reference* (MR) methods. These methods compute the wave-function in two steps. The first step consists of computing a suitable multi-determinantal wave-function with an ansatz that is qualitatively correct for the concerned physical situation. This step accounts for the dominant electron-correlation effects arising due to equally important contributions from several determinants - a type of correlation referred to as *static or non-dynamical correlation*. The subsequent step consists of improving this description by the addition of remaining dynamical electron correlations as in post-HF treatments.

The multi-configuration self-consistent field (MCSCF) method is one of the simplest MR method which can be used to construct qualitatively correct MR wave-functions [104]. Since the situations where HF fails usually involve unpaired electrons distributed in close-lying orbitals, the MCSCF wave-function consists of important SDs arising from a small number of such orbitals, known as active orbitals $\varphi_p, \varphi_q, \ldots$.

$$\Phi_{MCSCF} = \sum_I C_{\varphi_p,\varphi_q,\cdots} |\varphi_{p,\sigma_1}\varphi_{q,\sigma_2}\ldots\rangle \tag{1.66}$$

The complete active space self-consistent field (CASSCF) is a variant of MCSCF when the above wave-function includes *all* SDs resulting from distributing n electrons in m active orbitals and is denoted as CAS(m,n). The MCSCF/CASSCF wave-functions are optimized by applying variational treatment to both the coefficients and orbitals appearing in equation (1.66). The CASSCF procedure basically amounts to repeatedly performing a full CI treatment within the active space followed by a mixing of active and inactive orbitals to regenerate better active orbitals. The resulting equations are similar to HF-SCF equations, although the cost of the SCF procedure increases steeply with the number of SDs included. Currently, the CAS(12,12) wave-function is considered to be computationally expensive for routine applications. In the recent two decades, a number of new methods have emerged which manage to construct approximate CASSCF wave-functions corresponding to a large number of active orbitals.

1.4.1.5 Multi-Reference Dynamical Correlation Methods

Since MCSCF and all other related methods construct a qualitative MR wave-function, as in the HF method, the dynamical electron correlation is missing which often leads to inaccurate quantitative results. In principle, this can be recovered by the inclusion of additional determinants in equation (1.66). However, this becomes computationally inefficient as the number of determinants to be included is very large as in the case of post-HF methods, also suffers from numerical difficulties. This makes it necessary to develop dynamical correlation methods based on MCSCF wave-functions.

A commonly occurring situation requiring MR treatment is a low-lying electronically excited state that can be thought of as a single-electron excitation from a SR ground-state wave-function. Many excited states close to the Franck-Condon (FC) region are of this character. In such a case, the dynamical correlation of ground-state can be effectively transferred to the excited state using much simpler treatments avoiding a detailed MCSCF treatment. The equation-of-motion CC (EOM-CC) and linear response CC (LR-CC) methods are of this type [103, 105]. Although they are usually considered to be SR methods, they can also be viewed as MR methods for addressing the special physical situation of single-excitation. Their accuracy is adequate for many situations, but falls when one moves substantially away from the FC region. They can not be applied in photochemical reactions which take place far away from FC point.

Several multi-reference dynamical correlation methods have been developed in the past few decades. The multi-reference CI (MRCI) method has been most reliable of them [106, 107]. It suffers from size-consistency issues which necessitates Davidson-corrections (the MRCI+Q method). Many variants of MRCC methods have been explored although their routine use is still not possible.

The CASPT2 method has now emerged as a viable alternative. It has been adapted to treat a single state as well as to simultaneously treat multiple states. The method is also size-consistent and computationally efficient as compared to MRCI or MRCC, but its accuracy is somewhat lower. The CASPT2 is currently the method of choice for many interesting applications in computational photochemistry. In the works discussed in this thesis, we have used the Molpro quantum chemistry [108] package for performing most of the calculations at the MRCI or CASPT2 treatments following CASSCF. Occasionally, another program package COLUMBUS [109] has been used for MRCI.

1.4.2 Time-Dependent Methods for Nuclear Wave-Functions

It is necessary to account for quantum effects of nuclear motion to describe rovibrational spectra, vibronic effects in electronic spectroscopy, tunneling phenomena, and reactive scattering of molecules. This requires numerical solution of the nuclear Schrödinger equation relevant for the corresponding situation. In this subsection, we discuss some of the concepts and methods involved in computations of nuclear wave-functions.

When a molecular system is described by time-independent Hamiltonian, such as when it is not subject to time-dependent external fields or perturbations, its dynamics can be described using either time-independent or time-dependent forms of Schrödinger equation. The nuclear Hamiltonian can be represented in a suitable set of nuclear basis functions and resulting matrix can be diagonalized to obtain its eigenvalues and eigenfunctions. Such a time-independent approach can be used, for example, in computations of ground state rovibrational spectra of stable molecules. Dynamics starting from a specific nuclear state can then be easily described by resolving it in terms of computed eigenfunctions whose time evolution is a simple phase factor. However, this approach is not suitable in many situations because it requires large number of eigenstates to be computed.

An alternative is to describe the time evolution of a particular state of the molecular system through time-dependent Schrödinger equation (TDSE). Such a state can be chosen to represent the initial conditions of an experiment. It can be thought of as a *wave-packet* built from a superposition of a large number of energy eigenstates. The result of the time-evolution of the state can be related to the possible experimental outcomes.

A time-independent quantitity such as spectrum can be related to result of dynamics of an initial wave-packet prepared from interaction of light with ground electronic state. For example, the absorption spectrum of a molecule in an initial state Φ_0 is given by the following Fermi golden-rule expression,

$$P(E) = 2\pi \sum_{i \neq 0} |\langle \Phi_i | \hat{\mu} | \Phi_0 \rangle|^2 \delta(E - E_i) \tag{1.67}$$

where $\hat{\mu}$ is transition dipole operator. The spectrum can be calculated by computing all time-independent eigenvalues E_i and eigenfunctions Φ_i. However, it is possible to show that it can also be indirectly computed by a time-evolution of initial state $|\hat{\mu}\Phi_0\rangle$ as follows [110, 111].

$$P(E) = \int \mathrm{d}t \, e^{\frac{iEt}{\hbar}} \, \langle \hat{\mu}\Phi_0 | e^{-\frac{i\hat{H}t}{\hbar}} | \hat{\mu}\Phi_0 \rangle \tag{1.68}$$

The time-dependent wave-packet approach has many advantages which has led to its extensive use [110, 112, 113]. Not only it directly reflects the experimental conditions, it is also possible to treat time-evolution of wave-packets using numerically efficient methods. Further, it serves as a starting point for approximate wave-packet motion using semi-classical concepts leading to the *on-the-fly* direct dynamics methods [114]. The direct-dynamics methods will be discussed in Chapter 4.

In this subsection, we will discuss wave-packet methods. Since such numerical methods which accord fully quantum treatment of nuclear motion have not been used in the works reported in this thesis, our discussion here will be brief.

1.4.2.1 Solution of Nuclear TDSE

Nuclear TDSE is a partial differential equation as follows.

$$i\frac{\partial}{\partial t}\Psi(\mathbf{Q},t) = \hat{H}(\mathbf{Q})\Psi(\mathbf{Q},t) \tag{1.69a}$$

$$\hat{H}(\mathbf{Q}) = \hat{T}(\mathbf{Q}) + \hat{V}(\mathbf{Q}) \tag{1.69b}$$

where $\mathbf{Q} = \{q_\nu, \nu = 1, f\}$ collectively denotes coordinates of f nuclear degrees of freedom or modes. Depending on inclusion of rotations, f is either $3N-3$ or $3N-6$. The operators $\hat{H}(\mathbf{Q}), \hat{T}(\mathbf{Q}), \hat{V}(\mathbf{Q})$ represent, respectively, nuclear Hamiltonian, kinetic energy and potential energy operators in chosen $\mathbf{Q}$ coordinate system. The scalar potential $\hat{V}(\mathbf{Q})$ is a complicated function of $\mathbf{Q}$ and can not usually be represented in a simple analytical form. When dealing with nuclear dynamics on a single PES, it is usually represented in a simple form by fitting the *ab initio* computed PES to a pre-defined analytical form [115, 116]. The precise expression for nuclear kinetic energy operator $\hat{T}(\mathbf{Q})$ depends on the nature of coordinates. When $\mathbf{Q}$ are chosen to be mass-scaled Cartesian coordinates, $\hat{T}$ is given by a simple expression.

$$\hat{T}(\mathbf{Q}) = -\frac{1}{2}\sum_\nu \frac{\partial^2}{\partial q_\nu^2} \tag{1.70}$$

In many cases, for example when dealing with floppy molecules, more general coordinates need to be chosen. Then expressions for $\hat{T}$ become very complicated. Methods have been available to choose a set of coordinates for which it can be represented in terms of sum of products of partial derivative operators acting on single coordinates [117]. When more than one electronic states are involved, $\hat{V}(\mathbf{Q})$ is diabatic potential matrix and $\hat{T}(\mathbf{Q})$ is diagonal matrix.

In order to solve TDSE, the wave-function Ψ is expanded as,

$$\Psi(\mathbf{Q}, t) = \sum_{J=1}^{M} C_J(t)\Phi(\mathbf{Q}) \tag{1.71}$$

where Φ_J are a set of orthogonal basis functions chosen to represent the state as it evolves in time. When substituted into equation (1.69a), this gives,

$$i\frac{\partial}{\partial t}\mathbf{c}(t) = \mathbf{H}\,\mathbf{c}(t) \tag{1.72}$$

where $\mathbf{c}$ is a column vector of coeffcients C_J and matrix $\mathbf{H}$ represents the Hamiltonian in the basis of Φ_J functions as,

$$H_{JI} = \langle \Phi_J | \hat{H} | \Phi_I \rangle = T_{JI} + V_{JI} \tag{1.73}$$

The equations (1.72) are a set of coupled first-order linear differential equations. Solution can be written as,

$$\mathbf{c}(t) = \mathsf{U}(t, t_0)\,\mathbf{c}(t_0) = e^{-i\mathbf{H}(t-t_0)}\,\mathbf{c}(t_0) \tag{1.74}$$

where $\mathbf{c}(t_0)$ represents initial state at $t = t_0$ and U is matrix of time evolution operator. Evaluation of U or its action on $\mathbf{c}(t_0)$ requires computation of elements of Hamiltonian matrix $\mathbf{H}$.

To proceed further, it is necessary to know chosen form of basis functions $\Phi_J(\mathbf{Q})$. For this, we consider one-dimensional equivalent of (1.69a) as follows.

$$\hat{H}(x) = \hat{T}(x) + \hat{V}(x) = -\frac{1}{2}\frac{\mathrm{d}^2}{\mathrm{d}x^2} + \hat{V}(x) \tag{1.75}$$

where, we have used x in place of q_1. It is usually possible to use a set of N orthogonal basis functions $\{|\phi_n\rangle = \phi_n(x), n = 1, \cdots, N\}$ with known analytical form such that kinetic energy matrix elements $T_{mn} = \langle \phi_m | \hat{T} | \phi_n \rangle$ can be evaluated analytically. Such a basis is known as *spectral basis*. However, since $\hat{V}(x)$ is a complicated function, it can be usually evaluated only by performing numerical integration.

Therefore, spectral basis functions $\phi_n(x)$ are not very useful unless they allow efficient evaluation or approximation of potential energy matrix elements V_{mn}. Therefore, usually they are constructed from n-th order orthogonal polynomials $P_n(x)$ arising in solution of one-dimensional problems with specific potentials, such as Hermite polynomials of harmonic oscillator problem. These polynomials satisfy

the following orthogonality relations,

$$\int w(x)P_m(x)P_n(x)\mathrm{d}x = \delta_{mn} \tag{1.76}$$

here $w(x)$ is a postive weight-function associated with the problem where these polynomials arise. The orthogonal spectral basis can be defined as $\phi_n(x) = \sqrt{w(x)}\, p_n(x)$.

Such a choice has the advantage Gaussian quadrature formula can be employed to *exactly* compute the overlap of any two functions $f(x)$ and $g(x)$ belonging to the space of $\phi_n(x)$ basis functions as,

$$\int f(x)g(x)\mathrm{d}x = \sum_{\alpha=1}^{N} w_\alpha f(x_\alpha)g(x_\alpha) \tag{1.77}$$

where x_α are N grid points located in the integration interval and w_α are the associated positive weights. Using equation (1.77), the overlaps of a pair of basis functions $\phi_m(x)$ and $\phi_n(x)$ (with $m, n < N$) and matrix element X_{mn} of position operator $\hat{x}$ between them can be written as,

$$\int \phi_m(x)\phi_n(x)\mathrm{d}x = \sum_{\alpha=1}^{N} w_\alpha \phi_m(x_\alpha)\phi_n(x_\alpha) = \delta_{mn} \tag{1.78a}$$

$$\int \phi_m(x)\hat{x}\phi_n(x)\mathrm{d}x = \sum_{\alpha=1}^{N} w_\alpha \phi_m(x_\alpha)x_\alpha\phi_n(x_\alpha) = X_{mn} \tag{1.78b}$$

By defining matrix $\mathbf{U}$ with elements as $U_{\alpha,m} = \sqrt{w_\alpha}\,\phi_m(x_\alpha)$, the above equations can be written as

$$\mathbf{U}^t\mathbf{U} = \mathbf{I} \tag{1.79a}$$

$$\mathbf{U}^t\mathbf{x}\mathbf{U} = \mathbf{X} \tag{1.79b}$$

where x is a diagonal matrix with grid points x_α along the diagonal. The equation (1.79b) means that simple matrix $\mathbf{U}^t$ diagonalizes matrix of position operator $\mathbf{X}$ in spectral basis, and the grid locations x_α are obtained as eigenvalues of $\mathbf{X}$.

Gaussian quadrature ensures that the above relations are exact for any N. With this, the potential energy matrix elements V_{mn} can be evaluated, *approximately*, as follows.

$$V_{mn} = \int \phi_m(x)\hat{V}(x)\phi_n(x)\mathrm{d}x \approx \sum_{\alpha=1}^{N} w_\alpha \phi_m(x_\alpha)V(x_\alpha)\phi_n(x_\alpha) \tag{1.80}$$

or in matrix form as

$$\mathbf{V} \approx \mathbf{U}^t \mathbf{v}(\mathbf{x}) \mathbf{U} \tag{1.81}$$

where $\mathbf{v}(\mathbf{x})$ is a diagonal matrix with elements $V(x_\alpha)$. Such a scheme for evaluation of matrix elments of potential energy operator is known as HEG (Harris. Engerholm and Gwinn) procedure after it was first proposed by Harris and coworkers [118]. The representation of Hamiltonian in spectral basis with potential energy matrix computed using HEG procedure is usually referred to as finite basis representation (FBR) [119].

Another representation, known as discrete variable representation (DVR) [120], can be obtained by recognizing that matrix $\mathbf{U}$ can be used to perform a basis change as follows.

$$\xi_\alpha(x) = \sum_m U_{\alpha,m} \phi_m(x) \tag{1.82}$$

The new basis set $\xi_\alpha(x), \alpha = 1, \ldots, N$ is known as DVR basis. It has the property that it vanishes at all other other grid points other than x_α.

$$\xi_\alpha(x_\beta) = \frac{\delta_{\alpha,\beta}}{\sqrt{w_\alpha}} \tag{1.83}$$

The DVR basis function $\xi_\alpha(x)$ is an eigenfunction of position operator $\hat{x}$ with eigenvalue x_α. It can be seen that it is localized around x_α with small amplitudes in other locations. As number of basis functions increase, it becomes even more localized and starts to resemble Dirac-delta behaviour of position operator eigenfunction $\delta(x - x_\alpha)$. The DVR basis is also known as *pseudo-spectral*, because of appearance of localized grid basis functions, but still it can be related to spectral basis.

The Hamiltonian can also be constructed in DVR basis. The relation between FBR and DVR can be summarized as follows.

$$\mathbf{H}^{\mathrm{FBR}} = \mathbf{T} + \mathbf{U}^t \, \mathbf{v}(\mathbf{x}) \, \mathbf{U} \tag{1.84a}$$

$$\mathbf{H}^{\mathrm{DVR}} = \mathbf{U} \, \mathbf{T} \, \mathbf{U}^t + \mathbf{v}(\mathbf{x}) \tag{1.84b}$$

Although both representation are equivalent because of the unitary transformation $\mathbf{U}$ connecting the two basis sets, the DVR basis has the advantage that potential energy $\mathbf{v}(\mathbf{x})$ is diagonal in this basis. However, the kinetic energy matrix $\mathbf{T}$ needs to be transformed after its construction in spectral basis.

Suitable functions $\Phi_J(\mathbf{Q})$ can be constructed in terms of DVR basis functions for

each degree of freedom as follows.

$$\Phi_J(\mathbf{Q}) = \Phi_{j_1,\ldots,j_f}(q_1,\ldots,q_f) = \prod_{\nu=1}^{f} \xi_{j_\nu}^{\nu}(q_\nu) \tag{1.85}$$

Here, $\xi_{j_\nu}^{\nu}(q_\nu)$ is a j_ν-th basis function for ν-th degree of freedom q_ν. Substitution of equation (1.85) into equation (1.71) leads to,

$$\Psi(\mathbf{Q},t) = \sum_{j=1}^{N_1} \cdots \sum_{j=1}^{N_f} C_{j_1,\ldots,j_f}(t) \prod_{\nu=1}^{f} \xi_{j_\nu}^{\nu}(q_\nu) \tag{1.86}$$

Such a product basis as in (1.85) simplifies the evaluation of matrix elements. It has been well-known that [119] the advantages of DVR basis emerge when multi-dimensional problem are to be treated. In this case, DVR basis considerably simplifies evaluation of potential energy matrix, while kinetic energy operator, due to its special form, can be efficiently transformed to DVR basis. Due to this, DVR has been extensively used in ro-vibronic problems [121] and quantum wave-packet dynamics [122]. A detailed discussion of the idea behind DVR method and its generality can be found in the works of Light and coworkers [123–125].

After computing Hamiltonian matrix, the TDSE equation (1.72) can be solved by making use of different types of algorithms that have been developed for propagative solution of linear differential equations. Some of the common schemes are the split-operator method, the Chebyshev polynomial method, the Lanczos iteration method, the second-order differencing method. For example, the split-operator method divides the time interval $T = (t_f - t_0)$ into N_t small time steps $\Delta t = T/N_t$, and computes action of $\mathsf{U}(t_f, t_0)$ on $\mathbf{c}(t_0)$ as,

$$\mathbf{c}(t_f) = e^{-i\mathbf{H}(t_f - t_0)}\,\mathbf{c}(t_0) = e^{-i\mathbf{H}\Delta t} \cdots e^{-i\mathbf{H}\Delta t}\mathbf{c}(t_0) \tag{1.87}$$

where, on $e^{-i\mathbf{H}\Delta t}$ is repeatedly applied N_t times on the starting vector $\mathbf{c}(t_0)$. For short-time Δt, it can be approximated as

$$e^{-i\mathbf{H}\Delta t} \approx e^{-i\mathbf{T}\Delta t} e^{-i\mathbf{V}\Delta t} \tag{1.88}$$

While application of $\mathbf{V}$ is straightforward in DVR basis, application of $\mathbf{T}$ can be carried out by transforming the vector resulting from first operation to FBR basis and transforming it back after second step. A special type of DVR method, known as Fourier grid method, considerably improves the efficiency of this step by making

it possible to carry out the above transformation steps using the very efficient fast Fourier transformation method [126, 127]. A comparison of different time-dependent propagation methods can be found in the references [128].

1.4.2.2 Advanced Methods and Algorithms

A major drawback of the standard method based on expansion (1.86) is exponential scaling of number of product basis functions M with the number of degree of freedom f, *.i.e.*, $M = N_1 \cdots N_f \approx N^f$. This causes computational bottlenecks in Hamiltonian matrix element evaluation and time propagation steps. Therefore, its use is limited to small-sized systems with upto 3-4 atoms (atmost 10 degrees of modes with a restricted number of basis functions for each degree).

In recent decades, a new method known as multi-configuration time dependent hartree approach (MCTDH) has been developed which allows good quality wave-packet dynamics to be carried out for much larger systems, when combined with appropriate methods for fitting of potentials [129–132]. The main idea of MCTDH is to modify the expansion (1.86) so that it can capture well the localized structure of wave-packet as it moves along the PES. In MCTDH, this is achieved by using time-dependent variationally optimized basis sets instead of fixed ones such as $\xi^{\nu}_{j_\nu}(q_\nu)$. The MCTDH expansion is,

$$\Psi(\mathbf{Q}, t) = \sum_{j_1=1}^{n_1} \cdots \sum_{j_p=1}^{n_p} C_{j_1,\ldots,j_p}(t) \prod_{\nu=1}^{p} \chi^{\nu}_{j_\nu}(Q_\nu, t) \tag{1.89}$$

where time-dependent basis functions $\chi^{\nu}_{j_\nu}(Q_\nu, t)$ are known as single-particle functions (SPFs) each corresponding to a particle. The f degrees in (1.86) have now been replaced by p particles of different types. The coordinate Q_ν of ν-th particle can be a appropriate combination of coordinates of original system. The SPFs are expanded in terms of products of time-independent basis functions of coordinates of original degrees of freedom which have been combined to form the particle as,

$$\chi^{\nu}_{j_\nu}(Q_\nu, t) = \sum_{l_1=1}^{N_1} \cdots \sum_{l_d=1}^{N_d} C^{j_\nu}_{l_1,\ldots,l_d}(t) \prod_{\mu=1}^{d} \xi^{\mu}_{l_\mu}(q^{\nu}_{\mu}) \tag{1.90}$$

where d original degrees of freedom $(q^{\nu}_{\mu}, \mu = 1, \ldots, d)$ combined to form Q_ν coordinate of ν-th particle. The main differences between MCTDH ansatz (1.89) as compared to standard ansatz (1.86) are 1. number of particles p is smaller than f 2. number of SPFs for each particle n_ν is much smaller than number of basis functions N_ν for

each original degree of freedom 3. The time-dependence of SPFs makes it possible to restrict to n_ν to a smaller number. This increases computational efficiency of the method. Application of time-dependent variation principle to MCTDH ansatz (1.89) leads to a complicated set of time propagation equations whose solution methods have been discussed in detail in references cited above. The MCTDH method has been succesfully applied to a wide range of chemical phenomenon such as photodissociation, photo-absorption spectra, pre-dissociation, resonance Raman spectra [133].

1.5 Structure of Thesis

The thesis is organized as follows. Since we have investigated two different aspects of non-adiabatic effects, the thesis is divided into two parts. In the first part, our focus is to understand the structure of intersection seam through *ab-initio* calculations. In the second part, computational studies have been carried out to understand non-adiabatic electronic relaxation effects in photochemical reactions.

In the **second chapter**, we study global features of an intersection seam in a simple triatomic system. It is well-known that seams have complicated structure in configuration space with different branches connected at special points. A major difficulty in studying such structure for polyatomic molecules is that their seams are irregular and high-dimensional. However, in triatomic system, the seam is one-dimensional curve avoiding these difficulties. Limited studies focused on global seam structure have been available in the literatue. In this chapter, we present a numerical study of mapping the seam in configuration space by considering a model one-electron system (H_3^{++}). Our results indicate an interesting pattern of seam branches.

In the **third chapter**, we have considered how NACTs can be used to understand local structure of a seam by considering ethylene as our prototype system. To examine seam in the vicinity of a CI geometry, we compute line integrals of NACTs along a series of closed contours around the CI. We attempt to relate the behaviour NACs along these contours to understand the progression of the seam within certain 2-dimensional planes.

The **fourth chapter** is an account of computational methods of photochemistry. Here, we review a number of basic concepts and computational methods for understanding photochemical reactions. The differences between classical and modern views of photochemistry are discussed. With an example from literature, role played by CIs in emergence of modern view is highlighted. The basic elements of computational pathway approach for photochemistry are discussed, with emphasis on how this approach integrates important structural details of excited PESs to

provide a static mechanistic picure of a photochemical reaction. The limitations of this approach are pointed out and importance of obtaining additional dynamical information is emphasized. An overview of nuclei dynamics method used in photochemistry is also given.

In the **chapter five**, we present a comparative study to understand experimentally observed differences in electronic relaxation of acrolein and crotonaldehyde using high-level multi-reference calculations and *ab-initio* multiple spawning method (AIMS). The important features of photochemical model used in context of α, β-enones is ascertained for both the molecules by characterizing local minima and minimum-energy CIs of their singlet and triplet states using CASSCF and MRCI methods. We have also discussed results from AIMS dynamics simulations.

In the **sixth chapter**, we have tried to understand electronic relaxation in photochemical electrocyclic reactions involving heteroatom by a detailed study on a model nitrone system - photochemical conversion of Formaldonitrone to Oxaziridine. The nature of excited states at ground state equilibrium geometry has been ascertained. First excited state PES has been explored by locating minima and minimum-energy CI structures. Pathway approach has been used to locate minimum energy paths connecting these structures to provide a picture of photochemical relaxation pathways for this system. AIMS dynamics has been used to confirm ultrafast nature of this process.

Chapter 2

Exploring Intersection Seam in a Simple Triatomic Molecular System

2.1 Introduction

In the past few decades, the role of CIs in promoting non-adiabatic effects has been extensively investigated [3, 4]. The CI geometry at which two adiabatic electronic states are degenerate is not an isolated point in nuclear configuration space. It is a part of a set of continuously connected geometries referred to as the intersection seam of two states. As discussed in Chapter 1(section 1.2.1), the Born-Huang formalism makes it possible to describe non-adiabatic effects in terms of PESs and their geometry-dependent NACs. In this formalism, the effects can be pictured to arise from the intersection seam region of the nuclear configuration space. The intersection seam can be defined as a subspace of nuclear configuration space in which the electronic states are exactly degenerate. It can be thought of as an extended and thin geometric object embedded in the larger configuration space. The most common case of two-state seam is a $(N_i - 2)$-dimensional hypersurface of the full N_i-dimensional configuration space. Even though couplings are singular on the intersection seam itself, they do remain rather large within a region of non-negligible volume around the seam. This feature causes the electron-nuclear wave-function to develop significant components along all the electronic states involved in the formation of seam.

Apart from couplings, the nuclear dynamics in the vicinity of a seam is strongly influenced by the topography of PESs along the branching space modes where the degeneracy is lifted. For CI seams, the topography is now well-established to be

double-cone in nature [87]. The effect of PES topography is particularly prominent for the case of symmetry-induced CIs occurring in Jahn-Teller (JT) systems [56]. Here, part of the seam where JT degeneracy exists is usually of low dimension, being spanned by only the totally-symmetric modes. As a consequence of the well-known JT theorem, the energy of one state is always lowered along a number of active branching space modes. Therefore, when viewed from any point on the JT seam, the double-cone is vertically oriented. Such a topography is responsible for the well-known symmetry-breaking distortions of the JT effect [56], and it can be captured in terms of simple models with a small number of parameters [134,135]. A significant part of the current understanding of non-adiabatic effects on molecular vibronic spectra and dynamics comea from numerous theoretical studies and experimental interpretations based on JT models and their generalizations to multi-state multi-mode situations [44, 136].

The situation is somewhat different for accidental intersections. Although the PES topography around such a seam remains conical, the orientation of the double-cone and extent of degeneracy breaking within branching plane strongly depends on the particular location on the seam [87]. Further, the seam also has its own curvature which can influence dynamics further away from it [92, 137]. The net result is a situation which is not amenable for a description in terms of a generic JT-like model.

Although accidental intersections have been discussed in early works [138–140], they received increased attention after the development of efficient algorithms for locating them [141,142]. A number of their interesting features have been investigated in the works of Yarkony, Ruedenberg and others. It has been found to be important to account for the presence of such accidental seams in many computational studies. As discussed in Chapter 4, a special seam point which is a local minimum along seam coordinates plays an important role in photochemistry and has been used for rationalization of photochemical reaction mechanisms [12, 143]. Situations which benefit from a characterization of extended-seam portions running close to the computed reaction paths have also been reported [144]. A variety of on-the-fly dynamics methods monitor the magnitude of NACs to detect entry of trajectories into the seam regions [10, 11]. Recently, several methods to generate adiabatic/diabatic PESs suitable for non-adiabatic wave-packet dynamics have attempted to accurately describe accidental seams and their topography [116, 145–148].

Motivated by these studies, we have carried out computational studies to numerically construct an intersection seam in a larger region of nuclear configuration space for a simple case - the H_3^{++} molecular system. In this chapter, results from this study have been presented and discussed. The goal of these studies, to be detailed out in the next section, is to exhibit how different branches of a seam are connected via the

confluence points and the role played by 3-state intersections for their connectivity with other seams. The section 2.2 includes a brief description of seams and their features relevant for this work. Details about the system are provided in section2.3. Computational details and results of the seam construction and its visualization are presented in section 2.4.2. The section 2.5 summaries our findings and suggests possibilities for future works.

2.2 Intersection Seams

The conditions for a geometry $\mathbf{Q}$ to be on the intersection seam, the role of symmetry and resulting seam classification have been well-understood, see Ref. [87, 92]. As discussed in Chapter 1, for two-state case, one represents the Hamiltonian in a basis of many-electron functions $\Phi_1(\mathbf{Q})$ and $\Phi_2(\mathbf{Q})$ which are assumed to be smooth and decoupled from their orthogonal complement throughout a region.

$$\mathbf{H}(\mathbf{Q}) = \begin{pmatrix} H_{11}(\mathbf{Q}) & H_{12}(\mathbf{Q}) \\ H_{12}(\mathbf{Q}) & H_{22}(\mathbf{Q}) \end{pmatrix} \tag{2.1}$$

The seam is defined to be the set of geometries $\mathbf{Q}^*$ where $\mathbf{H}(\mathbf{Q}^*)$ has degenerate eigenvalues. This leads to the following two independent conditions

$$G(\mathbf{Q}^*) = H_{11}(\mathbf{Q}^*) - H_{22}(\mathbf{Q}^*) = 0 \tag{2.2a}$$

$$W(\mathbf{Q}^*) = H_{12}(\mathbf{Q}^*) = 0 \tag{2.2b}$$

Symmetry enforced (or required) intersection results when both these conditions are satisfied due to symmetry reasons. Example is a pair of degenerate states at geometries where symmetry group has degenerate irreps. In this case, the entire extended region of high-symmetry subspace where this degeneracy exists is the intersection seam. The condition (2.2b) can also be satisfied at a geometry $\mathbf{Q}$ belonging to a subspace of lower symmetry, when the pair of states belong to different irreps of the corresponding symmetry group. In this case, the condition (2.2a) can be satisfied accidentally for a subset of geometries within the symmetry subspace. If the symmetry subspace has dimension N_s, then the seam is $(N_s - 1)$-dimensional and such a seam is referred to as symmetry-allowed accidental type. When both conditions can only be met accidentally at special geometry of full N_i-dimensional configuration space for a pair of states of same symmetry, then a $(N_i - 2)$-dimensional accidental same-symmetry seam results. As discussed by Rudenberg [87], the symmetry-allowed

accidental seam can be often thought of as being part of an accidental same-symmetry seam when the latter intersects with a symmetry subspace. Such a situation does not arise for triatomic molecules as the same-symmetry seam in this case is of lower dimension (one-dimensional) as compared to the possible dimension of a possible symmetry subspace (two-dimensional for C_{2v}).

The quantities, $\mathbf{g} = \boldsymbol{\nabla} G(\mathbf{Q}^*)$ and $\mathbf{h} = \boldsymbol{\nabla} W(\mathbf{Q}^*)$, when non-zero, define a plane called the branching plane (also called the g-h plane) at the seam point $\mathbf{Q}^*$. The degeneracy lifting within the branching plane in the vicinity of a seam point can be described by a double-cone [55].

2.2.1 Confluences

An interesting feature of seams is that they can have one or more branches connected together at special geometries known as *confluences or intersection nodes*. Although accidental seams were already discussed in the early works of Carrington [138] and Davidson [139], confluences were noticed and further investigated only after the works of Ruedenberg [149, 150] and Yarkony [151]. Initial studies of Ruedenberg on Ozone molecule confirmed the existence of a seam of two lowest states passing through the C_{2v} plane at three locations where the states are of same symmetry. A later study [152] completely characterized this seam and established that it forms a closed-curve within the 3-dimensional nuclear configuration space, and it passes through the C_{2v} plane at three additional locations. It was then established that, at these latter locations, the seam is connected with another symmetry-allowed C_{2v} seam for the same-pair of states. Therefore, these three locations were identified to be confluence points connecting symmetry-allowed and same-symmetry branches of the seam of two lowest states of Ozone.

Referring to them as *doubly diabolical*, Yarkony located confluences of symmetry-allowed and same-symmetry branches in a variety of triatomic molecules using a systematic procedure for their location based on orthogonal intersection-adapted coordinates [153–155]. He demonstrated how a confluence of different branches of seam arises from a factorization of conditions (2.2) and pointed out different effect of confluence on local PES topography and geometrical phases. Matsika and Yarkony developed an iterative algorithm to locate the entire confluence subspaces based on an analytical representation of PES and derivative-couplings using second-order degenerate perturbation theory, and applied it to a tetratomic molecule [156].

2.2.2 Three State Intersections

The seams of neighbouring pair of states can be connected through 3-state intersections (3-SI). Although 3-SIs are rare in configuration space, efficient methods to locate general 3-SIs were developed [93, 94] and successfully applied by Yarkony and coworkers [157, 158].Even 3-SIs involving ground-state have been found in simple organic molecules such as Pyrazolyl radical [159] and Malonaldehyde [160]. Martinez and coworkers investigated possible role of Malonaldehyde 3-SI in its S_2 photochemistry [161]. Deriving evidence from these studies, it has been conjectured [161] that the seam of a pair of states not only fully connected, but also connected to the seam for pair of neighbouring states via the 3-SIs. A recent review by Matsika provides an excellent overview of 3-SIs and documents their prevalence and importance in chemistry [162].

Motivated by their importance in non-adiabatic dynamics, in this work we seek to numerically construct and visualize an intersection seam for a simple triatomic system over a substantially larger region of configuration space. The goal is to explore the seam connectivity for a pair of states through an example, .i.e., how its different branches are connected together at confluences and 3-SIs and how its geometry is affected by the seams of neighbouring states. A homonuclear triatomic molecular system has been chosen so that all types of branches are feasible. Although this can be carried out for any such triatomic molecule, a simple one-electron system has been chosen to simplify the calculations.

2.3 The System - H_3^{++}

The molecular system, dication H_3^{++}, has been chosen for this study due its simplicity as a one-electron system. As a consequence, the results obtained only depend on the basis set chosen thus allowing accurate determination of intersection seams.

The related systems, H_3^+ and H_3 and their isotopologues, have been extensively studied. The cation H_3^+, being the most abundant and stable ion in interstellar space, has been a subject of several studies (see Ref. [163] for its rotation-vibration spectrum, and Refs. [164, 165] for a recent PES and reactive scattering calculations). Similarly, the neutral H_3 system has been of considerable interest in gas-phase reaction dynamics and reactive scattering methods [166–168]. Being a Jahn-Teller (JT) system with a high-lying D_{3h} CI seam between ground and first excited states, it has served as a prototype system in several studies to understand the geometric-phase effects of this

CI seam on reactive-scattering of H + H_2 and its isotopologues [169–174].

In contrast, the H_3^{++} system has been a subject of relatively small number of studies. Conroy [175] computed its ground state PES for linear, isosceles and equilateral configurations and concluded it to be repulsive with no minimum. Subsequently, its excited states were also considered and found to be repulsive [176, 177]. Berkowitz and Stocker [178] unsuccessfully tried to detect it by charge striping of H_3^+ at MeV energies.

As with many highly charged molecules [179, 180], the molecule is unstable and readily undergoes dissociation along purely repulsive PES into three channels. Two channels leading to H_2^+ + H^+ and H + 2 H^+ asymptotic products are, respectively 0.594 H and 0.5 H, below the third complete dissociation channel involving fully separated protons and electron with zero kinetic energy. The vertical ionization potential (IP) of cation H_3^+ at its reported D_{3h} equilibrium geometry [164] R=1.65 Bohr can be estimated to be 33.5 eV (compare IP of Li^+ as 75.6 eV). At this geometry, the electronic energy of ground state of H_3^{++} is -0.111857 H (using basis set used in this paper), indicating its dissociation into channels with bound electron. However, all excited states at this geometry are above the complete dissociation channel.

Clearly, H_3^{++} is a purely dissociative molecular system with no molecular bound states making it an uninteresting system to study. In this work, we have chosen the system as it makes it easy to numerically determine intersection seams. The results will be of relevance in future studies of its dissociation dynamics. A recent study [181] has considered controlling its dissociation using short laser pulses. Another study has explored the intriguing possibility of short-lived H_3^{++} as being precursor for other triatomic molecules [182] in early universe.

2.4 Results and Discussions

2.4.1 D_{3h} Scans

In order to select a pair of states and a basis set for this study, a number of scans were performed along the D_{3h} coordinate between 0.4Å and 6.0 Å for different basis sets. The basis sets were constructed from standard basis sets cc-pVQZ(spd) , cc-pV6Z(spdfg), cc-8Z(spdfgh) sets by augmenting them with 2 to 6 even-tempered gaussians (ETGs) for each shell. The augmentations were found to be necessary to obtain accurate results for excited states. Total 15 lowest energy states were computed by construction of Hamiltonian matrix using one-electron integrals and diagoalizing it. The procedure was implemented using *matrop* routines of MOLPRO [108]. Amongst

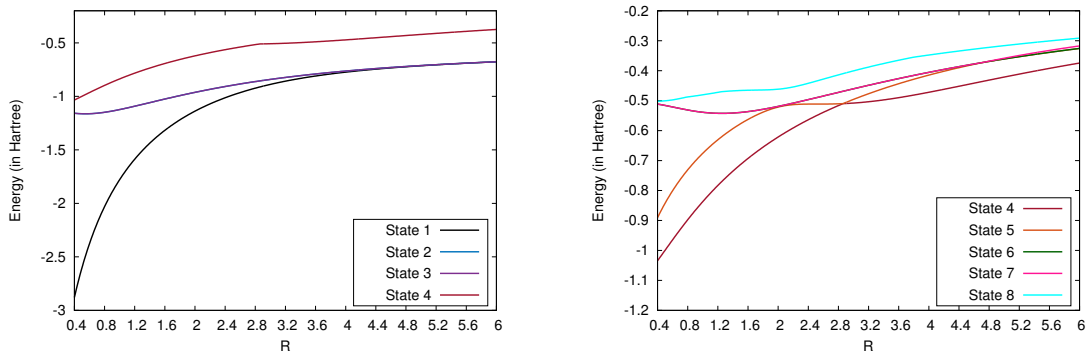

(a) States 1-4. **(b)** States 4-8.

Figure 2.1: D_{3h} scans.

Table 2.1: Irreducible representations of states at different geometries.

R Å	1	2	3	4	5	6	7	8	9	10
1.2	A_1'	E'	E'	A_2''	A_1'	E'	E'	E''	E''	A_1'
2.4	A_1'	E'	E'	A_2''	A_1'	E'	E'	A_1'	E''	E''
3.2	A_1'	E'	E'	A_1'	A_2''	E'	E'	A_1'	E''	E''
4.6	A_1'	E'	E'	A_1'	A_2''	E'	E'	E''	E''	A_1'
4.8	A_1'	E'	E'	A_1'	E'	E'	A_2''	E''	E''	A_1'

them , the lowest 9 electronic states are considered here. The results are shown in Figure 2.1 and Figure 2.2 for the basis cc-pV6Z(spdfg) augmented with 3 ETGs, which has been selected for this work. In these figures and rest of the chapter, only electronic energies of states are plotted since nuclear repulsion energy changes are much larger (typically 10-15 times) over the range of geometries.

The Figure 2.1a shows states 1-3 merging together to the asymptotic limit of -0.5 H. They can be seen to be well-separated from state 4 which has asymptotic limit of -0.125 H. These states are substantially away at R=6.0 Å from their asymptotic values. Table 2.1 lists the irreps of lowest 10 states at selected geometries.

Clearly, the states 2 and 3 belonging to $^2E'$ irreps form JT pair of states throughout the region. There are three notable features in Figure 2.1b whose close-up has been shown in Figure 2.2. The states 4 and 5 belonging to A_2'' and A_1' irreps exhibit a CI at R=2.86102 $\mathring{A}$ as seen in Figure 2.2b. States 6 and 7 which form another $^2E'$ JT pair, are well-separated from both upper 8th and lower 5th states except at two regions. The region around 2 Å indicates a possible 3-state intersection (3-SI) of A_1' and $^2E'$. As shown in Figure 2.2a, the states do not cross and reach a minimum gap of 2 mH at R=2.0435 Å. A 3-SI seen around R=4.7 Å is confirmed in Figure 2.2c to be at R=4.71305 Å where A_2'' state crosses with JT state $^2E'$.

We have confirmed that all the above discussed features and their locations are

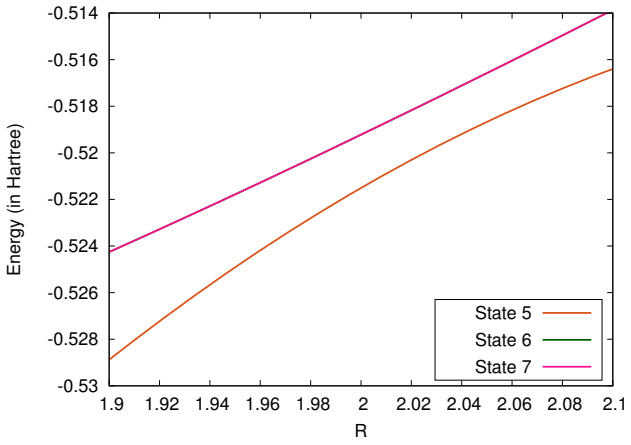

(a) Feature around 2.0 Å.

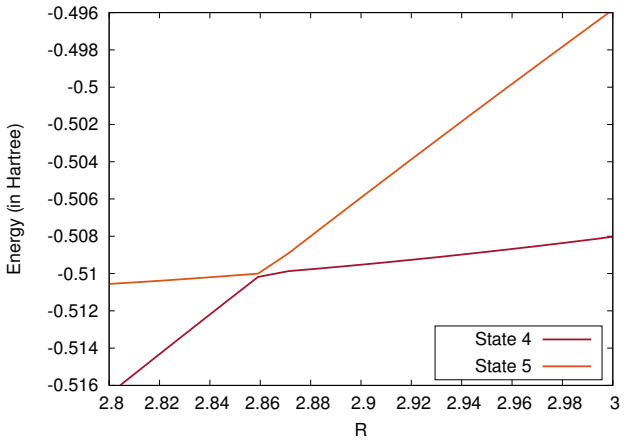

(b) Feature around 2.8 Å.

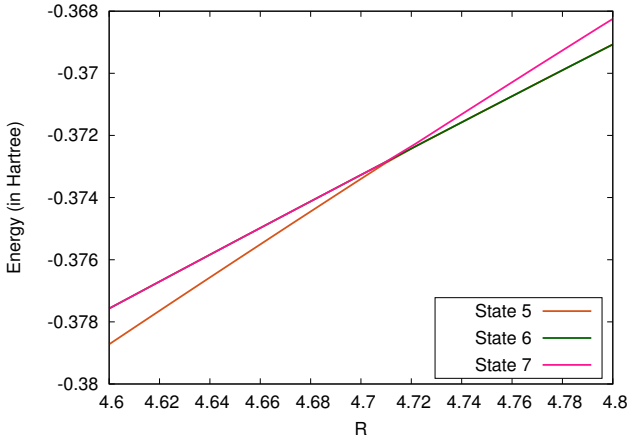

(c) Feature around 4.7 Å.

Figure 2.2: Blow up around features.

well-reproduced when a few augmented ETGs are included. For this reason, we have considered cc-pV6Z(spdfg)/3-ETG to be a suitable basis set for further studies at all other geometries. In most calculations, spatial symmetry was not used for

Hamiltonian construction or diagonalization. The integrals were computed to an accuracy of 10^{-20} for construction of the Hamiltonian before diagonalization.

2.4.2 Method for Construction of Seam

To numerically construct the various branches of intersection seam for a pair of states over a large configuration space, the most suitable candidates will be the JT pair of states. Since such states already have a fully symmetry required seam branch (the JT one), it is possible that additional non-JT branches exist. If a point on such a branch is located, it is possible to numerically track this seam in either direction. For JT states of either E' or E'' symmetry, such branches must connect states of same irreps in the C_s group. Therefore, it must be a same-symmetry CI seam branch of dimensionality one - *a line*. If the branch lies completely within the 2-dimensional C_{2v} subspace, then it must be a symmetry-allowed accidental seam, the dimensionality again turns out to be one. In this case, the states belong to A and B type irreps with reduction $E' \rightarrow A_1 + B'$ and $E'' \rightarrow A_2 + B''$. Here, B' and B'' are labels of C_{2v} irreps which transform, respectively, as symmetric and anti-symmetric with respect to the chosen plane of C_{2v} molecule. In our calculations, the molecule has been kept in xz plane and as a result it turns out that $B' \equiv B_1$ and $B'' \equiv B_2$. The state pair 2 and 3 and the pair 6 and 7, being JT pairs, are considered for further investigation.

Another possible choice is the pair 4 and 5, which have a CI at D_{3h} geometry R=2.86102 Å, as discussed in previous section (see Figure 2.2b). In this case, the states belong to different irreps in C_s group and the seam at this location will be symmetry allowed accidental CI seam of dimension 2. Since such a seam surface will be difficult to construct, we did not consider this further (see later).

The numerical strategy used for location and tracking of seams is straightforward and computationally inexpensive, due to the simplicity of electronic structure calculations on this system. A few geometries were scanned for a fixed value of a chosen geometrical parameter to identify an approximate geometry for an accidental CI. It is further refined by varying other geometrical parameters until a geometry is reached where states are numerically degenerate up to within a 1μH. This geometry then serves as a seed geometry to track the seam branch. After getting one representative seam geometry, we make a small displacement along one of the coordinates and readjusting the remaining ones until the degeneracy is restored within a 1μH. This procedure can be easily implemented for C_{2v} subspace where only one geometrical parameter needs to be varied. It becomes tedious for C_s subspace where the states are of same symmetry and two geometrical parameters need to be varied.

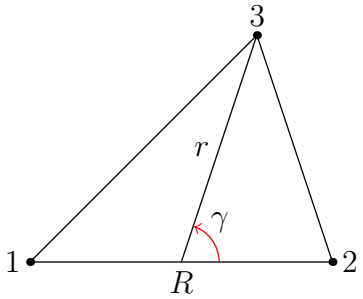

Figure 2.3: Jacobi coordinates.

After seams branches are fully constructed, we have computed contour integrals of non-adiabatic coupling (NAC) vector along a few closed contours encircling seam line at different reference geometries to verify that it is indeed a CI seam and not an avoided-crossing. The contours were chosen based on a procedure recommended by Baer and coworkers [1], by tracing the circular motion of one of the nuclei displaced from its position at the reference geometry while keeping other two nuclei fixed.

2.4.3 C_{2v} Seams

Initial attempts were aimed at construction of seams in C_{2v} subspace for states 2 and 3. For C_{2v} scans starting from equilateral geometry towards linearity, the states split as B_1+A_1 with B_1 being lower in energy. The energy gap continues to increase all the way towards linear geometry where the upper state A_1 becomes degenerate state with the upper B_2 state. For scans in the opposite direction leading to HeH^{++}, the lower state is A_1 and upper B_1 state continues to increase until it becomes degenerate with upper B_2 state. As a result, all the scans failed to produce a seed geometry and no other CI seam between states 2 and 3 could be detected. Therefore, we conclude that the only seam branch for states 2 and 3 is the JT seam.

Since the above scans also indicated presence of CI between states 6 and 7, attempts were made to construct their seam branches. Systematic scans were carried out using Jacobi coordinates as shown Figure 2.3, by fixing $\gamma = 90^\circ$ and using R as primary coordinate.

Two r-scans for $R = 0.85$ Å and $R = 3.0$ Å from equilateral geometry $r = \frac{\sqrt{3}}{2}R$ up to linear geometry $r = 0$ shown in Figure 2.4 clearly show presence of CIs whose locations were refined to be $(R, r) = (0.85, 0.34983)$ and $(R, r) = (3.0, 0.72180)$.

The result of tracking the seam branches starting at these seed geometries are shown in Figure 2.5. As shown in Figure 2.5a, with increasing values of R, both seams monotonically moved towards linear geometry $r = 0$ reaching it at $R = 0.925187$ Å

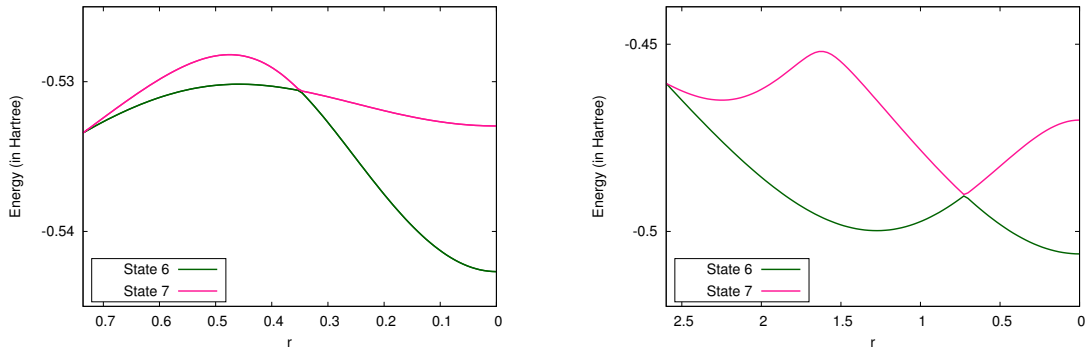

(a) At $R = 0.85$ Å. **(b)** At $R = 3.00$ Å.

Figure 2.4: Results of two r-scans.

and $R = 4.07348$ Å. In the reverse direction, the seams showed unusual movements as depicted in Figure 2.5b. The left branch curved up smoothly crossing the D_{3h} seam branch at $R \approx 0.804$ Å and continued on the acute side (with apex angle less than 60°). The other branch took a sharp turn around $R \approx 1.75$ Å and quickly moved to the acute side between $R = 2.0$ Å and $R = 2.1$ Å. It can be noticed that the point at which it crosses to the other side coincides with the special D_{3h} geometry $R = 2.0435$ Å(marked with black dot), discussed in 2.4.1 as the geometry where state 5 comes closest to the 6-7 state pair. Therefore, the reason for the sharp turn of the seam can be attributed to state 5 of symmetry A_1 approaching closer to the seam states of $A_1 + B_1$ symmetry.

Both the branches were tracked further in the acute apex angle region. As shown in Figure 2.5c, they meet around $(R, r) = (2.08, 3.88)$. From the figure, the meeting point appears to be a crossing-point between two seam lines with different slopes. However, all efforts to pick up their trails beyond $r = 3.88$ Å failed.

A closer look revealed that, in this region, state 8 becomes very close (≈ 0.2 mH) to both states 6 and 7. Using the same tracking procedure, two seam branches of 7 and 8 were located in this region as shown in Figure 2.5d. Since all the seams seemed to converge around the same location, this hinted at the possibility that a 3-state intersection (3-SI) existing in this region. Here, two of the states have symmetry of A_1 and the other one has B_1. Based on dimensionality reduction arguments, it is *not possible* to have a 3-SI in C_{2v} subspace with these symmetries (dimensionality reduction required for accidental triple degeneracy with 2 A_1 + 1 B_1 is 3, against the maximum available 2). This is confirmed by closer scan shown in Figure 2.5e. The 6-7 and 7-8 seams come closer, each one inducing sharp turn of the other. If the symmetry were to allow, a 3-SI would have been located in this region.

Due to existence of a 3-SI within D_{3h} subspace (see Figure 2.2c), the 6-7 seam

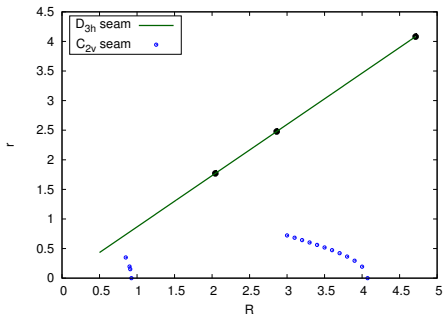

(a) Scan towards linear geometry.

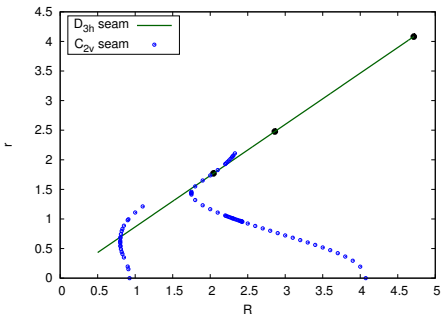

(b) Scan towards D_{3h} seam.

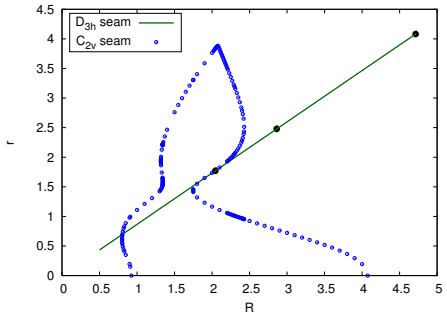

(c) Scan away from D_{3h} seam.

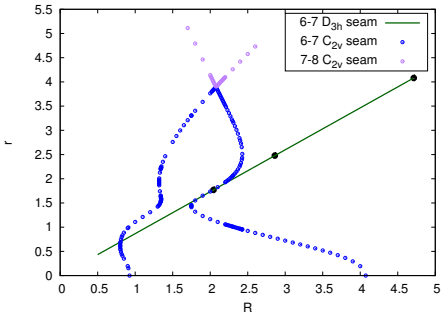

(d) Seam 7-8.

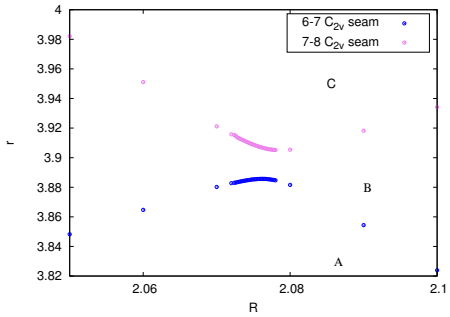

(e) Zoom of region.

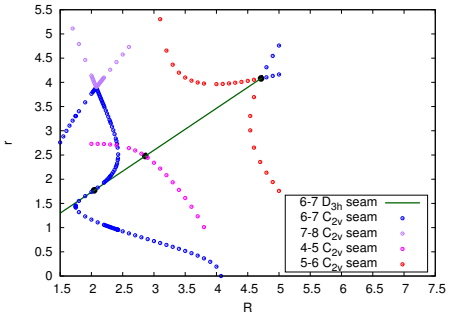

(f) Seams connected to 3-SI.

Figure 2.5: Results of C_{2v} scans.

and 5-6 seam branches are expected to be present around this region. Further, the CI of state 4 and 5 located on the D_{3h} line at $R = 2.86102$ Å can be imagined to be part of a C_s seam surface intersecting the C_{2v} subspace as a 4-5 seam line. Any possible intersection of this seam with 5-6 seams originating from 3-SI may induce another 3-SI of 4,5,6 states. The results of this exploration shown in Figure 2.5f show that such a situation does not arise.

2.4.4 C_s Seams

With the construction of (presumably) all C_{2v} branches of seam of states 6-7, the C_s branches were explored. This was done by choosing $\gamma > 90°$ and carrying out

scans of remaining two coordinates R and r until a degeneracy could be detected. The resulting geometry then acts as a seed geometry for seam tracking. The results are shown in Table. 2.2. The seed geometry is Y_{12} with $\gamma = 100°$.

Table 2.2: Geometries of C_s seam.

Geometry	R	r	γ
Y_1	1.5340	1.609	109.3
Y_2	1.5298	1.610	109.0
Y_3	1.5180	1.618	108.5
Y_4	1.5052	1.627	108.0
Y_5	1.4820	1.642	107.0
Y_6	1.4618	1.655	106.0
Y_7	1.4439	1.665	105.0
Y_8	1.4278	1.675	104.0
Y_9	1.4134	1.683	103.0
Y_{10}	1.4005	1.690	102.0
Y_{11}	1.3889	1.696	101.0
Y_{12}	1.3786	1.701	100.0
Y_{13}	1.3694	1.706	99.0
Y_{14}	1.3613	1.710	98.0
Y_{15}	1.3543	1.714	97.0
Y_{16}	1.3483	1.716	96.0
Y_{17}	1.3432	1.719	95.0
Y_{18}	1.3391	1.721	94.0
Y_{19}	1.3360	1.722	93.0
Y_{20}	1.3337	1.723	92.0
Y_{21}	1.3324	1.724	91.0
Y_{22}	1.3320	1.724	90.5
Y_{23}	1.3319	1.725	90.3
Y_{24}	1.3318	1.725	90.1
Y_{25}	1.3317	1.726	90.0

Seam tracking along decreasing value of γ shows that the C_s seam approaches C_{2v} region where $\gamma = 90°$. The point Y_{25} is verified to be a point on right side C_{2v} branch in Figure 2.5c. This point is a confluence of C_{2v} and C_s branches.

When tracking the seam along the direction with increasing value of γ, it was found that seam movement stagnated around the point Y_1 at $\gamma = 109.3$. By

calculating Jacobi coordinates with permuted nuclei labels, it was recognized that Y_1 is close to being a C_{2v} geometry. The coordinates of permuted geometry, $(R, r, \gamma) = (1.9983, 1.165, 90.1)$ shows that this geometry is in the region where C_{2v} apex angle is greater than 60°. Clearly, the C_s seam of Table. 2.2 connects an acute apex angle geometry Y_{25} to obtuse apex angle geometry Y_1. Both these points are confluence points.

Since further explorations of C_s space did not yield any seed geometries, only one C_s branch of 6-7 seam is deemed to be present.

2.4.5 Visualization of Seam

To visualize a seam as a curve in the 3-dimensional nuclear configuration space, it is necessary to make a choice of 3 internal coordinates. Since a seam point remains on the seam upon arbitrary permutation of nuclear labels of equivalent nuclei, it is convenient to choose a system of coordinates where all 6 permuted configurations are related in a simple way. The Jacobi coordinates (R, r, γ) are not convenient in this respect, as the coordinates of permuted configuration are related to the original through cumbersome kinematic rotations.

Amongst a variety of coordinate choices which accord a symmetric treatment for all permuted configurations, hyperspherical coordinates [183] and perimetric or Pekeris coordinates [139, 184] turn out be the most suitable. The hyperspherical coordinates were introduced by Smith and Whitten [185, 186] as a kind of symmetric coordinates for the three-body problem. Based on the work of Kuppermann [187], Johnson [183] introduced a convenient mapping procedure which allows Smith-Whitten coordinates to be visualized as a kind of spherical polar coordinates. Subsequently, a number of studies involving reactive scattering dynamics have employed this coordinate system.

We have used the modified Smith-Whitten coordinates (ρ, θ, ϕ) as described by Johnson in Ref. [183] (also see the work of Varandas and coworkers [188] for an application). While the hyper-radius ρ represents the size of the triangle formed by the three nuclei, the hyper-angles θ and ϕ represent different shapes of the triangle. Their ranges, $0 \leq r < \infty$, $0 \leq \theta \leq \frac{\pi}{2}$ and $0 \leq \phi \leq 2\pi$, have been chosen such that each unique nuclear configuration is represented by a single point in the upper-hemisphere of the corresponding Cartesian system (obtained by the standard spherical polar to Cartesian conversion scheme). All equilateral geometries are mapped on to the z-axis and all linear geometries on to the xy-plane. All C_{2v} geometries are represented by a set of three planes perpendicular to xy-plane and containing the z-axis. Each of

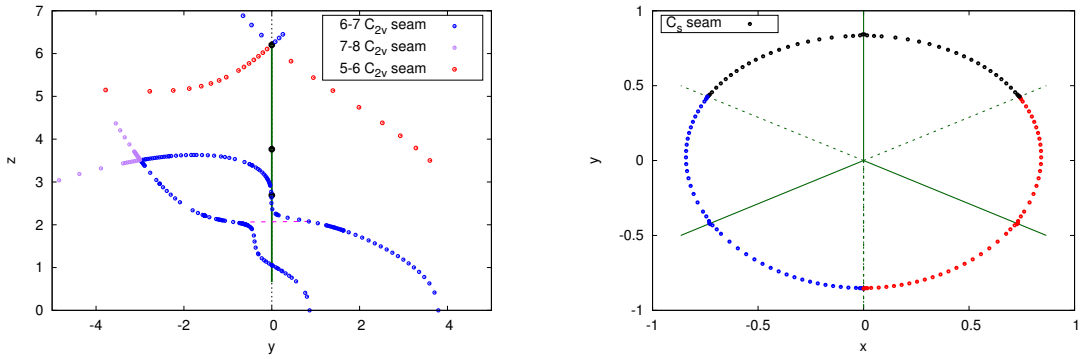

(a) C_{2v} Seam. **(b)** C_s Seam.

Figure 2.6: Projections of Seam in hyperspherical coordinates.

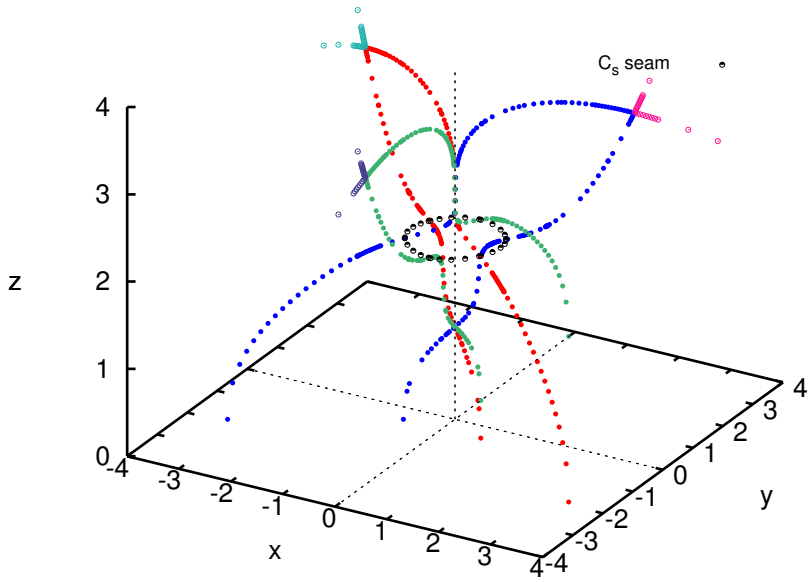

Figure 2.7: The 6-7 Seam in hyperspherical Coordinates. The three symmetry-equivalent C_{2v} branches are represented with in colors **blue**, **dark green**, **red**. The C_s branch is represented in **black**. The JT seam is represented by the thin dashed line along z-axis. The remaining lines are not part of this seam.

these planes is related to the other two by a rotation by 120° along the z-axis. Each plane represents all C_{2v} geometries with a specific nuclear label for the apex atom lying on the C_{2v} symmetry axis. The choice of mapping for ϕ used by Johnson makes the yz-plane to be one of the C_{2v} planes. The coordinates of nuclear configurations obtained by permutations of nuclear labels have the same ρ and θ, differing only in the azimuthal angle ϕ by a rotation of 120° around the z-axis or by a reflection about the C_{2v} planes.

The Figure 2.6 shows the computed seam branches along two planes. The C_{2v} seams running within the hyperspherical yz-plane are shown in Figure 2.6a. Since the C_s seam connects two C_{2v} points, it can be concluded that must be a closed curve when all its permuted counterparts are accounted for. The projection of this curve on xy-plane is shown in Figure 2.6b which confirms this. The entire seam with all its branches in 3-dimensions can be visualized as shown in Figure 2.7. This figure nicely exhibits its symmetry and trifurcation of the JT seam at the confluence points. It also clarifies that the C_s seam, represented by the black closed curve, indeed connects two different branches of C_{2v} seam related by nuclear permutational symmetry.

2.5 Summary

In this chapter, we have constructed and visualized complete intersection seam of a triatomic molecular system. Although the system considered is an unstable molecular species and currently of lesser importance, it is also interesting to note that a one-electron system already exhibits a complex seam-connectivity pattern involving several confluences, avoided-seam-crossings and 3-SIs. The closed nature of accidental same-symmetry C_s seam, to the best of our knowledge, has been only observed by Ruedenberg and coworkers for the Ozone molecule [152]. It would be interesting to see if such a pattern can also be found in other triatomic molecules.

In this work, we have not considered the behaviour of seam in asymptotic and highly repulsive regions. How the constructed seam continues in this region can not be determined from computations easily. It can be expected that, in these regions, the seam branches would interact with other state seams. As far as we are aware, it is not clearly established if accidental symmetry seams would be always connected to the corresponding symmetry-required portion. The simplicity of system studied here gives raise to the possibility to study this question by applying analytic degenerate perturbation theory at regions where exact zeroth-order states are known.

With advances in electronic structure methods, it is possible to develop efficient computational techniques for small molecules (3-5 atoms) with which one can map out their intersection seams between a pair of states and within a larger region of nuclear configuration space which is relevant for nuclear dynamics. Although the approach used by us for this work is very rudimentary, a combination of analytic gradient enabled multi-reference methods and degenerate perturbation theoretic framework to model local variation of seam curvature and branching space topography can be used to vastly improve this procedure. An understanding of different types of seam-connectivity and of the relation between symmetry-required and accidental branches

can be some help in such an effort.

The computed seam information is expected to be useful in non-adiabatic nuclear dynamics in a number of ways, such as constraining the form of adiabatic PES fits or for setting up of a diabatic Hamiltonian ansatz. It remains to be seen if such an information can be beneficially used at a level different from the underlying PESs.

Chapter 3

Study of Intersection Seams Using Non-adiabatic Couplings

3.1 Introduction

In the previous chapter, it has been shown through a case study that, for triatomic molecules, a picture of intersection seam between a pair of neighbouring electronic states in the nuclear configuration space can be constructed. Although the resulting picture is complicated by presence of seam branches and confluences, it may be simpler for other molecules where JT symmetry is absent. Despite this, clearly the approach can not be extended to tetratomic molecules and beyond. This is due to the high-dimensional and irregular nature of seam. For the same reason, investigations of seam in polyatomic molecules have been so far limited to systems with upto 4 atoms [189, 190].

When a seam is viewed as a static object, it is feasible to locate and characterize a few of its special local regions, just as one characterizes the equilibrium geometry of a molecule. Such investigations have been made possible by developments which extend analytical gradient techniques in quantum chemistry to CIs. Location of minimum energy structures and geometry optimizations on a CI seams is now possible for larger molecules [88, 91, 142, 191]. These have led to a number of applications in photochemistry where such information is used for qualitative mechanistic understanding [90].

To carry out non-adiabatic dynamics, the region around a seam is considered to be more important than the seam itself. Here, the seam reveals itself in two different ways. One is through NACTs which tend to remain large in this region and cause ultrafast non-adiabatic transitions when a wave-packet tries to cross the seam. From

a much earlier time, it has been recognized that NACTs need to be included in dynamics [53]. Another way the seam exerts influence is through the *geometric or topological* phases or the Berry phases it causes.

The NACTs and topological phases are connected to each other through an interesting property of the former. It has been shown that (see the next section for details) line integrals of NACTs along closed contours within the seam region can be used to compute these phases. This phase contains information about a seam point which the contour encloses. Initially such a phase was explicitly shown to exist in the context of JT CIs by considering the analytic behaviour of NACTs close to a seam point [8]. However, due to its topological origin, it was shown using *ab initio* calculations to also hold larger contours as long as the region inside does not contain CI points of other states [192,193]. Over the last two decades, many studies have made use of this feature of NACTs to identify nuclear configuration regions enclosing a seam where diabatization can be successfully carried out. Several numerical procedures based on computing such line-integrals of NACs have been developed and tested. These developments have led to many successful applications where such procedures have used to construct proper diabatic potential matrices, using which dynamics has been carried out [194–196].

Although line-integrals of NACTs over closed-contours have been mainly used so far to account for toplogical effects of seams, such integrals are also influenced by the seam itself. When geometry of the seam is known, such contours can be always setup to avoid or minimize the influence of the seam so that phase information can be extracted successfully. However, when contours are carried out without a knowledge of seam, there is a possibility of such contours running close to seam or even crossing it. In such a case, spiky NACTs can be expected to appear leading to failure of integration procedure. Such a situation has been encountered in a recent study on methylamine by Baer and coworkers [197]. Here, the angular component of NACTs along contours was shown by computations to display an unusually spiky behaviour with each spike contributing $\frac{\pi}{2}$ to ADT angles, with an overall zero topological phase. Since then, such features have been explained on the basis of two theorems proved by Baer and coworkers [198, 199].

Inspired by these developments and in view of the work discussed in Chapter 2, in this chapter, we have attempted to understand how a seam can influence line-integrals of NACTs over closed-paths and whether seam information can be extracted from procedures which have been used in the past for other purposes. For this, we have performed caclulations on two systems - a triatomic molecule and slightly larger polyatomic molecule.

3.2 Theory of Non-adiabatic Couplings

As discussed in section 1.2.3 of Chapter 1, a geometry-dependent unitary matrix $\mathbf{U}(\mathbf{Q})$ connecting electronic and nuclear wave-function components in adiabatic and diabatic representations as in equations (1.27b) and (1.29) can be obtained by solving the following ADT equation (see (1.37)),

$$\nabla \mathbf{U}(\mathbf{Q}) + \boldsymbol{\tau}(\mathbf{Q})\mathbf{U}(\mathbf{Q}) = 0 \tag{3.1}$$

It must be noted that the above equations are derived under the validity of group Born-Oppenheimer approximation, which essentially means that first-order NACTs between group of N electronic states and states in their orthogonal complement are negligible in a region of configuration space where the solution is being sought. The necessary and sufficient conditions for the existence of solutions of this equation, and numerical methods for obtaining them has been investigated in the works of Baer, Mead, Cederbaum and others. As shown by Baer [2,53], the solution can be formally written as follows.

$$\mathbf{U}(\mathbf{Q}) = \mathcal{P} \exp\left(- \int_{\mathbf{Q}_0}^{\mathbf{Q}} \boldsymbol{\tau}(\mathbf{Q}'|\Gamma) \cdot \mathrm{d}\mathbf{Q}' \right) \mathbf{U}(\mathbf{Q}_0) \tag{3.2}$$

According to this, the ADT matrix at a geometry $\mathbf{Q}$ is obtained by applying a path-ordered exponential (the first-term) to the ADT matrix at a chosen initial geometry $\mathbf{Q}_0$. To construct this, a path Γ connecting the initial geometry to the desired final geometry needs to be chosen and NACT matrix needs to be evaluated along this path, as indicated by $\boldsymbol{\tau}(\mathbf{Q}'|\Gamma)$. Baer [1] has shown that single-valued diabatic potential matrix is obtained only when this procedure, when applied to all closed paths starting and ending at a geometry, yields an ADT matrix which differs from the starting ADT matrix such that electronic and nuclear wave-functions also return to the starting ones with up to an overall phase [190]. For this to happen, the following quantity evaluated on a closed contour Γ,

$$\mathbf{D}(\Gamma) = \mathcal{P} \exp\left(- \oint_{\Gamma} \boldsymbol{\tau}(\mathbf{Q}'|\Gamma) \cdot \mathrm{d}\mathbf{Q}' \right) \tag{3.3}$$

needs to come out as a diagonal matrix with phase factors along its diagonal entries.

$$\mathbf{D}_{jk}(\Gamma) = \delta_{jk} e^{i\Theta_j(\Gamma)} \tag{3.4}$$

The matrix $\mathbf{D}(\Gamma)$ has been referred to as *topological matrix* [190, 200]. It depends

on Γ through the phase factors $\Theta_j(\Gamma)$, but it is *independent of starting point* on the path.

When electronic wave-functions are real, the $\mathbf{D}$ matrix is a diagonal matrix with ± 1 as entries. For this reason, when NACT matrices computed using *ab initio* methods satisfy these conditions for all closed contours in a given region, they have also been referred to as *quantized* by Baer and coworkers [16, 201]. The group of states satisfying these conditions are said to form a *Hilbert subspace*. For such states, the ADT equations can be solved to yield an approximate set of diabatic states. When these conditions are not satisfied, it means that diabatic states can not be obtained from the group of electronic states used to construct the NACTs. This usually indicates the necessity to expand the group by including more states. It has been argued that deviations of topological matrix from diagonality can be used as a measure of the extent of validity of group BO approximation. The valdity of quantization conditions for NACTs obtained using *ab initio* calculations and model diabatic potentials has been explored by Baer and coworkers for upto five states on a number of triatomic and tetra-atomic molecules [190, 193, 200, 202, 203].

For the two-state case, the anti-symmetric 2×2 NACT matrix can be written as,

$$\boldsymbol{\tau}(\mathbf{Q}) = \begin{pmatrix} 0 & \tau(\mathbf{Q}) \\ -\tau(\mathbf{Q}) & 0 \end{pmatrix} \tag{3.5}$$

and the ADT matrix $\mathbf{U}(\mathbf{Q})$ can be parameterized in terms of an ADT angle $\gamma(\mathbf{Q})$ as,

$$\mathbf{U}^{(2)}(\mathbf{Q}) = \begin{pmatrix} \cos\gamma(\mathbf{Q}) & \sin\gamma(\mathbf{Q}) \\ -\sin\gamma(\mathbf{Q}) & \cos\gamma(\mathbf{Q}) \end{pmatrix} \tag{3.6}$$

which leads, after integrating the ADT equations, to the following expression for ADT angle.

$$\gamma(\mathbf{Q}|\mathbf{Q}_0|\Gamma) = -\int_{\mathbf{Q}_0}^{\mathbf{Q}} \tau(\mathbf{Q}'|\Gamma) \cdot \mathrm{d}\mathbf{Q}' \tag{3.7}$$

The topological matrix in this case can be shown to be

$$\mathbf{D}(\Gamma) = \begin{pmatrix} \cos\alpha(\Gamma) & \sin\alpha(\Gamma) \\ -\sin\alpha(\Gamma) & \cos\alpha(\Gamma) \end{pmatrix} \tag{3.8}$$

where $\alpha(\Gamma) = \gamma(\mathbf{Q}_0|\mathbf{Q}_0|\Gamma)$. The quantization condition which makes $\mathbf{D}(\Gamma)$ diagonal is given as,

$$\alpha(\Gamma) = -\oint_{\Gamma} \tau(\mathbf{Q}|\Gamma) \cdot \mathrm{d}\mathbf{Q} = n\pi \tag{3.9}$$

where n is an integer referred to as *topological quantum number*. The off-diagaonal terms in equation (3.8) vanish only when the above condition is satisfied. It must be emphasized once again that topological quantum number depends only on the nature of closed loop Γ, not on the starting geometry. The topological matrix can either have two $+1$ or two -1 entries on diagonal [2, 53].

To check the validity of quantization conditions in a given region, closed contours of any shape can be used. From practical considerations, it is convenient to use simpler contour shapes which make it easy to evaluate the line integral in equation (3.9). This becomes relevant when NACTs need to be evaluated using numerical gradient calculations. This can be achieved by considering circular contours around a suitably chosen geometry $\mathbf{Q}^*$ serving as origin. Two coordinates Q_x and Q_y indicating two orthogonal displacement directions from the origin can be chosen to select a plane on which the contours can be setup. The coordinates along remaining independent displacements orthogonal to Q_x and Q_y are collectively indicated as Q_s. The circular contours can be expressed in terms of cylindrical polar coordinates (q, ϕ, Q_s), defined via $Q_x = q\cos\phi$ and $Q_y = q\sin\phi$. In this coordinate system, the NACT and displacement vectors can be written as,

$$\tau(\mathbf{Q}) = \frac{1}{q}\,\tau_\phi(q, \phi; Q_s)\,\hat{\boldsymbol{\phi}} + \cdots \tag{3.10}$$

$$\mathrm{d}\mathbf{Q}(\mathbf{Q}) = q\,\mathrm{d}\phi\,\hat{\boldsymbol{\phi}} + \cdots \tag{3.11}$$

where only angular components as indicated provide non-zero contributions for the contour integral. The quantization condition takes the following simple form for circular contours.

$$\alpha(q; Q_s) = -\int_0^{2\pi} \tau_\phi(q, \phi, Q_s)\mathrm{d}\phi = n\pi \tag{3.12}$$

The above integral can be computed by evaluating only angular component of NACT vector. Different contours can be obtained by varying contour radius q and remaining coordinates Q_s.

Although the origin $\mathbf{Q}^*$ can be chosen to be any geometry, in order to expose topological effects, it is usually chosen to be a CI geometry. For the case of symmetry-induced JT CIs, as shown by Longuet-Higgins [65] and Karplus [204] and others, it is possible to derive an expression for electronic Hamiltonian in a diabatic basis in the vicinity of such a CI in terms of two symmetry-degenerate JT active modes Q_x and Q_y. Using this, it can be shown that [2],

$$\tau_q(q, \phi, Q_s) = 0 \quad \text{and} \quad \tau_\phi(q, \phi, Q_s) = -\frac{1}{2} \tag{3.13}$$

which gives topological phase as,

$$\alpha(q;Q_s) = -\int_0^{2\pi} \tau_\phi(q,\phi,Q_s)\mathrm{d}\phi = \pi \tag{3.14}$$

Therefore, topological quantum number for circular contours around a JT CI is 1.

However, the expressions for radial and angular components in equation (3.13) do not hold for larger contour radii and for other types non-symmetric CIs. Both components show significant coordinate dependence. In particular, angular component τ_ϕ required for circular contour integrals shows strong ϕ-dependence. Baer and coworkers have incorporated this dependence in their *ab initio* calculations to show that topological quantum number still comes out to be π even when larger contours are used. They have further shown that failure to obtain π can be linked to the existence of CIs of other states inside the contour [2, 190, 202]. These studies have clearly established that quantization conditions can be fulfilled even for larger regions and make it possible to compute approximate diabatic potential matrix by solving ADT equations.

The ϕ-dependence of angular component $\tau_\phi(\phi)$ in these studies have shown interesting patterns. When two-state quantization is satisfied, $\tau_\phi(\phi)$ is found to have same sign along the contour and oscillates around the central value of $\frac{1}{2}$, typically forming two or more maxima. Engleman and Baer [205] have formulated a diabatic elliptic JT model Hamiltonian which can describe these variations for small displacements from the CI point. However, the model is not able to account for angular dependence observed in *ab initio* calculations for larger contour sizes. Several calculations by Baer and coworkers have shown two or more peaks with quantization conditions approximately satisfied [205–207]. Breakdown of 2-state quantization is usually indicated by the angular components changing sign somewhere along the contour [202].

A surprisingly different kind of angular dependence of τ_ϕ was observed by Baer and coworkers in their studies on NACTs in methylamine molecule [197–199]. While performing contour integrals for circular motions involving one of its NH_2 hydrogen atoms within the plane of symmetry of molecule, the τ_ϕ was found to display two sharp peaks of opposite signs. Region around each peak contributed a topological phase of magnitude $\frac{\pi}{2}$ to the contour integral, and contributions from both peaks were of opposite sign so that total topological phase turned out to be zero. This behaviour was significantly different from their previous results. It was also found to be observed for a number contours centered at different locations within the symmetry plane [199]. Interestingly, when the contour integral is performed along a circle slightly tilted away

from the symmetry plane, the peaks, although still sharp and spiky, were found to have same sign yielding the usual topological phase of π.

In these studies, the origin of contour is not placed on a CI geometry, but on a geometry where states are energetically closer. The spiky feature was attributed to a symmetry-allowed different-symmetry CI seam present in the symmetry plane. The observed features and topological phases (0 and π for different contours) were explained by Baer and coworkers on the basis of two theorems proved in a follow-up study [198]. The first theorem established that a phase of magnitude $\frac{\pi}{2}$ occurs whenever a contour (open or closed) passes through a CI seam. The second theorem proves that total topological phase for closed contour crossing a seam two times in opposite directions is always zero, with opposite contributions arising from each seam crossing.

Previous investigations have focused on computations of topological phases using contour integrals of NACTs to mainly establish the Hilbert subspace nature of states in a particular region of configuration space. The contour integrals have been used as a tool to identify regions where group BO approximation may become invalid, and to establish the presence of CIs between other states which are responsbile for this. In contrast, the above works on methylamine illustrate that contour integrals are affected by the seam itself. Therefore, angular NACTs and their contour integrals carry information on the seam and can be used to understand it.

Motivated by the above studies and in view of the work presented in previous chapter, we have carried out a numerical study to further understand how the NACT profiles and their contour integrals are influenced by the CI seam. Since the seam is a connected multi-dimensional structure, its presence near a plane in which contours are setup is reflected in the NACT profiles along the contours through the position, number and nature of peaks. For this study, we have considered the same-symmetry S_1/S_0 seam of ethylene molecule at two MECI geometries which have been well-characterized in previous studies. Since this seam is irregular and multi-dimensional, we have also carried out NACT calculations on simpler H_3 molecule to help understand and interpret ethylene results.

The rest of the chapter is organized as follows. In the next section, we present the results and plots from NACT calculations on H_3 molecule. This is followed by discussions on results of ethylene calculations.

3.3 Study of NACTs in H_3

This study has been carried to gain some basic understanding of the behaviour of components of NACTs along the contour and associated ADT angles and topological phase changes when different planes are selected. The idea is to choose a system where the direction of seam in the configuration is already known. In this case, it is possible to choose the plane of contour such that the contour passes close to the seam or crosses it. The H_3 system has been chosen for this study, due to its well-established JT seam between ground and first excited state.

(a) Single atom loop. **(b)** Three atom loops.

Figure 3.1: Contour generation for H_3 case.

Two sets of calculations have been carried out using SA2-CASSCF(3o,3e)/cc-pVDZ method. The contours have been setup by choosing a D_{3h} geometry with $R = 1.0$Å as origin. At this geometry, the ground state is doubly-degenerate and the third and fourth states are found to be far away in energy by more than 13 eV at SA4-CASSCF(3o,3e)/cc-pVDZ method. Therefore, it can be expected that JT seam is the only seam in this region. The contours were generated by a procedure similar to the one used in the works of Baer and coworkers. One or more atoms were displaced from their position in the reference geometry by a certain distance, and then they are moved in a chosen plane along a circular path around the origin.

In the first set of calculations, the contours were generated by moving one hydrogen atom as shown in Figure 3.1a. For this case, five circular contours each of radius $q = 0.1$ were generated by changing the plane in which the atom moves. The *Planar* contour was generated by moving the atom in the $y - z$ plane as shown in the figure. Remaining four ones were generated by rotating the displaced atom along y-axis by certain amount before the circular motion begins. For the *Perpendicular* contour, the rotation was by 90°. It can be noted that along both these contours, the molecular geometry never becomes equilateral. However, for the *Perpendicular* case, it does

come close to being equilateral. Therefore, the seam can be expected to influence the NACT profiles for this case.

Three more contours, labelled as *Tilted*, were chosen to bring them closer to the seam. For this, the plane of *Perpendicular* contour was tilted towards the other two atoms. Applying a tilt angle of 3.3098° produces a contour which passes through the seam exactly once. This is referred to as *Tilted(EQ)* contour, where EQ indicates that tilt was exactly equal to the amount required to hit the seam. Two other tilted cases, with tilt angles 6.6307° and 1.6542°, were also generated, labelled respectively as *Titled(GT)* and *Titled(LT)*. Here, GT and LT indicate the tilt angles were greater and lower than the angle required obtaining an equilateral geometry on the contour. Therefore, these contours may be expected to behave differently in terms of topological phases, while their NACT profiles may still be spiky as they still run close to the seam.

For the second set of calculations, the contours were generated by simultaneously moving all three hydrogen atoms as shown in Figure 3.1b. The *Planar* contour corresponds to motion as shown in figure. It can be seen that this intersects the seam at two different points. When ϕ reaches 0 and 180, the geometry becomes equilateral. The remaining three contours correspond to tilting the plane of motion of hydrogen atom located at the origin of coordinate axis shown in figure by rotating it about y-axis as before. It can be seen that the tilt moves the contour away from the seam. We have employed three tilt angles, 30°, 60° and 90°.

For each of these case, the pattern of atomic motion generates a closed path in nuclear configuration space. These paths are best visualized in hyperspherical coordinate system as has been done in the previous chapter. This helps to understand how the contours are topologically related to the JT seam running along z-axis. A three-dimensional view of the generated contours have been plotted in Figures 3.2, 3.4 and 3.5. Their projections on xy hyperspherical plane have been shown in Figures 3.3, 3.6. As can be noticed in Figures 3.2 and 3.3, *Planar* contour clearly encloses the seam. Interestingly, *Perpendicular* one only corresponds to a line, and no loop is involved. The motion corresponds to just going on a line and coming back on the same line. The tilted loops differ from each other - *tilted(EQ)* is seen to intersect the seam at exactly one point, *tilted(LT)* does not surround the seam, the *tilted(GT)* surrounds it. These features are clearly seen in projection plots. Another notable feature is that all the five loops meet at two common points - these can identified with two locations when the loop intersect with y-axis of Figure 3.1a.

The 3d-plot of *Planar* contour corresponding to 3-atom motions as in Figure 3.1b is shown in Figure 3.4. This clearly shows that this loop intersects the seam at two

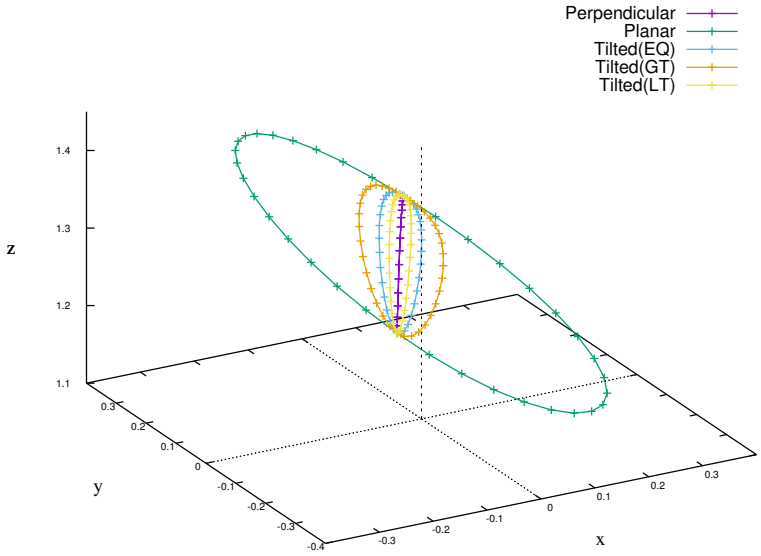

Figure 3.2: Hyperspherical representation of *Planar*, *Perpendicular*, *Tilted(EQ)*, *Tilted(GT)* and *Tilted(LT)* contours.

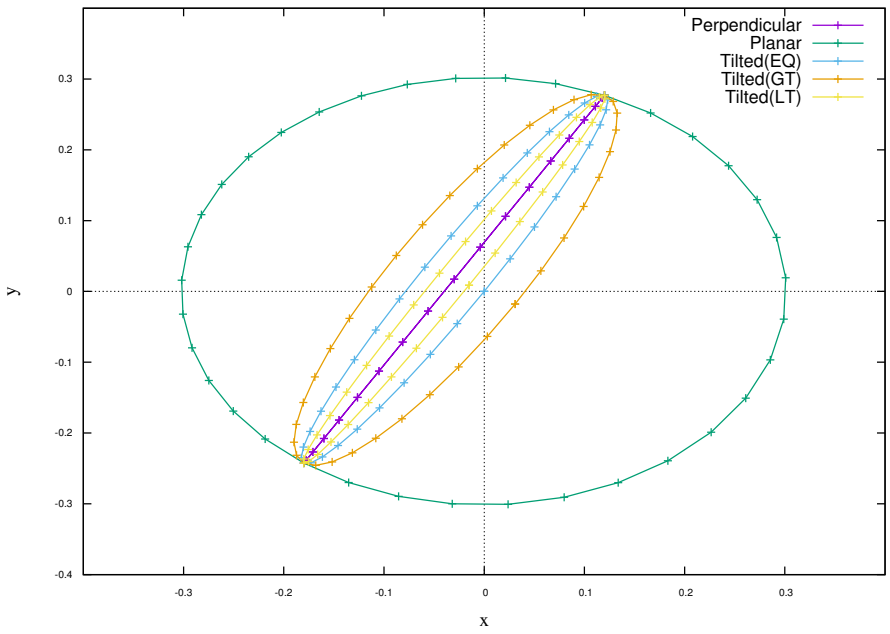

Figure 3.3: Projection on hyperspherical xy-plane of *Planar*, *Perpendicular*, *Tilted(EQ)*, *Tilted(GT)* and *Tilted(LT)* contours.

distinct points. Its projection plot is not shown as it is not informative. The 3d-plots of contours corresponding to titled 3-atom motions are shown in Figure 3.5 and their projections in Figure 3.6. These loops are seen to be irregular in shape, but all of them enclose the seam. Finally, we note that all contours except *Planar* are

closer to the seam. It is additionally clarified here that although $q = 0.1$ was used in calculations, for the purpose of better visualization the hyperspherical plots have used $q = 0.2$ to generate plots where relation to the seam is clearly visible.

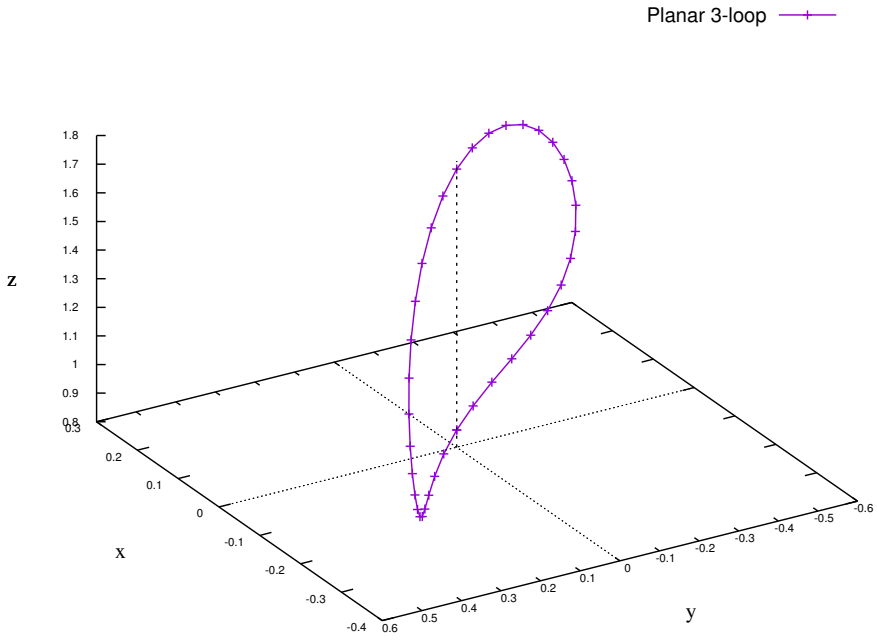

Figure 3.4: Hyperspherical representation of three atom *Planar* contour.

We now discuss the plots of angular components of NACTs (colored in blue) and ADT angle (colored in red) along the contour. The plots for eight contours are shown as subfigures **(a)** to **(h)** in Figure 3.7. It must be noted that, for the purpose of better visualisation of NACT features, the starting point for ϕ angle has been shifted by 90°.

The NACT profile for *Planar* contour shown in **(a)** in Figure 3.7a is typical of the behavior NACTs in JT-CIs. The NACT shows three maxima and minima as usual for second-order JT. They are not perfectly symmetric because the contour does not surround the seam in a symmetric way, as can be seen in its 3-dimensional plot. The NACT magnitudes are positive and oscillate between maximum value of 0.55 rad^{-1} and minimum value of 0.45 rad^{-1} consistent with $\tau_\phi = \frac{1}{2}$ for JT CI with topological quantum number of $n = 1$. This is confirmed in ADT angle plots which show that topological phase is 3.137 as expected.

The NACT profile for *Perpendicular* contour shown in **(b)** in Figure 3.7b is interesting. Two sharp peaks of equal magnitude but opposite sign are observed. Topological phase turns out be zero, with each peak contributing $\frac{\pi}{2}$. Although this

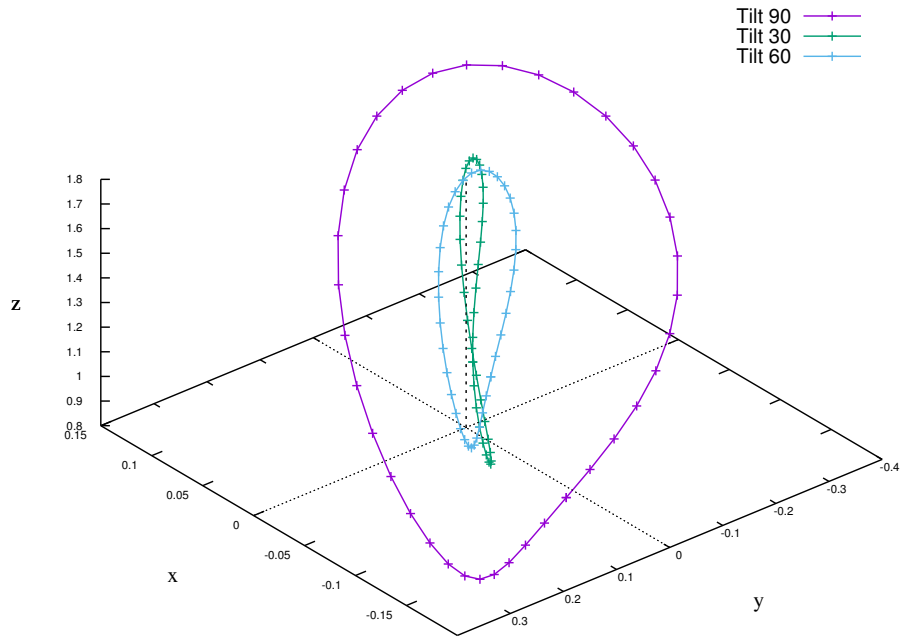

Figure 3.5: Hyperspherical representation of three atom loops for tilts of 90°, 60°, 30°.

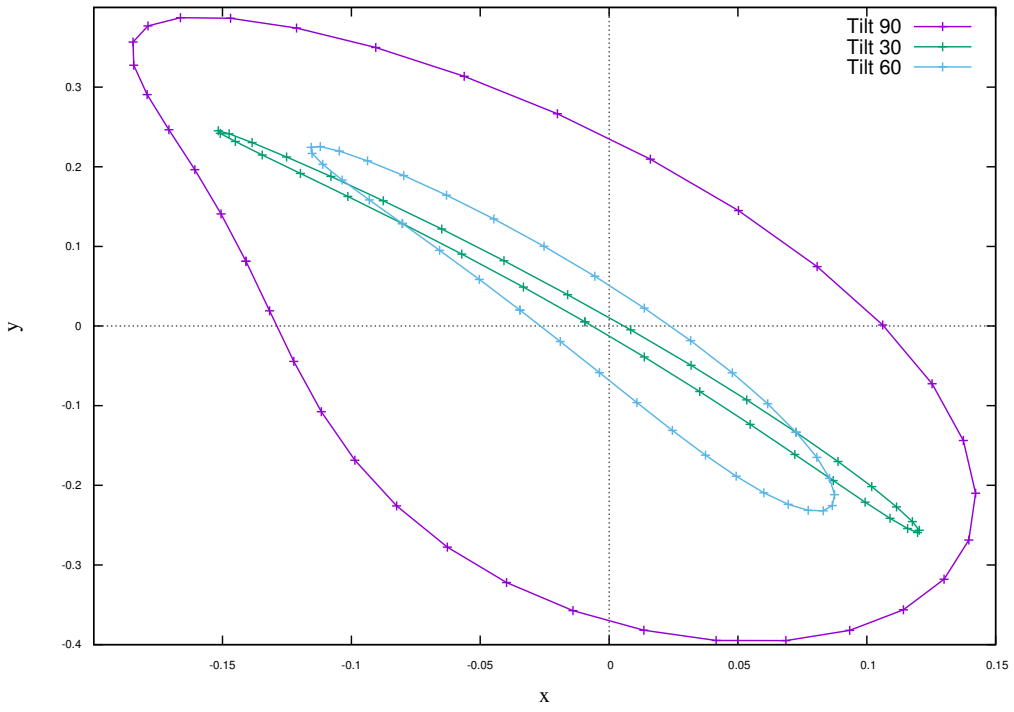

Figure 3.6: Projection on xy plane of three atom loops tilts of 90°, 60°, 30°

feature shows close resemblance to the methylamine case discussed before [197], it can be seen that this is not related to it. It can be understood from the shape of

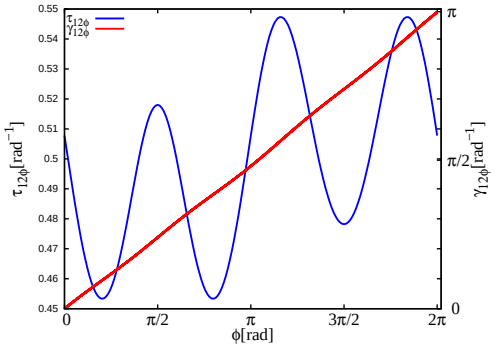

(a) *Planar* loop (α =3.137).

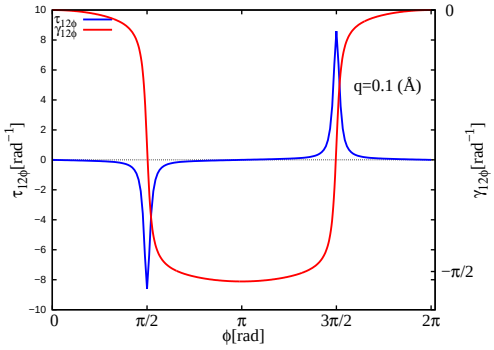

(b) *Perpendicular* loop ($\alpha = 0.0$).

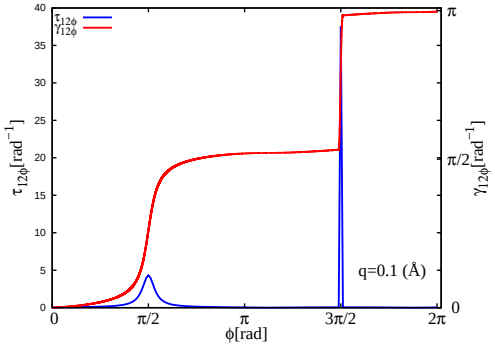

(c) *Tilted (EQ)* loop ($\alpha = 3.131$).

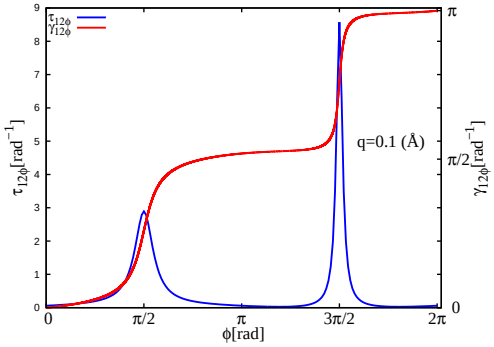

(d) *Tilted (GT)* loop ($\alpha = 3.140$).

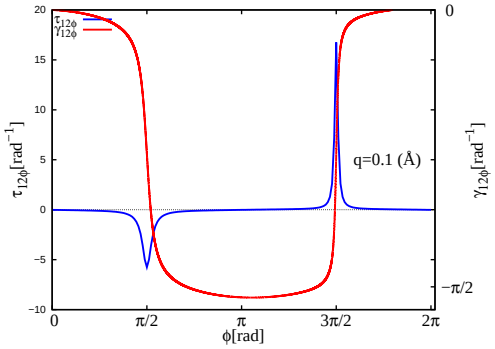

(e) *Tilted (LT)* loop ($\alpha = 0.00$).

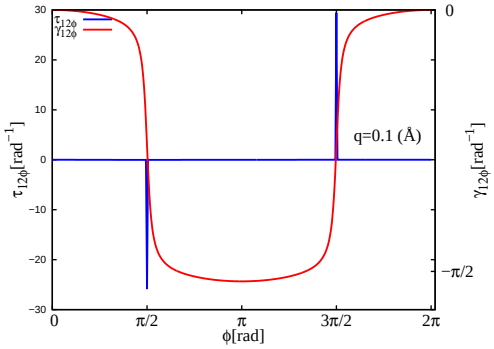

(f) Three atom *Planar* loop ($\alpha = 0.03$).

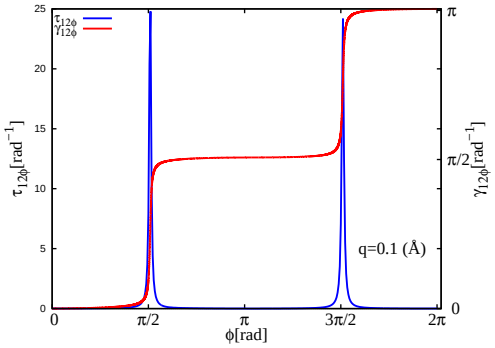

(g) Three atom loop tilt 30° ($\alpha = 3.15$).

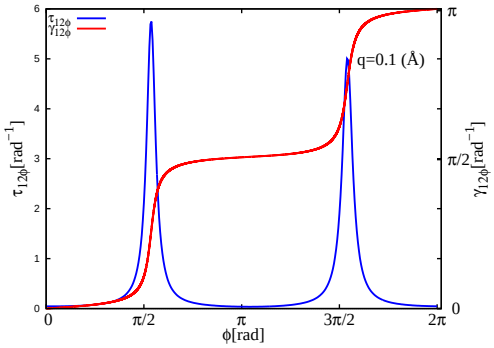

(h) Three atom loop tilt 60° ($\alpha = 3.16$).

Figure 3.7: Angular NACT ($\boldsymbol{\tau_{12}}$) and ADT angle ($\boldsymbol{\gamma_{12}}$) plots for different cases of H_3.

the contour. As discussed before, the contour in this case does not pass through the seam at all. It is not a closed contour at all - it corresponds to forward and backward motion along a line tracing the same set of geometries. The sharp nature of peaks arise at points when the contour passes close to the seam (see Figure 3.3). The equal and opposite magnitude of peaks can also be understood as arising from the same geometry reached when the path becomes close to the seam.

The above case illustrates that two sharp peaks of opposite signs can not be always taken as evidence for contour passing through the seam two times. In fact, it is possible to setup contours so that they come close to a seam two times giving appearance of two opposite signed peaks without enclosing or passing through the seam, and yielding a topological phase of 0.

The results for three Tilted contours presented in subfigures **(c)**, **(d)**, **(e)** can be understood from their 3d and projection plots in Figures 3.2 and 3.3. Since contour *Tilted(EQ)* hits the seam, one of its peak as shown in **(c)** can be seen to be very high in magnitude, $\approx$ 40 rad^{-1} which is almost 5 times larger as compared to previous case. The other peak is much broader and is of magnitude $\approx$ 5.

Interestingly, the sharp peaks seems to contribute $\frac{\pi}{2}$ to total topological phase which turns out to be 3.131 which is close to π. We think that this is an illustration of first theorem discussed by Levi and coworkers [198]. According to this theorem, an open contour path crossing the seam gives a contribution of $\frac{\pi}{2}$ to ADT angle change, which is precisely what is observed here. However, since the contour hits the seam only once and not twice, their second theorem does not apply here. At this time, it is unclear to us whether the observed total topological phase always needs to be π and not 0. We think that this can not be decided from numerical calculations and an analytical proof is needed to demonstrate what happens in cases when the contour hits the seam only once.

The case of *Tilted(GT)* contour in subfigure **(d)** is easier to understand. Since it encloses the seam, its topological phase is 3.140. The relative magnitudes of NACT peaks can be explained on the basis that one portion of the path comes much closer to seam than the other one. Therefore, these peaks can be interpreted to arise from around contours geometries which are closest to the seam (see Figure 3.3). For the other contour *Tilted(LT)*, the NACT profile in subfigure **(e)** shows opposite peaks of unequal magnitude. The peak of larger magnitude $\approx$ 17 can be seen to be about half the magnitude observed for *Tilted(EQ)* case indicating that it is away from the seam. The other broader peak of opposite sign is similar in magnitude to the corresponding one in *Tilted(GT)* case. The absence of topological phase in this case fits with observation that this loop does not surround the seam.

The contours generated from 3-atom motions are shown in subfigures **(f)**, **(g)** and **(h)**. The last two are easily understood from their closeness to the seam and their surrounding the seam, as shown in their 3d plots 3.5. The tilt of 90° has not been included as it is very similar to the 60° case. A noteworthy feature in these results is the *Planar* case shown in **(f)**. Since the contour passes through the seam exactly two times in opposite directions, this case is exactly same as in the methylamine case (except for relative separation between peaks). Here, the peaks are very sharp, equal in magnitude ≈ 30, and opposite in sign. Each peak can be seen to contribute exactly $\frac{\pi}{2}$ as predicted by the theorems discussed in Refs. [198, 199].

From these cases, it can be concluded that the magnitudes of peaks, their relative separation (here $\Delta\phi = \pi$), and how they contribute to ADT angles provide some information on how close the seam runs to the chosen plane. Contour crossing the seam can be detected with sharp NACTs yielding ADT angle contributions of $\frac{\pi}{2}$.

3.4 Study of NACTs in Ethylene

In this section [208], we discuss results from our NACT calculations in the vicinity of two MECIs found to be important in ethylene photochemisry. Our motivation to consider this system arises from the work of Baer and coworkers on methylamine [197–199], where NACT contour integrals were used to detect the presence of a seam. Using a series of such calculations, they characterized the location of seam in terms of coordinates of moving hydrogen atom relative to the remaining atoms. Ethylene was chosen mainly because of its MECIs points found using CI geometry optimization techniques have been reported previously [209, 210]. Important ones are twisted-pyramidalized (Tw-py), H-migration (H-mig), ethylidine, and C_{3v}-ethylidine MECIs. It has been shown that these MECIs are interconnected on the S_1/S_0 CI seam. Our idea is to use NACT computations to expose S_1/S_0 seam around Tw-py and H-mig MECIs. An important difference with respect to the methylamine case is that lack of a symmetry plane, which makes the location of the seam uncertain.

We have used SA3-CASSCF(6,6)/aug-cc-pVDZ method where averaging has been performed over three singlet states. For both the chosen MECIs, optimized geometries were found based on geometries which have been reported in literature. No symmetry was imposed in our calculations. The resulting MECI structures are shown in Figure 3.8. The NACT calculations have been carried out by employing DDR procedure in MOLPRO [108], where required angular components of NACTs were evaluated by finite-difference methods. The optimized geometries of MECIs have been listed in appendix B.

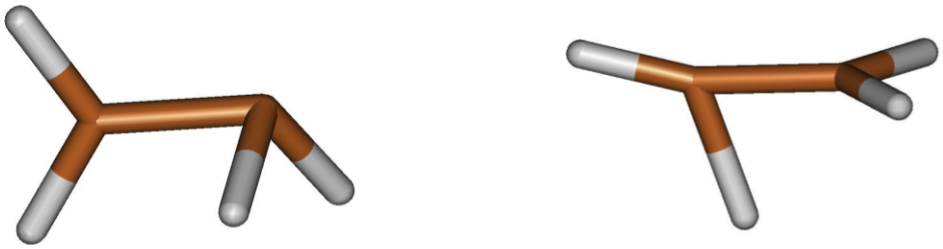

(a) Tw-py MECI. **(b)** H-mig-MECI.

Figure 3.8: MECIs of ethylene. **a:** Twisted-pyramidalized (Tw-py). **b:** Hydrogen-migration (H-mig).

Now we discuss the choice of planes where circular contours are setup. The Tw-py MECI is characterized by two geometrical features as shown in Figure 3.8a. Starting from planar geometry of ethylene, both CH_2 groups are twisted around the C-C bond relative to each other by 90°. After this, one CH_2 group is bent and pyramidalized while the other one remains almost stationary. This leaves the non-pyramidalized CH_2 and other carbon atom to approximately remain in a plane (see Figure 3.8a, dihedral angle of H-C-C-H is about 170°). Therefore, pyramidalization can be thought as occuring due to bending and side-way motions of CH_2 group with respect to this plane.

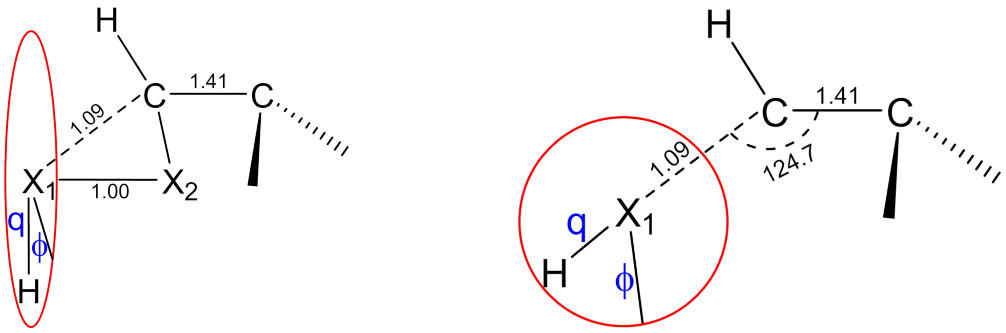

(a) Out-of-plane contour. **(b)** In-plane contour.

Figure 3.9: The contours (shown in **red**) for twisted pyramidalized MECI. **a**: The *out-of-plane* contour. Positions X_1 and X_2 show moving hydrogen w.r.t carbon. q and ϕ are its polar coordinates. ϕ is dihedral angle of this hydrogen with respect to HCX_1X_2 plane, that determines position of hydrogen along contour. **b.** The *in-plane* contour. X_1 shows origin of contour.

Two sets of circular contours with increasing radius were setup on two mutually perpendicular planes chosen as shown in Figures 3.9a and 3.9b. The first set involves displaced circular motion of one of the H-atom of non-pyramidalized CH_2 in a plane perpendicular to the CH_2-C plane. This plane has been shown by a red circular

contour in Figure 3.9a. In the following, we refer to these contours as *out-of-plane*, where the plane refered is the CH_2-C plane. The second set of contours, referred to as *in-plane*, were setup in the CH_2-C plane itself. In both cases, the origin of contours is the tw-py MECI. The circles of same radii in both these contour planes intersect at two geometries in CH_2 plane. If the seam is present in CH_2-C plane, then these two contours would expose it.

The plots of angular NACTs and ADT angles along the chosen contours for Tw-py case are shown in Figure 3.10. For visualization purposes, the starting angles are shifted by 90° so that the NACT peaks move towards the interior of the plot. The contour radii of $q = 0.1, 0.2, 0.3\mathring{A}$ have been used. The subplots **(a)**, **(b)**, **(c)** for *out-of-plane* contours show sharp peaks separated by nearly 180° angle. This can be seen in Table 3.1 where peak positions and energy differences of two states are listed. Large magnitudes of NACTs at peaks and small energy differences $\approx 1 - 2$ mH indicate that at these locations, the contour is close to the seam. The peak positions around 90° and 270° (after subtraction of extra 90° shift used for visualization) correspond to geometry where the contour passes through the CH_2-C plane. These results clearly indicate that the contour hits or comes close to the seam as it enters the plane.

The plot $q = 0.3$ shows two interesting features which are somewhat different from the other two plots. The peak on the right side is now much sharper almost corresponding to crossing a CI. The positions of the peaks 103.2° and 267.6° correspond to geometries slightly above CH_2 plane. The second peak at 267.6° corresponds to geometry in which the two hydrogens are closer. Assuming that peaks in each of these plots correspond to same kind of geometry, it can be seen that first peak decreases in magnitude while second one increases in magnitude.

The plots of ADT angle and topological phases suggest that each peak contributes nearly $\frac{\pi}{2}$. While $q = 0.1$ and $q = 0.2$ cases indicate that the contours surround the seam, nearly zero topological phase for $q = 0.3$ case suggests that seam has moved out from being inside the contour to outside, similar to the situation observed in H_3 case. In Table 3.2, we have listed the topological phases. To check the effect of third state on these results, we have carried out the 3-state ADT procedure as discussed in Refs. [211, 212]. The corresponding topological angles α^3 and diagonal elements of $\mathbf{D}$ matrix $(D^3_{11}, D^3_{22}, D^3_{33})$ shown in the same table indicate that two-states indeed form a Hilbert subspace in this region. The NACTs connecting these states to the third state turned out to be much smaller in magnitude.

These calculations suggest that seam may be located on CH_2-C plane or close to it. If it were indeed located within this plane, then *in-plane* contour should be able to intersect it in a manner similar to methylamine case. These plots are shown

in subplots **(d)**, **(e)**, **(f)** of Figure 3.10 and data is shown in Table 3.1 Although peaks are seen in expected locations, the are not sharp as before and much smaller in magnitude. Once again the opposite signed peak structure with zero topological phase is observed for $q = 0.3$.

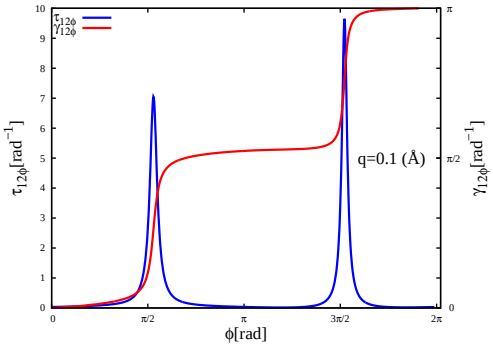

(a) q=0.1 (α =3.149).

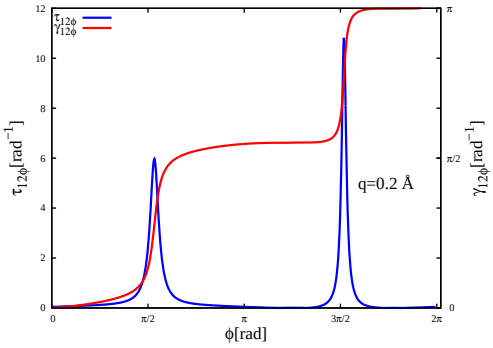

(b) q=0.2 (α =3.149).

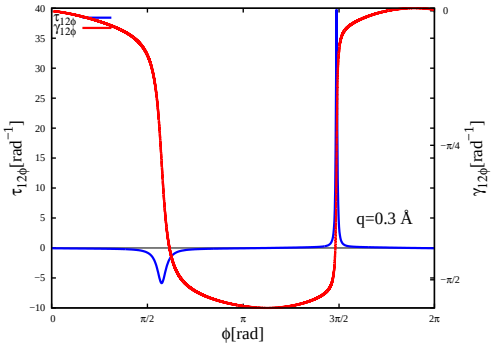

(c) q=0.3 (α =0.007).

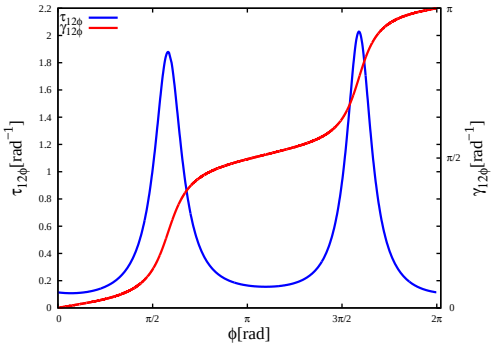

(d) q=0.1 (α =3.140).

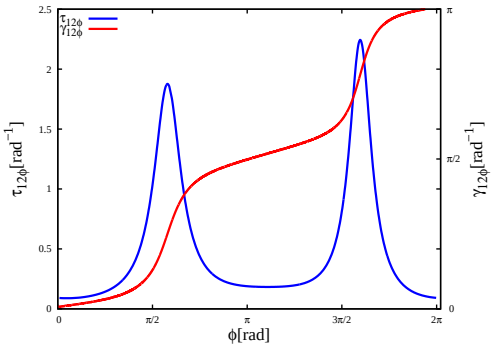

(e) q=0.2 (α =3.159).

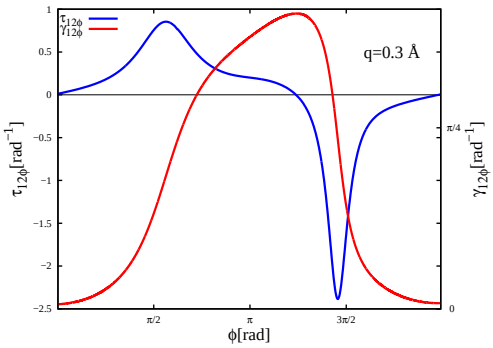

(f) q=0.3 (α =0.024).

Figure 3.10: Tw-py case: Angular NACT ($\boldsymbol{\tau_{12}}$) and ADT angle ($\boldsymbol{\gamma_{12}}$) plots for q=0.1, 0.2, 0.3 Å with their α values. **a, b, c** correspond to the *out-of-plane* contour. **d, e, f** correspond to the *in-plane* contour.

Table 3.1: Tw-py case: Angular positions (ϕ_m) of NACT peaks for out-of-plane (above) and in-plane contours (below). ΔE (in mH) is the energy gap of S_1 and S_0 states.

q (Å)	ϕ_{m1}	ΔE_{m1}	ϕ_{m2}	ΔE_{m2}	$\Delta\phi_m$
0.1	95.2	0.73	274.0	0.63	178.8
0.2	96.0	1.63	273.2	1.25	177.2
0.3	103.2	2.14	267.6	0.55	164.6
0.1	104.8	0.88	286.0	0.72	181.2
0.2	104.4	1.90	287.6	1.22	183.2
0.3	101.6	5.75	262.0	1.65	160.4

Table 3.2: Out-of-plane contour: Topological phases (α) found using 2- and 3-state diabatization procedures and diagonal elements of **D** matrix elements.

q (Å)	α^2_{12}	α^3_{12}	α^3_{13}	α^3_{23}	D^3_{11}	D^3_{22}	D^3_{33}
0.1	3.149	3.146	-0.071	0.022	-0.999	-0.997	0.997
0.2	3.149	3.144	-0.059	-0.124	-0.992	-0.998	0.990
0.3	0.007	0.007	0.040	0.011	0.999	0.999	0.999

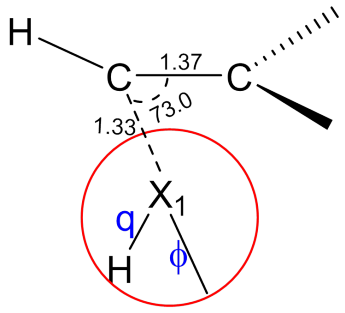

Figure 3.11: Contour for H-mig MECI. Angular NACT is calculated along circular contour (shown in **red color**). X_1 is origin.

Table 3.3: H-mig case: Angular positions (ϕ_m) of NACT peaks. ΔE (in mH) is the energy gap of S_1 and S_0 states.

q (Å)	ϕ_{m1}	ΔE_{m1}	ϕ_{m2}	ΔE_{m2}	$\Delta\phi_m$
0.1	64.0	0.28	226.4	0.51	162.4
0.2	71.6	0.41	225.6	0.98	154.0
0.3	79.6	0.48	226.0	1.29	146.4

For the case of H-mig MECI, only one plane has been chosen as shown in Figure 3.11. As can be seen from the molecular structure of MECI shown

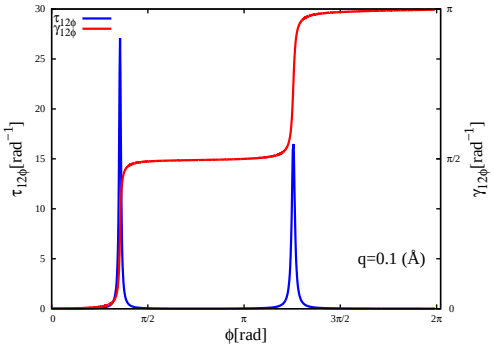

(a) q=0.1 (α =3.134).

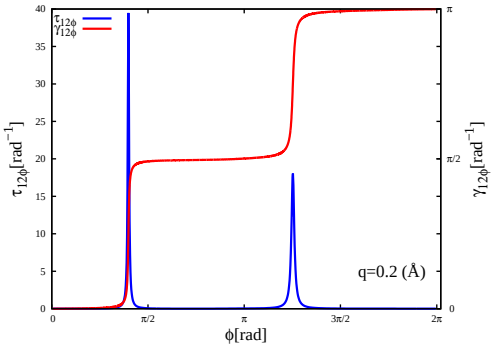

(b) q=0.2 (α =3.139).

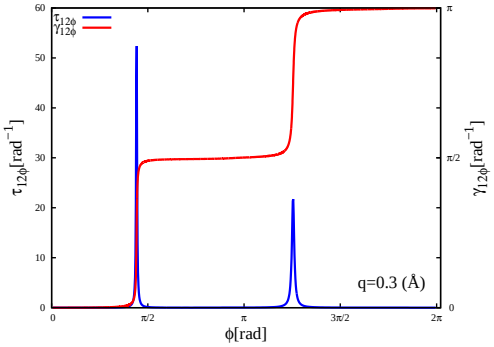

(c) q=0.3 (α =3.137).

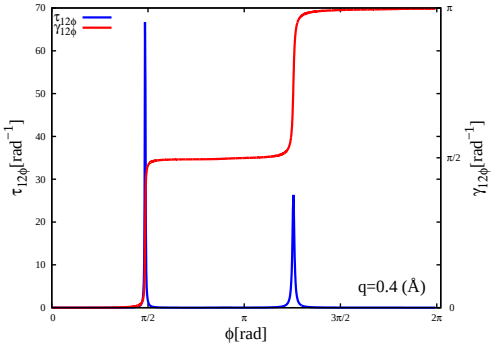

(d) q=0.4 (α =3.133).

Figure 3.12: H-mig case: Angular NACT ($\boldsymbol{\tau_{12}}$) and ADT angles ($\boldsymbol{\gamma_{12}}$) plots for q=0.1, 0.2, 0.3, 0.4 Å with thier α values.

in Figure 3.8b, both CH_2 group are twisted about C-C bond. Instead of pyramidalization, both hydrogen atoms of one of the CH_2 group move within the plane such that one of them is starting to migrate towards the other carbon atom. This MECI is known to be responsible for formation of ethylidine HC-CH_3 molecule [210].

The plots of NACTs and ADT angles for this case are shown Figure 3.12 and data on peak positions and state energies are listed in Table 3.3. It can be seen that both peaks are rather sharp, supported by even smaller energy differences. The magnitude of first peak increases from $q = 0.1\mathring{A}$ to $q = 0.3\mathring{A}$ and again each peak contributes $\frac{\pi}{2}$ to topological phase. The total topological phase being close to π also indicates that the contour surrounds the seam for all cases. Assuming that both peaks roughly correspond to seam, the shifting of peak position differences from 162.4° towards smaller angles to 146.4° indicates that, in this plane, the shape of the seam is curved.

3.5 Summary

In this chapter, we have discussed calculations performed to understand and appreciate how a seam influences the profiles of angular NACT and ADT angle along closed contours by considering two molecular systems. The first system H_3 is an example where the fixed geometry of its JT seam allows setting up of contours with different topological relation to the seam. This study helps to understand how different angular NACT profiles arise.

For the second system ethylene, the seam regions around two of its MECIs have been explored. When the results are taken together, it can be concluded for the Twpy MECI case, that S_1/S_0 seam exists close to the CH_2-C plane, but not exactly on it. We think that a minor change in geometry starting from MECI geometry can lead to another geometry on the CI seam where CH_2-C is exactly planar as opposed to its being nearly planar now. This may allow construction of a C_s-symmetry CI geometry resembling MECI geometry. For symmetry reasons, as in the case of methylamine, this plane will definitely contain full seam projection appearing as a symmetry-allowed seam. Such a geometry may be prove to be helpful in future studies.

We think that some of the studies presented here may prove useful in future investigations of seam using NACTs.

Chapter 4

Review of Non-adiabatic Effects in Photochemistry

4.1 Introduction

In this chapter, we discuss some of the basic and advanced conceptual considerations necessary for computational studies of photochemical reactions. We also provide an overview of methods of on-the-fly non-adiabatic dynamics with an emphasis on the method used in applications reported in this thesis. These methods are often employed in combination with algorithms based on static ab initio electronic structure calculations to obtain an enhanced understanding of photochemical reaction mechanism. This chapter also covers selected topics from the existing literature so as to provide a view on the current state of computational photochemistry.

Due to involvement of both ground and excited electronic states, most of the photochemical reactions with a few exceptions can be considered as non-adiabatic. All such reactions start with the absorption of a photon by a molecule in ground electronic state which promotes it to an excited electronic state. As nuclear motion takes place on the excited PES, a number of physical processes of widely different time-scales occur which collectively decide the fate of the molecule. The possibility of interest in photochemistry is radiationless conversion of absorbed energy to drive structural changes in the molecule (isomerizations) or chemical reactions producing molecular fragments. In such a case, some part of the chemical changes take place on excited PES and remaining part on ground PES, which is inherently non-adiabatic situation. Some photochemical reactions may involve chemical changes occurring entirely on the excited state and these are adiabatic photochemical reactions.

A wide range of applications of photochemical reactions have been reported in the

field of chemistry and biology. The familiar *cis-trans* photo-isomerization has been shown to be an important step in many natural photo-biological processes such as the event of vision [213, 214]. Another fundamental isomerization reaction, electrocyclic reaction in presence of light, plays an important role in the natural synthesis of the Vitamin-B_{12} [215]. The role of photochemistry is essential in many advanced technologies such as photo-switchable devices, organic light emitting diode, organized nano-scale motion etc. [216–218]. Therefore, photochemistry is an important field to understand and appreciate the outcome of complex nature of non-adiabatic effects.

Theoretical and experimental developments of the last few decades have brought vast improvement in our conceptual understanding of photochemical reactions. In early years, the radiationless physical processes responsible for photo-reactions were described in terms of semi-classical theories [219, 220]. The rates of these processes were estimated by applying the Fermi-golden rule and avoided-crossing models were used to elucidate proposals of mechanistic description [219, 221]. These theoretical models were not able to account for the ultrafast nature of photophysical processes which underlie many photochemical reactions. After improvements in time-resolution of spectroscopic techniques, many photo-reactions were reinvestigated and shown to involve ultrafast electronic relaxation steps.

Subsequent developments, beginning from early 1970s, changed these one-dimensional avoided-crossing descriptions to two-dimensional ones in which conical intersection (CI) appears as a key concept. In this modern paradigm of photochemistry, a CI geometry is identified as an important conceptual transient species that acts as *funnel* for conversion of excited state molecule to different ground state products. The CI concept made it possible to rationalize the outcome of many organic photochemical reactions [90,222]. Many ultrafast experiments have supported that molecules entering and exiting photochemical funnel region within time-scale of tens to hundreds of femtoseconds. Recently, Poli *et al.,* have presented experimental evidence for the retinal chromophore passing through the funnel region of its double bond photo-isomerization reaction within $200fs$ [214]. In another application, it has been demonstrated that the photo-stability of DNA chromophores arises from the presence of a CI funnel region [223, 224]. Therefore, even though a CI is only an unstable geometry on the intersection seam of PESs, in photochemistry it is often used as representative geometry of a molecular intermediate for mechanistic explainations.

Computational quantum chemistry has been routinely used to provide mechanistic understanding of thermal ground-state chemical reactions, by computing electronic structures and energetics of transition states and intrinsic reaction coordinate (IRC) connecting different intermediates. The difference between mechanisms of thermal

and photochemical reactions makes it necessary to develop new computational algorithms [12, 90]. The correct qualitative description of electronic structure of excited states can become challenging due to the multi-configurational character of electronic wave-functions near the funnel region. Further difficulties are associated with reaction path calculations which can not be described by a single PES. Instead, multiple reaction paths are needed to describe various branches connected through a CI. Many computational photochemistry algorithms mainly focus on practical characterization of the funnel region. Now a days, computational methodologies make it possible to locate the conical intersection geometry, and characterize its local topography, interstate couplings, the structure of nearby stationary geometries and their energetics [89, 90]. This helps in building a qualitative mechanistic picture. Additional information comes from approximate dynamical calculations based on trajectories. Together, these methods are helpful to a better understanding of molecular photochemistry.

The organization of the rest of the chapter is as follows. We begin with a brief discussion in section 4.2 on two basic mechanistic models which have been used in the earlier works on photochemistry. The emergence of a modern view of photochemistry is discussed in section 4.3. Here, we also discuss in some detail on how the conceptual understanding of *cis-trans* photo-isomerization of ethylene has evolved over last few decades. The basic concepts and considerations necessary to carry out computational study of photochemical reaction are discussed in section 4.4. In the last section 4.5, we have provided an overview of different types of non-adiabatic dynamics methodologies employed in such studies. This chapter is written so as to serve as a reference material for the following chapters which contain results from our studies on two photochemical investigations.

4.2 Classical View of Photochemistry

The final fate of a molecule after photoexcitation depends on the physical processes governing the evolution of its initial excited state. These can be divided into radiative and non-radiative processes. Radiative processes involve transition from a higher energy electronic state to a lower one through the emission of a photon. The radiative rate depends on the nature of electronic states via the transition dipole moment connecting them and increases with their energy gap. The non-radiative processes involve transition from one vibrational energy state to another one of equal energy and this amounts to redistribution of energy into different vibrational modes. This process is faster as compared to the radiative one by several orders of magnitude and

depends strongly on the nature of PESs involved.

These processes are schematically represented in terms of a figure known as *Jablonski diagram*, as shown in Figure 4.1. The horizontal lines on this figure represent the vibrational states of an electronic state, which itself is indicated by its spin-multiplicity such as singlet (S_1) or triplet (T_1). The most common singlet ground electronic state is indicated by (S_0) along with horizontal lines representing its vibrational energy levels. The absoption process, indicated by a straight arrow as (A) in Figure 4.1, takes the molecule from a vibrational state on S_0 to one of the vibrational states of the excited state S_1. The FC description of this process implies that it is almost instantaneous, approximately 10^{-15}s or less.

Three types of non-radiative deactivation processes indicated by curly arrows are possible - the internal conversion (IC), intersystem crossing (ISC) and intramolecular vibrational relaxation (IVR). In the IVR process, the electronic energy of initial state gets converted and redistributed among different vibrational modes of the same electronic state. This occurs in a timescale of 10^{-14}s to 10^{-11}s, and depends on the strength of vibronic and inter-mode couplings. If the energy redistribtion involves different electronic states, then the processes are referred to as IC and ISC according to whether the states are of same or different spin-multiplicity, respectively. The IC process occurs on a similar timescale as the IVR indicating their common origin. In contrast, the ISC is usually much slower 10^{-10}s to 10^{-8}s due to the smaller magnitude of spin-orbit coupling. The radiative processes are further classified as fluorescence (F) and phosphorescence (P) respectively, depending upon whether they correspond to a spin-allowed or to a spin-forbidden transition. The fluorescence and phosphorescence occur on a timescale of 10^{-10}s to 10^{-7}s and 10^{-6} to 1s respectively.

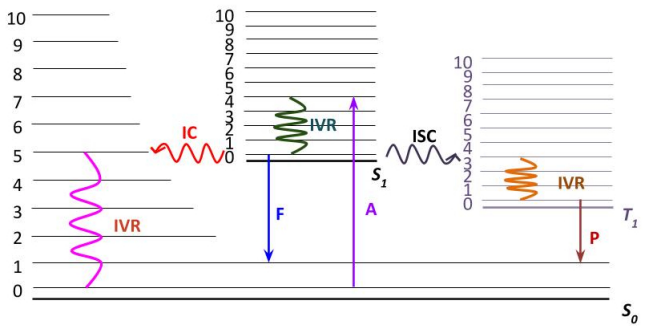

Figure 4.1: A schematic representation of Jablonski diagram (A: absorption; F: fluorescence; P: phosphorescence; IVR: intramolecular vibrational redistribution; IC: internal conversion; ISC: intersystem crossing). Reproduced with permission from [28].

The main advantage of Jablonski diagram in photochemistry is that it allows a simple visualization of different photo-induced physical processes, their outcomes

and the time-scales involved. However, it is not suitable to describe a wide variety of possible outcomes of a photochemical reaction where deactivation may take place via different mechanisms. Sometimes, such mechanisms may involve thermal reactions of vibrationally hot molecules produced via an IC processes or an intermolecular energy transfer process directly producing an excited state intermediate. As in mechanistic descriptions of thermally induced chemical reactions, a schematic energy profile diagram indicating the relative energies of reactants, products, different intermediates and mechanisms of their formation is suitable for this purpose. Such a diagram needs to separately represent postulated intermediates and key structures on PES of each involved electronic states, and indicate how they are reached through various physical processes and reaction paths. Even though most photochemical reactions are non-adiabatic, they usually start from an excited state at a well-defined geometry where the ground state has a simple electronic configuration and eventually proceed to form another bonding ground state configuration (product, intermediate) [29, 225, 226]. Therefore, it may be expected that the electronic configuration of some of the structures on the diagram can be understood by application of principles of chemical bonding.

One such schematic diagram of a photochemical reaction is shown in Figure 4.2. Upon excitation, the reactant $\mathbf{R}$ at its ground-state equilibrium structure goes to an excited state structure $\mathbf{R}^*$. According to the FC principle, the geometries of both these structures are nearly the same. However, $\mathbf{R}^*$ is an unstable structure on excited state PES due to the altered electronic forces. As a result, it undergoes immediate structural deformations to convert excess electronic energy into vibrational form. Ground-state photoproducts $\mathbf{P}$ and $\mathbf{P}'$ can be formed in two different ways - adiabatic and non-adiabatic pathways. Adiabatic reaction path is $\mathbf{R}^* \rightarrow \mathbf{M}^* \rightarrow \mathbf{TS}^* \rightarrow \mathbf{P}^*$ process followed by an emission of a photon to form the product $\mathbf{P}$. Non-adiabatic reaction mechanisms arise from IC processes to form a ground-state intermediate structure somewhere along a reaction path starting $\mathbf{R}^*$, which goes on to form final products. Two such possibilities are shown in this figure. One possibility involves IC around the minima $\mathbf{M}^*$ on the excited state arising from an avoided crossing with the ground state. Another possibility is IC at a structure $\mathbf{X}^*$ where the two PESs intersect. It is to be noted that both these possibilities may also endup regenerating the reactant as indicated by the arrows.

When a true surface-crossing exists along a reaction path and is energetically accessible from the FC region as shown in the left-side of the figure, one can make use of the semi-classical Landau-Zener [227] model to qualitatively account for the rate of transition. This model shows that internal conversion is very efficient at $\mathbf{X}^*$ geometry

where the energy gap is zero. In fact, the conversion can take place within one vibrational period (a few femtoseconds) upon reaching the crossing region. Therefore, photochemical reactions can take place on time scale of tens of femtoseconds to several picoseconds when such crossing mechanism is involved [228]. The widely different timescales reflect the nature of excited PES (such as local minima or energy barriers) along the reaction path connecting FC and crossing structures [28, 89, 229].

When surface-crossings are not present or not energetically accessible, then non-adiabatic transitions are better visualized as conversion of electronic energy of the upper state into a manifold of vibrational states associated with the lower electronic state. This also holds true for avoided crossings with significant energy gaps. Such a process is well-described by the Fermi-golden rule and rate of transition depends on the Frank-Condon factor and the density of vibrational states. This usually takes place around an avoided crossing region between an excited state minimum $\mathbf{M}^*$ and the ground state. Depending on the location of avoided crossing and its energy gap, this mechanism can be much slower and tends to compete with fluorescence [12].

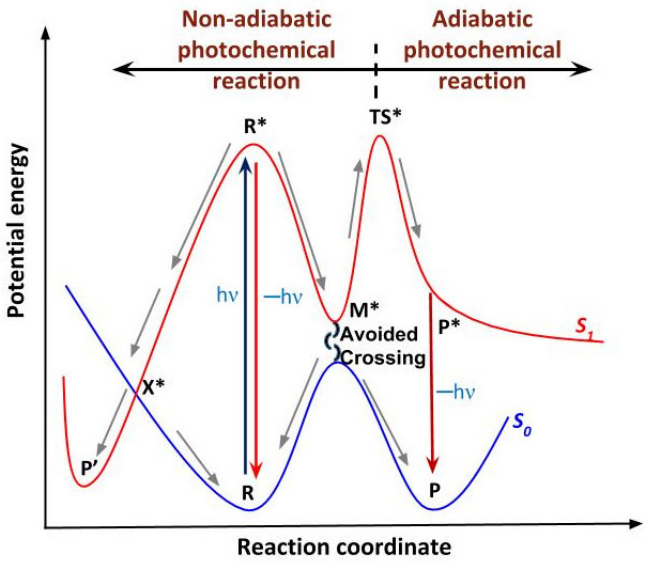

Figure 4.2: A schematic view of photochemical reaction. Reproduced with permission from [28].

4.3 Modern View of Photochemistry

The predominant view of photochemical reactions prior to 1970s had been that they take place in a manner similar to that of ground state thermal reactions, with avoided-crossings taking up the responsiblity to induce non-radiative transitions. The

mechanistic picture for ring closing photoisomerization of 1,3-butadiene presented by Vander Lugt and Oosteroff in their computational study [230] can be considered a best example of this view. Their proposal was that, upon photoexcitation, a stable intermediate ($\mathbf{M}^*$) is quickly formed on the 2^1A_1 excited state of butadiene around its avoided-crossing with same-symmetry 1^1A_1 ground state. Their limited computations indicated the presence of such a minimum on excited state.

A number of factors can be identified for the view to go unchallenged for some time. The time-resolution in experimental techniques was not sufficient to distinguish physical processes which are much faster than fluorescence. The *non-crossing rule* of Wigner [6] which forbids the existence of crossings between potential energy curves of same symmetry was assumed to hold for polyatomic molecules. The rule, if valid, can explain why avoided crossings exist and why they lead to minima on excited states. Although the non-validity of the rule was known, it was assumed that exceptions to the rule were rare. Therefore, at that time, it was reasonable to assume that 1^1A_1 and 2^1A_1 electronic states of 1,3-butadiene do not cross.

This view was challenged by both experimental and theoretical works. Experimental works provided clear evidence for complete lack of fluorescence which must occur if avoided-crossings with significant energy gap (more than few kcal/mol) were to exist. Theoretical models and computational studies indicated that same-symmetry crossings between low-lying states are not rare. Over the next decades, with further advances, a modern view has emerged which underlies the current understanding of photochemistry.

4.3.1 Role of Conical Intersections

One of the important development was the gradual shift in emphasis to CIs to recognize and appreciate their role in photochemical reactions. The lecture of Teller called for a refocus on PES intersections to understand internal conversions. During this period, Zimmerman [85, 222], Michl [231] and Salem [232] independently came up with different methods for construction of state correlation diagrams for a number of simple organic photoreactions without invoking orbital symmetry considerations. These works suggested that certain photoproducts can be formed by decay of the excited species at CI of ground and first excited PESs. Michl and Zimmerman termed these conical intersections (CI) as *funnels* which play significant role in deactivation of excited state. Their earlier proposals for presence of CI funnels in biradicolid systems were confirmed using 3-state models as well as *ab-initio* calculations to locate the position of funnel [233]. Using ab initio calculations, Varandas and coworkers

demonstrated the existence of CI between states of same-symmetry in a triatomic system [140].

With the ultrafast spectroscopic techniques, excited state lifetime of several conjugated hydrocarbons were measured. The lifetimes of dienes [234], cyclohexadienes [235], hexatrienes [236] and opsin bound retinal protonated Shiff bases [237] were found to be in sub-picoseconds. These observations clearly indicated CI funnels to be energetically accessible in these molecules, play an important role in their ultrafast relaxation. Developments of computational methods for location of same-symmetry CIs and further applications by Robb, Yarkony, Ruedenberg and others further confirmed the existence of CIs for many molecules [3, 34, 149].

4.3.2 The *Cis-Trans* Isomerization in Ethylene

In this subsection, we go through the literature tracing the evolution in our understanding of photoinduced *cis-trans* isomerization in ethylene. This is used as an exemplar of *cis-trans* photo-isomerization in conjugated hydrocarbons. The usual picture is that of a free torsion or rotation around C-C double bond which is partially weakened by the promotion of an electron from bonding π to anti-bonding π^* orbital. This has undergone considerable changes based on many experimental and theoretical studies carried out in last few decades.

4.3.2.1 One-dimensional Picture

Initial mechanistic understanding comes from the one-dimensional model of Mulliken using the torsion angle as reaction coordinate. The model employs four valence electronic states - referred to as N, V, T and Z states in Mulliken's notation [238]. State correlation diagram along the reaction coordinate is shown in Figure 4.3. Due to the stabilizing overlap of two atomic p-orbitals at the carbon atoms, the ground state geometry is planar (D_{2h}) and the electronic state (called N state) is a singlet state dominated by the closed-shell π^2 configuration.

Upon photo-absorption, one electron is promoted from bonding π MO to π^* anti-bonding MO. This transition is strongly symmetry-allowed and results in a singlet valence excited state (V state) dominated by the open-shell electronic configuration $\pi\pi^*$. At this geometry, a triplet T state from the $\pi\pi^*$ configuration and a higher energy singlet Z state from the doubly-excited π^{*2} configuration also arise. Due to exchange interactions, the triplet state is lower in energy as compared to the singlet V state. Electronic transition to Z state is forbidden by symmetry at planar geometry.

The V state favors a twisted D_{2d} geometry due to lowering of the energy of

π^* MO [239] upon torsion. Along the reaction coordinate, the energy of π orbital increases and the energy of π^* orbital decreases as shown in the left panel of Figure 4.3. At the twisted orthogonalized geometry (torsion angle of 90°), two orthogonal non-bonding *p*-orbitals form a *perfect* biradical. Any distortion (such as stretching or pyramidalization) would result in their partial overlap forming a biradicaloid state. This state is better described by transforming the π and π^* MOs into two non-bonding C-centered *p*-orbitals. This description results in three orbital configurations - one diradical (D) and two zwitterionic (Z) ones. This gives raise to four electronic states - ^{1}D, ^{3}D, ^{1}Z$_1$, ^{1}Z$_2$ states.

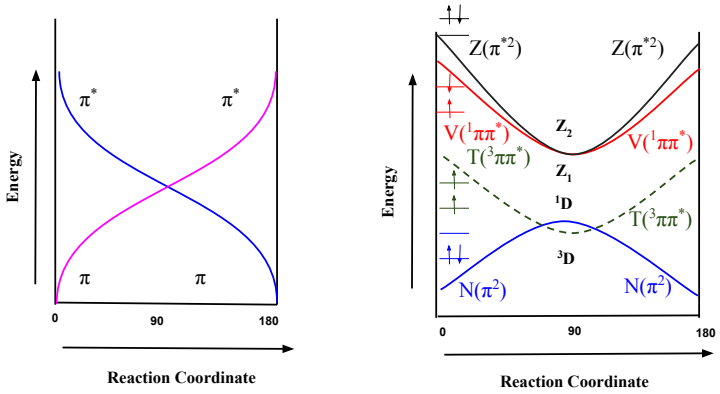

Figure 4.3: The orbital and state correlation diagrams of *cis-trans* isomerization of ethylene. Left panel: Orbital correlation diagram. Right panel: State correlation diagram along with orbital configurations. Redrawn with permission based on original figure in Ref. [29].

The state correlation diagram shown in the right panel of Figure 4.3 correlates N,V,T,Z states of planar geometry with D,Z states of twisted orthogonalized geometry. As can be seen, the electronic energies of all excited states (V, T and Z) decrease along the reaction coordinate reaching minimum at 90°. In contrast, the ground-state energy increases reaching maximum at the perfect biradical geometry. Here, both N and T states are close in energy and cross each other as shown in figure. Both V and Z states become exactly degenerate at 90° and are equivalent to the Z$_1$ and Z$_2$ states discussed before. Using the state correlation diagram, it is possible to imagine that upon photo-excitation the molecule relaxes to the ground state through the avoided crossing between N and V states. Therefore, torsion motion can be considered to be the main reaction coordinate.

Evidence for dominance of torsional motion in electronic relaxation of the V state also comes from the UV absorption spectra of ethylene. The experimental absorption

spectra shows a diffuse band in vacuum UV region (180-145 nm). This was assigned by Wilkinson and Mulliken to the V⟵N transition along with superimposed Rydberg bands [240, 241]. The transition extends towards 207 nm with a weak vibrational structure. There has been a long controversy over the vibrational structure of the V state. Initially, this was assigned to the C=C stretching motion [241]. Later reinvestigation by McDiarmid and Charney assigned this to the torsion mode [242]. Theoretical studies of Buenker and Peyerimhoff also supported this assignment [243]. Other theoretical calculations confirmed twisted othogonalized (D_{2d}) geometry to be a local minimum [244]. Therefore, torsional motion was considered to be the reaction coordinate and continued to as a basis for the assignment of ethylene spectrum for a long time [245].

Computational studies indicated a large energy gap (nearly 60 kcal/mol) between N and V states at twisted geometry. This implies that the excited V state must be have longer lifetime and fluorescence from it must be observable. However, no detectable fluorescence was found in experimental studies on photoexcited ethylene [246]. All these observations suggested a much shorter excited state lifetime and presence of ultrafast deactivation mechanisms in action. Clearly, these could not be accounted for using this one-dimensional model.

4.3.2.2 Two-dimensional Picture

Further improvements of one-dimensional model came from different directions. As discussed before, Teller linked ultrafast relaxation mechanisms to the existence of CIs. The works of Salem [221] and Michl [247] attempted to understand the formation of CI funnels in distorted biradicaloid electronic structures using qualitative 3×3-CI models. Their works suggested that the energy gap of two lowest singlet states of a wide-variety of biradicaloids is controlled by an interplay between electron replusion effects and the difference in electronegativities of the terminal functional groups. In case of twisted orthogonalized ethylene which can be considered as a nearly perfect biradical [233], these electronegativity differences can easily arise from a pyramidalization of terminal CH_2 groups. It was found that even a small symmetric pyramidalization of a terminal CH_2 group can result in large change in dipole moments [221,247,248] - an effect termed as *sudden polarization*. This effect can be understood using 3×3-CI model of biradicaloid electronic structures [233]. This pointed towards a possible role for a second coordinate - possibly pyramidalization coordinate - in ethylene photochemistry.

Hudson and coworkers [249] revised the assigment of vibrational progression in

absorption spectrum by arguing that lower energy Rydberg state of planar ethylene and V state cross somewhere along the torsion mode. Soon, Martinez and Bennun arrived at the same conclusion and confirmed that the twisted D_{2d} geometry to be a saddle point rather than a local minimum [250]. Simulations of absorption spectra from first principles demonstrated that the vibrational progression of V state arises from a combination of torsional, C-C stretching and CH_2 scissoring motions [251–253]. Therefore, the one-dimensional coordinate *i.e*, torsional motion is not the only one which participates in N⟵V relaxation process. Futher, the absence of fluorescence and sub-picosecond lifetime of many conjugated systems (butadiene [254], hexadiene [255], stilibine [256], etc.) was confirmed from many femto-second experiments. These suggested a short excited state lifetime for ethylene as well.

Inclusion of the pyramidalization coordinate to extend the one-dimensional model comes from the works of Ohmine, Klessinger, Martinez and others. Signatures for the wagging, rocking and out-of-plane vibrations are seen in the resonance Raman spectra [251, 252, 257]. Klessinger *et al.,* and Martinez *et al.,* concentrated on the same twisted pyramidalized CI from two different approaches. Following Ohmini's work [258] on H-migration CI in ethylene, Klessinger *et al.,* explored a substantial region potential energy surface and found two CI geometries - a twisted-pyramidalized and a H-migration ones [259]. Ben-Nun and Martinez carried out *ab-initio* multiple spawning (AIMS) dynamics to establish that $S_0 \longrightarrow S_1$ non-adiabatic transitions mainly occur at twisted-pyramidalized-like CI structures [15]. Their study also identified four classes of energetically accessible CIs - twisted-pyramidalized (tw-py), ethylidine (eth), hydrogen migration (H-mig), and C_{3v}-ethylidine (C_{3v}-eth). Both tw-py and eth CI correspond to a minima on the crossing seam (MXC). The topography of PES around the minimum structures were also characterized [260]. The H-mig CI was found to be a saddle point which connects two symmetry equivalent tw-py MXCs [209, 260]. Another semi-classical dynamical study carried out by Barbatti *et al.,* focused on the crossing seam of ethylene. Their studies have shown a direct impact on various deactivation channels and demonstrates a complicated structure of the crossing seam [14, 210].

Despite the complexity of electronic relaxation dynamics indicated by these studies, it is possible to provide a simple and intuitive two-dimensional mechanistic picture. On the V state, initial CC bond stretching is followed by twisting around the C-C bond. Subsequently, one of the methylene units pyramidalizes reaching a tw-py CI geometry. This two-dimensional model emphasizes the importance of two nuclear coordinates - torsional and pyramidalization - in the excited state deactivation of

ethylene.

The model has been successfully employed as a prototype to understand the mechanism of *cis-trans* isomerization in many other systems, including the biological molecules such as rhodopsin [261] and retinal protonated Schiff base (RPSB) [262]. Somewhat recently, time-resolved photoionization experiments established the excited lifetime of ethylene to be 50 *fs* [246, 263]. This can be considered to be one of the fastest process leading to a chemical change. In conclusion, we consider the photochemistry of ethylene *cis-trans* isomerization to be the most successful one amongst many photochemical investigations where two-dimensional picture is used.

4.4 Computational Photochemistry

The primary objective of computational photochemistry is to propose and validate mechanisms for photochemical reactions by making use of methods of electronic structure and nuclear dynamics. As in the case of mechanisms of ground state thermal reactions, the proposals include a sequence of steps each describing specific atomic displacements taking one intermediate structure to another one. A complete photochemical reaction mechanism would involve delineating all possible pathways a reactant molecule may take after the absorption of light until the formation photoproducts.

The most commonly used approach for computational modeling of photochemical reactions is the *pathway approach* of Fuss and coworkers [264], as outlined in the reviews of Robb [90]. The approach makes use of local properties of PESs such as gradients and Hessians to identify and characterize key structures such as minima, saddle points, barriers, surface crossings (CI). Reaction paths connecting these structures are then computed as minimum energy paths (MEPs). Computation of reaction paths starts from the Frank-Condon structure and proceeds to upto formation of different ground state products, identifying energetics and structural information of all key structures.

A reaction path of photochemical reaction must have at least two branches: one located on the excited state PES and another on the ground state PES. The two branches are connected via a CI funnel where excited reactant or intermediate converts into the ground state by a non-adiabatic transition. Structure of funnel is expected to be related to the photoproduct structures just as a transition state is related to the product in a thermal reaction. Thus, a knowledge of CI funnel structure is important for rationalization and prediction of possible photoproducts. Similarly, the energetic accessibility of a funnel region from reactant is related to the lifetime of excited state.

Therefore, identification of CI funnel and its characterization plays a central role in computational photochemistry.

Computational investigations of photochemical reactions usually require the following three steps.

1. Determination of nature and energies of low-lying excited states at the reactant ground state geometry (or FC geometry), and identification of a low-lying electronic state which can be populated by a photoexcitation from the ground state.

2. Geometry optimizations performed to find key structures on the excited and ground-state PESs. This involves finding local minima on the excited state, minimum energy CI geometries.

3. Minimum energy path (MEP) computations to establish how structures found in the previous steps are connected by a reaction path starting from the FC geometry. This also provides an estimate of energy barriers if any to reach them. Similarly, possible MEPs starting from CI funnel into different valleys on ground PES and resulting photoproducts are identified.

From these static calculations, mechanistic descriptions can be proposed for the photochemistry of system. The information obtained from such studies are only structural *i.e* it describes the motion of a vibrationally cold molecule moving with infinitesimal momentum. It does not allow estimation of experimental quantities such as excited lifetime, quantum yields, branching ratios, transient emission or absorption spectra.

To obtain such dynamical information, one needs to go beyond the static approach and consider time-evolution of a molecule from *ab-initio* molecular dynamics or wave packet quantum dynamics. Recent studies have shown that dynamical treatment becomes important when the system does not follow MEPs [261]. Approximate dynamical simulations can provide semi-quantitative information to compute quantities such as excited-state lifetime and quantum yields that can compared with experimental results. Therefore, to reach a better understanding of photochemical reactions, it is important to complement static computations with dynamical ones [34].

4.4.1 The CI Funnel

The role a CI funnel plays in determining photochemical reactivity can be elucidated by making an analogy with similar role played by a transition state (TS) in ground

state reactions. In some sense, CI funnel represents the photochemical analogue of transition state [12]. Both are critical structures with different local description of PES around them. The TS is a structure which is a local stationary point - a first-order saddle point on a PES. It is decribed by a single vector - the transition vector - which is the normal mode corresponding to the imaginary frequency. In a thermal reaction, the TS forms an energetic barrier (see Figure 4.4a) which separates reactant and product valleys via a single reaction path. The intrinsic reaction coordinate (IRC) method is a way to identify this reaction path as a MEP passing throught TS.

A photochemical funnel is characterized by its CI structure - where ground state PES spikes and excited state PES dips to touch each other to form degeneracy. It is not a minimum on excited state or a saddle point on ground state, as energy derivatives are not defined at the CI. As discussed in Chapter 1, it is described by two modes - $\vec{\mathbf{g}}$ and $\vec{\mathbf{h}}$ vectors which span a two-dimensional plane known as branching or g-h plane (see Figure 4.4b). A CI funnel can be characterized by specifying these vectors. Unlike TS which is a unique structure, each point on the CI seam can serve as a photochemical funnel. The funnel associated with minimum energy CI point on the seam can serve as a special funnel.

The CI structure of a funnel also presents a barrier of a different nature for photochemical reactions. The excited molecule must traverse this barrier to get converted into ground state. Unlike TS, the CI connects excited state and ground state pathways. The g-h plane of a CI serves as a reaction coordinate space in which decay to the ground state happens. Therefore, CI gives raise to many pathways which can lead to different ground state products (see Figure 4.4b). On the other hand, the uni-direction of the transition vector means that it always drives a thermal reaction towards a single product.

4.4.2 Internal Conversion Efficiency of a CI funnel

A classical trajectory representing a molecule passing a CI funnel can be considered to have reached the ground state at the CI geometry of the funnel. However, the transition can take place at any geometry within the funnel. A qualitative understanding of excited to ground state transition can be obtained by considering the one-dimensional curve-crossing Landau-Zener (LZ) model [227]. According to this semi-classical model, the transition probability P_{IJ} between two adiabatic electronic states I and J at a geometry Q around the cossing-point is given by the following expression [228].

$$P_{IJ} = \exp\left(-\frac{\pi}{4}\,\xi\right) \qquad \xi = \left|\frac{\Delta E(\mathbf{Q})}{\hbar\,\dot{\mathbf{Q}}\cdot\boldsymbol{\tau}_{IJ}(\mathbf{Q})}\right| \tag{4.1}$$

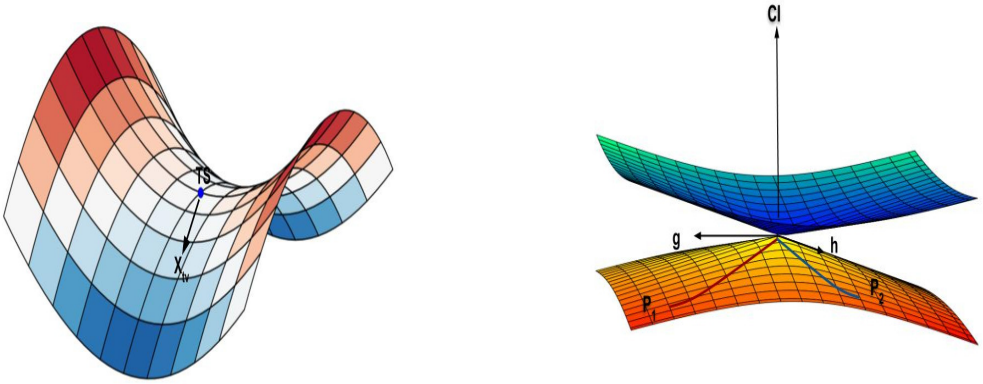

(a) TS **(b)** CI

Figure 4.4: Comparison of the role of (a) a transition state (TS) in thermal reactivity and (b) a conical intersection (CI) in photochemical reactivity.

Here, ξ is known as Massay parameter, $\Delta E(\mathbf{Q}) = E_I - E_J$ is energy difference between the states, $\dot{\mathbf{Q}}$ is trajectory velocity, and $\boldsymbol{\tau}_{IJ}$ is NAC. According to Equation 4.1, the transition probability increases with decreasing energy gap, increasing magnitude of NAC and increasing component of trajectory velocity along the NAC vector.

Even though LZ model predicts conversion efficiency of 100% when a trajectory passes through a CI geometry, this is really not an accurate or complete picture as it is based on semi-classical considerations. In general, it has been established that topography of PESs around CI also influences the IC efficiency of a CI funnel. Therefore, the local shape of PES around CI, its energetic and topology of excited PES affect the decay probability. The effect of various topology of CI along a reaction coordinate has been discussed in reference [265].

A detailed discussion on first-order description of CI and topographic parameters is given in Chapter 1. The local topography of PESs in the vicinity of a CI can be characterized by relative orientation. This was first discussed by Rudenberg who introduced a nomenclature for it [87]. According to this, local topography of PES can be classified as *peaked* and *sloped* ones (sometimes also *intermediate* indicating a border between the two). The peaked vs sloped classification is by the tilt parameters s_x and s_y which represent projection of seam energy gradient along the branching plane vectors (see section 1.3). If both s_x and s_y vanish, such a CI is referred to as peaked. For a perfectly peaked CI, the PESs form a vertically oriented elliptic double-cone in the branching plane. When the tilt parameters are such that both PESs have opposite signs of energy gradients, it is still referred to as peaked CI. On the other hand a sloped CI is tilted with non-vanishing values for s_x and s_y such that both PESs are sloping in the same direction (same sign for energy gradients).

Relaxation around a peaked CI can be considered to be more efficient as compared to the sloped one. The bond selectivity of retinal protonated shiff base in *cis-trans* isomerization, photostability of photochromic system are some of the examples where peaked-sloped distinction has been successfully employed [99]. Since two PES gradients at a sloped CI PESs are oriented in the same direction, the force at the ground surface would drive the wave packet to the intersection region where it may recross to the excited surface opening multiple deactivation channels. On the contrary, the gradients are pointed in different direction at the peaked CI and possibility of recrossing is much smaller leading to fewer pathways.

4.4.3 Construction of Photochemical Reaction Path

Even though a CI funnel controls efficient internal conversion, its existence does not guarantee its involvement in a photochemical process. To ensure facile conversion, it is important that a funnel can be reached from the excited reactant structure. If a funnel exists in higher-energy region of the excited PES far away from the FC region, it can not be involved. Another possibility is for a funnel to exist in lower energy region, but separated by an energy barrier on the exicted PES. Many experiments [266, 267] indicate onset of ultrafast internal conversion (detected by loss of fluorescence) when reactant excess energy is enough to overcome a barrier on the excited state which prevents funnel from being reached at lower excess energies.

To confirm possible involvement of a CI funnel, it is necessary to compute a photochemical reaction path connecting the FC geometry to the funnel passing through any lower energy intermediates (if they exist) or transition states. To complete path characterization, ground-state reaction paths starting from CI structure leading to different products also need to be characterized.

Reaction path calculations are usually based on the concept of minimum energy path (MEP). This is a path connecting a structure to a nearby minima or a saddle point. It is defined as the path taken by a classical particle with infinitesimal kinetic energy sliding down to reach a local minimum (similar consideration apply for connecting to a saddle point). MEP can be used as a special representative of different reaction paths followed by molecules. An advantage of MEP is that it is completely characterized by structure of PES alone. Therefore, it can be computed by same geometry optimization methods as used for locating stationary points such as minima, saddle points, or CI points. These points arise as special points along the MEP.

MEP calculations are carried out by combination of intrinsic reaction coordinate

(IRC) and intrinsic reaction direction (IRD) calculations [34, 90, 229, 268]. The latter method is used to compute steepest relaxation directions in starting from FC or a CI point. Once directions are identified, standard IRC calculations can be used to obtain steepest descent path along these directions leading to MEP.

4.4.4 Dyanamical Aspects

The CI funnel and MEP calculations only provide structural information. Since molecules always have finite kinetic energy, classical trajectory starting from a geometry on PES is different from MEP. Despite this, MEP is useful in reaction conditions where vibrationally cold excited states are formed, such as in cold gas-jets, reactants enclosed in low-temperature inert matrices. However, in many cases, these structural informations are not sufficient. In vibrationally hot reactions, excited reactants have sufficient amount of kinetic energy. The resulting trajectories on PES will deviate substantially from MEP. Such trajectories sample substantially high-energy structures and may lead to entirely different products. Therefore, a photochemical reaction path characterized by MEP does provide realistic descriptions.

Dynamical treatments remedy this situation to some extent by considering several trajectories starting with different initial conditions. This makes it possible to sample widely different regions of PESs and ascertain effects of kinetic energy specifically channeled into different modes. For example, dynamics simulations of ethylene have shown that only a small porition of trajectories are converted to ground state through minimum CI geometry [260]. Therefore, to better understand the photochemical reactivity, it is usually necessary to go beyond static picture of MEPs. Proper descriptions of motion of nuclei (quantum, semi-classical or classical) provide additional information such as reaction time-scale, excited state lifetimes, branching ratios, quantum yields and other details.

4.5 Methods of Non-adiabatic Dynamics

Given the necessity of accounting for physical effects arising from the dynamics of nuclei, this section is intended to give an overview of state-of-the-art methods of non-adiabatic dynamics methods which are currently used in photochemical studies. A number of methods have been developed in the last three decades, each of them making use of different approximations based on the nature of nuclei. These methods fall into two categories depending on their treatment of electronic structure.

The first approach is a two-step procedure which involves, in the first step, *a priori*

determination of an analytic representation of PESs. For this purpose, interpolation or fitting techniques are employed on PES data obtained from electronic strucutre calculations. The dynamics is performed in the second step by a solution TDSE using a wave-packet for representing wave-function of nuclei. As discussed in the Chapter 1, this also requires adiabatic-to-diabatic transformations to obtain a diabatic PES representation which allows numerical wave-packet propagation methods to be employed. Although this approach yields very accurate results, it is feasible to apply this only for small molecules with up to 4 atoms. For polyatomic molecules, the construction of global PES and its analytic representation is a major problem. In particular, for f-dimensional PES, the fitting of a PES requires N^f energy points where N in number of internal coordinate. Therefore, it is not possible to perform dynamics of polyatomic molecule with this approach [110, 112, 113]. It is usually applied for reactive scattering small molecules.

However, it is possible to construct approximate vibronic model Hamiltonians in the diabatic representation, with parameters in the Hamiltonian adjusted to reproduce electronic structure calculations around the FC region. Recent computational advances in multi-state multi-mode dynamics make it possible to treat larger molecules with many degrees of freedom [129, 269]. However, the quality of PESs makes it difficult to employ them for photochemical applications.

Over the last two decades, another class of methods known as direct dynamics methods have been developed. These methods replace PES determination step by an *on-the-fly* calculation of PESs and coupling elements between electronic states in the vicinity of a smaller number of geometries. The term *on-the-fly* refers to calculation of electronic structure during time propagation. The nuclear wave-function is represented in terms of a collection of classical-like trajectories evolving on the PES. A detailed account of direct dynamics methods can be found in Refs. [114, 270, 271].

The main advantage of direct dynamics approaches is that it makes it not necessary to precompute global PES. As a result, it samples only important regions of PES, thereby strongly reducing computational expenses arising from electronic structure calculations. This feature makes it feasible to perform dynamical studies on larger molecules. In the recent years, this approach has gained considerable interest in photochemistry. Replacing the wave-packet with a collection of trajectories makes it possible to develop several methods which are closer in spirit to classical molecular dynamics simulations, yet include important quantum effects in an approximate way. Direct dynamics methods closely resemble *ab-initio* molecular dynamics (AIMD) methods which have been extensively used for a number of ground state problems [272, 273], and can be viewed as its extension for non-adiabatic cases

encountered in photochemistry.

A variety of direct dynamics methods that have been developed so far can be broadly divided into two classes depending on how the nuclei are represented, how their time-evolution is treated, and how non-adiabatic transitions arise. We briefly discuss these approaches in the next two subsections.

4.5.1 Trajectory-based Methods

In this method, the nuclei are treated as point-mass particles evolving according to classical equations of motion on a potential generated by electronic wave-functions. The method relies on semi-classical approximations [274]. In semi-classical limit *i.e.*, $\hbar \longrightarrow 0$, a wave packet of nuclei can be represented as an ensemble of trajectories which move on the potential according to Newtonian mechanics. Since classical trajectories are restricted to move only one PES at a time, description of non-adiabatic transition requires some approximate ad hoc treatments that allow these trajectories to either sense the presence of another PES or to have quantum amplitudes which can influence it. These methods can also be viewed as mixed quantum-classical (MQC) method which maintains a self consistency between quantum (electronic) and classical (nuclei) degrees of freedom.

In Ehrenfest class of methods [11, 275], trajectories are associated with position and momentum which change according to classical equations of motion. Associated with each trajectory is an electronic wave-function which contains components or coefficients from each of electronic states at molecular geometry indicated by the position of the trajectory. These components can be used to compute an average electronic potential felt by the trajectories as they move. The components evolve as per TDSE for electronic wave-function. Thus, trajectories can be considered as simultaneously moving on all PESs. Non-adiabatic transitions are accounted for by a continuous variation of the weight coefficients of trajectories. Main drawback of Ehrenfest method is the qualitatively incorrect treatment of non-adiabatic transition due to the mean field. If a single trajectory leaves strong coupling region, then it evolves on an effective potential which is unphysical because trajectory is needed to be either on one state or another state [276].

The trajectory surface-hopping (TSH) methods improve this deficiency by branching of the trajectory among electronic states in non-adiabatic region. [276–279]. Here, an ensemble of trajectories evolve on the *pure* adiabatic or diabatic states and non-adiabatic effect is introduced by a stochastic process known as *hopping*. The transition between electronic states is determined by a stochastic algorithm which,

based on non-adiatic couplings, computes the probability for a trajectory to remain on same state or to hop to another state.

Several hopping algorithms have been developed [278] amongst them, most popular one is Tully's fewest switches algorithm (FSA) [276]. The FSA minimizes the number of hopping events in one time step and is based on independent trajectories. Unlike the Ehrenfest method where transition probability is smooth, hopping introduces instantaneous transition probability which results in discontinuous transitions for a single trajectory. Since TSH involves an ensemble of independent trajectories, electronic transitions will turn out to be smooth when averaging is taken.

Hopping can be considered an external perturbation which must be applied to maintain self-consistency between classical and quantum motions, given the absence of terms which naturally couple these motions. The hopping event induces a discontinuous change in electronic energy, and hence total energy is not conserved in this process. This is rectified by re-scaling of velocity of component along the non-adiabatic coupling vector. This changes nuclear kinetic energy to compensate the discontinuity in electronic energy. There are some instances where the kinetic energy is insufficient to conserve the total energy and such hops have to be rejected - a situation known as *frustating hop* [279, 280].

Another limitation of TSH methods arises from the use of independent trajectory approximation. This results in lack of coherence effects [281, 282]. This is one of the primary reason why surface-hopping method is applicable in long time-scale dynamics (photochemistry of *pico-second* time scale) where coherence of the initial wave packet is lost. Nevertheless, there are also other variants of surface-hopping which have been developed to improve these issues. A brief summary of recent development of the surface-hopping method can be found from ref [283].

Due to the classical mechanical description of dynamics of independent trajectories of TSH methods, their computational implementation is straightforward. This only requires local information of PESs such as energies, gradients, and non-adiabatic couplings. Their computational scaling only depends upon simulation time and quality of electronic structure theory [284].

4.5.2 Gaussian Wave-packet Methods

These are another class of approximate methods which represent a wave-packet in the basis of time-dependent generalized Gaussians - known as Gaussian wave-packet (GWP) methods. Motivated by the pioneer work of Heller [285, 286], they are able to describe quantum effects at lower computational costs when approximations are

used. An interesting aspect of GWPs is that they provide a connection between the standard grid-based method and trajectory based methods, and lead to direct dynamics variants. The key difference between trajectory based and GWP is that the basis functions, which can be thought of as trajectories, are subject to evolution equations very different from that of classical trajectories.

There are two types of GWP methods which have been used in photochemistry. First is the full multiple spawning (FMS) method and the other is the variational multi-configurational Gaussian (v-MCG) methods. The v-MCG approach and its direct dynamics variant (DD-vMCG) have been developed within the time-propagation framework of MCTDH by replacing grids with time dependent Gaussians. The parameters of Gaussian basis (such as widths, positions and momenta) are determined by an application of time-dependent variation principle. Due to this, the motion of full GWP will approximate evolution of the wave packet it represents. This results in a faster convergence *i.e*, fewer Gaussians would be needed.

A detailed description of v-MCG and DD-vMCG methods can be found in ref [287, 288]. The FMS method and its direct dynamics variant - *ab-intio* multiple spawning (AIMS) - make use of frozen Gaussians whose parameters follow classical or semi-classical equation of motion. Their combining coeffcients are determined from TDSE. Non-adiabatic effects are introduced by a special algorithm known as *spawning*. In next sections, we provide a detailed description of theoretical and computational aspects of AIMS method and compare it with to other non-adiabatic methods.

4.6 *Ab Initio* Multiple Spawning (AIMS)

The AIMS method, developed by Martinez and coworkers, has been widely used in the field of photochemistry. We have also made use of this method for our works reported in next two chapters. For the purpose of completeness, we provide a brief discussion on important features and workings of this method. A full description may be found in ref [289–293].

A schematic depiction of AIMS method is shown in Figure 4.5. Here, an initial trajectory represented by red gaussian on the excited state moves according to Newton's equations. Upon reaching the intersection region, additional trajectories represented by blue gaussian are *spawned*. The method describes nuclear quantum dynamics in the basis of Gaussians associated with these trajectories. The spawning attempts to qualitatively capture wave-packet branching at CIs which is responsible for non-adiabatic population transfer.

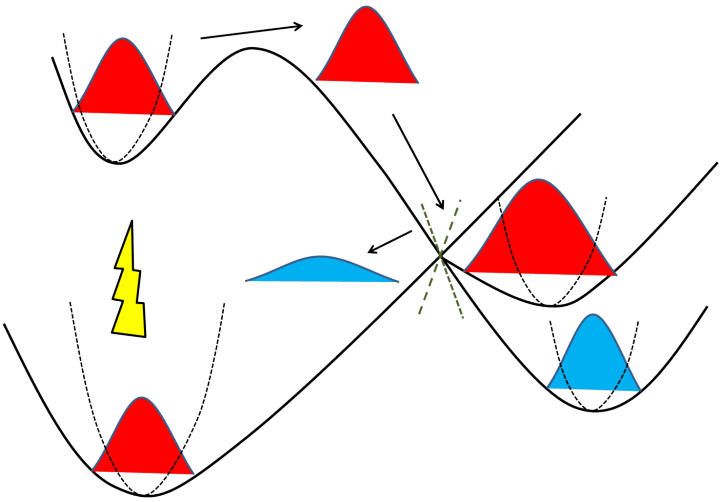

Figure 4.5: A Schematic representation of AIMS.

The AIMS method is based on frozen Gaussian approximation (FGA) dynamics of Heller [285, 294] where nuclear wave function is represented as a linear combination of frozen Gaussian *i.e.*, width of Gaussian is fixed. The FGA approach is based on a familiar quantum mechanical result - if gaussian wave packet is displaced in harmonic potential then its center follows classical trajectories with its shape and width remain the same. Keeping the spirit of FGA, the AIMS method has been exteneded to treat dynamics on multiple electronic surfaces. It can also be viewed as extension of familiar AIMD methods for photochemical applications.

4.6.1 Full Multiple Spawning

The AIMS method is based on a basic approach to dynamics, known as full multiple spawning (FMS). A FMS wave function is expressed as a sum of product of electronic and nuclear wave functions as follows.

$$\Psi(\mathbf{q}, \mathbf{Q}, t) = \sum_{i}^{N_{el}} \Phi_I(\mathbf{q}; \mathbf{Q}) \chi_I(\mathbf{Q}; t) \tag{4.2}$$

where $\Phi_I(\mathbf{q}; \mathbf{Q})$ is I^{th} electronic state, $\chi_I(\mathbf{Q}; t)$ is the associated time-dependent nuclear wave function. The labels $\mathbf{Q}$ and $\mathbf{q}$ denote nuclear and electronic coordinates, respectively. N_{el} is the number of electronic states.

Each nuclear wave function, $\chi_I(\mathbf{Q}; t)$, is given by a superposition of

multidimensional frozen Gaussian also known as trajectory basis function (TBF).

$$\chi_I(\mathbf{Q};t) = \sum_{j=1}^{N_I(t)} c_j^I(t)\chi_j^I(\mathbf{Q};\bar{\mathbf{Q}}_\mathbf{j}^\mathbf{I}(t),\bar{\mathbf{P}}_\mathbf{j}^\mathbf{I}(t),\bar{\gamma}_j^I(t),\alpha_j^I) \tag{4.3}$$

where index j labels TBFs associated with I^{th} electronic state. The combining coefficient $c_j^I(t)$ represents complex amplitude of j^{th} TBF on I^{th} electronic state. The number of TBFs associated with Ith electronic state $N_I(t)$ can be changed during simulation as new ones TBFs are spawned. Each TBF is parameterized by its phase space center or centeriod of Gaussian whose position and momentum are represented by $\bar{\mathbf{Q}}_\mathbf{j}^\mathbf{I}(t)$, $\bar{\mathbf{P}}_\mathbf{j}^\mathbf{I}(t)$, and a semi-classical phase $\bar{\gamma}_j^I(t)$. The width of Gaussian α_j^I is taken to be as time-independent as well as independent of the electronic state. Each individual TBF χ_j^I is expressed as multidimensional product of one-dimensional Gaussian $\chi_{j\rho}^I$.

$$\chi_j^I(\mathbf{Q};\bar{\mathbf{Q}}_\mathbf{j}^\mathbf{I}(t),\bar{\mathbf{P}}_\mathbf{j}^\mathbf{I}(t),\bar{\gamma}_j^I(t),\alpha_j^I) = e^{i\bar{\gamma}_j^I(t)}\prod_{\rho=1}^{3N}\chi_{\rho_j}^I(Q;\bar{Q}_{\rho_j}^I(t),\bar{P}_{\rho_j}^I(t),\alpha_{\rho_j}^I) \tag{4.4}$$

$$\chi_{\rho_j}^I(Q;\bar{Q}_{\rho_j}^I(t),\bar{P}_{\rho_j}^I(t),\alpha_{\rho_j}^I) = \left(\frac{2\alpha_{\rho_j}^I}{\pi}\right)^{1/4}\prod_{\rho=1}^{3N} e^{-\alpha_{\rho_j}^I(Q_{\rho_j}-\bar{Q}_{\rho_j}^I(t))^2+i\bar{P}_{\rho_j}^I(t)(Q_{\rho_j}-\bar{Q}_{\rho_j}^I(t))} \tag{4.5}$$

ρ represents 3N Cartesian coordinates of the molecule.

In FMS based methods, time propagation of centroid of Gaussian is governed by Hamilton's equation of motion.

$$\frac{\partial\bar{Q}_{\rho_j}^I}{\partial t} = \frac{\bar{P}_{\rho_j}^I}{m_\rho} \tag{4.6a}$$

$$\frac{\partial\bar{P}_{\rho_j}^I}{\partial t} = -\frac{\partial V_{II}(\mathbf{Q})}{\partial Q_{\rho_j}}\Big|_{\bar{\mathbf{Q}}_\mathbf{j}^\mathbf{I}(t)} \tag{4.6b}$$

$$\frac{\partial\bar{\gamma}_j^I}{\partial t} = -V_{II}(\bar{\mathbf{Q}}_\mathbf{j}(t)) + \sum_{\rho}^{3N}\frac{\left(\bar{P}_{\rho_j}^I(t)\right)^2}{2m_\rho} \tag{4.6c}$$

where m_ρ is mass of ρ^{th} degree of freedom and V_{II} is potential energy of Ith electronic state. The global phase factor associated with TBF is propagated semi-classically as in Equation (4.6c).

The coefficient $c_j^I(t)$ is determined by solving the nuclear TDSE within the basis

set of TBFs. The resulting coupled equation in matrix notation is given below,

$$\frac{\mathbf{dc^I(t)}}{\mathbf{dt}} = -\boldsymbol{i}(\mathbf{S_{II}^{-1}})\Big\{[\mathbf{H_{II}} - \boldsymbol{i}\dot{\mathbf{S}}_{\mathbf{II}}] + \sum_{\mathbf{J}\neq\mathbf{I}} \mathbf{H_{IJ}}\Big\}\mathbf{c^I} \tag{4.7}$$

where the overlap matrix $\mathbf{S}$, and its time derivative $\dot{\mathbf{S}}$ are defined as,

$$\mathbf{S}_{kl}^{II} = \langle \chi_k^I | \chi_l^I \rangle_{\mathbf{Q}} \tag{4.8a}$$

$$\dot{\mathbf{S}}_{kl}^{II} = \langle \chi_k^I | \frac{\partial}{\partial t} \chi_l^I \rangle_{\mathbf{Q}} \tag{4.8b}$$

These overlap matrices are block-diagonal in electronic label due to the orthogonality of electronic wave functions Φ_I. Since the TBFs are non-orthogonal, inverse of overlap matrix is needed for the computation of coefficients $c_j^I(t)$. These matrices can be computed analytically by an integration over nuclear coordinate. In equation (4.7), H_{IJ} represents matrix element of full molecular Hamiltonian which includes both electronic and nuclear degrees of freedom.

$$\mathbf{H}_{IkJl} = \langle \chi_k^I \Phi_I | H | \chi_l^J \Phi_J \rangle_{\mathbf{q},\mathbf{Q}} \tag{4.9}$$

In the FMS dynamics, the set of equations (4.6)-(4.8) need to be intergated with suitable time step. The time evolution of the complex coefficient requires diagonal H_{IkIl} and off-diagonal matrix elements H_{IkJl} of the Hamiltonian for each pair of TBFs. Evaluation of these matrix elements, in principle, requires entire range of PESs for all electronic states. Therefore, many approximations have been considered to simplify thier evaluation and to reduce computational cost. The localized nature of Gaussian basis sets enables to perform these integrals approximately. In the context of AIMS, zeroth-order saddle point approximation (SPA) is employed to calculate these integrals. For example, the matrix element associated with potential energy operator, $V_{IJ}(Q)$, can be expressed by a Taylor expansion of zeroth order about the centroid of the product of TBF's.

$$\langle \chi_k^I | V_{IJ} | \chi_l^J \rangle_Q \simeq V_{IJ}(\mathbf{Q}_{centeroid}^{IJ}) \langle \chi_k^I | \chi_l^J \rangle_Q \tag{4.10}$$

The $\mathbf{Q}_{centroid}^{IJ}$ is centroid of the product of TBF's, χ_k^I and χ_l^J.

Now, we discuss computational cost of AIMS method. For M electronic states, $\frac{M(M+1)}{2}$ number of single point electronic structure calculations are required at every step of dynamics. Clearly, this would be very costly and computational scaling will be of $O(N_{TBF}^2)$ order. However, by using zeroth-order SPA, this scaling can

be reduced to $O(N_{TBF})$, as the overlap of two TBFs will be nearly zero when they are sufficiently far apart. For larger molecules, computation cost can be further reduced by introducing the independent first generation (IFG) approximation. Here, the initial basis functions representing the wave-packet are uncoupled from each other *i.e.*, neglecting any coherence between them. However, the IFG itself does not indicate that FMS does not include any coherences between the Gaussians because the basis functions are coupled through the solution of nuclear Schrödinger equation. Therefore, IFG approximation decreases the computational cost.

4.6.2 Spawning Procedure

One of the distinguishing feature of FMS dynamics is the spawning. This is a method for incremental addition of TBFs during the course of dynamics simulation. This allows nuclear TDSE to be solved much more accurately.

The key advantage of spawning is that it allows expansion of nuclear basis to be carried out only when it is essential for qualitative description of physical effects. In case of non-adiabatic dynamics, an example of such situation is, the branching of a wave-packet caused by non-adiabatic transition around an intersection region. While one branch continues to move on the original PES, the other branch moves on the other PES involved intersection. In AIMS, such a physical situation is taken into account by creating a new TBF on the second PES. This basis augmentation - referred to as spawning - greatly increases the efficiency of simulation while maintaining its accuracy.

For spawning to be succesful, it is important to consider two questions 1.When to spawn 2. How to spawn?

4.6.2.1 When to spawn?

Since spawning increases number of TBFs, is important to minimize the number of spawning events. Therefore, it is important to restrict it to events when a TBF enters a region of its associated PES where it is close to another PES. For adiabatic PES, the magnitude of NAC can be used as an indication. In AIMS, an effective coupling is defined whose magnitude is monitored to detect possibility of non-adiabatic events. This quantity is defined as follows.

$$\Lambda_{IJ}^{eff} = |\dot{\mathbf{Q}} \cdot \boldsymbol{\tau}_{IJ}(\mathbf{Q})| \quad \text{For adiabatic} \tag{4.11}$$

$$W_{IJ}^{eff} = \frac{V_{IJ}(\mathbf{Q})}{V_{II}(\mathbf{Q}) - V_{JJ}(\mathbf{Q})} \quad \text{For diabatic} \tag{4.12}$$

The effective coupling has calculated at each time step, for each TBF at the geometry corresponding to its position. If norm of the coupling is greater than a pre-defined threshold, the spawning threshold, then spawning is *turned on* which indicates that a TBF (or sometimes more than one) likely to placed on other coupled state. The old TBF is referred to as *parent* and the new basis as *child*. The time at which the coupling exceeds from the spawning threshold is referred to as t_{spawn}.

In order to identify the region where the child TBF is to be placed, a copy of the parent is propagated forward in time by solving only the classical equations for its motion. The propagation stops when the coupling again falls below the spawning threshold. This will sample the region of PES where non-adiabatic transition are possible - known as spawning region. The time at which this coupling is maximum is referred to as t_{max}. This is the time at which the parent and child TBFs, if they were already moving on their PESs, would have maximum overlap. This geometry, $\mathbf{Q}_m$, therefore represents ideal location for the child TBF to have been, in order to capture the non-adiabatic population transfer. The child TBF is placed on its PES at this geometry by copying its basis parameters from its parent TBF.

4.6.2.2 How to Spawn?

Before resuming propagation with new basis set, the position and momentum of the child need to be readjusted so that energy conservation is maintained. According to classical molecular dynamics, the classical energy of parent and child should be conserved. Although this is not necessary condition for quantum case, it is imposed to prevent accumulation of errors from finite basis set approximation used in FMS. There are many ways to choose the phase-space parameters of child TBF. Most common is position-preserving approach where the child TBF is assumed to have the same position as the parent TBF, *i.e.*, $Q_{parent} = Q_{child} = Q_m$ and its momentum is changed in the direction of NAC vector so as to ensure conservation of classical energy. The momentum of child TBF is calculated as,

$$\mathbf{P}^I_{new} = \mathbf{P}^J_{old} - D\hat{\boldsymbol{\tau}}_{\boldsymbol{IJ}} \tag{4.13}$$

P^I_{new} and P^J_{old} represent the momentum of new child TBF and old parent TBF, respectively. The $\hat{\boldsymbol{\tau}}_{\boldsymbol{IJ}}$ is unit vector define along NACT vector and D is a scalar variable.

$$\hat{\boldsymbol{\tau}}_{\boldsymbol{IJ}} = \frac{\boldsymbol{\tau}_{\boldsymbol{IJ}}}{|\boldsymbol{\tau}_{\boldsymbol{IJ}}|} \tag{4.14}$$

This spawning is very similar to momentum jump or hopping that takes place in surface-hopping methods. There are some instances where position-preserving approach is not feasible, related frustated hops. Since geometry $\mathbf{Q}_m$ is only a desirable geometry, this problem is solved by adjusting Q_{child} along its electronic energy gradient so that energy conservation holds. Both position and momentum can also be adjusted in optimal spawning algorithms [295, 296].

After placing the child basis, it is back propagated from t_{max} to t_{spawn} on its associated PES to obtain its positions and momentum values at t_{spawm}. The dynamics is restarted with the coefficient of child basis is set to be zero, $c_{child}(t_{spawn}) = 0$. It is important to note that spawning procedure only creates a new TBF, but extent of its importance in non-adiabatic population transfer is decided by the nuclear Shrödinger equation. A flow chart for spawning procedure is shown in Figure 4.6.

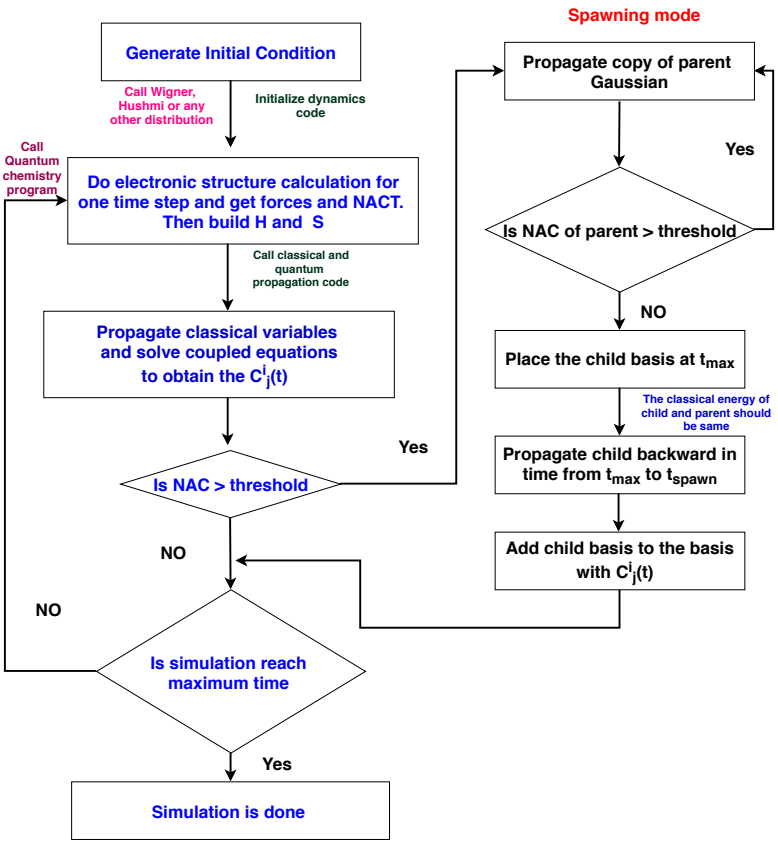

Figure 4.6: A flow chart of spawning algorithm.

4.6.3 Comparison with other methods

A number of methods which makes use of the concept of phase-space trajectories have appeared. Methods which are closed related to FMS/AIMS are G-MCTDH **??**, vMCG and its direct dynamics variant, CCS method [297]. It is of interest to compare it with them to understand their similarities and differences.

All these methods start with the same ansatz representing nuclear wave-function in terms of multi-dimensional Gaussians containing trajectory-like phase-space (position and momentum) and and non-classical (width and combining coefficients) parameters. Both G-MCTDH and vMCG seek to determine them fully from quantum mechanics by applying TDVP. The only difference between them is that vMCG excludes width parameter from optimization. Therefore, the TBFs are fully coupled with each other and with complex amplitudes. Hence, the resulting trajectories are very different from corresponding classical version. Quantum evolution of parameters allows faster convergence with respect to basis set size, and there is no need to increase the size of basis set during simulation. However, both the methods employ higher-order SPA for evaluation of matrix elements. This requires evaluation of second derivatives of PESs at each evolution time-step. This makes both these methods to be applicable only for small to medium sized molecules.

Both CCS and FMS/AIMS methods overcome these limitations by placing external restrictions on trajectory parameters, *i.e.,* by demanding that their evolution is as per classical mechanics with appropriate forces computed from PESs. While CCS method propagates trajectories using PES forces averaged over the entire trajectory, the FMS goes one step to employ instantaneous ones. Both of them solve TDSE/TDVP for quantum evolution of combining coefficients. Therefore, FMS method can be viewed as most approximate amongst them. This makes it computationally efficient, specially when it is combined with spawning procedures.

The AIMS also has close resemblance with TSH methods, considering that both make use of classical propagation of TBFs. Although TSH does not involve the concept of Gaussians, the resulting equations for individual trajectories are the same as FMS. The FMS improves TSH method with following features - **(a)** trajectories can be coupled by not making use of IFG approximation **(b)** multiple coupled trajectories result from spawning events **(c)** description of non-adiabatic population transfer via TDSE within the space of TBFs. **(d)** solving to the problem of frustrated hops. As a result, FMS/AIMS methods shows faster convergence as compared to TSH, and allow a much smaller number of trajectories be averaged. Therefore, AIMS can be viewed as a method intermediate between v-MCG and TSH methods.

4.7 Summary

In this chapter, a discussion on the basic concepts and perspective on important developments in the area of computational photochemistry has been given. It is here that theoretical concepts for description of non-adiabatic radiationless photochemical processes were successfully applied. The understanding of photochemical reactions at molecular level has considerably improved by further developments of computational methodologies based on *ab initio* electronic structure and nuclear dynamics.

We have discussed basic concepts and physical processes in terms of which mechanistic understanding of photochemical reactions are presented. From a historical perspective, one of the most important development has been recognizing the relevance of CI funnels. This led a shift from a simple one-dimensional picture based on avoided crossings to a two-dimensional picture based on true curve crossings. The discussion on C-C double bond isomerization in ethylene carried out in section 4.3 to evince how this two-dimensional picture is able to account for all modern ultrafast time-scale experiments on this and related system.

A review of computational concepts and computational methods for studying the photochemical reaction has been presented. The pathway approach discussed in Ref. [264] provides a general approach for investigations of computational photochemical mechanism. Using computational methods making use of local knowledge of PESs involved, it allows one to compute reaction paths and characterize key structural intermediates along the reaction path. The location of CI funnel, its local topography, its accessibility from FC point and any barriers involved, and pathways leading to ground state photoproducts can be studied systematically using this approach.

It is pointed out that pathway approach is static in nature and can not give a complete picture of a photoreaction. It is necessary to augment it with approaches to extract dynamical information. Therefore, modern approach to photochemistry is viewed as a synergistic approach where both static and dynamical pictures complement to each other. This provides a much richer understanding as compared to either of them.

Finally, we have presented an overview of approximate dynamics methods which have proved useful for photochemical studies. Direct dynamics methods are specially useful because of their use of trajectories. These trajectories represent possible deviations of static MEPs, and also allow dynamical information to be computed from them. We have discussed AIMS method which we view as an good compromise between computational efficiency and accuracy.

Chapter 5

A Comparative Study of Electronic Relaxation in Acrolein and Crotonaldehyde

5.1 Introduction

The photochemistry of small organic molecules with one or more functional groups is surprisingly rich [226, 298]. The absorption of a UV-vis photon results in opening up of several energy dissipation channels on ground and excited states and leads to a variety of photoproducts. Key to systematization, rationalization and prediction of such varied outcomes lies in understanding of molecular relaxation processes occurring at picosecond and sub-picosecond timescales. In particular, it is necessary to gain an understanding of different factors - general as well as molecule-specific ones - which influence the rates of these processes. Such factors may vary from a static feature of PESs to complicated dynamical effects of geometric phases. This approach underlies the modern view of photochemistry presented in previous chapter [29, 226, 298].

As discussed before, IC and ISC are two important physical processes responsible for radiationless state transitions. Even though they take place on different timescales, their efficiency is dependent on factors that are specific to molecules and states. Also important are specific nuclear motions on PESs required to bring the molecules in the vicinity of regions where such processes can take place efficiently. These motions are not only influenced by static factors such as nature of PESs (presence of minima or barriers) but also by dynamical factors such as presence and nature of functional groups involved. They result in a competetion between IC and ISC and sometimes also with radiative processes such as fluorescence [12, 266].

An approach commonly used in the literature is to develop simple models which can capture the photochemistry of a class of related molecules arising from substitutions on a simpler prototype molecule containing one more functional groups. A classic example is thermal Diels-Alder 4+2 cyloaddition where electronic nature of substituents is linked to how they affect the barrier of transition state [299]. The nature of substituents can alter the behaviour, sometimes significantly. However, when substituents are simple in nature, it can be assumed that model may still retain its validity. In such cases, photochemistry of substituted molecule can be related to changes in model parameters. Sometimes, the model may even need to be extended to include additional electronic states or pathways so that it can be used in different situations. Some examples of this approach are the photochemical models developed by Robb and coworkers on conjugated hydrocarbons, α,β-enones, protonated Schiff bases and others [12, 90, 300].

In this chapter, we report results from our computational investigations to understand the origin of experimentally observed differences in electronic relaxation behaviour of two related α,β-enone molecules - acrolein (AC) and crotonaldehyde (CR). Although the differences are not large, but significant. They can affect relative rates of IC and ISC processes in these molecules, which in turn may lead to differences in their photoisomerization and photodissociation channels. In this context, we also seek to verify important features that underlie Robb's model [301] for AC by employing high-level multi-reference calculations, and further extend its applicability to CR.

5.2 Photochemistry of α,β-enones

Enones are a class of molecules with two functional groups - an ethyleneic (C=C) and an aldehydic (CHO) group. The rich and varied chemistry of enones arises from an interplay between these two units, specially when these groups are in conjugation as in the case of α,β-enones. The photochemistry of α,β-enones has played an important role in enhancing their utility in organic chemistry due to a number of photoreactions they undergo, for example α-clevage, H-abstraction, *cis-trans* isomerization, cycloadditions, intramolecular rearrangements etc. [226, 302]. The α,β-enones not only display characteristic photochemistry of -C=O and C=C chromophores, but also different reactions and rearrangements arising from extended conjugation between them.

The simplest member of α,β-enones is acrolein (AC) - H_2C=CH-CHO (see Figure 5.1a). It has been used as a prototype to understand the photochemistry

of α,β-enones [226]. Due to the conjugation between C=C and C=O π systems, AC is planar molecule. The restricted rotation around the central C-C bond with partial double-bond character results in two ground state conformers, s-trans and s-cis, depending on relative orientation of C=O and C=C groups around this bond. The s-trans conformer is most stable and separated from s-cis one by a barrier of approximately 7 kcal/mol [303].

Although conjugation is similar to butadiene, unsymmetric nature of two π systems and inductive effect of C=O significantly alters the energies of π and π^* orbitals. However, it has relatively small effect on the energy of non-bonding n-orbital corresponding to oxygen lone pair. This orbital interaction results in lowering of $\pi \rightarrow \pi^*$ transition energy as compared to an isolated ethylene. The $n \rightarrow \pi^*$ transition also decreases relative to the carbonyl group. Such synergestic interaction between n and π orbitals leads to different photochemical pathways. In contrast to conjugated systems such as butadiene, the heteroatom (oxygen) of the carbonyl group introduces an additional $n\pi^*$ singlet S_1 and triplet T_1 states originating from promotion of an electron from n orbital to somewhat delocalized antibonding π^* orbital of C=C bond. Similarly, singlet S_2 and triplet T_2 states arise from electron promotion between delocalized bonding π antibonding π^* orbitals of the C=C bond. The UV-visible spectrum of AC can be understood in terms of these valence electronic states. High-lying valence and Rydberg states appear in the vaccum UV region.

(a) Acrolien **(b)** Crotonaldehyde

Figure 5.1: Structure of Acrolein (AC) and Crotonaldehyde (CR).

The photochemistry of AC upon photoabsorption in deep, mid and near-UV regions (200 – 380 nm) mainly arises from excitation to S_1 state (band maximum at 335 nm (3.70 eV)). This gives raise to various product channels, three major ones being α-hydrogen loss, Norrish type-I and decarbonylation reactions [304–306]. Both T_1 and T_2 states have energies below the S_1 state. A number of experiments on AC (and also many α,β-enones) have shown that its photochemistry is not so much

dependent on whether it is initiated from S_1 state or from energy transfer via triplet sensitization. This has supported the view that α,β-enone photochemistry can be understood from triplet intermediates formed from efficient ISC to T_1 and T_2 states. Therefore, its S_1 state can be considered as a precursor state from which ISC takes place. The lifetimes of triplet states have been estimated from experiments to be few picoseconds [307, 308].

The reason for the absence of $S_1 \rightarrow S_0$ IC in AC molecule was first explained by Robb and coworkers [301]. In this important computational study, they introduced a general model to qualitatively understand the photochemistry of α,β-enones. Based on CASSCF calculations, they identified two major non-radiative pathways which are energetically accessible from S_1 excitation. First pathway involves S_1 undergoing IC S_0 state through a S_1/S_0 CI region at 90° methylene-twisted geometry. In their calculations, MECI on this seam was found to be located 15 kcal/mol^{-1} above planar S_1 minima. Along the second pathway, S_1 state decays to the ground state through a series of ISC transitions involving T_1 and T_2 states. This pathway required both in-plane and out-of-plane motions and involved passing through S_1/T_2, T_1/T_2 and T_2/S_0 surface-crossings.

While absence of IC is easily attributed to the energy barrier for access to the S_1/S_0 CI seam, Robb and coworkers had to present a number of static features involving S_1, T_1, T_2 states to explain why the triplet pathway, despite unfavourable magnitudes of spin-orbital interactions, becomes favourable. The planar nature of S_1/T_2 and T_1/T_2 crossings implied that they could be easily reached from the planar S_1 minimum. The empirical rules of El-Sayed support higher ISC rates for $S_1 \rightarrow T_2$ [309]. Another important consideration was both T_1 and T_2 states being energetically close to the S_1 minimum. Taken together, these considerations make ISC to be most facile relaxation channel for S_1 state. Their model was also extended to explain the formation of oxetene from ring closure of s-cis conformer from deep UV S_1 excitations. A schematic picture of their photochemical model is shown in Figure 5.2. The model has been well-supported by absorption linewidth [307] and cavity ring-down [308] measurements. Therefore, triplet relaxation pathways are considered to be essential to understand S_1 photochemistry of α,β-enones.

The photochemistry arising from excitation to $\pi\pi^*$ S_2 state (193 nm, 6.42 eV for AC) is much more complicated due to opening up of several different photodissociation channels. Initially, Fang [310] carried out a detailed theoretical study on photodissociation pathways of AC by mapping reaction pathways for three primary deactivation channels on singlet and triplet states. More recently, Lee and coworkers [311] have presented a more complete picture of photodissociation channels

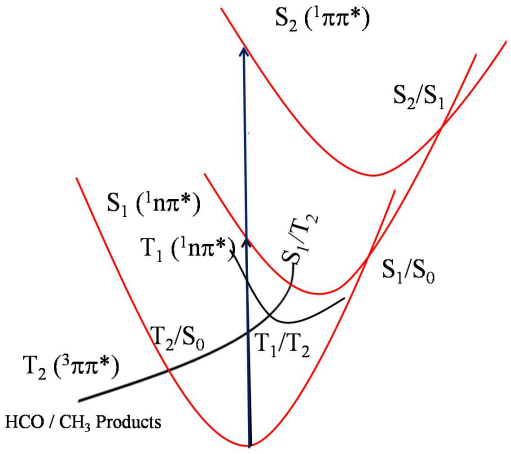

Figure 5.2: A schematic diagram of different ultrafast processes of the α,β-enones. Redrawn with permission based on original figure in Ref. [18].

of AC at 193 nm. They observed a total of 15 photoproducts, identified 9 primary and 2 secondary dissociation channels, and determined branching ratios of all dissociation pathways. It is not clear if any of these dissociations occur from adiabatic reaction pathways on S_2 PES. All dissociations are thought to arise from pathways on ground or first excited state, after ultrafast IC from S_2 into the S_1 vibrational manifold.

Another interesting α-β enone is crotonaldehyde (CR) - a β-methyl substituted acrolein (see Figure 5.1b). It is an ubiquitous pollutant found in atmosphere and interstellar medium [312,313]. UV photolysis of AC and CR in low-temperature Argon matrices have been shown to yield different isomerization products [314], indicating significant differenes in their photochemical behaviour. A most recent work is by Chakraborty and coworkers [315] who reported and rationalized formation of oxetene type of intermediates upon UV photodissociation of CR. A number of computational studies on low-lying exited states of CR have also been reported [316, 317].

In the last two decades, femto-second time-resolved techniques have been increasingly used to study the nature and times-scales of electronic relaxation pathways in small and medium sized molecules. In this context, both cyclic and acyclic α,β-enones have received further attention [17, 318]. Their ultrafast $S_2 \rightarrow S_1$ IC and competitive interplay between IC and ISC processes on S_1 state makes them suited for such studies. They also offer possibilities to introduce substitutions within their framework structure. Stolow and coworkers [18] have used time-resolved photo-electron spectroscopy (TRPES) to study the effect of single methyl substitution at various positions of AC. The resulting molecules - crotonaldehyde (CR), methyl vinyl ketone (MVK) and methacrolein (MA) - show somewhat different S_1 decay times

upon UV excitation to their S_2 state. The estimated decay times were 900-1000 *fs* for AC and MVK, 2000 *fs* for MA and 500 *fs* for CR. The quantum yield of HCO radical, a photoproduct known to arise from triplet α-clevage channel, was found to be very low for the case of CR as compared to the remaing ones.

Based on CASSCF calculations, Stolow and coworkers have proposed a qualitative model to explain the observed differences. It was found that static features of PESs of all substituted molcules were very similar to that of AC. This suggested that dynamical factors due to torsion of Me group around C-C bonds may be responsible. Due to inertial nature of Me group, it has been proposed that the momentum along torsional coordinate plays an important role in deciding the efficacy of sloped S_1/S_0 CI seam. Fast torsional motion of -CH2 as in the case of AC leads to inefficient IC of S_1 state leading to *diabatic passage* where S_1 electronic character is maintained for a period long enough for ISC to take place. In contrast, slower torsional motion of -CHMe group in CR leads to efficient IC resulting in *adiabatic passage* through S_1/S_0 CI seam. This provides an explanation for low quantum yield of triplet channel products [19].

In recent times, the interplay between IC and ISC for a variety of systems has been considered in a number of TRPES experiments as well as *ab-initio* calculations [17, 19, 20, 318–329]. To understand factors affecting the rate of IC between S_1 and S_0, a systematic substitution with methyl group has been used to evaluate whether it promotes or hinders non-adiabatic transitions. The general picture resulting from these studies is that upon excitation to $\pi\pi^*$ S_2 state, the molecule efficiently relaxes to the S_1 state by accessing S_2/S_1 CI seam through high-amplitude twisting and pyramidalization motions. Once it is on S_1 state, the molecule relaxes to the ground state by a non-adiabatic transition through either ISC or IC process. The rate of IC between S_1 and S_0 state depends upon (a) twisting motion of ethylenic moeity (b) velocity of wave-packet passing through the CI. The rate of ISC depends upon magnitude of spin-orbit coupling and existence of singlet-triplet crossings near the region on S_1 where the wave-packet reaches. Existence of any energetic, structural and dynamical barriers prevent quick and efficient access to the S_1/S_0 CI seam resulting in slowing of IC and opening up triplet channels. For example, a recent study of 2-cyclopentaenone (CPO) and its methylated derivatives [318] shows interesting situation where the quantum yields of singlet and triplet channels are 0.65% and 0.35%, respectively.

In summary, femto-second experiments clearly indicate that electronic relaxation of α,β-enones involves a complicated situations where two relaxation processes of different time scales compete with each other. The measured IC time scales vary from

0.5 (CR) to 3.0 *ps* (a methylated derivative of CPO). It is remarkable to note that, in contrast to all α,β-enones, CR exhibits the fastest IC. Although inertial effects of methyl group seem to provide a correct explanation for the observed differences, it is intuitive and qualitative and needs to be further supported by excited state dynamics.

In this chapter, we discuss results from a compartive study of AR and CR carried out using a combination of high-level multi-reference and *ab-initio* non-adiabatic dynamics calculations. Our objective is two-fold. First one is to establish an accurate static picture of various structural intermediates on singlet and triplet states for both these molecules. This verifies many of the features in Robb's photochemical model of AC, and extends it to CR. Second and main objective is to carry out suitable non-adiabatic dynamic simulations which can provide estimates of S_2 and S_1 decay rates, as well as the dynamical inertial effects of Me substitution which are supposed to be operative in CR.

The remaining sections of this chapter are organized as follows. The section 5.3 presents static picture of both molecule at MRCI level. We have confirmed the location and energetics of various minima and MECI structures on relevant singlet and triplet states, and highlight any differences in their geometry and topography between AC and CR. The results from AIMS dynamics simulations on AC and CR are discussed in section 5.4. Finally, section 5.5 provides summary of our results along with a brief discussion on possible future studies.

5.3 *Ab initio* Calculations

5.3.1 Computational Details

We have carried out CASSCF/cc-pVDZ and MRCI/cc-pVDZ calculations using the COLUMBUS package [109, 330, 331]. Active space employed is CAS(5o,6e) - six electrons distributed amongst five valence MOs (4 π-type and 1 n-type MOs for planar/C_s symmetry configurations). This is the smallest active space which can qualitatively describe electronic structures of ground state S_0, 2 lowest singlet S_1, S_2 and triplet T_1, T_2 states. At the equilibrium geometry of S_0, the computed excited states are found to be dominated by single-electron excitations with $n \rightarrow \pi$ and $\pi \rightarrow \pi^*$ character. This active space can be considered to have adequate flexibility to describe multi-reference electronic structures at non-planar and distorted geometries where one or two bonds are partially broken.

For CASSCF calculations, 2-state and 3-state averaging schemes, referred to SA2-CAS(5,6) and SA3-CAS(5,6), have been used. The calculations to locate minimum

structures on S_0, S_1, T_1, T_2 states have been carried without state-averaging, while 3-state averaging has been used for S_2 state. For locating MECI between any two states of same or different spin multiplicity, 2-state averaging of corresponding states has been used, except for MECI of S_2 and S_1 where 3-state averaging has been used. Stationary structures and crossing points have been located at both CASSCF and MRCI levels, except in a few cases where MRCI level optimizatons did not fully converge. Only valence orbitals have been correlated in MRCI calculations.

From previous studies, it is known that minimum structures on S_0, S_1, T_1 states are planar for AC and have a plane of symmetry for CR. This has been used to carry out geometry optimizations in C_s symmetry, whereever possible. The S_1/T_2 and T_1/T_2 MECIs have also been established to be of similar nature (planar for AC and C_s for CR). In our calculations, this has been verified to hold true at MRCI level as well.

5.3.2 Stationary Structures and Relative Energies

The bond-lengths of framework atoms for all sationary structures and their energies relative to the corresponding ground state equilibrium structure are shown in Table 5.1 for both AC and CR molecules. The Cartesian coordinates of all structures have been listed in Appendix A.

While AC ground state is planar, for CR all atoms except methyl group hydrogens lie in a plane. A C_s structure for CR can then be constructed such that one of the methyl hydrogen lies in this plane and other two hydrogen atoms can be placed symmetrically.

As can be seen from the table, the geometrical parameters of planar framework are similar for ground state of AC and CR. The partial double bond character of central C-C bond can be seen by comparing its bond length optimized bond lengths of terminal C-CH_3 bonds. While the latter ones are 1.501 Å which is typical for C-C single bonds, the former bond is shorter by 7%.

The optimized structures $S_1^{\min}$ and $T_1^{\min}$ arising from $n\pi^*$ electronic configuration have been reported in some earlier studies [308,316,332,333]. The fact that framework skeleton of these structures are planar for both AC and CR has been verified at MRCI level. Major changes relative to ground state are 1.significantly elongated C=O bond (by almost 0.15 Å) 2. shortened central C-C bond (by almost 0.1 Å) 3.relatively elongated terminal C-C bond (by 0.06 Å). For each molecule, the geometries of their singlet and triplet structures are very similar. This similarity also extends to their energies with triplet stable by less than 0.2 eV at MRCI level. As discussed by Robb

and coworkers, this similarity is one of the key reason for ISC to become an important deactivation mechanism in α,β-enones. Our results are also in general agreement with previously reported structures of $^{1,3}n\pi^*$ states [332, 333].

In contrast, the framework geometry of minimum $T_2^{\min}$ arising from $\pi\pi^*$ configuration is non-planar. The terminal group, CH_2 for AC and CHMe for CR, is skewed by almost 90° keeping the rest of atoms almost constrained to the original plane. The T_2 state is confirmed to dominated by $\pi \rightarrow \pi^*$ excitation localized on the vinyl groups (-CH=CH_2 or -CH=CHMe). As a result, a significantly stretched C=C bond is observed in $T_{2_{min}}$. When compared to $S_0^{\min}$ structure, both CASSCF and MRCI predict elongated C=C bond (0.126 Å and 0.118 Å for AC and 0.130 Å and 0.121 Å for CR). However, C=O and C-C bond lengths remain almost unchanged.

It is interesting to note that energy of $T_2^{\min}$ is lower as compared to that of $T_1^{\min}$. This is reverse of the usual situation of $E(T_2) > E(T_1)$ found for most molecules at FC geometry. This has also been observed in previous studies. Further, it is lowest energy minimum structure amogst all stationary structures. This, in combination with its similarity with ground state (except for C=C bond length), makes it an important structure to be considered for ISC (see later).

We have also found a local minimum on S_2 state for both molecules. Such a minimum has been reported for AC at CASSCF level by Godunov and coworkers [334]. The main geometric features of $S_2^{\min}$ are that its C=O and C=C bonds are considerably elongated and the terminal CH_2/CHMe group is twisted by nearly 50°. Apart from this twisting, the remaining atoms lie in a plane.

The energies of these structures shown in table are in general agreement with previous theoretical and experimental estimates. At the FC geometry, the S_1 excitation energy for AC is 3.81 eV which agrees well with experimental value of 3.70 eV (335 nm) [311]. However, computed S_2 FC excitation energies are overestimated by several tenths of eV, even at the MRCI level (7.09 eV for AC as compared to 6.41 eV or 193 nm from experiments). Such an overestimation is also seen to be present in other computational studies [335]. It has attributed to mixing with a Rydberg state lying approx 1 eV higher [336].

5.3.3 Conical Intersections

In table 5.2, important geometrical parameters of all MECI structures and their energies relative to corresponding ground states are presented. The Cartesian coordinates are listed in Appendix A.

As discussed, S_2/S_1 MECI plays an important role in ultrafast IC process from

Table 5.1: Otimized geometrical parameters (bond lengths in Å) of AC (above) and CR (below) and their relative energies (in eV) at CASSCF and MRCI levels.

	$R_{C=O}$		R_{C-C}		$R_{C=C}$		ΔE (in eV)	
States	CAS	MRCI	CAS	MRCI	CAS	MRCI	CAS	MRCI
$S_0^{\min}$	1.205	1.214	1.477	1.481	1.344	1.349	0.0	0.0
S_1^{FC}	-	-	-	-	-	-	3.74	3.81
S_2^{FC}	-	-	-	-	-	-	7.07	7.09
$S_1^{\min}$	1.350	1.345	1.375	1.384	1.403	1.404	3.19	3.34
$S_2^{\min}$	1.376	1.385	1.430	1.416	1.470	1.466	6.15	6.26
T_1^{FC}	-	-	-	-	-	-	3.48	3.54
T_2^{FC}	-	-	-	-	-	-	3.79	3.91
$T_1^{\min}$	1.340	1.335	1.387	1.397	1.390	1.391	3.05	3.15
$T_2^{\min}$	1.218	1.230	1.445	1.447	1.470	1.467	2.61	2.88
$S_0^{\min}$	1.205	1.214	1.475	1.476	1.345	1.350	0.0	0.0
S_1^{FC}	-						3.78	3.88
S_2^{FC}	-	-	-	-	-	-	7.14	7.67
$S_1^{\min}$	1.353	1.347	1.377	1.384	1.403	1.404	3.25	3.36
$S_2^{\min}$	1.375	-	1.435	-	1.475	-	6.20	-
T_1^{FC}	-						3.55	3.61
T_2^{FC}	-						3.85	3.94
$T_1^{\min}$	1.343	1.337	1.390	1.397	1.390	1.390	3.11	3.18
$T_2^{\min}$	1.219	1.229	1.445	1.445	1.475	1.471	2.65	2.76

S_2 to S_1 state. The $S_1^{\min}$ state lies almost 3.75 eV (4.31 eV) below energy of S_2 state at FC geometry for AC (CR) molecule. The amount of electronic energy dissipated into vibrational modes is substantial and this is the reason for a variety of photo-dissociation pathways reported in literature.

The S_2/S_1 MECI is highly twisted along both C-C bonds - both terminal -CHO and -CH2/CHMe groups are twisted along corresponding backbone C-C bond. Further, in contrast to $S_2^{\min}$ structure, -CHO group is significantly pyramidalized and -CH2/CHMe group, to a lesser extent, is also pyramidalized. Between these structures, the bond distances of framework atoms are somewhat similar. Interestingly, these structures are also energetically close to each other (energy gap max 0.05 eV). This may have consequences for IC dynamics of S_2 state (see later).

Previous studies have emphasised the role S_1/S_0 MECI plays in α,β-enones [18, 301]. This structure involves almost 90 ° twisting of terminal -CH2/CHMe group

around C=C bond, with a small degree of pyramidalization around the terminal carbon. The remaining part of the molecule remains planar as before.

In our calculations, this MECI for AC and CR is located approximately 1.08 eV (25 kcal/mol) above their respective $S_1^{\min}$ at MRCI level. This value is consistent with previous reported CASSCF value of Martinez and coworkers [18]. This result suggests a possibility that even a higher barrier may be involved to reach this MECI from $S_1^{\min}$. However, we did not manage to obtain a transition state that would connect them. Instead, a transition state corresponding to *cis-trans* isomerization on the S_1 state was found. This barrier is found to be 0.58 eV (13.5 kcal/mol) for AC and 0.56 eV (13.0 kcal/mol) for CR, indicating similar torsional barriers of these two molecules on the S_1 state. Our calculations suggest that S_1/S_0 MECI is perhaps located a steep PES upward slope starting from $S_1^{\min}$, consistent with sloped topography of its branching space.

An objective of our study is also to verify structural and energetic aspects of Robb's photochemical model for AC [301] using accurate multi-reference methods, and to extend its applicability to CR. For this, we have located MECI structures on S_1/T_2, T_1/T_2 and T_2/S_0 seams. In agreement with Robb's work, we find that both S_1/T_2 and T_1/T_2 MRCIs are infact planar, and their geometrical parameters being similar for both AC and CR. Both of them can be easily reached by in-plane deformations from $S_1^{\min}$. For example, for S_1/T_2, the deformations of C=O, C-C and C=C bonds are 0.021, 0.006, and 0.043 Å, respectively. These MECIs are also energetically located within a maximum of 0.07 eV above $S_1^{\min}$ at MRCI level.

Although our CASSCF results are in agreement Robb's energetics, MRCI results indicate that all the three states S_1, T_2, T_1 are energetically even more closer in the vicinity of $S_1^{\min}$. This suggests the possibility of a 3-state degeneracy of these states existing in this region. Although we have not managed to locate such a 3-state CI point, its existence can also explain facile ISC in these systems. It can be noted that such 3-state CIs have been already reported in aromatic carbonyl compounds [337–339]. These studies have proposed that such intersections enable direct S_1 to T_1 transition despite its low efficienty as per El-Sayed's rules. A very recent generalized trajectory surface hoping study on AC by Thiel and coworkers [340] highlighted the importance of S_1, T_1, T_2 near-degeneracy region in populating lowest triplet state by sequential hopping. They also established direct S_1 to T_1 as a major hopping event for ISC in AC.

It is important to note that CASSCF and MRCI geometries for various structures are in good agreement. Although MRCI energetics differ from CASSCF ones, the differences are not large enough to invalidate CASSCF results. This indicates that

active space used is adequate for qualitative description. Therefore, for these systems, CASSCF calculations do provide at least qualitatively correct picture of PESs for the states considered. This observation provides some justification for using CASSCF wave-functions for further dynamics calculations.

Table 5.2: Optimized geometrical parameters (bond lengths in Å) of intersection structures of AC (above) and CR (below) and their relative energies (in eV) at CASSCF and MRCI levels.

	$R_{C=O}$		R_{C-C}		$R_{C=C}$		ΔE (in eV)	
Intersections	CAS	MRCI	CAS	MRCI	CAS	MRCI	CAS	MRCI
S_1/S_0	1.383	1.361	1.303	1.311	1.487	1.486	4.25	4.29
S_2/S_1	1.347	-	1.472	-	1.474	-	6.20	-
S_1/T_2	1.334	1.324	1.364	1.378	1.451	1.447	3.30	3.41
T_1/T_2	1.309	1.295	1.369	1.387	1.474	1.475	3.28	3.35
T_2/S_0	1.219	1.230	1.443	1.445	1.446	1.466	2.95	2.77
S_1/S_0	1.384	1.363	1.303	1.310	1.492	1.489	4.28	4.29
S_2/S_1	1.347	-	1.472	-	1.477	-	6.19	-
S_1/T_2	1.338	1.329	1.365	1.377	1.450	1.444	3.36	3.42
T_1/T_2	1.312	1.299	1.369	1.385	1.474	1.471	3.33	3.37
T_2/S_0	1.218	-	1.445	-	1.466	-	2.94	-

5.3.4 Topographical Features of MECI

It is generally accepted that geometry of CI seam and topography of crossing PESs in branching space influence the efficiency of non-adiabatic transitions. Several studies have attempted to relate topography at PESs at MECI to understand electronic relaxations [87, 95, 99, 341]. As discussed in section 1.3 of Chapter 1, four parameters characterize the PES topographies around a CI point - cone tilts s_x, s_y, cone pitch Δ_{gh} and cone asymmetry d_{gh}. Here, we have computed topography parameters of AC and CR for S_2/S_1 at CASSCF level (MRCI had convergence issues) and S_1/S_0 MECIs at CASSCF and MRCI levels. The results are listed in tables 5.3 and 5.4. It can be noticed that both intersections are tilted ($s_x \neq 0, s_y \neq 0$ and asymmetric $\Delta_{gh} \neq 0$). The PESs in branching space have been plotted in Figures 5.3 and 5.4.

From Table 5.3 and Figure 5.3, it can be seen that S_2/S_1 MECI of both AC and CR is a peaked one. As is known, this supports efficient decay when trajectories arrive at the CI seam from regions of higher electronic energy. This is in agreement with $S_2 \rightarrow S_1$ IC being ultrafast. Although both MECIs are titled in a similar way,

AC funnel is more asymmetric and less steeper than CR. However, the differences are smaller than other cases and hence may not lead to significant differences in dynamics. Further, MECI geometry is not the most likely geometry where the transition takes place.

Table 5.3: Topographical parameters for S_2/S_1 MECI of AC and CR at CASSCF level.

Parameters	AC	CR
s_x	0.019	0.014
s_y	0.024	0.034
d_{gh}	0.031	0.058
Δ_{gh}	1.000	0.305

AC

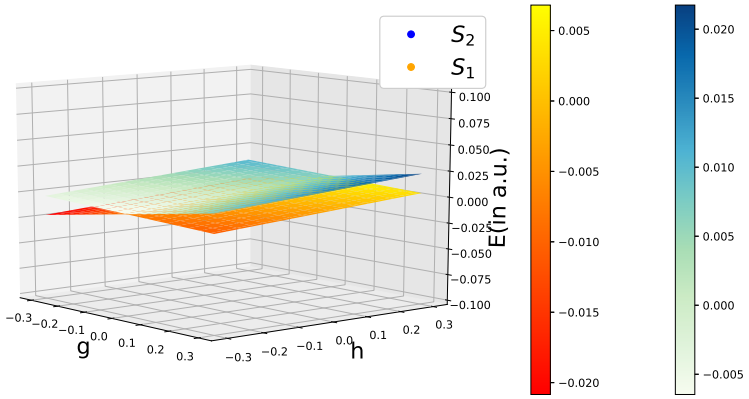

CR

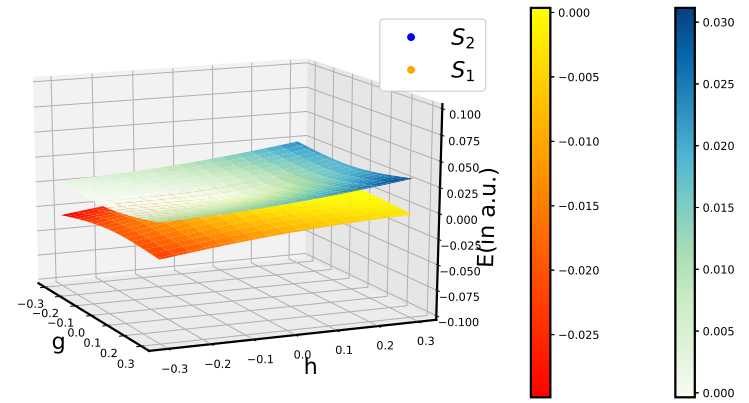

Figure 5.3: Adiabatic PESs around S_2/S_1 MECI for AC and CR.

Table 5.4: Topographical parameters for S_0/S_1 MECI of AC and CR at CASSCF and MRCI levels.

Parameters	AC			CR		
	CAS	MRCI	Previous[a]	CAS	MRCI	Previous
s_x	0.175	0.173	0.083	0.174	0.173	0.083
s_y	0.126	0.169	0.000	0.018	0.086	0.000
d_{gh}	0.046	0.061	0.021	0.046	0.060	0.021
Δ_{gh}	0.938	0.460	0.952	0.968	0.960	0.953

a: Previous topographical parameters [18] are computed at SA3-CAS(5,6) level of theory.

AC

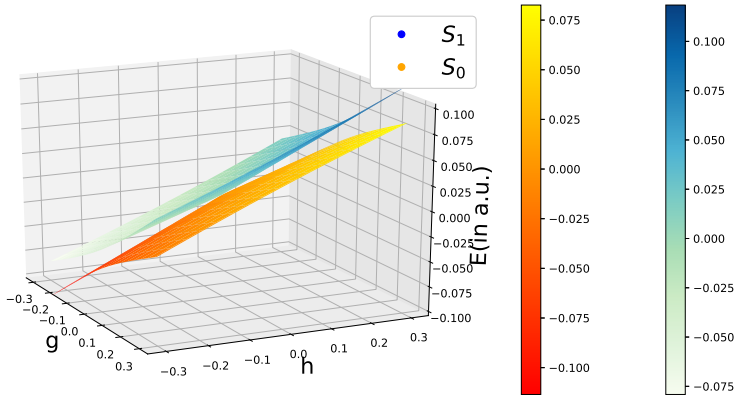

CR

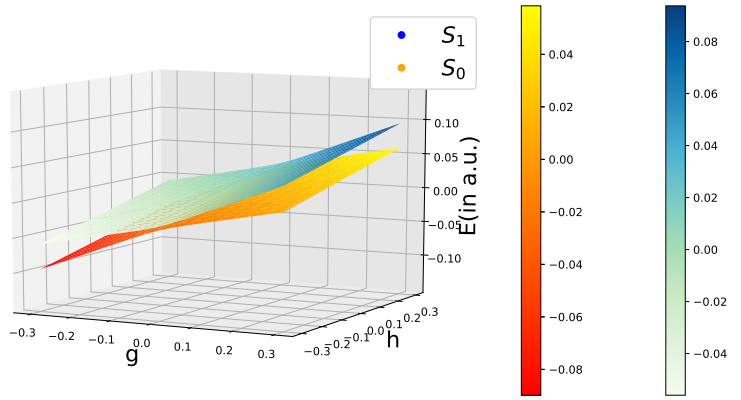

Figure 5.4: Adiabatic PESs around S_1/S_0 MECI for AC and CR.

In their previous work [18], Martinez and coworkers computed **g** and **h** vectors and topographical parameters of S_1/S_0 MECI for AC and Me substituents attempting to

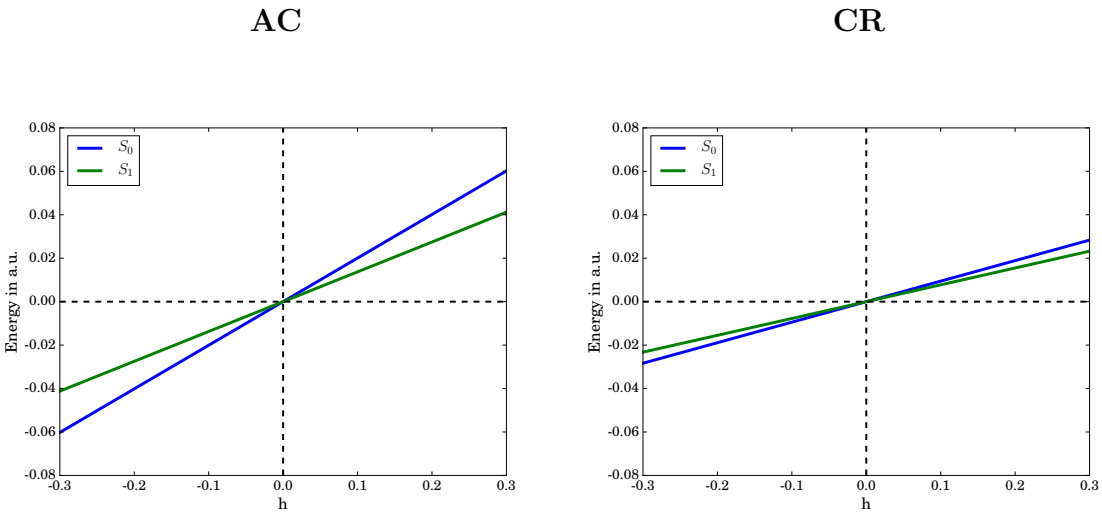

Figure 5.5: Projection of adiabatic PESs around S_1/S_0 MECI along h vector.

relate them to differences in experimental S_1 decay times. However, it was found that MECIs were almost similar in their topographical parameters and could not be used for this purpose. The **g** vector was shown to correspond to bond-alteration coordinate of the skeleton framework. The **h** vector corresponded to pyramidalization of central carbon. Again, they were found to be qualitatively similar for both molecules. It was proposed that motion of central carbon along **h** vector would be slowed by substituents attached to it and linked it to slower relaxation of MA. However, faster relaxation in CR required separate proposal as discussed in previous section.

In our calculations, in contrast to their result, a different topography of S_1/S_0 MECI was found for AC and CR. As can be seen in Table 5.4, although MECIs have similar asymmetry and pitch of cones, thier tilts are different. While the tilt along **g** vector is twice the previous reported value, along **h** vector is different for both molecules as well as previous result indicating no tilt. The MRCI tilt along **h** vector for AC is almost twice that of CR. This difference is reflected in Figure 5.4. While both MECIs are sloped (as in previous study), the AC is more sloped than CR along **h** direction. This is clearly seen in 2-dimensional PES plot shown in Figure 5.5.

We found the **g** and **h** vectors to correspond same type of motions as in the previous study, although in our case **h** vector also has pyramidalization of both central and -CHO carbon. If, as expected for sloped nature MECIs, a trajectory approaches MECI region from S_1^{min} along the gradient difference vector **g** direction, its behaviour is expected to be similar for both AC and CR. However, if the approach is along coupling vector **h** direction, then CR trajectory faces nearly degenerate PESs in a wider region of geometries near the seam as compared to AC. When this is combined with slow motion in CR along torsion seam coordinate as in previous study, it indicates

that CR is likely to survive for a longer time in a wider region nearly degenerate geometries. This may have indirect effect on S_1 relaxation differences between AC and CR.

From the above discussions, both molecules clearly exhibit qualitatively similar features of PESs. While there are some differences, the differences are still not large enough and it remains to be seen if dynamics calculations can be affected by them. We have found S_1, T_1, T_2 to be closer in energy around their minima and this provides additional support for the efficiency of triplet pathways. However, dynamical correlation does not seem to have significantly effect on the optimized structures, energetics and barriers.

5.4 Non-adiabatic Dynamics

In this section, we discuss the results of our nuclear dynamics calculations of AC and CR. The goal is to identify any differences in dynamics which can be related to their electronic relaxation behaviors.

5.4.1 Computational Details

We have performed calculations using AIMS method as implemented in FMS-MOLPRO program [342]. A brief description of AIMS has been given in section 4.6 of Chapter 4 . Here, we provide computational details of our simulations.

For both the molecules, dynamics was started with initial TBFs placed on the lowest bright state S_2 state and carried out for 500 *fs*. This time limit was chosen as we expected the S_2 to S_1 relaxation to be fast (less than 100 *fs*) and any differences in S_1 relaxation behaviour may be discernable within remaining 400 *fs*. The electronic wave functions were calculated at SA3-CAS(5,6)/6-31G* level. The basis choice of 6-31G* instead of cc-pVDZ used for static calculations was due to limitations of program capabilities.

In contrast to static calculations discussed in the previous section, the dynamics simulation includes only three singlet states, S_0, S_1 and S_2. The two triplet states which play an important role in S_1 photochemistry could not included due to limitations of current implementation of AIMS method to handle ISC dynamics. Further, the interpertation of TRPES experiments as discussed in Refs. [17, 18] is based on identification of S_1 relaxation differences in AC and CR due to S_1/S_0 IC. This is partially supported by experimental observations of low quantum yields of triplet channel products, especially for CR. In the present work, inclusion of triplet

states is not necessary as the goal here is mainly to understand the differences in singlet channels of AC and CR. However, triplet channel is important for AC as discussed in recent works and must be included in future computational studies.

The initial state of both AC and CR was represented in terms of 79 TBFs whose initial position and momentum were generated by a random sampling from the Wigner distribution of harmonic vibrations of the ground electronic state. To obtain the Wigner distribution, ground state and frequency calculation were done at MP2/6-31G* method. Each initial TBFs were propagated with AIMS algorithm. To integrate equations of motion, velocity-Verlet algorithm for TBFs and adaptive second-order Runga-Kutta method for complex coefficients is used as described in [289]. A time step of 20 au (0.5 *fs*) was used in the non-coupling region. The time step was adjusted to even smaller values (0.125 *fs*) if necessary (when TBFs enter coupling regions) so as to ensure conservation of classical energy and to ensure that TBFs will not jump over the CI region without spawning new TBFs. At the end of simulations, spawning events generated 631 and 571 additional TBFs for AC and CR respectively.

5.4.2 Results and Discussion

First, we consider the evolution of important geometrical parameters averaged over trajectories as shown in Figure 5.6. Upon photo-excitation to S_2 state, nuclear motions involving bond elongation, large amplitude pyramidalization and twisting move the system from FC region towards S_1 state by accessing the S_2/S_1 CI seam. Within the first 50 *fs*, both C=O and C=C bonds stretch by nearly 20% (plots **a** and **b** in Figure 5.6). Quick pyramidalization of -CHO and terminal -CH2/CHMe groups is also observed (plots **e** and **f**), along with twisting around C=C and C-C bonds (plots **c** and **d**). These confirm that initial motion is towards S_2/S_1 CI region whose MECI is also characterized by the above geometrical changes.

These plots also indicate that both AC and CR exhibit similar geometrical variations. One prominent difference is that CR motion along the torsion coordinate $\phi_{C=C}$ is slower throughout the dynamics. This is certainly in agreement with the inertial effect of methyl group as proposed by Stolow and coworkers [18]. In the context of the two-state and two-modes photo-relaxation picture (discussed in section 4.3), it can be said that after initial bond elongations, excess energy transferred into twisting and pyramidalization modes. Once these modes are activated, the molecule remains distorted until it reaches S_2/S_1 seam region.

The time evolution of average electronic state populations of AC and CR are shown in Figure 5.7 and Figure 5.8, respectively. Clearly, both the AC and CR

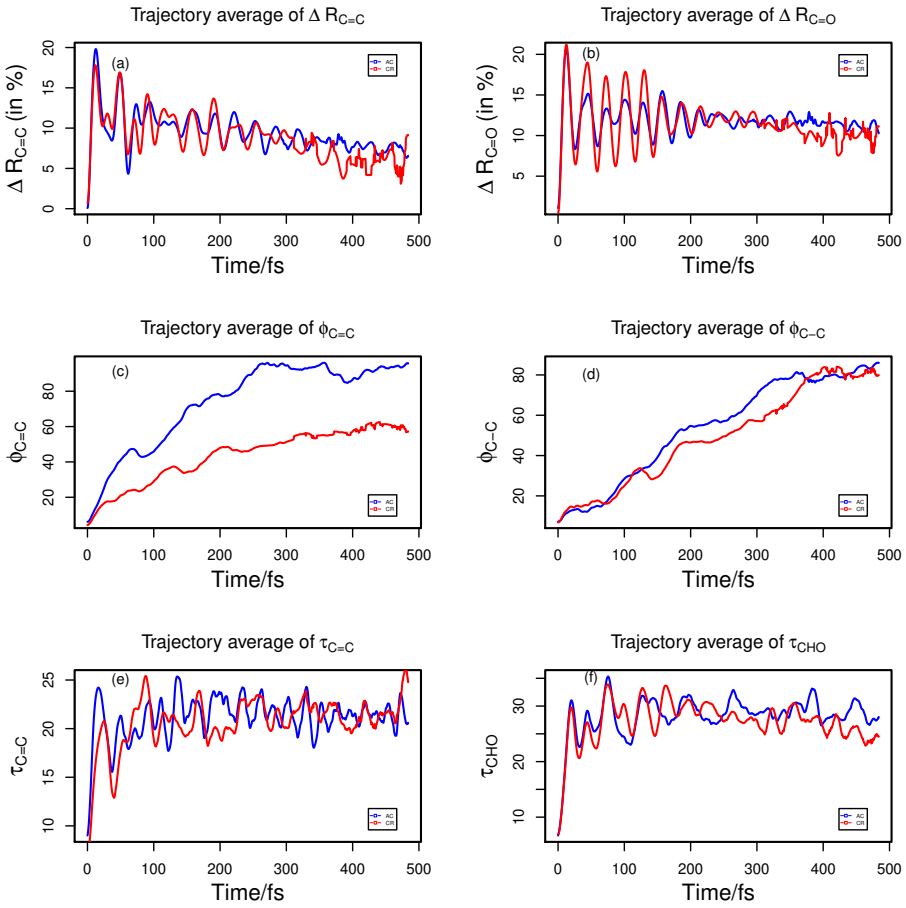

Figure 5.6: The trajectory average of key geometrical parameters of AC (**in blue**) and CR (**in red**). **a** and **b** are relative changes in $R_{C=O}$ and $R_{C=C}$ bond lengths. **c** and **d** are torsion coordinate (ϕ) of C=C and C-C bonds. **e** and **f** are pyramidalization(τ) of ethylenic (C=C) and aldehyde (CHO) groups

show ultrafast deactivation from S_2 state to the S_1 state. The population of S_2 stays unchanged for a short time after the start of propagation. This time can be associated with a residence time or latency time (τ_0) of initial wave-packet during which it stays on S_2 PES. Non-adiabatic transition to S_1 state can be considered to begin after this residence time.

Although deactivation can be described by an exponential decay function, the population change requires a non-exponential description to account for the residence period. Therefore, we fit the S_2 population decay data to the following function [343]:

$$S_2(t) = H(t-\tau_0)exp(-\frac{t-\tau_0}{\tau_{12}}) + H(\tau_0 - t) \tag{5.1}$$

$H\ (t-\tau_0)$ is Heaviside step function, where τ_0 is the latency time and τ_{12} is half life

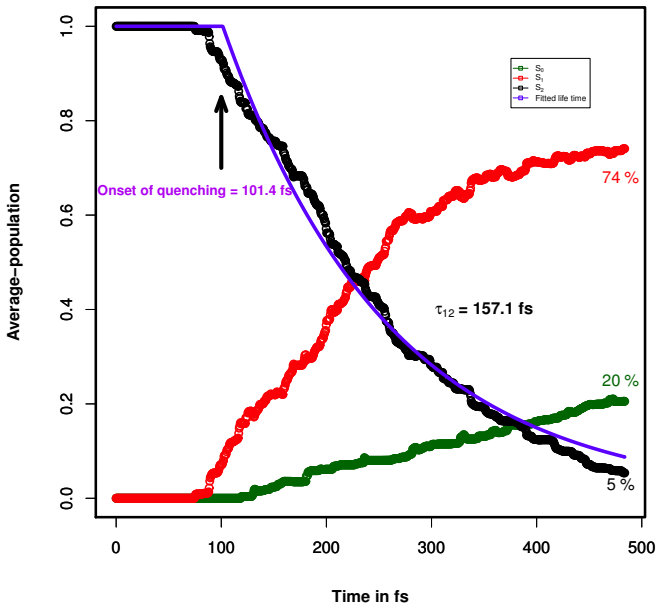

Figure 5.7: Population dynamics after photoexcitation of AC to S_2 state. Time evolution of average electronic population of the S_0, S_1 and S_2 state (shown in **green color**, **red color** and **black color**). The plot of fitted S_2 population is shown in **blue** color. The latency time and the fitted lifetime are predicted to be 101.4 *fs* and 157.1 *fs*, respectively.

time. The description of the model function is as follows.

$$\begin{cases} H(t-\tau_0) = 0 & t-\tau_0 < 0 \\ H(t-\tau_0) = 1 & t-\tau_0 > 0 \\ H(t-\tau_0) = \dfrac{1}{2} & t-\tau_0 = 0 \end{cases}$$

Upon fitting, the onset of quenching (τ_0) is found to be 101.4 *fs* for AC and 112.5 *fs* for CR. The latency time can be considered as the time required for redistributing the potential energy of the excited state to the selective vibrational modes which are essential for accessing the non-adiabatic region. From this point of view, the wave-packet on S_2 oscillates during this period. In this case, the S_2 dynamics during the latency period can be linked to nature of its PES. In previous section, we have pointed out that $S_2^{\min}$ and S_2/S_1 MECI are structurally similar and energetically close to each other. The presence of a minimum in the vicinity of the MECI suggests delayed electronic quenching. As a result, we expect that after leaving FC region the wave-packet performs back and forth motion in the region around the $S_2^{\min}$ structure.

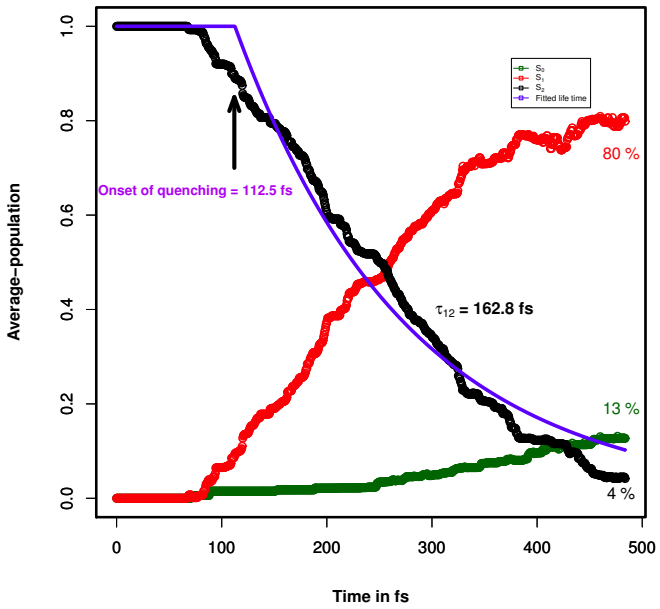

Figure 5.8: Population dynamics after photoexcitation of CR to S_2 state. Time evolution of average electronic population of the S_0, S_1 and S_2 state (shown in **green color**, **red color** and **black color**). The plot of fitted S_2 population is shown in **blue**. The latency time and the fitted lifetime are predicted to be 112.5 *fs* and 162.8 *fs*, respectively.

In previous studies, much shorter residence times (less than 50 *fs*) have been found in many conjugated systems [343, 344]. Therefore, longer residence times found here can be attributed to the presence of $S_2^{\min}$.

In the experimental work [18] on AC and CR reports two time-constants. One is a faster component t_1 of 45-110*fs* for AC and 50-90 *fs* for CR. The slower component t_2 is 900 *fs* for AC and 360-560 *fs* for CR. Although our residence time τ_0 agrees with experimental time constant t_1, it would not be correct to relate them. We think that is better to compare t_1 to total S_2 life time τ. From the fitting results, the actual S_2 population decay time τ_{12} is found to be 157.5 *fs* for AC and 162.8 *fs* for CR. The total lifetime can be estimated by adding residence time, i.e., $\tau = \tau_0 + \tau_{12}$. Therefore, we find total S_2 life time of AC and CR to be, respectively, $\tau_{\text{AC}} = 258.9$ *fs* and $\tau_{\text{CR}} = 275.3$ *fs*. Although our life-time estimates for AC and CR are similar, the values differ substantially from experimental values for t_1. It is known that life-times estimated from AIMS population overestimate the experimental results [246, 275, 345]. Overall, our present result of S_2 dynamics is in line with experiments, and life-time estimates reported here can be taken to be upperbound to experimental values.

It can be noticed that torsion angle around C=C bond is substantially different

between AC and CR already during the latency period, although it does not seem to influence the S_2 decay time.

Now we attempt to understand S_1 population decay behaviour, try to correlate it to experimental t_2 time constants. It can be noticed from the population plots that, by the end of simulation (500 *fs*), almost all of S_2 population has decayed for both molecules. However, S_1 populations do not still exhibit expected decay at the end of simulation, being 74% for AC and 80% CR. The build up of S_0 populations is slow, about 20% for AC and 13% for CR. Since substantial population stays on S_1 even after 500 *fs*, therefore our simulations indicate that both molecules stay on the S_1 surface and smaller number of trajectories reach the ground electronic state. Therefore, it can be expected that S_1 decay times for both molecules are longer than simulation time.

Since S_0 population of AC is larger than CR, our simulations indicate that $S_1 \rightarrow S_0$ transition in CR must be slower as compared to AC. This is exactly opposite of what is observed in TRPES experiment. We have also carried out fitting of all three populations curves to a sequential first-order kinetics model to estimate S_1 rate constants [346]. This indicates that S_1 decay times are approximately, 3.0 *ps* for CR and 1.2 *ps* for AC. Although AC results qualitatively agree with experimental t_2 estimates, our estimate for CR is substantially off. Therefore, our simulations are not able to account for experimental finding that CR shows much faster electronic relaxation as compared to AC.

Now, we analyze all non-adiabatic events which took place during the simulation. A summary of all spawning events at different CIs are tabulated in Table 5.5. Once again, it is clear that number of $S_1 \rightarrow S_0$ non-adiabatic transition are smaller as compared to $S_2 \rightarrow S_1$. Only in 30% (AC) and 26% (CR) of events, a child basis is spawned on S_0 surface. Further, both AC and CR show similar number of such spawning events at each crossing. Interestingly, AC shows somewhat larger number spawns indicating $S_1 \rightarrow S_2$ recrossing.

Table 5.5: Summary of all spawning events for AC and CR.

Molecule	Total no. of spawning event	S_2/S_1	S_1/S_0	S_1/S_2	S_0/S_1
AC	631	378	184	69	-
CR	571	377	152	25	17

In an earlier study [18], it was clearly established that bond-alteration of the single and double bonds is an important feature of the S_1 surface. A bond alternation coordinate can be defined as the sum of the terminal carbon-oxygen and terminal carbon-carbon bond lengths minus the central carbon-carbon bond length *i.e.,* R_{ba}

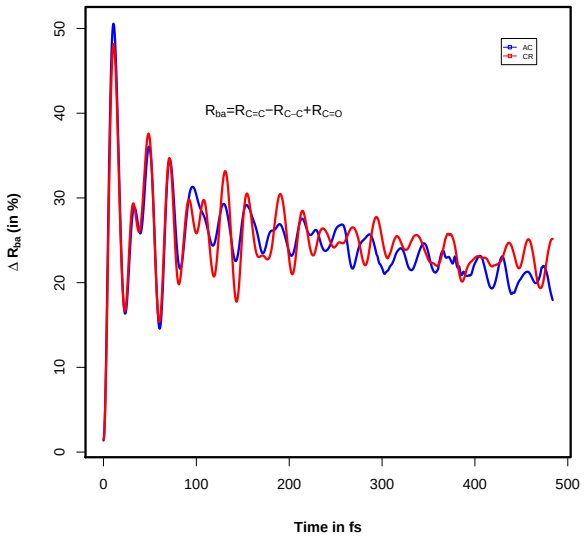

Figure 5.9: Trajectory average of relative change in bond-alteration coordinate of AC (in **blue color**) and CR (in **red color**).

= $R_{C=C}$ + $R_{C=O}$ - R_{C-C}. Figure 5.9 shows trajectory average of relative change in the bond-alteration coordinate from the ground electronic state. Within first 20 *fs*, the R_{ba} coordinate changes up to 50%, and immediately thereafter it exhibits an oscillatory feature and reaches 20% at the end of simulation. In both molecules, bond alternation coordinate not vanished at the end of simulation clearly indicating that trajectories are localized around $S_1^{\min}$ up to 500 *fs*.

Overall, our simulations indicate that AC and CR have similar relaxation behaviour. Although inertial differences between these molecules visible, they do not seem to have influence on non-adiabatic transitions at both CI seams involved.

Spawning is one of the most important ingredients of AIMS dynamics. Previous studies have established that spawning does not happen at MECI geometry, but at widely different geometries around the seam region [260]. Therefore, the collection of all spawning geometries characterizes the seam region accessed by the molecule. Further, spawning geometries are not necessarily geometries on the CI seam. From a dynamics perspective, the spawning picture is inline with the fact that non-adiabatic transitions occur in vicinity of CI seams. The spawning geometries are characterized by small electronic energy gaps ($\triangle E_{gap}$), and strongly affect the rate of population transfer.

Figure 5.10 and Figure 5.11 show dependence of average rate of population transfer on energy gap $\triangle E_{gap}$ for $S_2 \rightarrow S_1$ and the $S_1 \rightarrow S_0$ transitions. In these histograms,

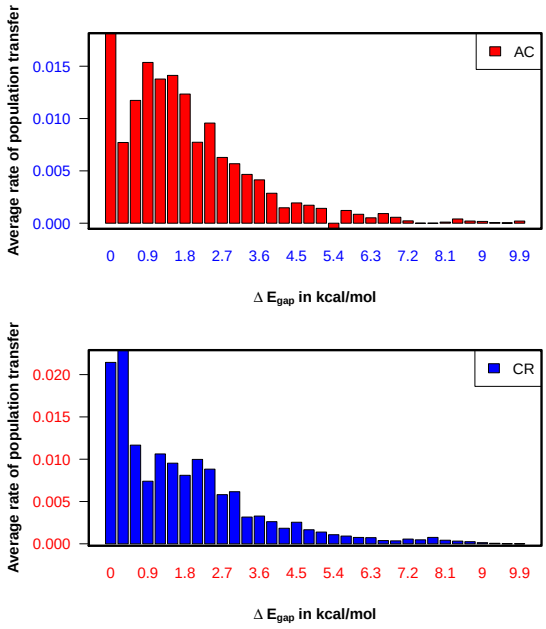

Figure 5.10: The average rate of the population transfer from S_2 to S_1 state as a function of the $\triangle E_{gap}$ for AC (in **red**) and CR (in **blue**).

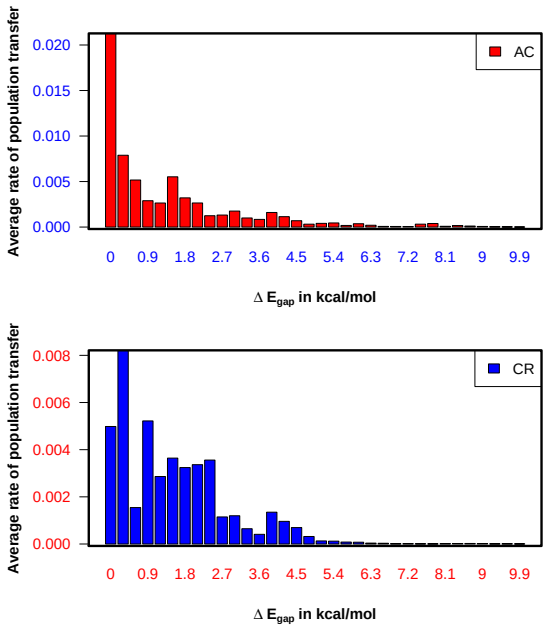

Figure 5.11: The average rate of the population transfer from S_1 to S_0 state as a function of the $\triangle E_{gap}$ for AC (in **red**.) and CR (in **blue**).

rates of population transfer estimated for different trajectories have been binned into bins with a width of $\triangle E_{gap}$=0.3 kcal/mol. For both CIs, the distributions depict an approximate Gaussian profile with a large width (0-3 kcal/mol) and reach maximum

at $\triangle E_{gap} = 0.3$ kcal/mol. It is clearly seen that transitions take place with smaller possibility when $\triangle E_{gap} > 5.0$ kcal/mol. This is consistent with a well-known fact that non-adiabatic transitions do occur at smaller energy gap of electronic states.

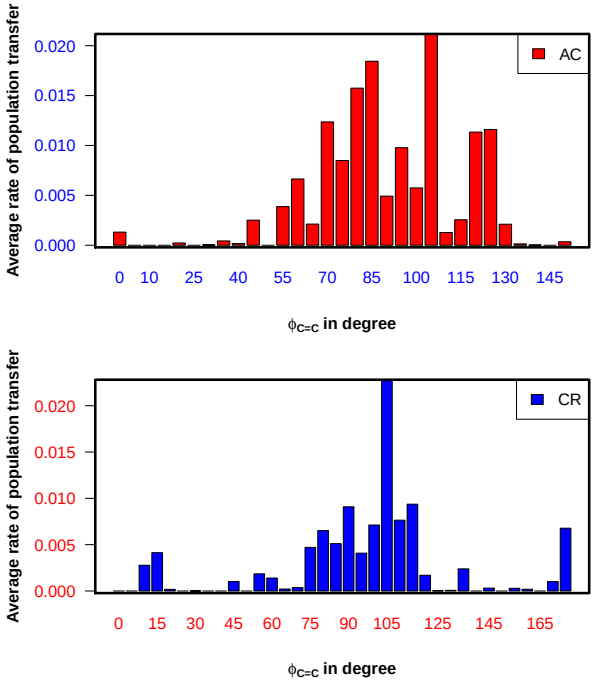

Figure 5.12: The average rate of population transfer from S_1 to S_0 as a function of torsion angle of C=C for AC (in **red**) and CR (in **blue**).

In addition, we have also examined several S_1/S_0 spawning geometries of both AC and CR. Most of these structures are found to be dominantly twisted and pyramidalized around ethylenic center. As emphasized earlier, twisting and pyramidalization coordinates are proposed to be important for S_1/S_0 transition. Therefore, it would be interesting to see the effect of torsion coordinate on rate of S_1/S_0 population transfer. A histogram plot of torsion angle (ϕ) of ethylenic group and rate of population transfer has been presented in Figure 5.12. Clearly, in both cases, rate of transfer becomes significant after torsion angle becomes larger than 70°. Further, AC shows large variations in torsion angles whereas CR shows a limited range.

5.5 Summary

The ultrafast nature of electronic relaxations in α,β-enones upon $\pi \rightarrow \pi^*$ transition to their S_2 state has received attention in recent years. In this chapter, we have

performed multi-reference *ab initio* computations and direct dynamics simulations to understand the origin of differences in decay times between two closely related α,β-enones - AC and CR molecules. To this end, we have attempted to verify the validity of important features, for both AC and CR molecules, of a α,β-enone photochemical model which has been extensively used in the literature. Dynamics studies are aimed to confirm the dynamical factors that have been invoked in qualitative explanations of these differences observed in recent femto-second photo-electron spectrocopy experiments.

Our CASSCF and MRCI geometry optimizations confirm structure and energetic ordering of important intermediates of singlet and triplet states appearing in α,β-enone photochemical model. Previously reported planar nature of local minima on S_1, T_1, S_0 states are established for both AC and CR. The MECIs on seam of S_1/T_2, T_1/T_2 are also confirmed to be planar.

Our high-level static calculations clearly indicate that both molecules have similar structure and energetic ordering of all intermediates and MECIs reported in previous studies. Some differences between AC and CR are found for topographical parameters of S_1/S_0 MECI, but they are not large enough. Therefore, we infer that the static pictures for both molecules must be essentially similar and that relaxation differences indeed appear to be dynamical in origin as previous works have suggested.

The dynamics studies using AIMS method have clearly supported the view that $S_2 \rightarrow S_1$ IC process is ultrafast and occurs by passing through S_2/S_1 CI seam on a time scale of 250 *fs* for both molecules. These results are in qualitative agreement with time constants from TRPES experiments. The delay in relaxation due to residence time on S_2 can be attributed to presence of a local minimum on S_2 in the vicinity of S_2/S_1 MECI and to the sloped nature of MECI. The initial motions are dominated by elongation along bond-alternation coordinate, pyramidalization of CHO group, and torsional motion of terminal CH_2/CHMe groups around C=C bond. Therefore, dynamics calculations support mechanistic picture of $S_2 \rightarrow S_1$ relaxation indicated by static calculations.

Our dynamics calculations are not able to explain S_1 decay differences. The inertial effect of Me group is visible in these simulations. CR seems to show more restricted range of torsional coodinates where decay rates are significant. However, simulation time considered in this study is not long enough, as S_1 populations did not show decaying pattern for both molecules. Therefore, it is difficult to reliably estimate S_1 decay times from these simulations. In clear disagreement with experiments, our calculations seem to suggest AC to show faster relaxation as compared to CR. We suggest that further dynamics calculations with a simulation time of upto a picosecond

and employing MS-CASPT2 methods may be able to reascertain our results and may form a basis for revisiting the experimental assignments given in Ref. [18]. Inclusion of two lowest triplet states in these simulations will also be helpful in clarifying the role of ISC in S_2 dynamics of α,β-enones.

Chapter 6

Electronic Relaxation in Photoelectrocyclic Reactions Involving Heteroatoms: Case Study of Formaldonitrone

6.1 Introduction

Pericyclic reactions are a fascinating class of widely-used and well-understood reactions in organic chemistry [347, 348]. Their concerted and cyclic nature makes it possible to connect reactant and product structures through continuous reaction pathways along which a few bonds are broken and formed simultaneosuly [349]. As shown by Woodward and Hoffmann [350], existence of a conserved symmetry element along a pathway allows construction of orbital correlation diagrams indicating how frontier molecular orbitals at reactant and product ends are correlated with each other. Based on conservation of orbital symmetry, reaction pathways to be classified as symmetry-allowed/forbidden. Application of these concepts lead to the emergence of a set of empirical rules - known as Woodward-Hoffmann (WH) rules - which can predict, based on number of π-electrons involved, whether a pericyclic reaction pathway is favourable or not. The stereochemistry of products can also be predicted as a consequence of reaction taking place along a symmetry-allowed pathway. The orbital correlation diagrams can be generalized to state-correlation diagrams which can be used in combination with non-crossing rule for same-symmetry states to reach the same conclusions as the WH rules. An interesting aspect of WH rule is that it predicts contrasting types of nuclear motions in thermal and photochemical

activation conditions, *.i.e.,* pathways allowed in thermal conditions are forbidden in photochemical conditions and vice-versa.

The correct prediction by WH rules of relative stereochemistry of functional groups attached to the cyclic framework of a pericyclic reaction is usually considered to be an evidence for the validity of symmetry principle on which it is based. Such a stereochemistry is the result of relative molecular motions which are mainly driven by electronic factors controlling the energetics of underlying bond-breaking and bond-forming processes. Therefore, WH rule is a very good example of how such electronic factors can be captured in terms of orbital symmetry considerations alone.

In photochemical context, the predominance of specific types nuclear motions which lead to WH-predicted stereochemistry must be related to the nature of excited state PESs. The observed high stereospecificity of photochemical pericyclic reactions must also be related to active nuclear motions taking the molecule away from its FC region. This specificity needs to be shaped precisely and very quickly after photoexcitation. If this does not happen, excess energy of photon is sufficient to take the molecule into a variety of photochemical avenues destroying specificity [351–353].

Such considerations have led to many studies using ultrafast spectroscopy to probe the nature of electronic factors, relaxation processes and their time scales in many photoinduced pericyclic reactions, specially the electrocyclic reactions. A classic example which has now been well-understood is photochemical ring-opening of 1,3-cyclohexadiene to 1,3,5-hexatriene [351, 354]. Time-resolved femto-second experiments have established that conrotatory motion implied by WH rule gets established within first 50 *fs* while the molecule is still within the FC region. The electronic relaxation is completed within 80 *fs* by passing through a CI region which channels the molecule towards WH-predicted product [354].

Another example is photoelectrocyclic interconversion between 1,3-butadiene and cyclobutene [352]. Here, in contrast to previous case, anti-WH products with stereochemistry opposite to that predicted by WH rules are also formed, often in significant yields. Excited state *ab initio* molecular dynamics simulations on ring-opening of cyclobutene indicate that preference for WH-predicted stereochemistry is established within 15 *fs* after electronic excitation. On the basis of femto-second experiments, explanation for exceptional behaviour in this system has been proposed [353].

Motivated by this, we have performed computational studies on a simple photoelectrocyclic ring-closure reaction involving heteroatoms. In this chapter, we present and discuss the results from our studies on photoconversion of nitrone to oxaziridine by taking a simple prototype system - the formaldonitrone (FN). Presence

of heteroatoms significantly changes the nature of excited states, destroys orbital symmetry, and cause the WH rule to become inapplicable. Therefore, it would be of some interest to understand how excited state electronic factors can still induce nuclear motions leading to stereospecific photoproducts as observed in many experiments. The chosen system also exhibits certain similarties as well as differences to other systems such as substituted ethylenes and allyl anion.

As in the previous chapter, we apply high-level multi-reference electronic structure as well as *ab initio* non-adiabatic molecular dynamics methods to understand the nature of nuclear distortions and electronic relaxation pathways of photoexcited FN molecule.

6.2 Photochemical Electrocyclic Reactions

A ring-closing electrocyclic reaction involves concerted cyclization of a conjugated π-electron system by converting one of its π-bond to σ-bond. The reverse reaction is called electrocyclic ring-opening. Electrocyclic reactions are an important class of pericyclic reactions where their unimolecular nature makes them to even more facile and highly stereospecific. They are some of most useful reactions for concerted opening and closing of ring structures in organic chemistry. Photochemical electrocyclic reactions take place very fast and have numerous applications in optical switching, photochromic devices, nanomechanical motors and serve as a vital step in the natural synthesis of many photo-biological molecules [215, 355, 356].

As pericyclic reactions, the stereochemical fate of electrocyclic reactions of the conjugated hydrocarbons is described by WH rules. To apply these rules, two types of reaction pathways - conrotatory and disrotatory - are considered. The conrotatory pathway arises when both the termimal groups rotate in the same direction. For a disrotatory pathway, the terminal groups rotate in opposite directions. A two-fold axis of symmetry is maintained along conrotatory pathway, while a molecular symmetry plane is preserved along a disrotatory pathway. Stereochemistry of the reaction product is different for both these pathways. For reactants with $4n + 2$ number of π-electrons, WH rules predict the reaction to proceed via disrotatory pathway under thermal conditions and conrotatory pathway under photochemical conditions. For systems with $4n$ number of π-electrons, the reaction proceeds via conrotatory pathway under thermal conditions and disrotatory pathway under photochemical conditions.

To understand the origin of these selection rules, as discussed in Refs. [226, 298, 347], we consider ring-closing electrocyclic reaction of a 4π-electron system - the allyl anion $\rightarrow$ cyclopropyl anion. According to W-H rule, allyl anion is expected to

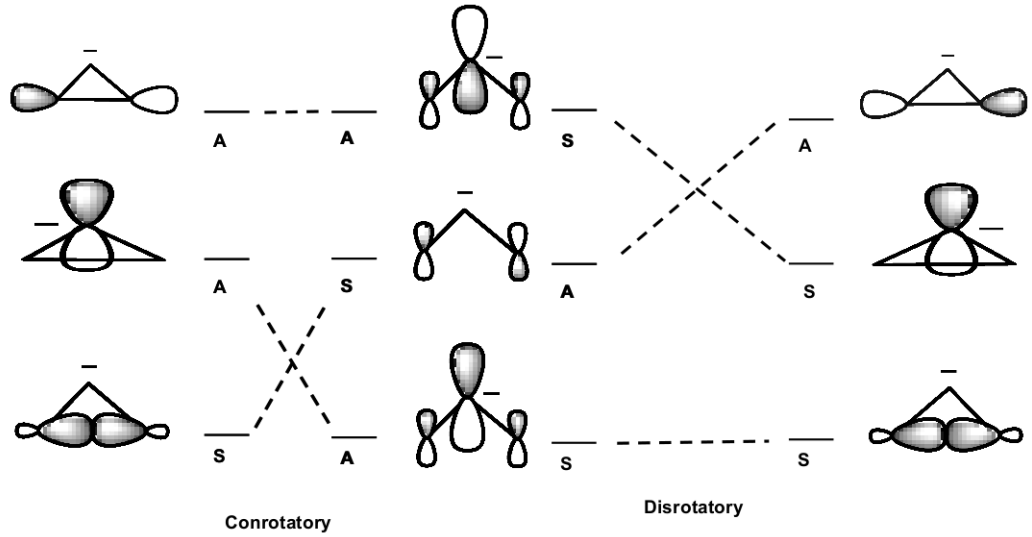

Figure 6.1: Orbital correlation diagrams of conrotatory and disrotatory pathways for allyl anion → cyclopropyl anion.

photocyclized in disrotatory manner and thermally cyclized in conrotatory manner. All the orbitals involved in the cyclization can be represented as being either symmetric or anti-symmetric with respect to symmetry element preserved during conrotation (C_2 axis) and disrotation (C_s plane) pathways. To construct an orbital correlation diagram (see Figure 6.1), a non-crossing rule is employed where crossing of same symmetry orbitals is forbidden. For the conrotatory ring-closure, the bonding orbitals of allyl anion and cyclopropyl anion are directly correlated. As a result, thermal cyclization is governed by conrotation pathway on ground state. For the disrotatory one, a bonding orbital correlates to an anti-bonding orbital. As a result, the reaction is considered to be symmetry-forbidden on ground state, but it is symmetry-allowed on excited state. Therefore, photochemical electrocyclization is predicted to proceed via disrotation.

The frontier MO symmetry arguments provide only qualitative understanding of electrocyclic reactions. For a better understanding, consideration of electronic states is necessary. Based on Longuet-Higgins suggestion [357], state correlation diagrams (see Figure 6.2) have been constructed from orbital correlation diagrams [221, 230, 357].

In terms of state correlation diagrams, reaction mechanism can be understood by correlating the symmetry of reactant and product electronic states. As can be seen from Figure 6.2, along the conrotatory pathway, the ground state electronic configuration of reactant and product transform into each other. Therefore,

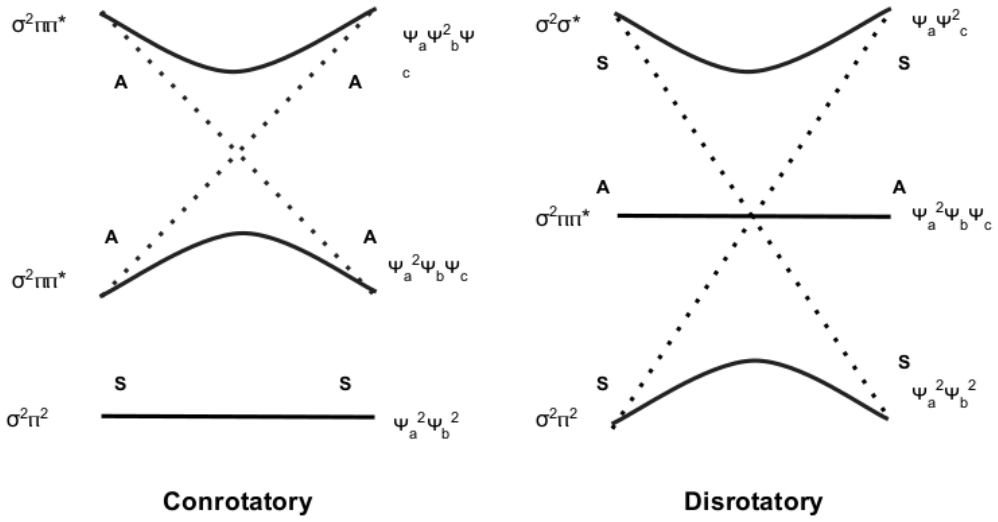

Figure 6.2: State correlation diagrams of conrotatory and disrotatory pathways for allyl anion → cyclopropyl anion.

cyclization of allyl anion is thermally allowed under conrotation pathway. On the other hand, the ground electronic state of allyl anion is directly correlated to the excited state of cyclopropyl anion under disrotatory pathway. This becomes symmetry-forbidden pathway. Again, using state correlation diagrams, the disrotatory path is seen to be favourable in excited state.

6.2.1 Perturbed Electrocyclic Reactions

As presented above, applications of WH rules require the existence of a conserved symmetry element with respect to which orbital and state symmetry correlations can be constructed. Despite this, the WH rules have also been applied, often successfully, to understand stereospecificity observed in electrocyclic reactions of many non-symmetric systems. Some examples are substituted hydrocarbons, and hydrocarbon systems with one or more heteroatom substitutions on the cyclic framework.

The justfication which is usually provided for this is that orbitals of such non-symmetric systems can be related to the orbitals of corresponding symmetric ones by small perturbations. This makes it possible to understand electrocyclic reactions of non-symmetric systems in terms of orbital and state correlation diagrams of their symmetric analogues. For non-symmetric systems, it has also been postulated that orbital topology is conserved during the reaction path [222, 358].

Although some of these applications have been successful, questions have been raised about the magnitudes of deviations from symmetry which make WH rules to

become inapplicable. For unsymmetrical systems mainly involving heteroatoms, the rules are not found be very useful. Introduction of heteroatom in a conjugated system breaks the π symmetry due to interaction of a planar non-bonding σ orbital of the heteroatom with π orbitals. As a result, electronic energy levels get perturbed by a mixing of non-bonding σ and π orbitals. Therefore, energetic difference between conrotation and disrotation becomes smaller. Consequently, the absence of symmetry does not allow description of reaction pathways by consideration of orbital and state correlation diagrams.

Using semi-empirical methods, Snyder and coworkers considered the effect of heteroatoms on stereochemical course of electrocyclic reactions. Series of hetero-acycles isoelectronic with allyl anion and butadienes were considered [359–361]. Calculations suggested that systems involving one heteroatom lead to dominant product with WH-like stereochemistry. However, orbital correlations were found to be inadequate for system involving more than one heteroatoms.

Afterwards, many experimental and theoretical studies attempted to generalize and expand the applicability of the W-H rules to electrocyclic reactions of hetero-acyclic conjugated systems. These investigations were mainly confined to thermal reactions of systems with a single heteroatom substitution. For example, thermal ring-opening of oxiranes, thiiranes and aziridine were shown to occur in a concerted manner in accordance with the W-H rules [362–366].

The effect of introducing heteroatom substituents on photoelectrocyclic reaction is not currently not well-understood. In absence of symmetry, neither the orbital topology is conserved nor any selection rule can be derived. Many experiments do report stereospecificity, regioselectivity, facile cyclizations in hetero-substituted systems. Another question which naturally arises in this context is whether photoinduced electrocyclization reaction in heterosubstitued systems occurs in a step-wise or a concerted manner and if a unified concept exists to describe reaction mechanisms.

In view of above, we intend to carry out computational investigation of a photo-electrocyclic reaction by considering a prototype example of such a reaction - nitrone to oxaziridine photoconversion.

6.3 System of Study - Nitrones

Nitrone, commonly known as N-oxide of imine, is a molecule with a -C-N-O functional group as shown in Figure 6.3. It is highly reactive species used as a general oxidizing reagent in organic chemistry. Considered as 1,3-dipole systems with

electrons delocalized over the -C-N-O functional group, they undergo a wide variety of thermal as well as photochemical reactions. Nitrones resulting from substitutions at C and N positions are found to have varied and rich photochemical properties [367]. As shown in Figure 6.3, nitrones are related to a number of distinct chemical structures with the same composition but with different functional groups, the important ones being oxaziridine and amide functional groups. The photoisomerization of nitrone to formamide, although long known since 1965, has recently attracted some attention due to the formation of amide bond providing linkage to peptide chemistry [368]. It has been now established that oxaziridine appears an intermediate in this photoreaction. Oxazirdine is also another important organic reagent used as an oxygen donor [369].

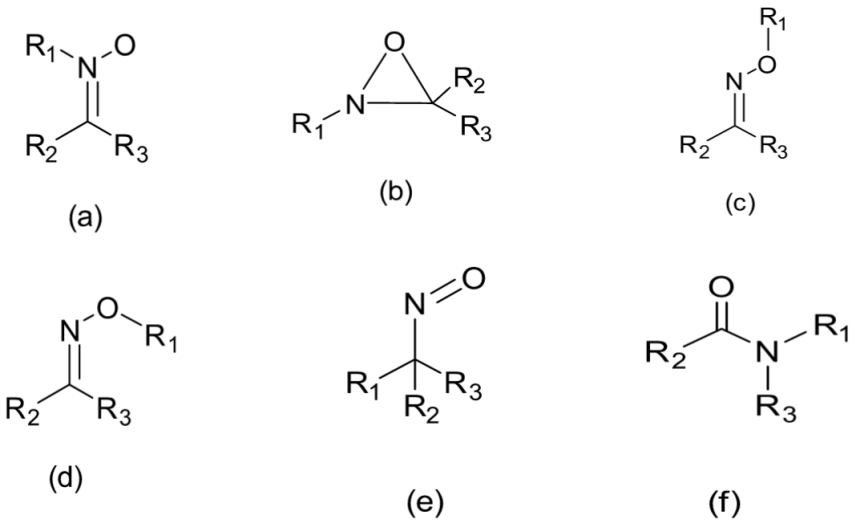

Figure 6.3: Important isomers of -CNO functional group - $R_1R_2CNOR_3$. In this study R_1, R_2, R_3 = H. **(a)** Formaldonitrone (FN). **(b)** Oxaziridine (Oxz). **(c)** anti-Formaldoxime (anti-FO). **(d)** syn-Formaldoxime (syn-FO). **(e)** Nitrosomethane (NM). **(f)** Formamide (FA).

A clear mechanistic picture of nitrone to formamide photoconversion and involvement of oxaziridine could not be established earlier due to several experimental inconsistencies. In early studies, Splitter and coworkers established that oxaziridine can be photochemically formed from nitrone, but found it to be unstable and undergoes thermally induced isomerization to form either formamide or to revert back to nitrone [21, 22, 370–372]. It is interesting to note that photochemical ring opening of oxaziridine in many cases led to highly regioselective and stereoselective products [22, 373, 374]. At the same time, there are also a few other thermal conversions of oxaziridine to amide which were found to be much less regioselective as compared

to photochemical ones [375, 376]. The photochemical and thermal conversions of oxaziridine to amide also been studied in experimental and theoretical works [374,377].

On the other hand, even though nitrone to oxaziridine photoisomerization is a simple electrocylic ring-closure reaction, its mechanistic details have not been fully understood. Earlier works supported formation of oxaziridine, but this could not be further investigated as oxaziridine is unstable and can not be isolated in experiments. It was firmly established that upon photoirridation nitrone undergoes facile conversion to formamide [22, 23, 367, 378–380]. Further, nitrone photoirradiation results were also found to be strongly dependent on substituents at N or C position, and several examples were found where stable oxaziridines are formed [21–23, 380–382]. Stable oxaziridines usually contain alkyl groups at C or N or both. As in the case of symmetry controlled photochemical reactions of conjugated hydrocarbons such as allyl anion [383, 384], photoexcitation of nitrone leads to formation of syn- and anti-oxaziridine isomers. It was proposed that this conversion is happens through conrotation and disrotation mechanisms, although, due to lack of conserved symmetry plane or axis element along the reaction path, no WH rules are strictly possible here [24, 385].

Much of the knowledge about photochemistry of nitrone comes from extensive investigations of Splitter and coworkers [21–24]. Two photochemical reaction pathways have been identified - 1. *cis-trans* isomerization 2. oxaziridine electocyclization. Tanaka and coworkers attempted to provide a clearer picture by concluding from their experiments that electrocyclization occurs in first excited state by a step-wise mechanism while *cis-trans* isomerization occurs either on triplet or ground state [386, 387]. This observation was also supported by detailed computational studies of Sevin and coworkers [388] who explored photochemical reaction possibilities of unsubstituted oxaziridine molecule. More recently, nitrone photochemistry has been revisited by Chattopadhyay and coworkers in a series of experimental and computational studies on substituted nitrones with conjugated hydrocarbon side-chains and/or aryl groups. They also established the nature of first two singlet excited states of these systems to be $\pi \rightarrow \pi^*$. Formation of oxaziridine starting from S_1 excitation of their nitrones via barrierless pathway involving S_1/S_0 CIs was also proposed [389–392]

In this chapter, we report results from our investigation on excited states, photochemical intermediates and reaction pathways, and electronic relaxation dynamics of formaldonitrone (FN) molecule upon S_1 photoexcitation. As in the previous chapter, we make use of high-level multi-reference and trajectory based direct-dynamics methods. FN is the simplest possible unsubstitued nitrone - with

chemical formula CH2=NHO. Although many stable isomers of FN have been isolated and characterized, FN itself, despite many experimental studies, could not be isolated until recently. Polasek *et al.*, [393] finally prepared and identified this molecule through femtosecond collisional neutralization of its cation radical. This has opened up possibilites for study of photochemical reactions of this simplest nitrone.

There are several reasons for choice of FN for our study. One reason is to use this as a prototype system to study photochemical electrocyclic reactions of simple molecules involving heteroatoms. Such electrocylic reactions, known as pseudo-pericyclic reactions, have been extensively investigtated since the work of Lemal and Birney [394, 395], particularly thermally induced ones. Notable aspects of these reactions are cyclic transition states, concerted mechanism, and absence of WH rules. For photochemical versions, there have been limited studies on such systems. For 1,3 case, the systems can be thought of as arising from isoelectronic substitutions involving heteroatoms in allyl anion.

In addition to this, FN system can be thought of as a model for investigation of *cis-trans* isomerization of a polarized π-bond. A number of studies of *cis-trans* isomerization of substituted ethylenes [14, 260, 396, 397] have shown a similar picture of ethylene as discussed in section 4.3 of Chapter 4 - important reaction coordinates are torsion and pyramidalization [15, 209]. Further studies have also shown the importance of hydrogen migration pathways in ethylene photoreactions [14, 15]. In contrast, studies of polar ethylenic systems such as $CH_2NH_2^+$ and CH_2SiH_2 have shown that torsional motion is sufficient to reach S_1/S_0 CI seam region [398, 399]. In this context, FN molecule can considered as an interesting case of a π bond in which two heteroatoms, N and O, strongly polarize it.

Another reason concerns with using FN as a prototype system for developing a model for photochemistry of substituted nitrones, in the same spirit as Robb's photochemical model for α,β-enones discusssed in Chapter 5. Despite a number of photochemical studies on substituted nitrones, no such model is currently available. However, the conjugated substituents of stable nitrones reported in literature strongly alter the nature of excited states. This casts doubts on usefulness of such models. Despite this, such a model is expected to be useful for simple substitutions as discussed in previous chapter.

For FN system, we attempt to understand the nature of low-lying electronic states, their PESs, and non-adiabatic relaxation pathways of electrocyclic and *cis-trans* photoisomerizations. For reasons discussed later, we have restricted our studies only to S_1 state of $n \rightarrow \pi^*$ character. Rest of the chapter is organized as follows. Section 6.4 describes results from static calculations. Relative energies of FN, its isomers, and

their interconversion energy barriers are discussed in section 6.4.1. The nature and energetics of valence excited states of FN are studied in section 6.4.2. Stationary structures on S_1 state, S_1/S_0 MECI are shown in 6.4.3. Excited reaction pathway connecting FC to MECI and ground state pathways from MECI are computed in 6.4.4. In 6.5, we describe results of AIMS simulations to obtain dynamical picture. Concluding remarks are given in section 6.6.

6.4 *Ab initio* Calculations

6.4.1 Ground State Isomers

As mentioned before, on ground state PES, FN has many isomers with different chemical structures connected by barriers. These isomers and their formation processes from FN are shown in Figure 6.4. Isomers nitrosomethane (NM : CH_3NO) and formaldoximes (anti/syn-FO : H_2=C-NOH) have been experimentally isolated and their tautomerization has been studied. Nitrone is considered as an intermediate in this interconversion. Adeney *et al.,* [400] have shown that FN undergoes an intramolecular [1,2]-H shift to yield NM and anti-FO.

In this subsection, we have computed optimized geometries and relative energies of these isomers. Transition states for their formation from FN and their barriers have also been found. The geometry optimization and energy calculations have been carried out at MP2/cc-pVTZ and CCSD/cc-pVTZ level of theory by using MOLPRO quantum chemistry package [108].

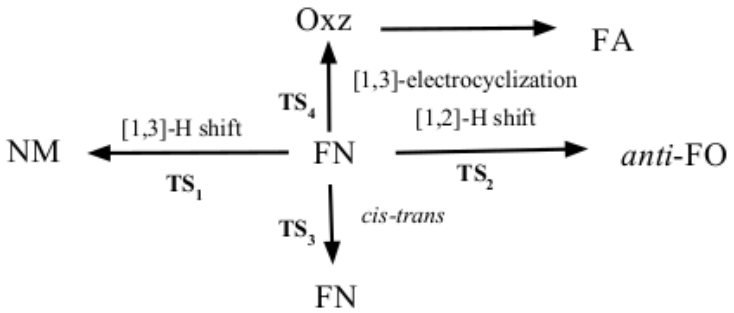

Figure 6.4: Possible ground state reactions of FN - *cis-trans*, [1,2]-H shift, [1,3]-H shift and [1,3]-electrocyclization. TS_1, TS_2, TS_3 and TS_4 are transition states for interconversion between these stable isomers.

Table 6.1: Relative energies of important isomers of FN. Results shown are for MP2/cc-pVTZ and CCSD/cc-pVTZ methods. Previous values are at CCSD(T) and 2RDM [25] using aVTZ basis, G2 [26], B3LYP/6-311G(d,p) [27] levels. All reported energies are relative to FN in kcal/mol.

Structures	Previous studies				Present study	
	G2	2RDM	CCSD(T)	DFT	MP2	CCSD
Formaldonitrone (FN)	0.0	0.0	0.0	0.0	0.0	0.0
Nitrosomethane (NM)	0.9	-0.3	0.7	3.5	0.9	-3.9
anti-Formaldoxime (anti-FO)	-11.0	-13.0	-11.7	-9.2	-11.2	-15.5
Oxaziridine (Oxz)	-	-	-	13.5	7.2	4.7
TS_1 (FN→NM)	-	54.8	54.3	50.6	51.6	51.5
TS_2 (FN→FO)	-	46.3	45.7	42.8	41.9	42.5
TS_3 (*cis-trans*-FN)	-	-	-	-	71.0	69.3
TS_4 (FN→Oxz)	-	-	-	55.3	55.9	54.1

Table 6.1 reports computed energies of isomers relative to FN. For comparison, earlier results from G2 calculations of Vladimiroff [26] for NM and FO, CCSD(T) and 2-RDM calculations of Mazziotti [25] and DFT study of Alcami [27] and coworkers have been also reported.

All methods predict FO to be most stable isomer lower in energy by 10-15 kcal/mol relative to FN. On the other hand, Oxz is unstable relative to FN by 4.7-7.0 kcal/mol at MP2/CCSD levels. At B3LYP/6-311G** level, this increase to 13.5 kcal/mol. Oxz is expected to be unstable due to additional strain due to its 3-membered ring. The energetic ordering of NM and FN is sensitive to method used. While CCSD predicts NM to be lower in energy as compared to FN, CCSD(T) and G2 reverse this trend. It can be concluded that NM and FN are nearly isoenergetic.

Regarding interconversion barriers, it can be noted that all barriers are found to be larger than 50 kcal/mol. The only exception is FN to FO conversion, which has lowest barrier about 40 kcal/mol. The *cis-trans* barrier is rather high at 70 kcal/mol, while electrocyclization barrier is about 55 kcal/mol. Such high interconversion barriers indicate that FN must be relatively stable with respect to unimolecular reactions. Due to their 1,3-dipolar nature, in condensed phase they undergo oligomerization through facile thermal cycloaddition reactions. Recently, FN has been transiently produced in gas phase experiments at low pressures [393].

However, it is possible to envisage that all these isomers can be reached by photoexcitation of FN. In this work, our goal is to establish which isomers are formed from its first excited state. Our primary interest is photochemical route for *cis-trans*

and electrocyclization reactions directly yielding FN and Oxz respectively. Other isomers may be possible at higher excitations to σ^* orbitals of NH and CH bonds.

6.4.2 FC Excited States

In this subsection, we discuss nature and energies of low-lying excited singlet states of FN at its FC geometry using a variety of multi-reference methods. The objective of these numeros calculations with different methods is to establish a suitable method and active space which can reliably describe the excited states. This is necessary in calculations for further investigations of reaction pathways and nuclear dynamics.

6.4.2.1 Computational Details

Since experimental absorbption spectrum of FN is not available, we have attempted to compute several excited states upto 7-8 eV above the ground state. Only valence excited states were targeted, as Rydberg excitations are expected to be higher in energy. The MP2/cc-pVDZ optimized ground state geometry was used for this calculation. All calculations in this subsection have been carried out using MOLPRO electronic structure package [108]. Since ground state of FN is planar, C_s symmetry has been imposed in these calculations.

We have employed SA-MCSCF, MS-CASPT2(RS2), MR-CISD and EOM-CCSD methods. SA-MCSCF calculations included 5 states (ground state and 4 singlet excited states) averaged using equal weights. Symmetry labels of these states are three A′ and two A″. We considered two active spaces - CAS(9o,10e) and CAS(7o,8e) - represented as CAS_A and CAS_B, respectively. CAS_A included 6 a′ and 3 a″ orbitals. CAS_B constructed from CAS_A by moving out two active natural orbitals of highest and lowest occupations.

The natural orbitals of CAS_A wave-function are depicted in the Figure 6.5, along with labels indicating their symmetry and ordering at HF level and natural occupations. The bonding and anti-bonding orbitals corresponding NH and NO bonds are clearly seen. The corresponding σ orbitals of CN do not get included due to their low energy. Most important orbitals for descriptions of valence excited states are - the 11a′ σ orbital describing O lone pair, and three π orbitals 1a″(π[C=N + NO]) and 2a″ (π[C=N]) and 3a″ (π^*). The π orbitals show the expected delocalization across CNO unit.

The SA-MCSCF calculations were followed by MR-CISD and MS-CASPT2 computations, with C, N, and O 1s orbital not correlated. A level shift of 0.2 hartree has been used in MS-CASPT2 calculation.

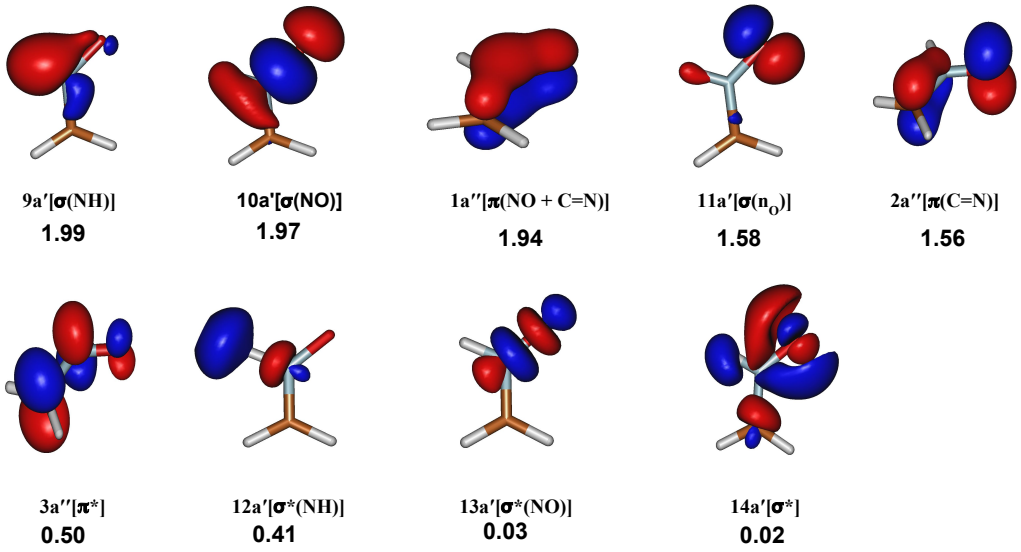

Figure 6.5: SA5-CASSCF(9o,10e) MOs with their natural occupation numbers.

Table 6.2: The vertical excitation energies (in eV) at EOM-CCSD, MCSCF, MS-CASPT2 and MR-CISD level of theory in cc-pVDZ basis set.

State	Nature	EOM	CAS^a_A	CAS^b_B	RS_A	RS_B	$MRCI_A$	$MRCI_B$	f^c
S_1	n_o-π^* (11a′- 3a″)	4.59	4.88	4.42	4.29	4.36	4.59	4.50	0.000
S_2	π-π^* (2a″-3a″)	6.13	6.74	6.43	5.50	5.34	6.28	6.29	0.293
S_3	π-σ^* (2a″-12a′)	6.50	6.17	5.89	6.40	6.44	6.54	6.45	0.002
S_4	n_o-σ^* (11a′-12a′)	7.51	7.61	7.64	7.38	7.41	7.52	7.50	0.134

[a] CAS_A: SA5-CAS(90,10e), [b] CAS_B: SA5-CAS(70,8e), [c] Oscillator strengths (f) at EOM-CCSD level.

6.4.2.2 Results and Discussions

The excitation energies and EOM-CCSD oscillator strengths for valence singlet excited states S_1 to S_4 are shown in Table 6.2. To ascertain the nature of transitions, we have inspected natural orbitals and occupations of each of these states at SA5-CAS(9o,10e) and MRCI levels. The wave-function coefficients expressed in terms of these orbitals clearly indicated that all computed states can be well-described in terms of two orbitals with natural occupations close to unity. Similar picture is also indicated for states written in terms of natural orbitals of SA5-CAS(9o,10e). This clearly indicates that all computed excited states have single excitation character at FC geometry. Therefore, EOM-CCSD results must be reliable for these states and close agreement with MRCI and CASPT2 is expected.

First excited state is of A′ symmetry and can be assigned as $n_O \rightarrow \pi^*$-type

transition. Its oscillator strength is found to be nearly zero, which supports this assignment. From natural orbital analysis, it can be further confirmed that S_1 transition originates from σ-type orbital 11a$'$ (localized on oxygen atom, see Figure) to π-type orbital 3$''$. The latter can be thought of as a delocalized anti-bonding orbital with dominant contributions from C and N atoms. Both EOM and MRCI transition energies for S_1 state are in excellent agreement with each other ($<$ 0.1 eV), while CASPT2 underestimates them upto 0.3eV. It can be noticed that CAS results show strong dependence on active space (CAS_A vs CAS_B). These differences are reduced to less than 0.1eV for CASPT2 and MRCI methods. This observation also holds true for other excited states. EOM-CCSD/MRCI results approximately correspond to 270 nm UV radiation for S_1 excitation.

Next two singlet excited states, S_2 and S_3, can be identified as arising from $\pi \rightarrow \pi^*$ and $\pi \rightarrow \sigma^*$ type of transitions. The S_2 state involves excitation from 2a$''$ orbital to 3a$''$ orbital. Both are π-type orbitals with significant contributions from C and N atoms. This transition carries a significant oscillator strength of 0.293 supporting its assignment. In contrast, S_3 state arises from 2a$''$ to 12a$'$. The latter orbital is a σ^* orbital corresponding to NH bond and has low oscillator strength of 0.002.

It can be observed that both states are close to within 0.3eV of each other, predicted to be in 190-200 nm (deep UV region). Once again, MRCI and EOM results are in excellent agreement and CASPT2 results for S_2 deviate substantially. Interestingly, an inversion of energy ordering of S_2 and S_3 states is observed at SA-MCSCF level - $\pi\pi^*$ state is predicted to be at higher energy as compared to $\pi\sigma^*$ state by 0.5-0.6 eV for both active spaces. This indicates importance of including dynamical electron correlation for obtaining correct order of $\pi\pi^*$ and $\pi\sigma^*$states. Although CASPT2 gets energy ordering correct, poor quality of S_2 excitation energy is a warning about its reliablity.

We have assigned S_4 state to $n_O \rightarrow \sigma^*$ type transition. The orbital to which the transition takes place is once again 12a$'$ orbital. This state is separated from S_3 by a larger energy (1.0 eV) and has significant oscillator strength of 0.134. All methods seem to provide equally good excitation energy for this state.

Some important conclusions relevant for reaction path and dynamics studies can be drawn from these calculations. First of all, it is essential to use multi-reference electron correlation methods (MRCI/CASPT2) for correct description and energetic ordering of S_2 and higher states. For S_1 state, CASPT2 may be used satisfactorily. Another important fact is that S_2 state and S_3 states are energetically close to each other. This means that any proper description of S_2 state from computations requires S_3 state to be also considered. Therefore, for proper S_2 dynamics, at least four states

$S_0 - S_3$ need to be considered. It can be expected that initial relaxation from $\pi\sigma^*$ states will open photodissociation pathways. Since this is beyond to scope of this work, we have restricted our study only to S_1 electronic state.

Therefore, we expect that present results would provide a starting point to begin the discussion of reaction pathways on the excited surface by the determination of structural aspects and energetics of stationary points such as minima, minimum energy conical intersection, etc.

Since our objective to explore photochemical pathways and dynamics on S_1 state can lead to substantial number of computations, we have considered a way to reduce computational costs. This is done by choosing a smaller active space CAS(5o,6e) which may be sufficient to descibe lowest two states through a 2-state averaging SA2-CAS(5,6) followed by MS-CASPT2 calculations. In MS-CASPT2, we have considered possibility to further reduce computational cost by not correlating doubly-occupied closed-shell orbitals. In order to test the reliability of these schemes, we have repeated the above excitation energy calculations. This confirms that nature and energetic position of first two electronic states S_0 and S_1 are correctly described within this scheme. The vertical excitation energy of S_1 state is found to be 4.370 eV which is in good agreement with EOM-CCSD result. Therefore, we conclude that CAS(5,6) active space gives a good balance between computational efficiency and flexibility for its use in computation of MS-CASPT2 and MRCI wave functions for further investigations on S_1 state.

6.4.3 Excited State Structures

As a step towards building photochemical pathways, we have located some key intermediates on S_1 excited state using standard geometry optimization methods. For energy calculations, we have used SA2-CASSCF(5,6)/cc-pVDZ method followed by MS-CASPT2 and MRCI methods with same basis set. All energy calculations and geometry optimizations reported in this subsection have been carried using COLUMBUS [109, 330, 331], except for MS-CASPT2 calculations where Molpro has been used. As usual, 3 core orbitals have not been correlated, and MS-CASPT2 uses the scheme mentioned in previous subsection.

Key geometrical parameters of located structures are shown in Figure 6.6, along with results for ground state structure (FC geometry) which has also been optimized again using above methods. Computed ground state structures for all three multi-reference methods agree with each other within 0.02Å, and are in agreement with previously reported CCSD, CCSD(T) structures [25].

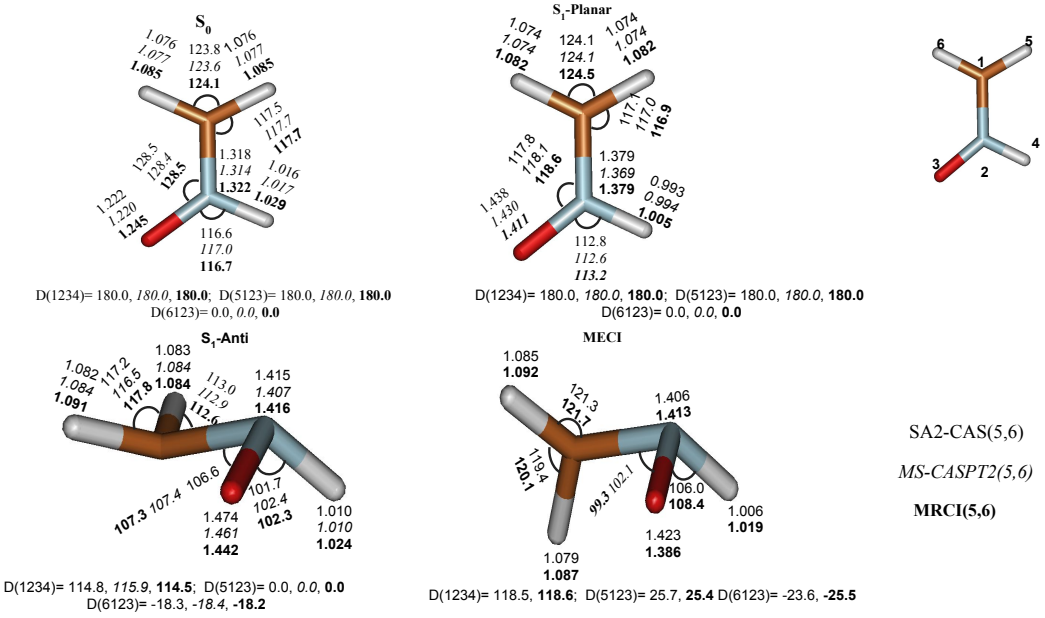

Figure 6.6: Key geometrical parameters of located structures at various level of theories (see text). Bold and italic values denote MRCI and MS-CASPT2 results. The bond lengths are in Å and angles are in degrees. The dihedral angles (D) are shown according to the numbering given in the inset.

Two stationary structures on S_1 state which may play important role in construction of photochemical pathways have been located. They are designated as S_1-*Planar* and S_1-*Anti*, and are shown in Figure 6.6. They have been located from geometry optimizations on S_1 by using different starting geometries. These are structurally and energetically distinct from each other.

Structure S_1-Planar is planar and has been obtained by geometry optimizations in C_s symmetry. It is a minumum w.r.t planar deformations and saddle point w.r.t out-of-plane deformations (see later). Its important differences w.r.t FC structure at CASSCF level are 1. N-O bond is longer by 0.216Å 2. C-N bond is longer by 0.06 Å. At MRCI level, these differences reduce to 0.166Å and 0.057Å respectively. Elongation of these framework bonds are in agreement with $n \rightarrow \pi^*$ nature of S_1 state which weakens them due to promotion of an electron to anti-bonding π^* orbital. For the same reasons, bond angles, CNO, NHO and CH_2 also change, with NHO changes being much larger as compared to CH_2. The importance of S_1-Planar structure is that it captures dominant geometrical changes due to relaxation of FC structure on S_1 PES. It can be noted that geometrical parameters of this structure agree well for all three methods.

The second structure S_1-Anti is found to be non-planar, and its existence is confirmed by all three methods. A main feature of S_1-Anti is that non-planarity arises

from pyramidalization of NHO and CH_2 groups. Interestingly, pyramidalizations happen in opposite directions (see Figure) - it is the reason for referring to this as Anti structure. The hydrogen atom (H_5) which is located anti to oxygen atom (O_3), very nearly remains in the CNO plane. Other two hydrogens (H_4 attached to the nitrogen atom and H_6 attached to the carbon atom) are seen to significantly move out of this plane in opposite directions. One hydrogen, H_4 attached to nitrogen, moves to a larger extent as compared to the other H_6 one attached to carbon.

Starting from FC geometry, this structure can be reached by two types of deformations - planar and non-planar. The non-planar distortions are mainly pyramidalizations of two terminal groups as discussed above. The planar deformations are mainly C-N and N-O bond elongations of 0.1Å and 0.2Å respectively, at MRCI level. It can be noted that these planar deformations are similar in magnitude to the ones required for reaching S_1-Planar from FC. Therefore, both the structures can be considered to be related to each other via non-planar distortions. We also note that our attempts to locate Syn-type equivalent of S_1-Anti have been unsuccessful.

Using geometry optimization techniques, a MECI structure on S_1/S_0 seam has been located. This is a non-planar structure with significant pyramidalization of NHO group. It can be noticed that it has some resemblance to twisted-pyramidalized MECI of ethylene. As with S_1-Anti, MECI structure also involves planar and non-planar deformations to reach it from FC geometry. By comparing MECI and FC structures, it is found that the only non-planar deformation required to reach MECI from FC is the out-of-plane bending of N-O. This is because, in MECI, CH_2 group is pyramidalized to a very small extent and NH bond is also in the same plane as CH_2-N. The planar deformations required are similar C-N and N-O bond elongations as observed for the other two structures.

In view of the relation between S_1-Planar and S_1-Anti and the nature of planar defomations as discussed above, it would be important to understand how MECI and S_1-Anti structures are related. This is also relevant when one considers that MECIs are often reached from nearby local minima. From figure, it can be seen that MECI can be easily reached from S_1-Anti by applying a torsion around C-N bond. The extent of NHO pyramidalization for both structures are similar. Largest change in bond lengths is NO bond shrinking by 0.056Å.

The MECI has been characterized by computing its **g** and **h** vectors and topographical parameters, as displayed in Figures 6.8 and 6.7. The **g** vector is found to be mainly NHO pyramidalization and **h** vector involves motions leading to ring-closure. The plots of branching space PESs clearly show that the MECI is peaked-type CI, suggesting an efficient non-adiabatic population transfer through this CI.

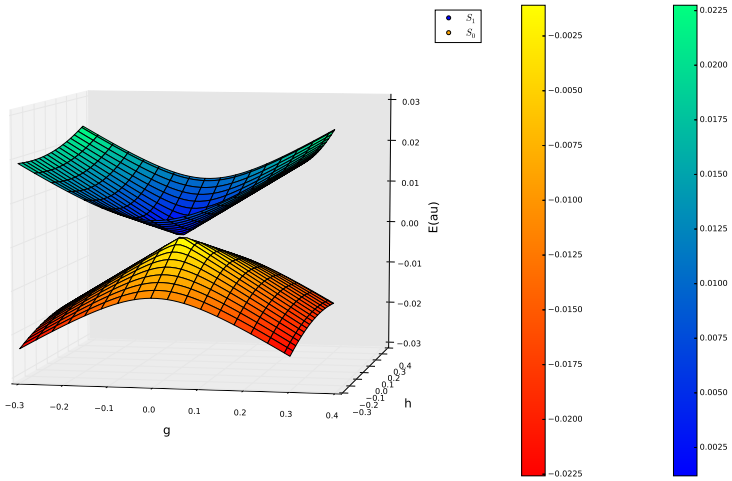

Figure 6.7: Adiabatic PESs around S_1/S_0 MECI.

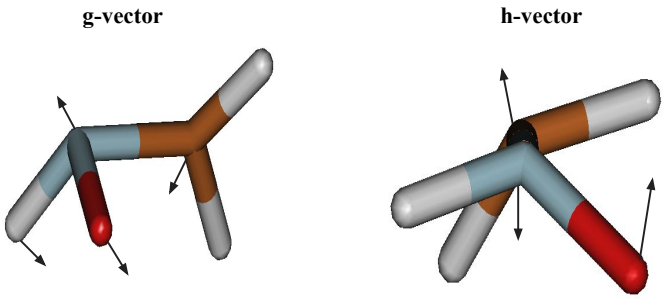

Figure 6.8: The **g** and **h** vectors of S_1/S_0 MECI.

Further, inspection of natural orbitals and wave-function coefficients reveals that electronic structure at all three geometries can be well-described as biradicaloid. This is formed from an oxygen-centered and a dominantly carbon-centered orbitals which have similar nodal structure as the n_O and anti-bonding π^* orbitals at FC geometry. This further confirms that CAS(5,6) is adequate for this problem.

The energies of all three structures relative to FC structure are shown in the Figure 6.9, where the structures have been placed on the x-axis in decreasing order of energy of their S_1 state. The energy gap between S_1 and S_0 is also indicated in the same figure. From this figure, it is clear that the energy gap also decreases in the

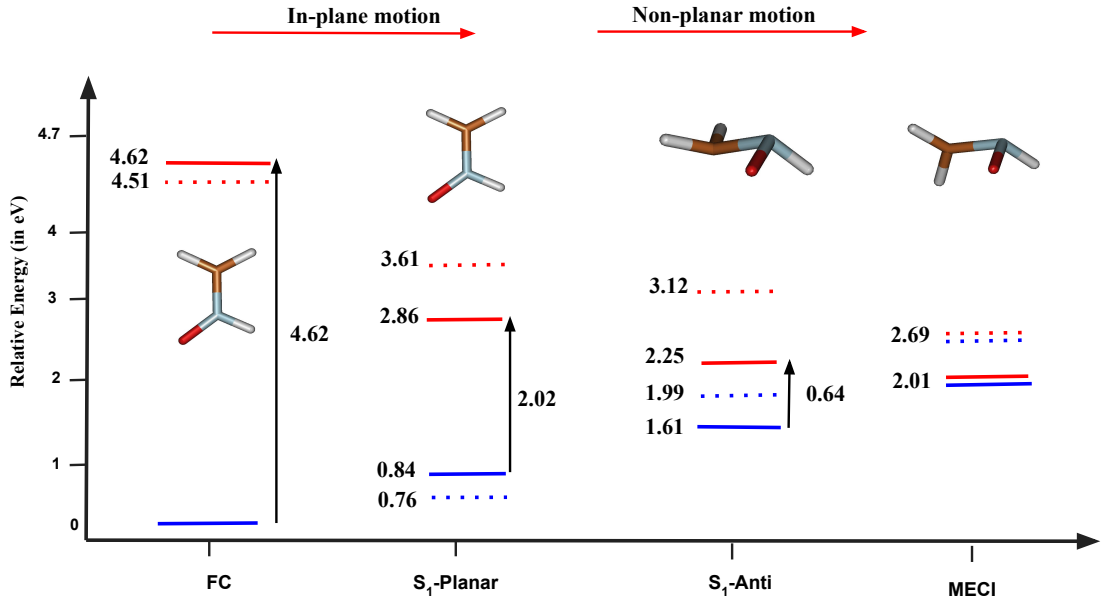

Figure 6.9: The relative energies (in eV) with respect to FC energy of stationary structures calculated at CASSCF and MRCI levels. **Red**/**blue** colors denote S_1/S_0 states, respectively. The solid and dashed lines indicate SA2-CAS(5,6)/cc-pVDZ and MRCI(5,6)/cc-PVDZ results, respectively. Black arrow denotes S_1/S_0 gap at CAS level.

same order as the energy of S_1 state reaching zero at MECI structure. At CASSCF level, an in-plane deformation involving elongation of C-N and N-O bonds taking FC structure to S_1-Planar lowers the energy of S_1 state by 1.76 eV, while the energy gap reduces from 4.62 eV to 2.02 eV. Out-of-plane NHO and CH_2 pyramidalization motions converting S_1-Planar to S_1-Anti further lowers the energy of S_1 by 0.61 eV and the gap decreases to 0.64 eV. Twisting motion of CH_2 around C-N bond lowers the energy by additional 0.24 eV to convert it to MECI structure where the energy gap vanishes. This picture also holds at MRCI level where the difference is that energy gaps are somewhat larger by 0.5-0.8 eV and lowering of S_1 energy are smaller.

Although such an ordering of structures constitutes a possible reaction path for connecting FC to MECI, it is not necessary that such a path energetically feasible. Based on similarity of planar distortions and relationship between these structures, it can be considered as a path to understand the type of nuclear motions which can take the molecule from its FC structure towards MECI.

Given these considerations and assuming that the MECI found is involved, two photochemical pathways are possible. First possibility is that molecule starts from FC and reaches S_1-Anti minimum, either directly or by going through S_1-Planar structure. This is then followed by another reaction path which goes through an

energy barrier to reach MECI. Second possibility is that molecule directly reaches MECI without going through S_1-Anti by either going through S_1-Planar or through an alterate path involving non-planar geometries. Both these possibilites are consistent with energies and structures found.

To understand non-planar distortions of S_1-Planar, we have carried out frequency calculations. It is interesting to note that this structure turns out to a third-order saddle-point with three imaginary frequencies $\nu = 866.7, 734.6, 208.79 cm^{-1}$. The normal modes corresponding to these frequencies are depicted in Figure 6.10. It can be noted that all of them correspond to out-of-plane motion confirming that it is a minimum with respect to planar deformations. Upon examination of these normal modes, the two high-lying vibrations, ν_1= 866.7 cm^{-1} and ν_2= 734.6 cm^{-1}, can be characterized as combinations of CH_2 wagging and NH bending motions. The third one corresponds to torsion of CH_2 group around C-N bond.

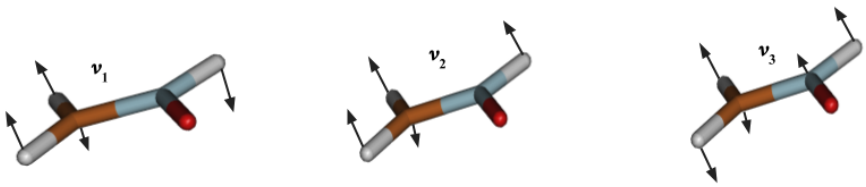

Figure 6.10: All out-of-plane frequencies and normal modes (shown by vector displacement) at S_1-Planar structure. First two high-lying normal modes, ν_1=866.7 and 734.6 cm^{-1}, are characterized as combinations of CH_2 wagging and NH bending motions. Third one (ν_3=208.79) is dominated by the torsion of CH_2 around C-N bond.

6.4.4 Photochemical Reaction Pathway

After obtaining key intermediates, we have carried out further geometry optimizations to locate any possible transition state structures. In particular, we tried to locate a transition state which can connect S_1-Anti minimum to MECI. However, such attempts turned out to be unsuccessful.

To clarify the role of S_1-Anti in relaxation from FC and to find out whether S_1-Anti or MECI can be reached from S_1-Planar structure through out-of-plane deformations, we have carried out series of calculations to construct minimum energy paths (MEP) from FC to ground state products. In this section, the results from these calculations are discussed. Based on these results, a mechanistic picture of

photochemical relaxation from S_1 state is suggested.

For calculating MEP from a structure with non-zero energy gradient, a simple gradient steepest descent procedure has been used. A small displacement (0.05 Å) in the direction opposite to gradient is applied to construct a displaced structure where the gradient is recalculated, and the procedure is repeated until gradient vanishes. The procedure is not optimal and does not work when steep valleys are present. For paths leading to CIs, the energy gap between the states is monitored and procedure is stopped when gap is small. Instead of mass-weighted coordinates which leads to IRC, Cartesian coordinates have been employed.

6.4.4.1 Excited State Pathways

Constuction of MEP starting at FC region faces conceptual difficulties when the ground state geometry is planar as it happens in this case. Steepest descent path from a planar geometry always leads to a planar minimum or a saddle point. Therefore, two types of MEP calculations have been attempted each providing a possible MEP. One calculation used a planar geometry of ground state for representing FC geometry as starting point. After reaching a planar minimum, frequency calculation is performed to identify non-planar deformations which can further lower energy. A small displacement is performed along one of these direction to obtain a non-planar structure with a non-zero gradient. Steepest descent from this structure eventually leads to a non-planar minimum or a saddle point. Another type of MEP calculation is to apply a small displacement to planar geometry of ground state along one of its non-planar normal modes to obtain a displaced FC structure. Once again, steepest descent from this yields another possible MEP.

All MEP calculations have been carried out using SA2-CASSCF(5,6)/cc-pVDZ method. The calculations were started from the MP2/cc-pvDZ optimized planar geometry for ground state. Initial displacements along MEP path from starting geometry were found to be, as expected, mainly dominated by CN and NO bond elongations. The energies of S_1 and S_0 states along the MEP are shown in Figure 6.11. From the energy profile, it can be seen that MEP leads to region where gradient of S_1 is nearly zero and energy gap does not change. The final planar minimum structure resulting was identified to be S_1-Planar.

Since S_1-Planar has three imaginary out-of-plane vibrational modes (as shown in Figure 6.10), a second branch of the MEP begins from a non-planar structure (A). The structure A has been obtained by distorting the S_1-Planar along modes ν_1 which involves NH bending motion. The resulting energy profile has been displayed

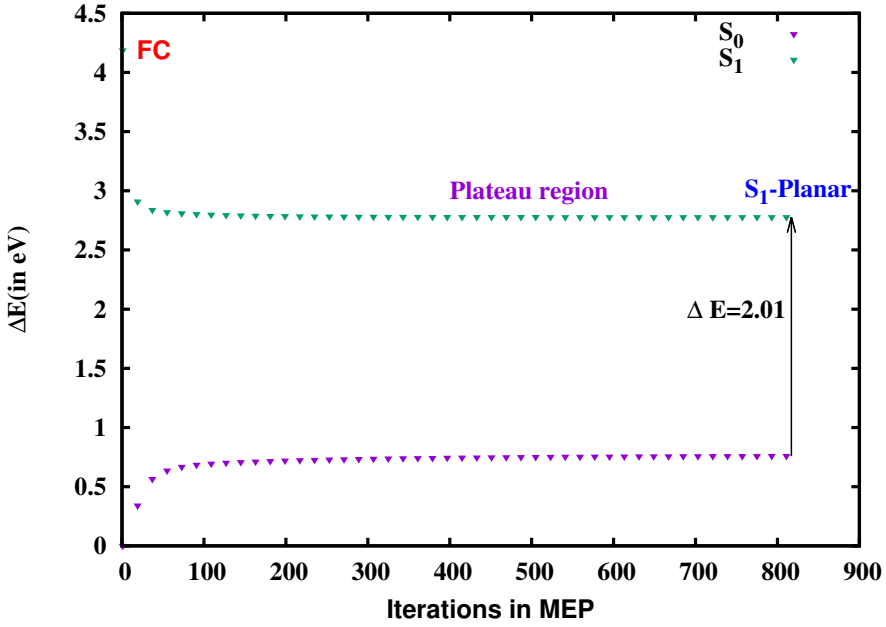

Figure 6.11: The energy profile along planar MEP.

in Figure 6.12. Along the MEP, it was found that energy gap between S_1 and S_0 keeps decreasing. The MEP calculations were stopped a geometry (I) where energy gap reaches $8.1*10^{-4}$ eV. Structure (I) turns out to be a CI geometry.

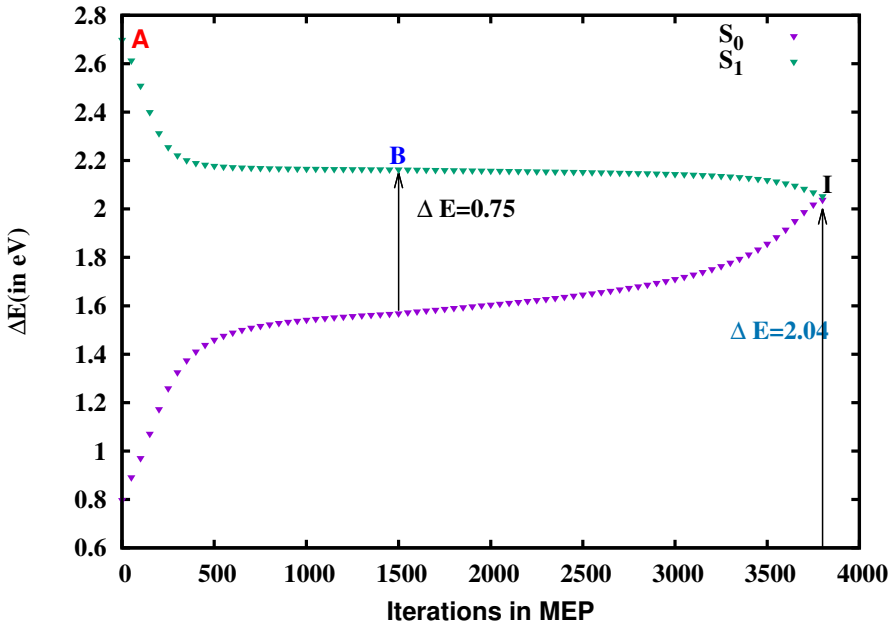

Figure 6.12: The second branch of MEP along out-of-plane direction. The $\triangle E$ is relative to the ground state energy. Important structures are labeled as A, B and I (discussed in text).

To understand the reaction coordinates, it is useful to consider a few representative structures along MEP. We have chosen a representative (B) along the second branch of MEP where S_1 energy change is slow. All important structures along the full MEP starting from FC have been shown in Figure 6.13. Major motions when going from A to B are identified to be pyramidalization of both CH_2 and NHO groups, although degree of distortion appears to be smaller at CH_2. It can be noticed that structure (B) is similar to S_1-Anti, although there are some differences. Therefore, it can be said that MEP is not able to move towards this minimum, presumably due to its shallow nature. The CI structure (I) is close to MECI structure, although NO bond is elongated in (I) by about 0.05Å.

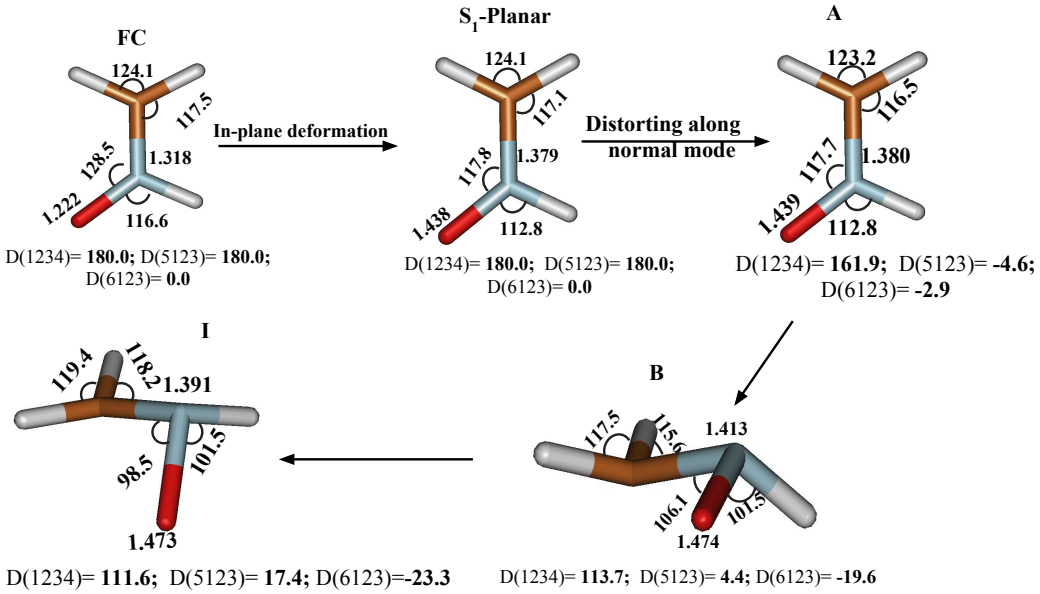

Figure 6.13: Key geometrical parameters of structures along FC→ MECI path.

From these calculations, it is clear that points on CI seam close to MECI region can be reached via a barrierless MEPs as shown in Figure 6.13. This strongly suggests that it might be possible to reach S_1-Anti and MECI directly from FC region via a barrierless pathway involving non-planar geometries. Attempts to compute such a MEP by starting from displaced FC geometry involved also led to geometries similar to S_1-Anti structure. However, the calculations encountered convergence issues with CASSCF method. We believe that such MEP exists and can be constructed with improved methods.

On the basis of stationary structures and computed MEPs, it can be identified that reaction coordinate connecting FC region to MECI is dominated by CN and NO bond elongations, NHO and (to a lesser extent) CH_2 pyramidalizations, and CH_2 torsional

motion along C-N bond. A combination of these defomations brings the molecule in close proximity of S_1/S_0 seam where facile non-adiabatic transition is expected to takes place via a peaked-CI. Our results clearly to point towards barrierless pathway connecting FC and MECI, although they have not been able to clarify the role of S_1-Anti minimum in this reaction step.

6.4.4.2 Ground State Pathways

The ground state branch of a photochemical pathway is a collection of possible reaction paths starting from MECI and proceeding on ground state PES leading to distinct photoproducts. Such paths can be determined by selecting a few suitable structures in vicinity of MECI and computing MEPs passing through them on ground state. Since many structures around MECI may lead to same ground state products, it is enough to compute MEPs along different relaxation valleys on ground state PES. Such valleys are characterized by steep decrease in energy and are separated by ridges.

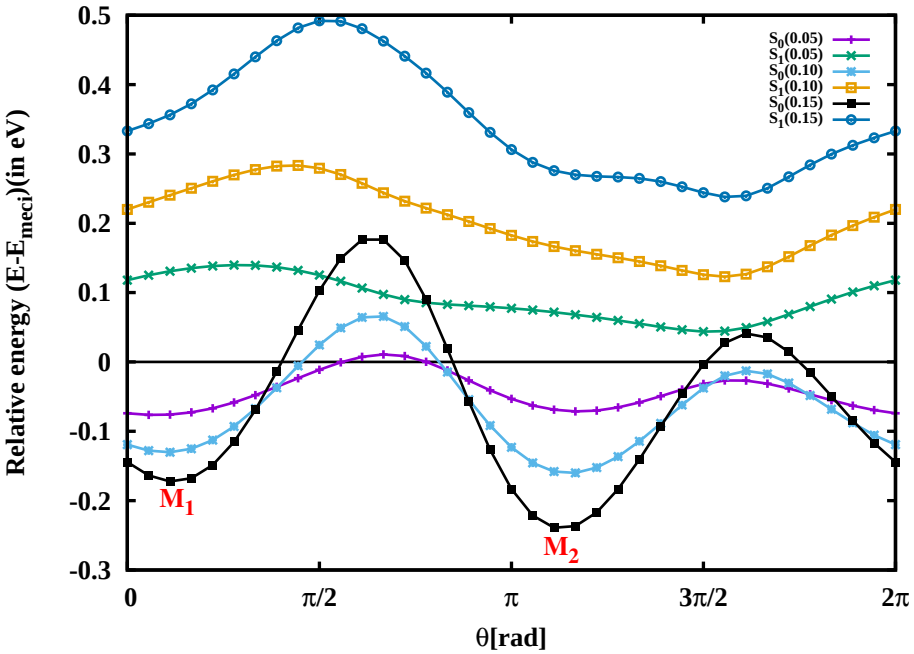

Figure 6.14: The energy profile of S_0 and S_1 states along circular cross-sections of radii, r=0.05, 0.10, 0.15 Å, centered on the vertex of MECI. M_1, and M_2 are two minimum points on the ground state PES representing two distinct valleys.

Identification of ground state valleys can be done using the intrinsic relaxation direction (IRD) method. The method involves computing a number of displacement

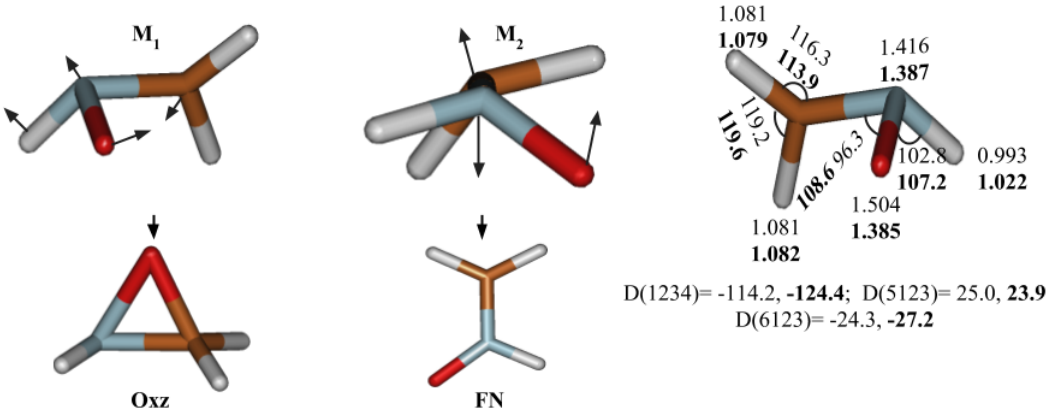

Figure 6.15: Initial gradient vectors at M_1 and and M_2 leading to Oxz and FN, respectively. Important geometrical parameters of M_1 and $\mathbf{M_2}$.

vectors at MECI geometry so that MEP computations can be initiated. The directions are selected to ensure computed MEPs lead to distinct ground state structure. A detailed description of IRD method can be found in Ref. [229, 268].

In this work, we have implemented a simplified variant of IRD by identifying possible relaxation directions by performing some restricted scan of PESs within the branching plane of MECI. We have performed SA2-CASSCF(5,6) energy calculations along circles of different radii (r =0.05, 0.10, 0.15 Å) in the plane formed by **g** and **h** vectors. The ground and excited state energy profile along these circular contours has been displayed in Figure 6.14. It can be seen that ground state PES displays two minima separated by two maxima, while excited state PES does not show such a feature. The two minima have been marked by M_1 and M_2 on the Figure. It can be noticed that with increasing radius, the depth of ground state minima increases. This suggests existence of two steep paths on the ground-state PES in the immediate vicinity of apex of the double-cone. These paths represent two preferential directions of downhill motion on ground state. As one moves along these paths, real valleys leading to ground state products develop.

We have computed two MEPs starting from M_1 and M_2 structures. The energy profiles of these MEPs have been shown in Figure 6.16. The structures at the end of MEP are found to be Oxz from M_1 and FN from M_2. The energy gradient vectors at M_1 and M_2 shown in Figure 6.15 confirm this. A comparision of some of the geometries along MEPs with their respective initial geometries shows that dominant distortions along M_1 MEP correspond to a large decrease in CNO angle from 96.3 ° to 56.3 °, while all other geometrical parameters slowly adjust towards their values in optimized Oxz structure. For M_2 MEP, such distortions correspond to loss of

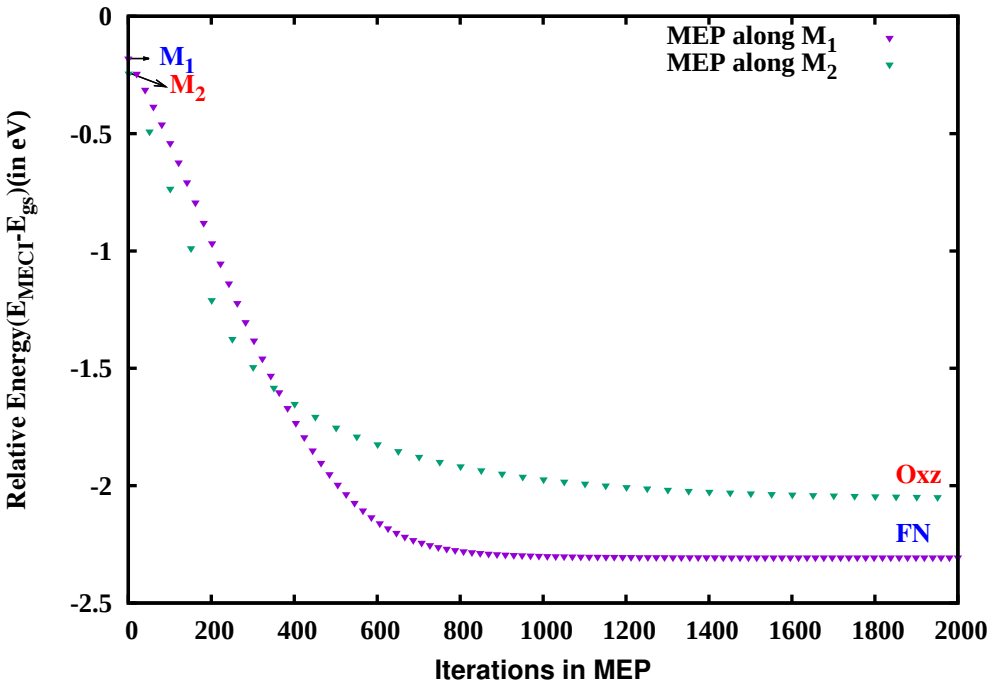

Figure 6.16: The ground state MEP starting in the vicinity of MECI. M_1 and M_2 points indicate initial points of two MEPs. FN and Oxz are two photo-products.

pyramidalization at NHO leading it back towards a planar conformation. We have confirmed that this reverts the molecule towards the starting FN stucture.

6.5 Non-adiabatic Dynamics

In this section, we discuss results of our non-adiabatic nuclear dynamics calculations on FN. The aim of study is to provide a dynamical picture for photochemical deactivation of FN on S_1 state. Although a barrierless path from FC region to MECI region has been proposed, the role of local minima such as S_1-Anti can not be ruled out completely. It can be noted that this minimum lies at somewhat higher energy (see Figure 6.9, MRCI results) as compared to MECI. Therefore, its involvement in electronic relaxation can be considered to be less significant. Given that MECI is not always involved, presence of local minima may influence S_1 decay time. This aspect is further investigated through non-adiabatic dynamics computations. Further motivation for this study is to identify particular nuclear deformations which are involved in electronic relaxations in photoelectrocyclic reaction FN $\rightarrow$ Oxz.

6.5.1 Computational Details

As in the previous chapter, we have carried out AIMS dynamics simulation using FMS-MOLPRO program [342]. The computational details of simulation are similar to the one given in the previous chapter. The main difference here is that, due to considerations discussed earlier, MS-CASPT2(5,6)/6-31G** method has been employed. After placement of an initial TBF on S_1 state (their phase-space position sampled from Wigner distribution of ground vibrational state), its nuclear dynamics has been followed for 200*fs*. A total of 35 independent TBFs have been used and these lead to 326 new TBFs generated through spawning. In MS-CASPT2 calculations, a level-shift of 0.2 has been applied and all 9 closed-shell orbitals of SA2-CASSCF(5,6) have not been correlated. The basis choice of 6-31G** instead of cc-pVDZ used for static calculations is mainly due to limitations of program capabilities.

6.5.2 Results and Discussions

A plot of time evolution of electronic populations of FN averaged over initial TBFs is displayed in Figure 6.17. As in the study reported in Chapter 5, a latency period τ_0 is assumed within which S_1 population remains unchanged. After this period, time evolution of S_1 population can be approximately described by an exponential decay with a time constant τ_{12}. The S_1 population in Figure 6.17 has been fitted to a function as described in Chapter 5 (see Equation 5.1).

The time constants obtained from this fitting are $\tau_0 = 32.8\,fs$ and $\tau_{12} = 120.8\,fs$. The latency time in this case is rather short as compared to the previous case. This value is similar to latency times reported in other AIMS studies of Martinez and coworkers [343]. The overall S_1 life-time, $\tau = \tau_0 + \tau_{12} = 153.6\,fs$, is clearly indicative of ultrafast electronic relaxation. This short life-time confirms absence of any barriers of local minima along the reaction path from FC region to the CI region where the decay happens. This also indicates that S_1-Anti structure does not play any significant role in FN. However, it may play a role in substituted nitrones.

The evolution of important geometrical parameters averaged over trajectories is shown in Figure 6.18. Within first 20 *fs*, both CN and NO bonds undergo significant stretching by nearly 12% and 40% respectively (plots **a** and **b**). Large pyramidalization of NHO group (plot **d**) and torsional motion of CH_2 around C-N bond (plot **c**) are also seen. These figures confirm that initial motion is indeed towards S_1/S_0 CI region whose MECI is also characterized by same type of geometrical changes. The NHO pyramidalization angle changes up to 40 ° in a short time period of 20 *fs* and shows oscillations around 30 ° during the rest of simulation. The steady

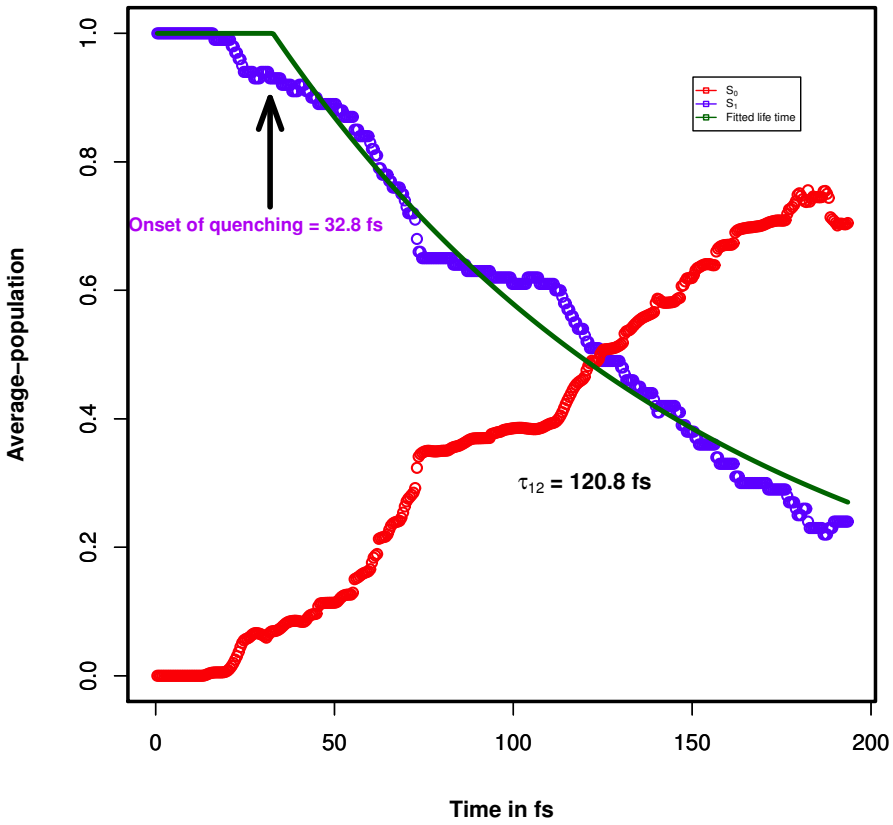

Figure 6.17: Population dynamics after photoexcitation of FN to S_1 state. The time evolution of average electronic population of S_0 and S_1 (shown in **red color** and **blue color**) and the fitted S_1 state (shown in **green color**). The latency time and the fitted life time are predicted to be 32.8 *fs* and 120.8 *fs*, respectively.

increase of CH_2 torsion angle (plot **c**) during the entire simulation indicates efficient conversion towards Oxz. The changes in oscillatory behaviour of bond lengths (plots **a** and **b**) after about 100 *fs* signal completion of non-adiabatic population transfer.

A representative trajectory has been chosen for further analysis. Figure 6.19 shows snap shots of this trajectory on excited state at selected times. It can be noticed that initial motion involves CN and NO stretching within first 20 *fs*. Out-of-plane motions *i.e* pyramidalization and twisting of NHO and CH_2 groups start after 20*fs*. The last two snapshots have been taken at 25 and 55 *fs* where spawning events occur. Although these structures are somewhat different, they are still twisted and pyramidalized. Therefore, it can be understood that the molecule remains in pyramidalized and twisted conformational state. This two-step relaxation (bond deformations followed by initiation of out-of-plane motions) is in accordance with established picture of

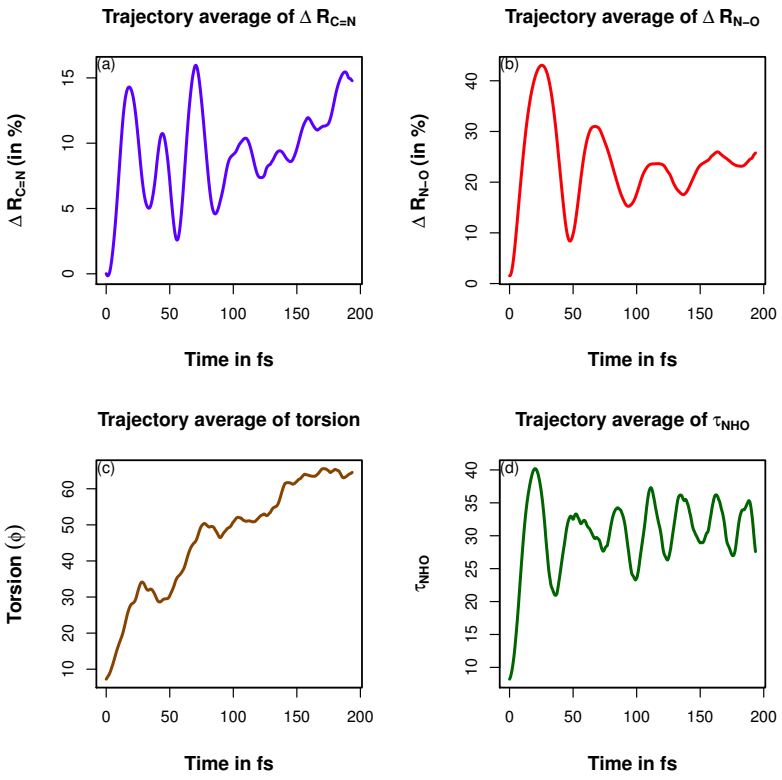

Figure 6.18: The trajectory average of in-plane and out-of-plane coordinates during the simulation. Plots **a** and **b** show relative changes in CN and NO bond lengths, respectively. Plots **c** and **d** show torsion (ϕ) around the CN bond and pyramidalization of NHO group.

retinal chromophore dynamics [401].

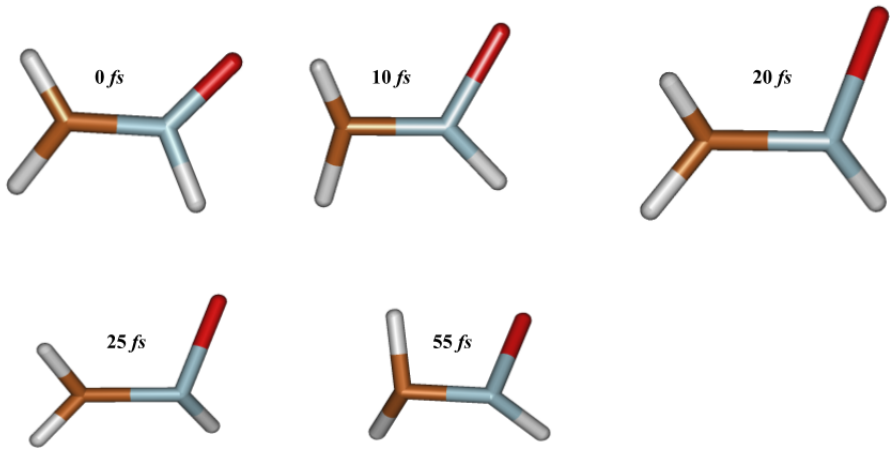

Figure 6.19: Snap shots along a representative trajectory moving on excited surface.

To understand the effect of out-of-plane motions on population transfer, in Figure 6.20 we have plotted expectation values of pyramidalization (τ_{NHO}) and

twisting coordinates (ϕ) over a time period covering first two spawning events. These plots are for another representative trajectory whose initial geometry is non-planar. This clearly illustrates that population transfer requires substantial amount of pyramidalization and twisting motions need to happen to access the CI region. This fact could not be clear from static studies as in MECI structure only oxygen atom is displaced out-of-plane.

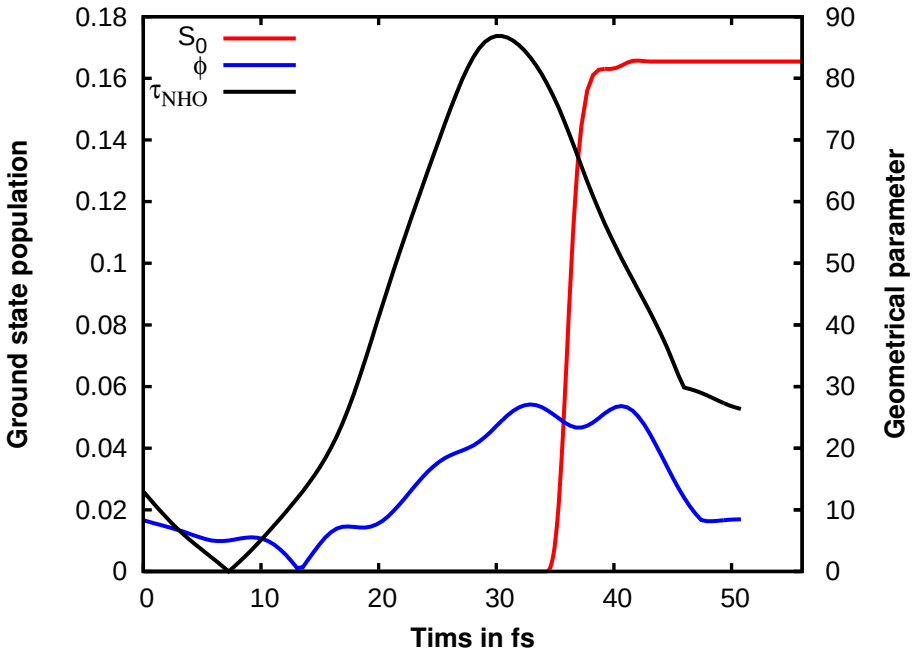

Figure 6.20: Expectation values of pyramidalization (τ_{NHO}) (**black color**) and the twisting coordinates (ϕ) (**blue color**) shown at right side y-axis and the ground state population (**red color**) shown at left side y-axis.

To characterize the regions where nonadiabatic transitions happen, we have collected all spawning regions and computed the rates of population transfer at each geometry of parent TBF as it travels through the region. For each geometry, two energetic quantities, the S_1-S_0 energy gap (denoted as $\triangle E_{\text{gap}}$) and the difference between electronic energy of S_1 state relative to the electronic energy of MECI structure (denoted as $\triangle E_{\text{excess}}$) have also been computed. It can be noted that electronic energy of MECI has been computed after reoptimizing its geometry at SA2-CASSCF(5,6)/6-31G** level. The results are presented as histogram plots in Figure 6.21, where the upper and lower panels correspond to $\triangle E_{\text{gap}}$ and $\triangle E_{\text{excess}}$, respectively.

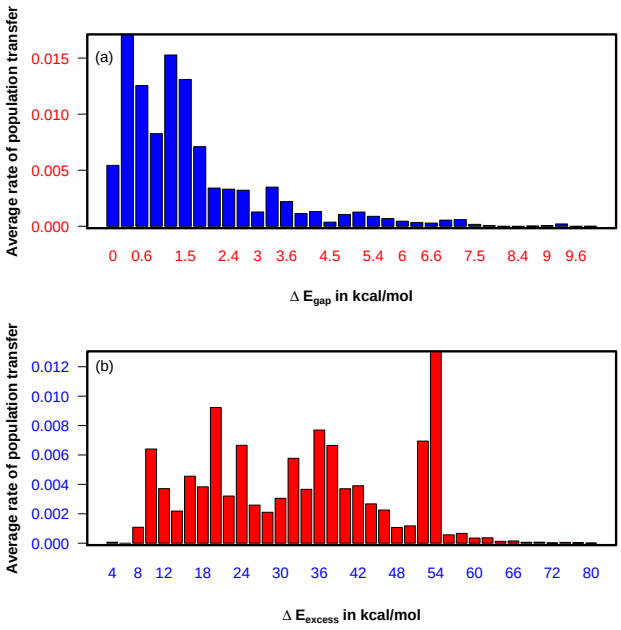

Figure 6.21: Average rate of population transfer as a function of $\triangle E_{\text{gap}}$ (in a) and $\triangle E_{\text{excess}}$ (in b).

The upper panel of Figure 6.21 shows how the average rate of population transfer per initial trajectory depends upon $\triangle E_{\text{gap}}$. This distribution shows an approximate Gaussian profile with a large width of (0-3 kcal/mol) and reaches a maximum at $\triangle E_{\text{gap}}$= 0.3 kcal/mol. It may be noted that geometries having $\triangle E_{\text{gap}}$ larger than 5 kcal/mol show a smaller rate of population transfer. This result is consistent with the fact that non-adiabatic transitions tend to occur at smaller energy gap of electronic states, but not necessarily at zero energy gap.

The lower panel shows how the average rate of population transfer depends on $\triangle E_{\text{excess}}$. The wide distribution in this graph shows that CI regions with higher in energy also contribute significantly to the population transfer. This is an indication that a large portion of CI seam energetically away from MECI region may also be involved in electronic relaxation.

6.6 Summary

In this chapter, we have performed a comprehensive computational study to understand photochemical deactivation of FN from its S_1 state. We have used different types of static multi-reference electronic structure calculations to develop a picture of molecular motions which are essential for the deactivation to take place. This picture is further supported by direct dynamics simulations which also indicates

time scales on which such motions occur.

We have carried out geometry optimization calculations to locate all conformers of FN on ground state PES, and estimated their energies relative to FN. These calculations establish that FN is separated from its isomers by energy barriers larger than 40 kcal/mol. Therefore, experimentally reported *cis-trans* and [1,3]-electrocyclization reactions of substitued nitrones do not take place for FN on its ground state.

In absence of absorption spectrum of FN, we have computed electronic states at its ground state equilibirum geometry using multi-reference and EOM-CCSD methods. The calculations support that first four low-lying valence states S_1,S_2,S_3,S_4 have single excitation character and arise from $n \rightarrow \pi^*$, $\pi \rightarrow \pi^*$, $\pi \rightarrow \sigma^*$, and $n \rightarrow \sigma^*$ type of electron promotions. Dynamical electron correlations are found to be important for correct energy ordering of S_2 and S_3 states.It is also confirmed that CASSCF(5,6) active space is able to qualitatively describe for S_1 state.

To understand how FN moves from FC region to its photochemical funnel, geometry optimizations on S_1 state have been performed to locate three important structures - two stationary structures S_1-Planar and S_1-Anti and a structure corresponding to MECI on S_1/S_0 seam. While all three strucutres are characterized by C-N and N-O bond-weakening elongations, S_1-Anti and MECI show significant degree of NHO pyramidalization. Using a series of MEP calculations, existence of a barrierless pathway from FC to MECI passing through S_1-Planar has been shown. We have proposed that a direct barrierless pathway from FC to MECI exists. The reaction coordinate along this involves C-N and N-O stretchings, NHO pyramidalizations and CH_2 torsions along C-N bond. IRD computations from MECI confirm the presence of two valleys on ground state PES leading to formation of Oxz and FN.

The picture of photochemical relaxation suggested by static calculations has been confirmed from direct dynamics simulations. This confirms ultrafast nature of photorelaxation of FN on S_1 state and provides a decay time of 154 *fs*. Initial molecular motions as predicted by dynamics are in agreement with ones based on MEP calculations.

Chapter 7

Summary and Future Outlook

In the preceeding chapters , the theory and concepts of non-adiabatic effects are discussed and presented our research works on thier two important aspects, structural and dynamical. In this chapter, a summary of these works is presented and future directions are identified.

In Chapter 1 and Chapter 4, we have introduced and reviewed the current state-of-the-art modeling of non-adiabatic processes in molecular systems from both theoretical and computational perspectives. In Chapter 2 and Chapter 3, we have focused on understanding the structural aspects of conical intersection and thier seams. The focus of Chapter 5 and Chapter 6 had been to utilize *ab initio* static computations and methods of non-adiabatic dynamics to understand electronic relaxation and photochemical pathways in two small organic molecules.

7.1 Conical Intersection Seams

The works on structure of CI seams have been motivated by the fact that CI seam, which influences strength of non-adiabatic effects, is a highly complex multi-dimensional geometric entity and so far not fully characterized in detail except for small systems. In particular, there have been limited number of studies on global aspects of seams such as seam branch connectivities and their relation to 3-state intersections, etc. In Chapter 2, we have undertaken a study of global structural features of CI seam by considering a simple one-electron triatomic molecular system as a starting point. By a simple numerical approach to track a seam in the nuclear configuration space, a seam of this system exhibiting several branches of different types of CIs has been fully constructed in a large part of the coordinate space. A visualization of the seam in hyperspherical coordinates revealed an interesting seam-

connectivity pattern.

Motivating by the structure of CI seam in one-electron system, in Chapter 3 we have investigated the possibility to indirectly infer the local geometric/topographic structure of CI seam in polyatomic molecule using series of non-adiabatic coupling calculations (NACTs). Ethylene has been considered as a model system to explore the local seam structure at two of its MECIs. We have also considered H_3 system to obtain a better understanding of effect of seam on profiles of non-adibatic coupling along closed contours. The nature and position of peaks in this profiles indicate that the CI seam branch of ethylene exists close to CH_2-C plane.

In future, these works can be extended to exploring the possibility to include the seam information (its branches, geometry, confluences, and 3-SI points) within nuclear dynamics. Recent methods developed for construction of global multi-state adiabatic/diabatic PESs have highlighted the necessity of including such an information to obtain accurate results [115, 116, 145, 147, 148, 402–405]. Alternatively, we think that it may also be feasible to embed relevant seam information into the nuclear basis functions. Given the importance of NACTs in diabatization the work in Chapter 3 underlines the utility of knowing the location of CI seams in such a procedure.

7.2 Computational Photochemistry

The works reported in Chapters 5 and 6 are motivated by effect of substituents on relaxation behaviour of simple molecules, as these have often proved to be helpful in understanding the dynamics around CIs. Two distinct classes of substituents, methyl and heteroatom substitutions, were considered to obtain insight into the dynamics around CI in two prototype photochemical reactions, cis-trans isomerization and 1,3-electrocyclization.

In Chapter 5, we have attempted to explain the experimentally observed differences in electronic relaxation behaviour of acrolein with that of its methylated derivatives, despite similarities in their electronic structures. Our AIMS simulations clearly establish that ultrafast relaxation in S_2 state is indeed very similar for both acrolein and crotonaldehyde. Our studies did not turn out to be conclusive enough to attribute the experimentally observed differences to the corresponding differences in ultrafast relaxation from S_1 state.

In Chapter 6, the effect of heteroatom on photo-electrocylization reaction has been studied by taking formaldonitrone as a model system. We carried out a computational study on a prototype nitrone-oxaziridine system. Through multi-

reference static calculations, we have determined the photoproducts through FC reaction path studies. This was augmented with a 200fs two-state AIMS simulation to establish ultrafast deactivation and barrier-less relaxation from the S_1 state.

Now a days, substitutions around functional groups such as selective methylation of organic chromophores can be employed to decipher ultrafast CI-mediated dynamics in the excited states. In this direction, our works can be further extended to explore competitive dynamics of IC and ISC. The photochemistry of α, β-enones needs to be revisited by further quantum dynamical simulations at higher level of theory as well as inclusion of triplet states. The nitrone photodynamics arises as an interesting case of substituted ethylene. The methyl and deuterium substituents are expected to change the excited state dynamics and shall motivate new ultrafast experiments.

Appendix A

Details of Optimized Geometries of Acrolein and Crotonaldehyde

In this appendix, we give the Cartesian optimized geometries of acrolein (AC) and crotonaldehyde (CR) used in Chapter 5.

A.1 Acrolein

Table A.1: S_0, CAS(5,6)/cc-pvDZ, E_{S_0} = -190.841434794 au

Atom	X	Y	Z
C	0.592959	-0.732241	-0.000000
C	-0.505552	-1.506497	0.000000
C	0.512677	0.743412	-0.000000
O	1.483366	1.457517	0.000000
H	1.590185	-1.155475	-0.000000
H	-0.499088	1.175199	-0.000000
H	-1.500170	-1.075002	0.000000
H	-0.440375	-2.586266	-0.000000

Table A.2: S_0, MRCI(5,6)/cc-pvDZ, E_{S_0} = -191.3297071632

Atom	X	Y	Z
C	-0.506461	-1.503997	0.000000
C	0.602338	-0.735110	-0.000000
C	0.512042	0.742688	-0.000000
O	1.479003	1.477314	0.000000
H	1.605414	-1.162248	-0.000000
H	-0.521338	1.152495	-0.000000
H	-1.500998	-1.054865	0.000000
H	-0.452653	-2.591298	-0.000000

Table A.3: S_1, CAS(5,6)/cc-pvDZ, E_{S_1} = -190.72404158 au

Atom	X	Y	Z
C	-0.530085	-1.531694	0.000000
C	0.585088	-0.679752	0.000000
C	0.503519	0.693397	-0.000000
O	1.591619	1.493238	0.000000
H	1.575904	-1.119715	0.000000
H	-0.422843	1.253534	-0.000000
H	-1.538628	-1.140132	0.000000
H	-0.403818	-2.603727	-0.000000

Table A.4: S_1, MRCI(5,6)/cc-pvDZ, E_{S_1} = -191.2070335192 au

Atom	X	Y	Z
C	-0.531415	-1.531182	0.000000
C	0.590298	-0.685675	0.000000
C	0.507953	0.696300	-0.000000
O	1.573904	1.517062	0.000000
H	1.587290	-1.127834	0.000000
H	-0.437187	1.245964	-0.000000
H	-1.542730	-1.127530	0.000000
H	-0.411350	-2.610779	-0.000000

Table A.5: T_1, CAS(5,6)/cc-pvDZ, E_{T_1} = -190.729472542 au

Atom	X	Y	Z
C	-0.525070	-1.530321	0.000000
C	0.579521	-0.686434	0.000000
C	0.501830	0.699196	-0.000000
O	1.590165	1.482396	0.000000
H	1.571601	-1.123631	-0.000000
H	-0.420011	1.265750	-0.000000
H	-1.534792	-1.140883	0.000000
H	-0.399367	-2.602719	-0.000000

Table A.6: T_1, MRCI(5,6)/cc-pvDZ, E_{T_1} = -191.2141123935 au

Atom	X	Y	Z
C	-0.526369	-1.531014	0.000000
C	0.582856	-0.691740	0.000000
C	0.505729	0.702979	-0.000000
O	1.576512	1.499811	0.000000
H	1.581555	-1.130545	-0.000000
H	-0.430523	1.265021	-0.000000
H	-1.539715	-1.131835	0.000000
H	-0.403654	-2.610487	-0.000000

Table A.7: T_2, CAS(5,6)/cc-pvDZ, E_{T_2} = -190.745327503 au

Atom	X	Y	Z
C	-0.592644	-1.532580	0.000000
C	0.604663	-0.679202	-0.000000
C	0.550726	0.765215	0.000000
O	1.551948	1.460415	0.000000
H	1.595832	-1.122047	0.000000
H	-0.443328	1.229611	0.000000
H	-0.944461	-1.977163	-0.923810
H	-0.944461	-1.977163	0.923810

Table A.8: T_2, MRCI(5,6)/cc-pvDZ, E_{T_2} = -191.2284787174 au

Atom	X	Y	Z
C	-0.577977	-1.545535	-0.000000
C	0.609021	-0.682080	0.000000
C	0.548708	0.764097	0.000000
O	1.554956	1.472063	-0.000000
H	1.613459	-1.115068	-0.000000
H	-0.462341	1.216261	0.000000
H	-0.981638	-1.940780	-0.932513
H	-0.981638	-1.940780	0.932513

Table A.9: S_1/T_2, SA2-CAS(5,6)/cc-pvDZ, E_{S_1/T_2} = -190.720171809 au and -190.720171809 au

Atom	X	Y	Z
C	-0.549118	-1.547033	0.000000
C	0.599839	-0.659650	0.000000
C	0.513808	0.701835	0.000000
O	1.603963	1.471216	0.000000
H	1.590732	-1.097220	0.000000
H	-0.435158	1.228107	0.000000
H	-1.555518	-1.153267	0.000000
H	-0.414922	-2.617338	0.000000

Table A.10: S_1/T_2, MRCI(5,6)/cc-pvDZ, E_{S_1/T_2} = -191.2044813531 au and -191.2044813405 au

Atom	X	Y	Z
C	-0.548579	-1.546388	0.000000
C	0.602435	-0.667861	0.000000
C	0.517624	0.708190	0.000000
O	1.587606	1.488808	0.000000
H	1.600142	-1.107431	0.000000
H	-0.448849	1.224008	0.000000
H	-1.558401	-1.141684	0.000000
H	-0.419896	-2.624360	0.000000

Table A.11: T_1/T_2, SA2-CAS(5,6)/cc-pvDZ, E_{T_1/T_2} = -190.720995685 au and -190.720995685 au

Atom	X	Y	Z
C	-0.558779	-1.555795	-0.000006
C	0.608294	-0.654763	-0.000061
C	0.521804	0.712145	0.000026
O	1.592703	1.465670	0.000066
H	1.598645	-1.092252	-0.000133
H	-0.440260	1.219362	0.000208
H	-1.563338	-1.158683	-0.000406
H	-0.422145	-2.625440	0.000575

Table A.12: T_1/T_2, MRCI(5,6)/cc-pvDZ, E_{T_1/T_2} = -191.2067265014 au and -191.2067264936 au

Atom	X	Y	Z
C	-0.558779	-1.555795	-0.000006
C	0.608294	-0.654763	-0.000061
C	0.521804	0.712145	0.000026
O	1.592703	1.465670	0.000066
H	1.598645	-1.092252	-0.000133
H	-0.440260	1.219362	0.000208
H	-1.563338	-1.158683	-0.000406
H	-0.422145	-2.625440	0.000575

Table A.13: T_2/S_0, SA2-CAS(5,6)/cc-pvDZ, E_{T_2/S_0} = -190.744936855 au and -190.744936846 au

Atom	X	Y	Z
C	-0.691359	-1.461874	0.006521
C	0.571818	-0.719173	0.035795
C	0.775950	0.705871	-0.064929
O	1.868858	1.187666	-0.308465
H	1.419913	-1.317789	-0.295364
H	-0.109523	1.349473	-0.003667
H	-0.828968	-1.843598	-1.012059
H	-1.120231	-2.158925	0.710431

Table A.14: T_2/S_0, MRCI(5,6)/cc-pvDZ, E_{T_2/S_0} = -191.2278133117 au and -191.2278134640 au

Atom	X	Y	Z
C	-0.685760	-1.440312	-0.039432
C	0.609229	-0.752924	-0.059632
C	0.755952	0.684652	-0.048065
O	1.851413	1.242714	-0.068845
H	1.534189	-1.331117	-0.090233
H	-0.181283	1.273312	-0.020345
H	-1.055472	-1.888968	-0.961719
H	-1.019530	-1.914167	0.883714

Table A.15: S_1/S_0, SA3-CAS(5,6)/cc-pvDZ, E_{S_1/S_0} = -190.685217908 au and -190.685218316 au

Atom	X	Y	Z
C	-0.658036	-0.119698	-0.010113
C	0.814824	-0.121652	-0.220373
C	1.569542	0.884561	0.120873
O	2.904572	1.247086	0.092344
H	-1.080348	-0.678525	0.816773
H	-1.317268	0.064872	-0.850194
H	1.265098	-0.998107	-0.675176
H	1.287326	1.842421	0.587846

Table A.16: S_1/S_0, MRCI(5,6)/cc-pvDZ, E_{S_1/S_0} = -191.1720338054 au -191.1720334301 au

Atom	X	Y	Z
C	-0.656830	-0.132086	-0.016281
C	0.814880	-0.127339	-0.222635
C	1.579929	0.881464	0.118821
O	2.883853	1.271791	0.108322
H	-1.091547	-0.636143	0.846411
H	-1.330044	0.113261	-0.837186
H	1.279572	-1.002965	-0.679044
H	1.269383	1.844339	0.592586

Table A.17: S_2/S_1, SA3-CAS(5,6)/cc-pvDZ, E_{S_2/S_1} = -190.613489845 au and -190.613490094 au

Atom	X	Y	Z
C	-1.762795	-0.002749	-0.463393
C	-0.406856	-0.268895	0.052521
C	0.361459	0.810508	0.695086
O	-0.396000	1.305966	1.692620
H	1.032248	1.503433	0.199721
H	-1.874709	0.738033	-1.247886
H	-2.637161	-0.189927	0.150095
H	-0.027419	-1.283464	0.091122

Table A.18: S_1-TS, SA3-CAS(5,6)/cc-pvDZ, E_{S_1} = -190.702480252 au

Atom	X	Y	Z
C	0.000276	0.132265	-1.940958
C	0.008186	-0.408286	-0.562436
C	-0.008787	0.371758	0.530421
O	-0.002368	-0.088693	1.795318
H	0.028699	-1.486401	-0.428314
H	-0.029644	1.454868	0.504890
H	0.923016	0.176160	-2.506569
H	-0.923039	0.148573	-2.507099

Table A.19: S_2, SA3-CAS(5,6)/cc-pvDZ, E_{S_2} = -190.615387515 au

Atom	X	Y	Z
C	-0.007819	0.121552	-1.976675
C	0.006944	-0.415853	-0.607970
C	0.065450	0.419537	0.551787
O	-0.115282	-0.108695	1.809984
H	-0.093551	-1.482652	-0.443315
H	0.223620	1.487622	0.489250
H	0.629828	-0.311095	-2.735914
H	-0.814318	0.764158	-2.308787

Table A.20: S_2,MRCI(5,6)/cc-pvDZ, E_{S_2} = -191.0998108968 au

Atom	X	Y	Z
C	-0.014315	0.113498	-1.971279
C	-0.016664	-0.414853	-0.603701
C	0.072477	0.410218	0.544491
O	-0.038761	-0.104897	1.826134
H	-0.088521	-1.492330	-0.436411
H	0.226784	1.487772	0.457529
H	0.706609	-0.246389	-2.704824
H	-0.809989	0.768852	-2.327511

A.2 Crotonaldehyde

Table A.21: S_0, CAS(5,6)/cc-pvDZ, E_{S_0} = -229.884027479 au

Atom	X	Y	Z
C	-2.540832	0.195883	0.000000
C	-1.163273	-0.399157	-0.000000
C	-0.014144	0.299569	-0.000000
C	1.303840	-0.363743	0.000000
O	2.348957	0.236892	-0.000000
H	1.294656	-1.464096	0.000000
H	-0.003691	1.383640	-0.000000
H	-1.108660	-1.484979	-0.000000
H	-2.506959	1.285686	0.000000
H	-3.101332	-0.131007	-0.879406
H	-3.101332	-0.131007	0.879406

Table A.22: S_0, MRCI(5,6)/cc-pvDZ, E_{S_0} = -230.4851186700

Atom	X	Y	Z
C	-2.540608	0.192685	0.000000
C	-1.161501	-0.396972	-0.000000
C	-0.011574	0.309355	-0.000000
C	1.302168	-0.363818	0.000000
O	2.364174	0.223952	-0.000000
H	1.265033	-1.473665	0.000000
H	-0.003020	1.399262	-0.000000
H	-1.096502	-1.488338	-0.000000
H	-2.508591	1.287563	0.000000
H	-3.102444	-0.139211	-0.882967
H	-3.102444	-0.139211	0.882967

Table A.23: S_1, CAS(5,6)/cc-pvDZ, E_{S_1} = -229.764580488 au

Atom	X	Y	Z
C	-2.540926	0.211182	-0.000000
C	-1.194813	-0.449917	0.000000
C	0.019597	0.252152	0.000000
C	1.259711	-0.347309	0.000000
O	2.412961	0.359365	0.000000
H	1.427650	-1.416447	0.000000
H	-0.006164	1.336823	-0.000000
H	-1.168658	-1.534223	0.000000
H	-2.451811	1.298891	-0.000000
H	-3.124565	-0.077195	-0.879374
H	-3.124565	-0.077195	0.879374

Table A.24: S_1, MRCI(5,6)/cc-pvDZ, E_{S_1} = -230.3614653263 au

Atom	X	Y	Z
C	-2.540452	0.209329	-0.000000
C	-1.194701	-0.450789	0.000000
C	0.017134	0.257983	0.000000
C	1.263436	-0.343666	-0.000000
O	2.426185	0.337330	0.000000
H	1.416514	-1.424341	0.000000
H	-0.011521	1.348219	-0.000000
H	-1.162137	-1.540954	0.000000
H	-2.448274	1.301976	-0.000000
H	-3.128957	-0.079183	-0.882852
H	-3.128957	-0.079183	0.882852

Table A.25: T_1, CAS(5,6)/cc-pvDZ, E_{T_1} = -229.769876847 au

Atom	X	Y	Z
C	-2.540284	0.212534	-0.000000
C	-1.191822	-0.445138	0.000000
C	0.011287	0.250379	0.000000
C	1.263870	-0.351557	-0.000000
O	2.402683	0.360061	0.000000
H	1.438375	-1.419134	0.000000
H	-0.011145	1.335154	-0.000000
H	-1.167121	-1.529907	0.000000
H	-2.454049	1.300495	-0.000000
H	-3.122695	-0.077871	-0.879397
H	-3.122695	-0.077871	0.879397

Table A.26: T_1, MRCI(5,6)/cc-pvDZ, E_{T_1} = -230.3683082563 au

Atom	X	Y	Z
C	-2.540009	0.211666	-0.000000
C	-1.192456	-0.446974	0.000000
C	0.008189	0.253883	0.000000
C	1.268193	-0.348391	-0.000000
O	2.411395	0.344304	0.000000
H	1.434976	-1.425814	0.000000
H	-0.017051	1.344345	-0.000000
H	-1.162599	-1.537587	0.000000
H	-2.448771	1.304446	-0.000000
H	-3.127548	-0.077677	-0.882976
H	-3.127548	-0.077677	0.882976

Table A.27: T_2, CAS(5,6)/cc-pvDZ, E_{T_2} = -229.786543159 au

Atom	X	Y	Z
C	-0.589820	-1.511636	0.006534
C	0.608405	-0.652435	-0.016987
C	0.550861	0.790092	0.037942
C	-1.085360	-2.167954	-1.252203
O	1.547714	1.492013	0.016917
H	1.601073	-1.090348	-0.076912
H	-0.444072	1.248615	0.101410
H	-0.832918	-1.994886	0.948814
H	-2.081103	-2.589796	-1.106683
H	-1.130312	-1.456021	-2.079506
H	-0.421463	-2.984640	-1.561079

Table A.28: T_2, MRCI(5,6)/cc-pvDZ, E_{T_2} = -230.3837613438 au

Atom	X	Y	Z
C	-0.571011	-1.529546	0.012123
C	0.614265	-0.658711	-0.006635
C	0.543073	0.784472	0.025748
C	-1.087532	-2.154730	-1.251998
O	1.540066	1.503567	0.003508
H	1.620699	-1.084393	-0.052675
H	-0.470175	1.226127	0.073339
H	-0.859734	-1.977679	0.964594
H	-2.088687	-2.575472	-1.103952
H	-1.134427	-1.421835	-2.067758
H	-0.429746	-2.972725	-1.589712

Table A.29: S_1/T_2, SA2-CAS(5,6)/cc-pvDZ, E_{S_1/T_2} = -229.760698588 au and -229.760698691 au

Atom	X	Y	Z
C	-2.548679	0.209995	-0.000000
C	-1.213117	-0.467624	0.000000
C	0.044756	0.254356	0.000000
C	1.273609	-0.338766	-0.000000
O	2.398616	0.384996	0.000000
H	1.407468	-1.415236	0.000000
H	0.017603	1.338147	-0.000000
H	-1.185065	-1.550324	0.000000
H	-2.446483	1.296459	-0.000000
H	-3.137077	-0.070298	-0.879230
H	-3.137077	-0.070298	0.879230

Table A.30: S_1/T_2, MRCI(5,6)/cc-pvDZ, E_{S_1/T_2} = -230.3591107606 au and -230.3591107593 au

Atom	X	Y	Z
C	-2.546958	0.209228	0.000000
C	-1.211667	-0.465997	-0.000000
C	0.037868	0.258348	-0.000000
C	1.279072	-0.337393	0.000000
O	2.406653	0.366265	0.000000
H	1.400831	-1.424027	0.000000
H	0.008466	1.348203	-0.000000
H	-1.178343	-1.554881	0.000000
H	-2.443514	1.300659	-0.000000
H	-3.139758	-0.072897	-0.882533
H	-3.139758	-0.072897	0.882533

Table A.31: T_1/T_2, SA2-CAS(5,6)/cc-pvDZ, E_{T_1/T_2} = -229.761532836 au and -229.761551266 au

Atom	X	Y	Z
C	-2.554289	0.208847	-0.000236
C	-1.223121	-0.475107	0.000301
C	0.054583	0.259617	0.000266
C	1.287971	-0.334319	-0.000225
O	2.390260	0.377622	-0.000293
H	1.399442	-1.415979	-0.000752
H	0.025839	1.342814	0.000604
H	-1.191567	-1.557087	0.000552
H	-2.446552	1.294803	-0.000409
H	-3.144586	-0.067793	-0.879547
H	-3.145105	-0.067462	0.878829

Table A.32: T_1/T_2, MRCI(5,6)/cc-pvDZ, E_{T_1/T_2} = -230.3613312348 au and -230.3613305547 au

Atom	X	Y	Z
C	-2.556672	0.207719	0.000117
C	-1.225635	-0.472596	-0.000143
C	0.045588	0.268277	-0.000160
C	1.297573	-0.323973	0.000355
O	2.391322	0.377480	0.000436
H	1.396013	-1.415994	0.000770
H	0.013551	1.357611	-0.000578
H	-1.187031	-1.560545	-0.000544
H	-2.449486	1.298712	0.000752
H	-3.151425	-0.071228	-0.882416
H	-3.151572	-0.072243	0.882224

Table A.33: T_2/S_0, SA2-CAS(5,6)/cc-pvDZ, E_{T_2/S_0} = -229.775761892 au and -229.775762086 au

Atom	X	Y	Z
C	-0.674650	-1.463184	-0.015132
C	0.582223	-0.709791	0.024219
C	0.786547	0.717575	-0.067810
C	-1.294422	-2.404032	0.975713
O	1.878687	1.204199	-0.299856
H	1.439405	-1.302658	-0.296891
H	-0.101817	1.358931	-0.015936
H	-0.820504	-1.809371	-1.044732
H	-2.246143	-2.786505	0.606538
H	-0.610119	-3.249883	1.075848
H	-1.451867	-1.985835	1.974738

Table A.34: S_1/S_0, SA2-CAS(5,6)/cc-pvDZ, E_{S_1/S_0} = -229.726778298 au -229.726778934 au

Atom	X	Y	Z
C	-0.781517	-1.176535	0.236636
C	-0.124471	0.073539	-0.271734
C	1.354061	0.108421	-0.466322
C	2.143770	0.740719	0.355420
O	3.492888	0.999628	0.520939
H	-0.720980	0.707425	-0.921411
H	1.773986	-0.412146	-1.322107
H	1.889215	1.321877	1.257208
H	-1.837920	-1.010916	0.459215
H	-0.725918	-1.985263	-0.504156
H	-0.288048	-1.538328	1.142174

Table A.35: S_1/S_0, MRCI(5,6)/cc-pvDZ, E_{S_1/S_0} = -230.3273451688 au and -230.3273447913 au

Atom	X	Y	Z
C	-0.775995	-1.170453	0.246548
C	-0.122676	0.065917	-0.292168
C	1.353520	0.110797	-0.480875
C	2.145580	0.731722	0.357329
O	3.465078	1.004637	0.561868
H	-0.734737	0.735645	-0.898128
H	1.790029	-0.393878	-1.344479
H	1.857107	1.295738	1.275263
H	-1.835534	-1.003156	0.476993
H	-0.725498	-1.999644	-0.480593
H	-0.268547	-1.518006	1.156467

Table A.36: S_2/S_1, SA2-CAS(5,6)/cc-pvDZ, E_{S_2/S_1} = -229.656634632 au and -229.656636207 au

Atom	X	Y	Z
C	-1.749461	0.018369	-0.472978
C	-0.388428	-0.267320	0.024878
C	0.376847	0.792441	0.701597
C	-2.962621	-0.252205	0.367664
O	-0.388704	1.266276	1.703773
H	1.057995	1.493188	0.232433
H	-1.822212	0.821178	-1.202063
H	-0.013521	-1.284927	0.040588
H	-3.876515	-0.176702	-0.224654
H	-2.920276	-1.249322	0.813169
H	-3.028620	0.471233	1.188681

Table A.37: S_2, SA2-CAS(5,6)/cc-pvDZ, E_{S_2} = -229.656088216 au

Atom	X	Y	Z
C	0.017108	0.144618	-1.945153
C	-0.033975	-0.404922	-0.577377
C	0.149114	0.407649	0.586148
C	-1.047488	1.070790	-2.461569
O	-0.006322	-0.109013	1.850839
H	-0.222939	-1.460881	-0.420041
H	0.434801	1.449299	0.521682
H	0.588980	-0.414836	-2.677241
H	-0.726643	1.563020	-3.381383
H	-1.973143	0.524757	-2.683148
H	-1.297738	1.841875	-1.729244

Table A.38: S_1-TS, SA2-CAS(5,6)/cc-pvDZ, E_{S_1} = -229.743820271 au

Atom	X	Y	Z
C	0.040455	0.101518	-1.937941
C	0.058049	-0.413201	-0.545188
C	-0.048318	0.386123	0.528866
C	-1.249557	0.182979	-2.702789
O	-0.050457	-0.044622	1.804927
H	0.152482	-1.484537	-0.385750
H	-0.146422	1.464283	0.476771
H	0.951635	-0.028365	-2.513598
H	-1.120621	0.732403	-3.637280
H	-1.626402	-0.816016	-2.957029
H	-2.025591	0.678847	-2.114870

Appendix B

Details of MECI geometries for Ethylene NACT calculations

In this appendix, we give the Cartesian optimized meci geometries of ethylene which is used in NACTs calculations in chapter 3. These two meci's are optimized at SA3-CASSCF(6,6)/aug-cc-pvdz level of theory.

B.1 Twisted-pyramidalized MECI (tw-py)

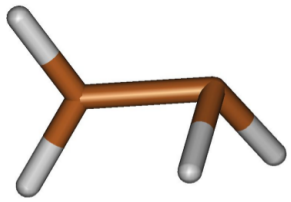

Table B.1: E_{S_0} = -77.897606874837 au E_{S_1} = -77.897604612826 au E_{S_2} = -77.772808829293 au

Atom	X	Y	Z
C	0.0000000000	0.0000000000	0.0000000000
C	0.0000000000	0.0000000000	1.4137910000
H	0.0000000000	0.9351949395	-0.5506081236
H	-1.1266388222	-0.4554432579	1.1837566514
H	0.3182500340	-0.9013091743	1.9467917013
H	-0.1562956078	-0.8902118582	-0.6105123940

B.2 Hydrogen-migration MECI (H-mig)

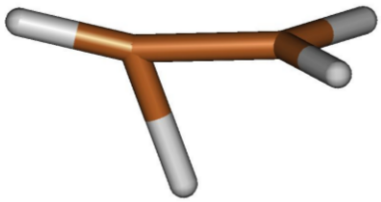

Table B.2: E_{S_0} = -77.877217385540 au E_{S_1} = -77.877187641045 au E_{S_2} = -77.775964097636 au

Atom	X	Y	Z
C	0.000000	0.000000	0.000000
C	0.000000	0.000000	1.371543
H	0.279545	0.000000	-1.023951
H	-0.100109	-0.933661	1.996840
H	0.015769	0.909789	1.979008
H	-1.275171	0.087559	0.390460

Bibliography

[1] M. Baer, Physics Reports **358**, 75 (2002).

[2] M. Baer, *Beyond Born-Oppenheimer: electronic nonadiabatic coupling terms and conical intersections* (John Wiley & Sons, Hoboken, New Jersey, USA, 2006).

[3] D. R. Yarkony, Chemical Reviews **112**, 481 (2011).

[4] X. Zhu and D. R. Yarkony, Molecular Physics **114**, 1983 (2016).

[5] I. G. Ryabinkin, L. Joubert-Doriol, and A. F. Izmaylov, Accounts of Chemical Research **50**, 1785 (2017).

[6] J. Von Neuman and E. Wigner, Physikalische Zeitschrift **30**, 467 (1929).

[7] E. Teller, Journal of Physical Chemistry **41**, 109 (1937).

[8] G. Herzberg and H. Longuet-Higgins, Discussions of the Faraday Society **35**, 77 (1963).

[9] G. A. Worth and L. S. Cederbaum, Annu. Rev. Phys. Chem. **55**, 127 (2004).

[10] B. F. E. Curchod and T. J. Martinez, Chemical Reviews **118**, 3305 (2018).

[11] R. Crespo-Otero and M. Barbatti, Chemical Reviews **118**, 7026 (2018).

[12] F. Bernardi, M. Olivucci, and M. A. Robb, Chemical Society Reviews **25**, 321 (1996).

[13] M. Garavelli, Theoretical Chemistry Accounts: Theory, Computation, and Modeling (Theoretica Chimica Acta) **116**, 87 (2006).

[14] M. Barbatti, M. Ruckenbauer, and H. Lischka, The Journal of Chemical Physics **122**, 11614 (2005).

[15] M. Ben-Nun and T. J. Martinez, Chemical Physics Letters **298**, 57 (1998).

[16] M. Baer and A. Alijah, Chemical Physics Letters **319**, 489 (2000).

[17] O. Gessner, E. t.-H. Chrysostom, A. Lee, D. Wardlaw, M.-L. Ho, S.-J. Lee, B.-M. Cheng, M. Zgierski, I.-C. Chen, J. Shaffer, *et al.*, Faraday Discussions **127**, 193 (2004).

[18] A. Lee, J. Coe, S. Ullrich, M.-L. Ho, S.-J. Lee, B.-M. Cheng, M. Zgierski, I. Chen, T. Martinez, and A. Stolow, The Journal of Physical Chemistry A **111**, 11948 (2007).

[19] A. Stolow, Annu. Rev. Phys. Chem. **68**, (2017).

[20] O. Schalk, A. E. Boguslavskiy, and A. Stolow, The Journal of Physical Chemistry A **114**, 4058 (2010).

[21] J. Splitter and M. Calvin, The Journal of Organic Chemistry **23**, 651 (1958).

[22] J. S. Splitter and M. Calvin, The Journal of Organic Chemistry **30**, 3427 (1965).

[23] J. S. Splitter and M. Calvin, Tetrahedron Letters **9**, 1445 (1968).

[24] J. S. Splitter, T.-M. Su, H. Ono, and M. Calvin, Journal of the American Chemical Society **93**, 4075 (1971).

[25] A. E. DePrince III and D. A. Mazziotti, The Journal of Chemical Physics **133**, 034112 (2010).

[26] T. Vladimiroff, Journal of Molecular Structure: THEOCHEM **401**, 141 (1997).

[27] M. Alcami, O. Mó, M. Yáñez, A. Luna, J.-P. Morizur, and J. Tortajada, The Journal of Physical Chemistry A **102**, 10120 (1998).

[28] B. Lasorne, G. A. Worth, and M. A. Robb, Wiley Interdisciplinary Reviews: Computational Molecular Science **1**, 460 (2011).

[29] M. Klessinger and J. Michl, *Excited states and photochemistry of organic molecules* (Wiley-VCH, New York, USA, 1995).

[30] A. W. Jasper, C. Zhu, S. Nangia, and D. G. Truhlar, Faraday Discussions **127**, 1 (2004).

[31] J. C. Tully, The Journal of Chemical Physics **137**, 22A301 (2012).

[32] W. Domcke, D. Yarkony, *et al.*, *Conical intersections: electronic structure, dynamics & spectroscopy* (World Scientific, Singapore, 2004), Vol. 15.

[33] T. Yonehara, K. Hanasaki, and K. Takatsuka, Chemical Reviews **112**, 499 (2011).

[34] M. Olivucci, *Computational photochemistry* (Elsevier, Amsterderm, Netherland, 2005), Vol. 16.

[35] H. Köppel, D. R. Yarkony, and H. Barentzen, *The Jahn-Teller Effect: Fundamentals and Implications for Physics and Chemistry* (Springer Science & Business Media, Springer Series in Chemical Physics, 2009), Vol. 97.

[36] M. Born and K. Huang, *Dynamical theory of crystal lattices* (Clarendon press, Oxford classic texts in the physical sciences., 1954).

[37] W. Kutzelnigg, Molecular Physics **90**, 909 (1997).

[38] N. C. Handy and A. M. Lee, Chemical Physics Letters **252**, 425 (1996).

[39] R. N. Porter, R. M. Stevens, and M. Karplus, The Journal of Chemical Physics **49**, 5163 (1968).

[40] H. C. Longuet-Higgins, U.öpik, M. H. L. Pryce, and R. A. Sack, Proceedings of the Royal Society of London A: Mathematical, Physical and Engineering Sciences **244**, 1 (1958).

[41] C. A. Mead, The Journal of Chemical Physics **70**, 2276 (1979).

[42] D. G. Truhlar and C. A. Mead, Physical Review A **68**, 032501 (2003).

[43] T. Pacher, L. Cederbaum, and H. Köppel, Advances in Chemical Physics **84**, 293 (1993).

[44] H. Köppel, W. Domcke, and L. Cederbaum, Advances in Chemical Physics **57**, 59 (1984).

[45] J. Michl, *Topics in Current Chemistry Fortschritte der Chemischen Forschung* (Springer, Springer, Berlin, Heidelberg, 1974), Vol. 46, pp. 1–59.

[46] S. Matsika and P. Krause, Annu. Rev. Phys. Chem. **62**, 621 (2011).

[47] R. Baer, D. M. Charutz, R. Kosloff, and M. Baer, The Journal of Chemical Physics **105**, 9141 (1996).

[48] C. A. Mead, The Journal of Chemical Physics **72**, 3839 (1980).

[49] B. Lepetit and A. Kuppermann, Chemical Physics Letters **166**, 581 (1990).

[50] B. Kendrick and R. T. Pack, The Journal of Chemical Physics **104**, 7502 (1996).

[51] J. C. Juanes-Marcos, A. J. C. Varandas, and S. C. Althorpe, The Journal of Chemical Physics **128**, 211101 (2008).

[52] S. Adhikari and G. D. Billing, The Journal of Chemical Physics **111**, 40 (1999).

[53] M. Baer, Chemical Physics Letters **35**, 112 (1975).

[54] C. A. Mead and D. G. Truhlar, The Journal of Chemical Physics **70**, 2284 (1979).

[55] D. R. Yarkony, The Journal of Physical Chemistry A **105**, 6277 (2001).

[56] I. Bersuker, *The Jahn-Teller Effect* (Cambridge University Press, Cambridge, 2006).

[57] J. J. Sakurai and J. Napolitano, *Modern Quantum Mechanics*, 2 ed. (Cambridge University Press, Cambridge University, 2017).

[58] D. J. Griffiths and D. F. Schroeter, *Introduction to Quantum Mechanics*, 3 ed. (Cambridge University Press, Cambridge University, 2018).

[59] L. S. Cederbaum, in *Conical Intersections* (Worldscientific Singapore, Singapore, 2004), Chap. 1, pp. 3–40.

[60] L. Piela, *Ideas of quantum chemistry* (Elsevier, USA, 2013).

[61] M. Born and R. Oppenheimer, Annalen der Physik **389**, 457 .

[62] E. F. Valeev and C. D. Sherrill, The Journal of Chemical Physics **118**, 3921 (2003).

[63] F. London, Z. Physik **74**, 132 (1932).

[64] W. Lichten, Phys. Rev. **131**, 229 (1963).

[65] H. Longuet-Higgins, Proceedings of the Royal Society of London. Series A, Mathematical and Physical Sciences **344**, 147 (1975).

[66] M. V. Berry, Proc. R. Soc. Lond. A **392**, 45 (1984).

[67] C. A. Mead, Reviews of Modern Physics **64**, 51 (1992).

[68] W. Lichten, Phys. Rev. **164**, 131 (1967).

[69] F. T. Smith, Phys. Rev. **179**, 111 (1969).

[70] C. A. Mead and D. G. Truhlar, The Journal of Chemical Physics **77**, 6090 (1982).

[71] M. Baer, Molecular Physics **40**, 1011 (1980).

[72] M. Baer and R. Englman, Chemical Physics Letters **335**, 85 (2001).

[73] H. Köppel, *Conical Intersections: Electronic Structure, Dynamics and Spectroscopy* (World Scientific, Singapore, 2004), pp. 175–204.

[74] M. Baer, S. H. Lin, A. Alijah, S. Adhikari, and G. D. Billing, Physical Review A **62**, 032506 (2000).

[75] M. Baer and R. Englman, Molecular Physics **75**, 293 (1992).

[76] H.-J. Werner and W. Meyer, The Journal of Chemical Physics **74**, 5802 (1981).

[77] C. Petrongolo, G. Hirsch, and R. J. Buenker, Molecular Physics **70**, 825 (1990).

[78] L. S. Cederbaum, J. Schirmer, and H. D. Meyer, Journal of Physics A: Mathematical and General **22**, 2427 (1989).

[79] A. Thiel and H. Köppel, The Journal of Chemical Physics **110**, 9371 (1999).

[80] H. Köppel, J. Gronki, and S. Mahapatra, The Journal of Chemical Physics **115**, 2377 (2001).

[81] H. Köppel and B. Schubert, Molecular Physics **104**, 1069 (2006).

[82] D. R. Yarkony, Rev. Mod. Phys. **68**, 985 (1996).

[83] S. C. Althorpe, *Conical Intersections: Theory, Computation and Experiment* (World Scientific, Singapore, 2011), Vol. 17, pp. 155–194.

[84] B. K. Kendrick, The Journal of Physical Chemistry A **107**, 6739 (2003).

[85] H. E. Zimmerman, Journal of the American Chemical Society **88**, 1564 (1966).

[86] E. Teller, Israel Journal of Chemistry **7**, 227 (1969).

[87] G. J. Atchity, S. S. Xantheas, and K. Ruedenberg, The Journal of Chemical Physics **95**, 1862 (1991).

[88] T. W. Keal, A. Koslowski, and W. Thiel, Theoretical Chemistry Accounts **118**, 837 (2007).

[89] A. G. Kutateladze, *Computational methods in photochemistry* (CRC Press Taylor & Francis Group, 6000 Broken Sound Parkway NW, Suite 300 Boca Raton, FL 33487-2742, 2005).

[90] M. A. Robb, M. Garavelli, M. Olivucci, and F. Bernardi, Reviews in Computational Chemistry **15**, 87 (2000).

[91] M. Dallos, H. Lischka, R. Shepard, D. R. Yarkony, and P. G. Szalay, The Journal of Chemical Physics **120**, 7330 (2004).

[92] D. R. Yarkony, *Conical intersections: electronic structure, dynamics and spectroscopy* (World Scientific, Singapore, 2004), Vol. 15, pp. 41–127.

[93] S. Matsika and D. R. Yarkony, The Journal of Chemical Physics **117**, 6907 (2002).

[94] S. Han and D. R. Yarkony, The Journal of Chemical Physics **119**, 5058 (2003).

[95] D. R. Yarkony, The Journal of Chemical Physics **114**, 2601 (2001).

[96] D. R. Yarkony, The Journal of Chemical Physics **112**, 2111 (2000).

[97] D. R. Yarkony, The Journal of Chemical Physics **114**, 2614 (2001).

[98] D. R. Yarkony, Theoretical Chemistry Accounts **98**, 197 (1998).

[99] M. Ben-Nun, F. Molnar, K. Schulten, and T. J. Martínez, Proceedings of the National Academy of Sciences **99**, 1769 (2002).

[100] G. J. Atchity and K. Ruedenberg, The Journal of Chemical Physics **110**, 4208 (1999).

[101] A. Szabo and N. S. Ostlund, *Modern quantum chemistry: introduction to advanced electronic structure theory* (Dover Publications Inc New edition edn, Newyork, USA, 2012).

[102] T. Helgaker, P. Jorgensen, and J. Olsen, *Molecular electronic-structure theory* (John Wiley & Sons, The Atrium, Southern Gate, Chichester, West Sussex PO19 8SQ, England, 2014).

[103] O. Christiansen, Theoretical Chemistry Accounts **116**, 106 (2006).

[104] H.-J. Werner, in *Advances in Chemical Physics* (John Wiley and Sons, Ltd, Singapore, 2007), pp. 1–62.

[105] J. F. Stanton and R. J. Bartlett, The Journal of Chemical Physics **99**, 5178 (1993).

[106] H.-J. Werner and P. J. Knowles, The Journal of Chemical Physics **89**, 5803 (1988).

[107] P. G. Szalay, T. Muller, G. Gidofalvi, H. Lischka, and R. Shepard, Chemical Reviews **112**, 108 (2011).

[108] H.-J. Werner, P. J. Knowles, G. Knizia, F. R. Manby, M. Schütz, *et al.*, MOLPRO, version 2015.1, a package of ab initio programs, 2015, see, http://www.molpro.net.

[109] H. Lischka, R. Shepard, I. Shavitt, R. Pitzer, M. Dallos, T. Muller, P. Szalay, F. Brown, R. Ahlrichs, H. Boehm, *et al.*, COLUMBUS, an ab initio electronic structure program, release 7.0, www.univie.ac.it/columbus,2012.

[110] D. J. Tannor, *Introduction to quantum mechanics: a time-dependent perspective* (University Science Books, Sausalito, CA USA, 2007).

[111] E. J. Heller, Accounts of Chemical Research **14**, 368 (1981).

[112] W. Domcke and G. Stock, Advances in Chemical Physics, Volume 100 **100**, 1 (1997).

[113] N. Balakrishnan, C. Kalyanaraman, and N. Sathyamurthy, Physics Reports **280**, 79 (1997).

[114] G. A. Worth and M. A. Robb, in *The Role of Degenerate States in Chemistry* (Wiley-Blackwell, 10.1002/0471433462.ch7, 2003), Chap. 7, pp. 355–431.

[115] A. J. C. Varandas, in *Conical Intersections: Electronic Structure, Dynamics and Spectroscopy* (World Scientific, Singapore, 2004), Chap. 5, pp. 205–270.

[116] B. R. L. Galvo, V. C. Mota, and A. J. C. Varandas, The Journal of Physical Chemistry A **119**, 1415 (2015).

[117] F. Gatti and C. Iung, Physics Reports **484**, 1 (2009).

[118] D. O. Harris, G. G. Engerholm, and W. D. Gwinn, The Journal of Chemical Physics **43**, 1515 (1965).

[119] H. D. Meyer, Numerical Methods of Quantum Dynamics Discrete Variable Representation (DVR) Integrators, 2017.

[120] J. C. Light and T. Carrington Jr, Advances in Chemical Physics **114**, 263 (2000).

[121] J. A. Bentley, R. E. Wyatt, M. Menou, and C. Leforestier, The Journal of Chemical Physics **97**, 4255 (1992).

[122] U. Manthe, H. Köppel, and L. Cederbaum, The Journal of Chemical Physics **95**, 1708 (1991).

[123] J. Lill, G. Parker, and J. Light, Chemical Physics Letters **89**, 483 (1982).

[124] Z. Bačić, R. Whitnell, D. Brown, and J. Light, Computer Physics Communications **51**, 35 (1988).

[125] Z. Bačić and J. C. Light, Annu. Rev. Phys. Chem. **40**, 469 (1989).

[126] M. Feit, J. Fleck Jr, and A. Steiger, Journal of Computational Physics **47**, 412 (1982).

[127] D. Kosloff and R. Kosloff, Journal of Computational Physics **52**, 35 (1983).

[128] C. Leforestier, R. Bisseling, C. Cerjan, M. Feit, R. Friesner, A. Guldberg, A. Hammerich, G. Jolicard, W. Karrlein, H.-D. Meyer, *et al.*, Journal of Computational Physics **94**, 59 (1991).

[129] H.-D. Meyer, F. Gatti, and G. A. Worth, *Multidimensional quantum dynamics: MCTDH theory and applications* (John Wiley & Sons, USA, 2009).

[130] M. H. Beck, A. Jäckle, G. Worth, and H.-D. Meyer, Physics Reports **324**, 1 (2000).

[131] U. Manthe, Quantum Molecular Dynamics with Wave Packets, 2002.

[132] H.-D. Meyer, Introduction to MCTDH, 2016.

[133] H.-D. Meyer, Wiley Interdisciplinary Reviews: Computational Molecular Science **2**, 351 (2012).

[134] T. A. Barckholtz, International Reviews in Physical Chemistry **17**, 435 (1998).

[135] T. A. Barckholtz and T. A. Miller, The Journal of Physical Chemistry A **103**, 2321 (1999).

[136] S. Mahapatra, Accounts of Chemical Research **42**, 1004 (2009).

[137] M. A. Robb, in *Conical Intersections: Theory, Computation and Experiment, edited by W. Domcke, D. R. Yarkony and H. Köppel* (World Scientific, Singapore, 2011), Chap. 1, pp. 3–50.

[138] T. Carrington, Faraday Discuss. Chem. Soc. **53**, 27 (1972).

[139] E. R. Davidson, Journal of the American Chemical Society **99**, 397 (1977).

[140] A. Varandas, J. Tennyson, and J. Murrell, Chemical Physics Letters **61**, 431 (1979).

[141] M. R. Manaa and D. R. Yarkony, The Journal of Chemical Physics **99**, 5251 (1993).

[142] M. J. Bearpark, M. A. Robb, and H. B. Schlegel, Chemical Physics Letters **223**, 269 (1994).

[143] I. Schapiro, F. Melaccio, E. N. Laricheva, and M. Olivucci, Photochem. Photobiol. Sci. **10**, 867 (2011).

[144] L. Blancafort, ChemPhysChem **15**, 3166 (2014).

[145] C. M. R. Rocha and A. J. C. Varandas, Phys. Chem. Chem. Phys. **20**, 10319 (2018).

[146] X. Zhu and D. R. Yarkony, Molecular Physics **108**, 2611 (2010).

[147] X. Zhu and D. R. Yarkony, The Journal of Chemical Physics **136**, 174110 (2012).

[148] X. Zhu and D. R. Yarkony, The Journal of Chemical Physics **137**, 22A511 (2012).

[149] S. Xantheas, S. T. Elbert, and K. Ruedenberg, The Journal of Chemical Physics **93**, 7519 (1990).

[150] S. S. Xantheas, G. J. Atchity, S. T. Elbert, and K. Ruedenberg, The Journal of Chemical Physics **94**, 8054 (1991).

[151] M. Riad Manaa and D. R. Yarkony, The Journal of Chemical Physics **93**, 4473 (1990).

[152] G. J. Atchity, K. Ruedenberg, and A. Nanayakkara, Theoretical Chemistry Accounts **96**, 195 (1997).

[153] M. S. Gordon, V.-A. Glezakou, and D. R. Yarkony, The Journal of Chemical Physics **108**, 5657 (1998).

[154] N. Matsunaga and D. R. Yarkony, The Journal of Chemical Physics **107**, 7825 (1997).

[155] G. Chaban, M. S. Gordon, and D. R. Yarkony, The Journal of Physical Chemistry A **101**, 7953 (1997).

[156] S. Matsika and D. R. Yarkony, The Journal of Physical Chemistry A **106**, 2580 (2002).

[157] S. Matsika and D. R. Yarkony, Journal of the American Chemical Society **125**, 10672 (2003).

[158] S. Han and D. R. Yarkony, The Journal of Chemical Physics **119**, 11561 (2003).

[159] S. Matsika and D. R. Yarkony, Journal of the American Chemical Society **125**, 12428 (2003).

[160] J. D. Coe and T. J. Martnez, Journal of the American Chemical Society **127**, 4560 (2005).

[161] J. D. Coe, M. T. Ong, B. G. Levine, and T. J. Martinez, The Journal of Physical Chemistry A **112**, 12559 (2008).

[162] S. Matsika, in *Conical Intersections: Theory, Computation and Experiment, ed. W. Domcke, D. R. Yarkony and H. Köppel* (World Scientific, Singapore, 2011), Chap. 3, pp. 83–116.

[163] J. Tennyson, O. L. Polyansky, N. F. Zobov, A. Alijah, and A. G. Csszr, Journal of Physics B: Atomic, Molecular and Optical Physics **50**, 232001 (2017).

[164] S. Mukherjee, D. Mukhopadhyay, and S. Adhikari, The Journal of Chemical Physics **141**, 204306 (2014).

[165] S. Ghosh, S. Mukherjee, B. Mukherjee, S. Mandal, R. Sharma, P. Chaudhury, and S. Adhikari, The Journal of Chemical Physics **147**, 074105 (2017).

[166] W. H. Miller, Annu. Rev. Phys. Chem. **41**, 245 (1990).

[167] F. Fernndez-Alonso and R. N. Zare, Annu. Rev. Phys. Chem. **53**, 67 (2002).

[168] S. C. Althorpe and D. C. Clary, Annu. Rev. Phys. Chem. **54**, 493 (2003).

[169] C. A. Mead, The Journal of Chemical Physics **72**, 3839 (1980).

[170] A. Kuppermann and Y.-S. M. Wu, Chemical Physics Letters **205**, 577 (1993).

[171] S. Mahapatra, H. Köppel, and L. S. Cederbaum, The Journal of Physical Chemistry A **105**, 2321 (2001).

[172] B. K. Kendrick, The Journal of Physical Chemistry A **107**, 6739 (2003).

[173] J. C. Juanes-Marcos and S. C. Althorpe, The Journal of Chemical Physics **122**, 204324 (2005).

[174] B. K. Kendrick, J. Hazra, and N. Balakrishnan, The Journal of Chemical Physics **145**, 164303 (2016).

[175] H. Conroy, The Journal of Chemical Physics **41**, 1341 (1964).

[176] H. Conroy and B. L. Bruner, The Journal of Chemical Physics **47**, 921 (1967).

[177] H. Conroy, The Journal of Chemical Physics **51**, 3979 (1969).

[178] E. H. Berkowitz and H. Stocker, The Journal of Chemical Physics **55**, 4606 (1971).

[179] D. Schrder and H. Schwarz, The Journal of Physical Chemistry A **103**, 7385 (1999).

[180] D. Mathur, Physics Reports **391**, 1 (2004).

[181] E. Ltstedt and K. Midorikawa, Journal of Physics B: Atomic, Molecular and Optical Physics **47**, 204018 (2014).

[182] B. Mukherjee, D. Mukhopadhyay, S. Adhikari, and M. Baer, Molecular Physics **0**, 1 (2018).

[183] B. R. Johnson, The Journal of Chemical Physics **73**, 5051 (1980).

[184] G. J. Atchity, K. Ruedenberg, and A. Nanayakkara, Theoretical Chemistry Accounts **96**, 195 (1997).

[185] F. T. Smith, Journal of Mathematical Physics **3**, 735 (1962).

[186] R. C. Whitten and F. T. Smith, Journal of Mathematical Physics **9**, 1103 (1968).

[187] A. Kuppermann, Chemical Physics Letters **32**, 374 (1975).

[188] Z. Xu, M. Baer, and A. J. Varandas, The Journal of Chemical Physics **112**, 2746 (2000).

[189] D. R. Yarkony, The Journal of Physical Chemistry A **105**, 2642 (2001).

[190] M. Baer, T. Vèrtesi, G. Halsz, A. Vibòk, and S. Suhai, Faraday Discuss. **127**, 337 (2004).

[191] T. Mori and T. J. Martínez, Journal of chemical theory and computation **9**, 1155 (2013).

[192] M. Baer, The Journal of Chemical Physics **107**, 2694 (1997).

[193] G. Halász, Á. Vibók, A. M. Mebel, and M. Baer, The Journal of Chemical Physics **118**, 3052 (2003).

[194] B. Mukherjee, S. Mukherjee, and S. Adhikari, Journal of Physics: Conference Series **759**, 012050 (2016).

[195] S. Mukherjee, D. Mukhopadhyay, and S. Adhikari, The Journal of Chemical Physics **141**, 204306 (2014).

[196] P. Puzari, B. Sarkar, and S. Adhikari, The Journal of Chemical Physics **121**, 707 (2004).

[197] C. Levi, G. Halász, Á. Vibók, I. Bar, Y. Zeiri, R. Kosloff, and M. Baer, The Journal of Chemical Physics **128**, 244302 (2008).

[198] C. Levi, G. Halász, Á. Vibók, I. Bar, Y. Zeiri, R. Kosloff, and M. Baer, International Journal of Quantum Chemistry **109**, 2482 (2009).

[199] C. Levi, G. Halász, Á. Vibók, I. Bar, Y. Zeiri, R. Kosloff, and M. Baer, The Journal of Physical Chemistry A **113**, 6756 (2009).

[200] A. Mebel, G. Halász, A. Vibók, A. Alijah, and M. Baer, The Journal of Chemical Physics **117**, 991 (2002).

[201] M. Baer, The Journal of Physical Chemistry A **104**, 3181 (2000).

[202] G. Halász, Á. Vibók, A. M. Mebel, and M. Baer, Chemical Physics Letters **358**, 163 (2002).

[203] gnes Vibk, G. J. Halsz, and M. Baer, Chemical Physics Letters **399**, 7 (2004).

[204] M. Karplus and K. Tang, Discussions of the Faraday Society **44**, 56 (1967).

[205] M. Baer, A. M. Mebel, and R. Englman, Chemical Physics Letters **354**, 243 (2002).

[206] G. Halász, A. Vibók, S. Suhai, and M. Baer, The Journal of Chemical Physics **127**, 244101 (2007).

[207] G. Halász, Á. Vibók, D. Hoffman, D. Kouri, and M. Baer, The Journal of Chemical Physics **126**, 154309 (2007).

[208] This part of the work has been carried out in collaboaration with Prof. Michael Baer.

[209] M. Ben-Nun and T. J. Martinez, Chemical Physics **259**, 237 (2000).

[210] M. Barbatti, J. Paier, and H. Lischka, The Journal of Chemical Physics **121**, 11614 (2004).

[211] A. Alijah and M. Baer, The Journal of Physical Chemistry A **104**, 389 (2000).

[212] S. Srivastava, M. Baer, and N. Sathyamurthy, Molecular Physics **113**, 436 (2015).

[213] R. Schoenlein, L. Peteanu, R. Mathies, and C. Shank, Science **254**, 412 (1991).

[214] D. Polli, P. Altoè, O. Weingart, K. M. Spillane, C. Manzoni, D. Brida, G. Tomasello, G. Orlandi, P. Kukura, R. A. Mathies, *et al.*, Nature **467**, 440 (2010).

[215] N. A. Anderson, J. J. Shiang, and R. J. Sension, The Journal of Physical Chemistry A **103**, 10730 (1999).

[216] D. A. Parthenopoulos and P. M. Rentzepis, Science **245**, 843 (1989).

[217] J. Burroughes, D. Bradley, A. Brown, R. Marks, K. Mackay, R. Friend, P. Burns, and A. Holmes, nature **347**, 539 (1990).

[218] Z. Shuai and Q. Peng, Physics Reports **537**, 123 (2014).

[219] M. Bixon and J. Jortner, The Journal of Chemical Physics **48**, 715 (1968).

[220] K. F. Freed, Accounts of Chemical Research **11**, 74 (1978).

[221] L. Salem, Science **191**, 822 (1976).

[222] H. E. Zimmerman, Accounts of Chemical Research **5**, 393 (1972).

[223] C. E. Crespo-Hernández, B. Cohen, P. M. Hare, and B. Kohler, Chemical Reviews **104**, 1977 (2004).

[224] C. Reichardt, C. Guo, and C. E. Crespo-Hernandez, The Journal of Physical Chemistry B **115**, 3263 (2011).

[225] J. Michl and V. Bonacic-Koutecky, *Electronic aspects of organic photochemistry* (Wiley, New York, USA, 1990).

[226] N. J. Turro, V. Ramamurthy, and J. C. Scaiano, *Principles of molecular photochemistry: an introduction* (University science books, Sausalito, California, 2009).

[227] C. Zener, in *Proc. R. Soc. Lond. A*, The Royal Society (PUBLISHER, ADDRESS, 1932), No. 833, pp. 696–702.

[228] M. Desouter-Lecomte and J.-C. Lorquet, The Journal of Chemical Physics **71**, 4391 (1979).

[229] M. Garavelli, P. Celani, M. Fato, M. J. Bearpark, B. R. Smith, M. Olivucci, and M. A. Robb, The Journal of Physical Chemistry A **101**, 2023 (1997).

[230] W. T. A. Van der Lugt and L. J. Oosterhoff, Journal of the American Chemical Society **91**, 6042 (1969).

[231] J. Michl, Mol. Photochem **4**, 243 (1972).

[232] L. Salem, Journal of the American Chemical Society **96**, 3486 (1974).

[233] V. Bonačić-Koutecký, J. Koutecký, and J. Michl, Angewandte Chemie International Edition **26**, 170 (1987).

[234] M. O. Trulson and R. A. Mathies, Journal of Physical Chemistry **94**, 5741 (1990).

[235] S. Pullen, L. A. Walker II, B. Donovan, and R. J. Sension, Chemical Physics Letters **242**, 415 (1995).

[236] D. R. Cyr and C. C. Hayden, The Journal of Chemical Physics **104**, 771 (1996).

[237] Q. Wang, R. W. Schoenlein, L. A. Peteanu, R. A. Mathies, and C. V. Shank, Science **266**, 422 (1994).

[238] A. Merer and R. S. Mulliken, Chemical Reviews **69**, 639 (1969).

[239] R. S. Mulliken and C. Roothaan, Chemical Reviews **41**, 219 (1947).

[240] R. S. Mulliken, The Journal of Chemical Physics **66**, 2448 (1977).

[241] P. G. Wilkinson and R. Mulliken, The Journal of Chemical Physics **23**, 1895 (1955).

[242] R. McDiarmid and E. Charney, The Journal of Chemical Physics **47**, 1517 (1967).

[243] R. Buenker, S. Peyerimhoff, and H. Hsu, Chemical Physics Letters **11**, 65 (1971).

[244] K. B. Wiberg, C. M. Hadad, J. B. Foresman, and W. A. Chupka, The Journal of Physical Chemistry **96**, 10756 (1992).

[245] W. Siebrand, F. Zerbetto, and M. Z. Zgierski, Chemical Physics Letters **174**, 119 (1990).

[246] H. Tao, T. Allison, T. Wright, A. Stooke, C. Khurmi, J. Van Tilborg, Y. Liu, R. Falcone, A. Belkacem, and T. Martinez, The Journal of Chemical Physics **134**, 244306 (2011).

[247] V. Bonačić-Koutecký, P. Bruckmann, P. Hiberty, J. Koutecký, C. Leforestier, and L. Salem, Angewandte Chemie International Edition **14**, 575 (1975).

[248] B. R. Brooks and H. F. Schaefer III, Journal of the American Chemical Society **101**, 307 (1979).

[249] J.-s. Ryu and B. S. Hudson, Chemical Physics Letters **245**, 448 (1995).

[250] M. Ben-Nun, J. Quenneville, and T. J. Martínez, The Journal of Physical Chemistry A **104**, 5161 (2000).

[251] M. Ben-Nun and T. J. Martinez, The Journal of Physical Chemistry A **103**, 10517 (1999).

[252] K. K. Baeck and T. J. Martinez, Chemical Physics Letters **375**, 299 (2003).

[253] A. Hazra, H. H. Chang, and M. Nooijen, The Journal of Chemical Physics **121**, 2125 (2004).

[254] W. Fuss, W. Schmid, and S. Trushin, Chemical Physics Letters **342**, 91 (2001).

[255] S. Lochbrunner, W. Fuss, W. E. Schmid, and K.-L. Kompa, The Journal of Physical Chemistry A **102**, 9334 (1998).

[256] S. Pedersen, L. Banares, and A. Zewail, The Journal of Chemical Physics **97**, 8801 (1992).

[257] R. J. Sension and B. S. Hudson, The Journal of Chemical Physics **90**, 1377 (1989).

[258] I. Ohmine, The Journal of Chemical Physics **83**, 2348 (1985).

[259] L. Freund and M. Klessinger, International Journal of Quantum Chemistry **70**, 1023 (1998).

[260] B. G. Levine and T. J. Martinez, Annu. Rev. Phys. Chem. **58**, 613 (2007).

[261] A. Migani, A. Sinicropi, N. Ferré, A. Cembran, M. Garavelli, and M. Olivucci, Faraday Discussions **127**, 179 (2004).

[262] C. Punwong, J. Owens, and T. J. Martinez, Urbana **51**, 61801 (2005).

[263] T. Mori, W. J. Glover, M. S. Schuurman, and T. J. Martinez, The Journal of Physical Chemistry A **116**, 2808 (2012).

[264] W. Fuss, S. Lochbrunner, A. Müller, T. Schikarski, W. Schmid, and S. Trushin, Chemical physics **232**, 161 (1998).

[265] M. A. Robb and M. Olivucci, Journal of Photochemistry and Photobiology A: Chemistry **144**, 237 (2001).

[266] B. E. Kohler, Chemical Reviews **93**, 41 (1993).

[267] E. Riedle, T. Weber, U. Schubert, H. Neusser, and E. Schlag, The Journal of Chemical Physics **93**, 967 (1990).

[268] P. Celani, M. A. Robb, M. Garavelli, F. Bernardi, and M. Olivucci, Chemical Physics Letters **243**, 1 (1995).

[269] H. Köppel, *"Vibronic coupling effects in spectroscopy and non-adiabatic transitions in Molecular Photodynamics" in Molecular Quantum Dynamics edited by F. Gatti* (Springer, Springer Heidelberg, 2014), pp. 147–180.

[270] G. Worth, M. Robb, and B. Lasorne, Molecular Physics **106**, 2077 (2008).

[271] M. Persico and G. Granucci, Theoretical Chemistry Accounts **133**, 1526 (2014).

[272] C. Leforestier, The Journal of Chemical Physics **68**, 4406 (1978).

[273] R. Car, Phys. Rev. Lett. **55**, 2471 (1985).

[274] D. Bohm, Phys. Rev. **85**, 166 (1952).

[275] B. F. Curchod and T. J. Martínez, Chemical Reviews **118**, 3305 (2018).

[276] J. C. Tully, The Journal of Chemical Physics **93**, 1061 (1990).

[277] W. Domcke and D. R. Yarkony, Annu. Rev. Phys. Chem. **63**, 325 (2012).

[278] M. Barbatti, R. Shepard, and H. Lischka, *Conical Intersections: Theory, Computation and Experiment* (World Scientific, Singapore, 2011), pp. 415–462.

[279] M. Barbatti, Wiley Interdisciplinary Reviews: Computational Molecular Science **1**, 620 (2011).

[280] E. Fabiano, T. Keal, and W. Thiel, Chemical Physics **349**, 334 (2008).

[281] C. Zhu, S. Nangia, A. W. Jasper, and D. G. Truhlar, The Journal of Chemical Physics **121**, 7658 (2004).

[282] G. Granucci, M. Persico, and A. Zoccante, The Journal of Chemical Physics **133**, 134111 (2010).

[283] L. Wang, A. Akimov, and O. V. Prezhdo, The Journal of Physical Chemistry Letters **7**, 2100 (2016).

[284] M. Barbatti, M. Ruckenbauer, F. Plasser, J. Pittner, G. Granucci, M. Persico, and H. Lischka, Wiley Interdisciplinary Reviews: Computational Molecular Science **4**, 26 (2014).

[285] E. J. Heller, The Journal of Chemical Physics **62**, 1544 (1975).

[286] E. J. Heller, Accounts of Chemical Research **39**, 127 (2006).

[287] D. Mendive-Tapia, B. Lasorne, G. A. Worth, M. A. Robb, and M. J. Bearpark, The Journal of Chemical Physics **137**, 22A548 (2012).

[288] B. Lasorne, M. Robb, and G. Worth, Physical Chemistry Chemical Physics **9**, 3210 (2007).

[289] M. Ben-Nun, T. J. Martinez, *et al.*, Advances in Chemical Physics **121**, 439 (2002).

[290] J. Quenneville, M. Ben-Nun, and T. J. Martınez, Journal of Photochemistry and Photobiology A: Chemistry **144**, 229 (2001).

[291] T. J. Martinez, M. Ben-Nun, and R. Levine, The Journal of Physical Chemistry **100**, 7884 (1996).

[292] M. Ben-Nun and T. J. Martinez, The Journal of Chemical Physics **108**, 7244 (1998).

[293] B. G. Levine, J. D. Coe, A. M. Virshup, and T. J. Martinez, Chemical Physics **347**, 3 (2008).

[294] E. J. Heller, The Journal of Chemical Physics **75**, 2923 (1981).

[295] S. Yang and T. J. Martínez, *Conical Intersections: Theory, Computation and Experiment* (World Scientific, Singapore, 2011), pp. 347–374.

[296] S. Yang, J. D. Coe, B. Kaduk, and T. J. Martínez, The Journal of Chemical Physics **130**, 04B606 (2009).

[297] D. V. Shalashilin and M. S. Child, Chemical physics **304**, 103 (2004).

[298] J. D. Coyle, *Introduction to organic photochemistry* (John Wiley & Sons, ADDRESS, 1986).

[299] K. N. Houk, R. J. Loncharich, J. F. Blake, and W. L. Jorgensen, Journal of the American Chemical Society **111**, 9172 (1989).

[300] A. Migani and M. Olivucci, *Conical intersections: Electronic structure, dynamics and spectroscopy* (World Scientific, Singapore, 2004), pp. 271–320.

[301] M. Reguero, M. Olivucci, F. Bernardi, and M. A. Robb, Journal of the American Chemical Society **116**, 2103 (1994).

[302] D. Schuster, In The Chemistry of Enones·, Patai, S., Rappoport, Z., Eds, 1989.

[303] C. Puzzarini, E. Penocchio, M. Biczysko, and V. Barone, The Journal of Physical Chemistry A **118**, 6648 (2014).

[304] J. Coomber and J. N. Pitts Jr, Journal of the American Chemical Society **91**, 547 (1969).

[305] E. P. Gardner, P. D. Sperry, and J. G. Calvert, Journal of Physical Chemistry **91**, 1922 (1987).

[306] S.-H. Jen and I.-C. Chen, The Journal of Chemical Physics **111**, 8448 (1999).

[307] K. W. Paulisse, T. O. Friday, M. L. Graske, and W. F. Polik, The Journal of Chemical Physics **113**, 184 (2000).

[308] N. C. Hlavacek, M. O. McAnally, and S. Drucker, The Journal of Chemical Physics **138**, 064303 (2013).

[309] M. El-Sayed, The Journal of Chemical Physics **36**, 573 (1962).

[310] W.-H. Fang, Journal of the American Chemical Society **121**, 8376 (1999).

[311] C. Chaudhuri and S.-H. Lee, Physical Chemistry Chemical Physics **13**, 7312 (2011).

[312] T. E. Graedel, D. T. Hawkins, and L. D. Claxton, *Atmospheric chemical compounds: sources, occurrence and bioassay* (Elsevier, ADDRESS, 2012).

[313] E. Zervas, X. Montagne, and J. Lahaye, Environmental science & technology **36**, 2414 (2002).

[314] D. E. Johnstone and J. R. Sodeau, Journal of the Chemical Society, Faraday Transactions **88**, 409 (1992).

[315] A. K. Ghosh, S. Datta, A. Mukhopadhyay, and T. Chakraborty, The Journal of Physical Chemistry A **117**, 8710 (2013).

[316] O. Bokareva, V. Bataev, and I. Godunov, Computational and Theoretical Chemistry **1149**, 8 (2019).

[317] O. Bokareva, V. Bataev, and I. Godunov, Journal of Molecular Structure: THEOCHEM **913**, 254 (2009).

[318] O. Schalk, M. S. Schuurman, G. Wu, P. Lang, M. Mucke, R. Feifel, and A. Stolow, The Journal of Physical Chemistry A **118**, 2279 (2014).

[319] G. Wu, A. E. Boguslavskiy, O. Schalk, M. S. Schuurman, and A. Stolow, The Journal of Chemical Physics **135**, 164309 (2011).

[320] S.-H. Lee, K.-C. Tang, I.-C. Chen, M. Schmitt, J. Shaffer, T. Schultz, J. G. Underwood, M. Zgierski, and A. Stolow, The Journal of Physical Chemistry A **106**, 8979 (2002).

[321] O. Schalk, A. E. Boguslavskiy, A. Stolow, and M. S. Schuurman, Journal of the American Chemical Society **133**, 16451 (2011).

[322] T. Wolf, T. S. Kuhlman, O. Schalk, T. Martínez, K. B. Møller, A. Stolow, and A.-N. Unterreiner, Physical Chemistry Chemical Physics **16**, 11770 (2014).

[323] O. Schalk, A. E. Boguslavskiy, M. S. Schuurman, R. Y. Brogaard, A. N. Unterreiner, A. Wrona-Piotrowicz, N. H. Werstiuk, and A. Stolow, The Journal of Physical Chemistry A **117**, 10239 (2013).

[324] S. P. Neville, Y. Wang, A. E. Boguslavskiy, A. Stolow, and M. S. Schuurman, The Journal of Chemical Physics **144**, 014305 (2016).

[325] G. Wu, S. P. Neville, O. Schalk, T. Sekikawa, M. N. Ashfold, G. A. Worth, and A. Stolow, The Journal of Chemical Physics **144**, 014309 (2016).

[326] A. Stolow, Faraday Discussions **163**, 9 (2013).

[327] R. J. MacDonell, O. Schalk, T. Geng, R. D. Thomas, R. Feifel, T. Hansson, and M. S. Schuurman, The Journal of Chemical Physics **145**, 114306 (2016).

[328] S. Oesterling, O. Schalk, T. Geng, R. D. Thomas, T. Hansson, and R. de Vivie-Riedle, Physical Chemistry Chemical Physics **19**, 2025 (2017).

[329] M. S. Schuurman and A. Stolow, Conical Intersections. Series: Advanced Series in Physical Chemistry, ISBN: 978-981-4313-44-5. WORLD SCIENTIFIC, Edited by Wolfgang Domcke, David R Yarkony and Horst Köppel, vol. 17, pp. 633-667 **17**, 633 (2011).

[330] H. Lischka, R. Shepard, R. M. Pitzer, I. Shavitt, M. Dallos, T. Müller, P. G. Szalay, M. Seth, G. S. Kedziora, S. Yabushita, *et al.*, Physical Chemistry Chemical Physics **3**, 664 (2001).

[331] H. Lischka, T. Müller, P. G. Szalay, I. Shavitt, R. M. Pitzer, and R. Shepard, Wiley Interdisciplinary Reviews: Computational Molecular Science **1**, 191 (2011).

[332] C. S. Page and M. Olivucci, Journal of Computational Chemistry **24**, 298 (2003).

[333] O. S. Bokareva, V. A. Bataev, V. I. Pupyshev, and I. A. Godunov, International Journal of Quantum Chemistry **108**, 2719 (2008).

[334] O. Bokareva, V. Bataev, V. Pupyshev, and I. Godunov, Spectrochimica Acta Part A: Molecular and Biomolecular Spectroscopy **73**, 654 (2009).

[335] B. Saha, M. Ehara, and H. Nakatsuji, The Journal of Chemical Physics **125**, 014316 (2006).

[336] F. Aquilante, V. Barone, and B. O. Roos, The Journal of Chemical Physics **119**, 12323 (2003).

[337] G. Cui, Y. Lu, and W. Thiel, Chemical Physics Letters **537**, 21 (2012).

[338] W.-H. Fang and D. L. Phillips, ChemPhysChem **3**, 889 (2002).

[339] W.-H. Fang, Accounts of Chemical Research **41**, 452 (2008).

[340] G. Cui and W. Thiel, The Journal of Chemical Physics **141**, 124101 (2014).

[341] J. P. Malhado and J. T. Hynes, The Journal of Chemical Physics **145**, 194104 (2016).

[342] B. G. Levine, J. D. Coe, A. M. Virshup, and T. J. Martinez, Chemical Physics **347**, 3 (2008).

[343] T. S. Kuhlman, W. J. Glover, T. Mori, K. B. Møller, and T. J. Martínez, Faraday Discussions **157**, 193 (2012).

[344] L. Liu, J. Liu, and T. J. Martinez, The Journal of Physical Chemistry B **120**, 1940 (2016).

[345] H. Tao, B. G. Levine, and T. J. Martinez, The Journal of Physical Chemistry A **113**, 13656 (2009).

[346] We would like to thank Prof. Naresh Patwari for his suggestions and discussion on this aspect.

[347] S. Sankararaman, *Pericyclic reactions: a textbook: reactions, applications and theory* (Vch Verlagsgesellschaft Mbh, ADDRESS, 2005).

[348] P. Sykes, *A guidebook to mechanism in organic chemistry* (Pearson Education India, ADDRESS, 1986).

[349] R. B. Woodward and R. Hoffmann, *The conservation of orbital symmetry* (Elsevier, ADDRESS, 2013).

[350] R. B. Woodward and R. Hoffmann, Angewandte Chemie International Edition in English **8**, 781 (1969).

[351] M. Garavelli, C. Page, P. Celani, M. Olivucci, W. Schmid, S. Trushin, and W. Fuss, The Journal of Physical Chemistry A **105**, 4458 (2001).

[352] M. Ben-Nun and T. J. Martínez, Journal of the American Chemical Society **122**, 6299 (2000).

[353] W. Fuß, W. E. Schmid, S. A. Trushin, P. S. Billone, and W. J. Leigh, ChemPhysChem **8**, 592 (2007).

[354] S. Deb and P. M. Weber, Annu. Rev. Phys. Chem. **62**, 19 (2011).

[355] D. Geppert, L. Seyfarth, and R. de Vivie-Riedle, Applied Physics B **79**, 987 (2004).

[356] S. Kobatake, S. Takami, H. Muto, T. Ishikawa, and M. Irie, Nature **446**, 778 (2007).

[357] H. Longuet-Higgins and E. Abrahamson, Journal of the American Chemical Society **87**, 2045 (1965).

[358] M. J. S. Dewar, Angewandte Chemie International Edition in English **10**, 761 (1971).

[359] J. P. Snyder, The Journal of Organic Chemistry **45**, 1341 (1980).

[360] B. Schilling and J. P. Snyder, Journal of the American Chemical Society **97**, 4422 (1975).

[361] L. Carlsen and J. P. Snyder, Tetrahedron Letters **18**, 2045 (1977).

[362] J. E. Fowler, I. L. Alberts, and H. F. Schaefer III, Journal of the American Chemical Society **113**, 4768 (1991).

[363] Y. Yamaguchi, H. F. Schaefer III, and I. L. Alberts, Journal of the American Chemical Society **115**, 5790 (1993).

[364] Y. Jean, F. Volatron, and N. T. Anh, Journal of Molecular Structure **93**, 167 (1983).

[365] F. Volatron, N. T. Anh, and Y. Jean, Journal of the American Chemical Society **105**, 2359 (1983).

[366] V. Bakulev, V. Kartsev, and V. Mokrushin, Chemistry of Heterocyclic Compounds **25**, 1203 (1989).

[367] G. G. Spence, E. C. Taylor, and O. Buchardt, Chemical Reviews **70**, 231 (1970), see review: for all reactions of nitrone to oxaziridine and subsequent experimental references.

[368] Y. Zhang, M. L. Blackman, A. B. Leduc, and T. F. Jamison, Angewandte Chemie International Edition **52**, 4251 (2013).

[369] K. S. Williamson, D. J. Michaelis, and T. P. Yoon, Chemical Reviews **114**, 8016 (2014), see the review:Various reactions of oxaziridine.

[370] W. D. Emmons, Journal of the American Chemical Society **78**, 6208 (1956).

[371] W. D. Emmons, *ibid.* **57**, 5739 (1957).

[372] E. Schmitz, *Dreiringe mit zwei Heteroatomen: Oxaziridine, Diaziridine, cyclische Diazoverbindungen. Mit 5 Abbildungen* (Springer-Verlag, ADDRESS, 1967), Vol. 9, pp. 6–66.

[373] L. Kaminsky and M. Lamchen, Journal of the Chemical Society C: Organic 2295 (1966).

[374] A. Lattes, E. Oliveros, M. Riviere, C. Belzeck, D. Mostowicz, W. Abramskj, C. Piccinni-Leopardi, G. Germain, and M. Van Meerssche, Journal of the American Chemical Society **104**, 3929 (1982).

[375] E. Oliveros, H. Antoun, M. Riviere, and A. Lattes, Journal of Heterocyclic Chemistry **13**, 623 (1976), expt evidence for the less regioselective product formation from the ring opening of Oxaziridine.

[376] E. Oliveros, M. Rivière, and A. Lattes, Journal of Heterocyclic Chemistry **17**, 1025 (1980).

[377] E. Oliveros, M. Riviere, J. Malrieu, and C. Teichteil, Journal of the American Chemical Society **101**, 318 (1979).

[378] G. F. Field and L. H. Sternbach, The Journal of Organic Chemistry **33**, 4438 (1968).

[379] E. Meyer and G. Griffin, Angewandte Chemie **79**, 648 (1967).

[380] H. Shindo and B. Umezawa, Chemical and Pharmaceutical Bulletin **10**, 492 (1962).

[381] D. R. Boyd, P. B. Coulter, W. J. Hamilton, W. B. Jennings, and V. E. Wilson, Tetrahedron letters **25**, 2287 (1984).

[382] E. Lipczynska-Kochany and J. Kochany, Journal of Photochemistry and Photobiology A: Chemistry **45**, 65 (1988).

[383] J. M. Hostettler, L. Castiglioni, A. Bach, and P. Chen, Physical Chemistry Chemical Physics **11**, 8262 (2009).

[384] D. J. Mann and W. L. Hase, Journal of the American Chemical Society **124**, 3208 (2002).

[385] D. Boyd, W. Jennings, R. Spratt, and D. Jerina, Journal of the Chemical Society D: Chemical Communications 745 (1970).

[386] K. Shinzawa and I. Tanaka, The Journal of Physical Chemistry **68**, 1205 (1964).

[387] K. Koyano and I. Tanaka, The Journal of Physical Chemistry **69**, 2545 (1965).

[388] B. Bigot, D. Roux, A. Sevin, and A. Devaquet, Journal of the American Chemical Society **101**, 2560 (1979).

[389] P. Saini and A. Chattopadhyay, RSC Advances **4**, 20466 (2014).

[390] P. Saini and A. Chattopadhyay, RSC Advances **5**, 22148 (2015).

[391] P. Saini and A. Chattopadhyay, Journal of Chemical Sciences **127**, 1757 (2015).

[392] P. Saini, M. Banerjee, and A. Chattopadhyay, The Journal of Physical Chemistry A **120**, 396 (2016).

[393] M. Polášek and F. Tureček, Journal of the American Chemical Society **122**, 525 (2000).

[394] J. A. Ross, R. P. Seiders, and D. M. Lemal, Journal of the American Chemical Society **98**, 4325 (1976), first description of Psuedo-pericyclic reactions.

[395] S. Sharma, T. Rajale, D. B. Cordes, F. Hung-Low, and D. M. Birney, Journal of the American Chemical Society **135**, 14438 (2013).

[396] M. Barbatti, A. J. Aquino, and H. Lischka, The Journal of Physical Chemistry A **109**, 5168 (2005).

[397] I. Borges Jr, A. J. Aquino, and H. Lischka, The Journal of Physical Chemistry A **118**, 12011 (2014).

[398] G. Zechmann, M. Barbatti, H. Lischka, J. Pittner, and V. Bonačić-Kouteckỳ, Chemical Physics Letters **418**, 377 (2006).

[399] M. Barbatti, A. J. Aquino, and H. Lischka, Molecular Physics **104**, 1053 (2006).

[400] P. D. Adeney, W. J. Bouma, L. Radom, and W. R. Rodwell, Journal of the American Chemical Society **102**, 4069 (1980).

[401] R. González-Luque, M. Garavelli, F. Bernardi, M. Merchán, M. A. Robb, and M. Olivucci, Proceedings of the National Academy of Sciences **97**, 9379 (2000).

[402] A. Thiel and H. Köppel, The Journal of Chemical Physics **110**, 9371 (1999).

[403] H. Köppel, J. Gronki, and S. Mahapatra, The Journal of Chemical Physics **115**, 2377 (2001).

[404] H. Köppel, Faraday Discuss. **127**, 35 (2004).

[405] H. Guo and D. R. Yarkony, Phys. Chem. Chem. Phys. **18**, 26335 (2016).